UCL
Université catholique de Louvain

Université catholique de Louvain, École Polytechnique de Louvain,
Institut de la Matière Condensée et des Nanosciences

FIRST-PRINCIPLES STUDY OF PHOSPHORS FOR WHITE LEDS APPLICATIONS AND OF THE TEMPERATURE DEPENDENCE OF THE ELECTRONIC STRUCTURE

Dissertation présentée en vue de l'obtention du grade de Docteur en Sciences de l'Ingénieur

SAMUEL PONCÉ

Membres du jury
Prof. Bernard Piraux, président
Prof. Xavier Gonze, promoteur
Prof. Tom Leyssens
Dr. Andrea Marini
Dr. Masayoshi Mikami
Prof. Gian-Marco Rignanese

January 2015

Samuel Poncé : *First-Principles Study of Phosphors for White LEDs Applications and of the Temperature Dependence of the Electronic Structure,* January 2015

PUBLICATIONS

Hereafter is the list of publications by the author during the phD thesis.

[9] A. Marini, S. Poncé and X. Gonze, *A Many–Body approach to the electron–phonon problem based on a rigorous merging with Density–Functional and Density–Functional Perturbation Theory*, to be submitted.

[8] S. Poncé, G. Antonius, Y. Gillet, P. Boulanger, J. Laflamme Janssen, A. Marini, M. Côté and X. Gonze, *Temperature dependence of electronic eigenenergies in the adiabatic harmonic approximation*, Physical Review B **90**, 214304 (2014).

[7] G. Antonius, S. Poncé, P. Boulanger, M. Côté and X. Gonze, *Many-body effects on the zero-point renormalization of the band structure*, Physical Review Letters **112**, 215501 (2014).

[6] B. Van Troeye, Y. Gillet, S. Poncé and X. Gonze, *First-principles characterization of the electronic and optical properties of hexagonal $LiIO_3$*, Optical Materials **36**, 1494 (2014).

[5] S. Poncé, G. Antonius, P. Boulanger, E. Cannuccia, A. Marini, M. Côté and X. Gonze, *Verification of first-principles codes: Comparison of total energies, phonon frequencies, electron-phonon coupling and zero-point motion correction to the gap between ABINIT and QE/Yambo*, Computational Materials Science **83**, 341 (2014).

[4] B. Bertrand*, S. Poncé*, D. Waroquiers, M. Stankovski, M. Giantomassi, M. Mikami and X. Gonze, *Quasiparticle electronic structure of barium-silicon oxynitrides for white-LED application*, [*The two first author contributed equally to this work] Physical Review B **88**, 075136 (2013).

[3] S. Poncé, B. Bertrand, P.F. Smet, D. Poelman, M. Mikami and X. Gonze, *First-principles and experimental characterization of the electronic and optical properties of CaS and CaO*, Optical Materials **35**, 1477 (2013).

[2] D. Waroquiers, A. Lherbier, A. Miglio, M. Stankovski, S. Poncé, M.J.T. Oliveira, M. Giantomassi, G.M. Rignanese and X. Gonze, *Band*

widths and gaps from the Tran-Blaha functional: Comparison with many-body perturbation theory, Physical Review B **87**, 075121 (2013).

[1] G. Bonny, D. Terentyev, R.C. Pasianot, S. Poncé, and A. Bakaev, *Interatomic potential to study plasticity in stainless steels: the FeNiCr model alloy*, Modelling and Simulation in Materials Science and Engineering **19**, 085008 (2011).

We are at the very beginning of time for the human race.
It is not unreasonable that we grapple with problems.
But there are tens of thousands of years in the future.
Our responsibility is to do what we can, learn what we can,
improve the solutions, and pass them on.

— Richard P. Feynman —

ACKNOWLEDGEMENTS

Foremost, I would like to express my sincere gratitude to my advisor Prof. Xavier Gonze for the continuous support of my Ph.D study and research, for his patience, motivation, enthusiasm, and immense knowledge. His guidance helped me in all the time of research and writing of this thesis. I could not have imagined having a better advisor and mentor for my Ph.D study.
Besides my advisor, I would like to thank the rest of my thesis committee: Profs. Gian-Marco Rignanese, Bernard Piraux, Tom Leyssens, Andrea Marini and Masayoshi Mikami, for their encouragement, insightful comments, and hard questions.

I would like to acknowledge the whole Abinit, LaTeX, Linux, Python, Fortran-community for support, ideas and some great software.
Doing the Ph.D study was by far one of the best decisions I made: it helped me gain some intellectual confidence while working in a dream environment filled with wonderful people. During these four years, I have met the funny Swedish Martin Stankovski with whom I have shared an home for six months, the fantastic Canadian Gabriel Antonius with whom I have done the 400 blows, the Canadian Capitain Jonathan Laflamme Janssen who's insight helps me tremendously and the melomane organist Yannick Gillet with who I have also shared the office and tons of ideas. I want also to thank all the members of the NAPS who lived in the Sc. 17 with me: Nicolas, Gian-Marco, Jean-Christophe, Jean-Michel, Sadia, Nicky, Annette, Luc, Andrès, Aurélien, Xavier, David, Geoffroy, Anna, Matteo, Sriram, Michiel, Marco and Jean-Jo.
A thesis is not the work of one man but the contribution of many great fellows who helped and taught me a lot. I am in debts to (alphabetical order) Gabriel Antonius, Bruno Bertrand, Giovanni Bonny, Jean-Michel

Beuken, Andrès Botello, Paul Boulanger, Elena Cannuccia, Michel Côté, John Kay Dewhurst, Simon Dubois, Matteo Giantomassi, Yannick Gillet, Xavier Gonze, Geoffroy Hautier, Alain Jacques, Jonathan Laflamme Janssen, Nicolas Leconte, Aurélien Lherbier, Andrea Marini, Anna Miglio, Masayoshi Mikami, Micael Oliveira, Yann Pouillon, Gian-Marco Rignanese, Sangeeta Sharma, Martin Stankovski, Nicola Thrupp, Michiel Van Setten, Matthieu Verstraete and David Waroquiers.

Last but not the least, I would like to thank my family: my parents Michel and Thérèse, my sister Marie, my godfather Bernard and my grandmother Simone. They have always believed in me and helped me to surpass myself. Finally, I would like to dedicate this thesis to my fiancée Marie.

CONTENTS

INTRODUCTION 1

I THE TEMPERATURE DEPENDENCE OF ELECTRONIC EIGENENERGIES 11

1 THEORY OF THE TEMPERATURE DEPENDENCE 13
- 1.1 Historical framework . . . 14
- 1.2 Temp. dep. in adiabatic harmonic approx. . . . 17
  - 1.2.1 Fluctuations of atomic positions . . . 18
  - 1.2.2 Eigenenergies as derivatives with respect to electronic occupation numbers f_n . . . 21
  - 1.2.3 The Fan and Debye-Waller contributions . . . 24
- 1.3 From the adiabatic approximation to AHC . . . 25
  - 1.3.1 Wavevectors and translational invariance . . . 25
  - 1.3.2 The temperature dependence in the adiabatic harmonic approximation for the solid periodic case . . . 27
  - 1.3.3 The rigid-ion Hamiltonian . . . 29
  - 1.3.4 The rigid-ion approximation . . . 30
  - 1.3.5 Beyond the rigid-ion approximation . . . 32
- 1.4 Finite differences over atomic displacements . . . 33
  - 1.4.1 The frozen-phonon approach . . . 33
  - 1.4.2 Frozen-phonon expression of the different terms entering into the ZPR . . . 34
- 1.5 Beyond the Rayleigh-Schrödinger perturbation theory . . . 35
- 1.6 Conclusions . . . 39

2 V&V OF FIRST-PRINCIPLES CODES 41
- 2.1 The V&V framework . . . 42
- 2.2 Validation of the theory . . . 44
- 2.3 Verification methodology . . . 47
- 2.4 Diamond: calculations details . . . 50
- 2.5 Verifications results for diamond . . . 51
  - 2.5.1 Ground-state and phonons . . . 51
  - 2.5.2 Electron-phonon coupling and zero-point motion renormalization . . . 53
  - 2.5.3 Analysis of the convergence with respect to the number of **q**-wavevectors . . . 57
  - 2.5.4 Pseudopotential choices . . . 59

2.6 Conclusions 60
3 APPLICATION TO SOME SEMICONDUCTORS 63
3.1 Temperature dependence of semiconductors in LDA 64
3.1.1 Aluminum Nitride 66
3.1.2 Boron Nitride 69
3.1.3 Diamond 72
3.1.4 Silicon 77
3.2 Analysis of the convergence rate 81
3.3 MB effects on the ZPR 85
3.3.1 DFPT calculations 86
3.3.2 Many-body corrections 86
3.3.3 Temperature dependence of the bandgap 88
3.4 Conclusion 90

II EU-DOPED BA-SI OXYNITRIDES FOR WLEDS APPLICATIONS 93
4 BSON HOST MATERIAL 95
4.1 Historical context 95
4.2 Numerical approach 98
4.3 Results and discussion 100
4.3.1 Crystallographic structure 100
4.3.2 Quasiparticle band structure and density of states . 103
4.3.3 Effective masses 104
4.3.4 Energy shifts and electrostatic potential 106
4.3.5 Absorption spectra at the RPA level 110
4.4 Conclusion BSON 111
5 EUROPIUM-DOPED BSON 113
5.1 Quality of the Eu psp 114
5.1.1 The LDA+U methodology 114
5.1.2 EuO as a test case 115
5.2 Europium-doped BSON ground state calculations 118
5.3 Stokes shift 122
5.4 Europium-doped excited state calculations 125
5.4.1 The core-hole approach 126
5.4.2 The depleted-shifted 4f approach 132
5.5 Importance of the atomic relaxation 135
5.6 Effect of spin-orbit coupling 139
5.7 Glimpse at the ZPR of undoped BSON compounds 140
5.8 Conclusion 143
6 CONCLUSIONS AND PERSPECTIVES 147

III APPENDIX 151

A TEMPERATURE DEPENDENCE 153
A.1 Convention for periodic system . . . 153
A.2 Perturbation theory . . . 153
A.3 The dynamical equations . . . 156
A.4 Phonon wavefunctions . . . 159
A.5 Statistical physics . . . 160
A.6 Static electronic dielectric function . . . 166
A.7 Finite-difference DW_{NRIA} equation . . . 167
A.8 Symmetry Properties . . . 169
A.8.1 Ground states wavefunction . . . 169
A.8.2 Electron-phonon matrix element . . . 171
A.9 Calculation details for diamond . . . 173
A.9.1 Frozen-phonon calculations . . . 174
A.9.2 Many-body effects . . . 174
A.9.3 DFPT calculations . . . 175
A.9.4 Interpolating the many-body effects . . . 175
A.9.5 G_0W_0 calculation of the bare band gap . . . 175
A.10 Calculation details for GaAs . . . 177
A.11 Total energy . . . 178

B CONVERGENCE STUDIES 181
B.1 Convergence studies . . . 181
B.2 The LDA+U methodology . . . 185
B.3 Ground state . . . 187
B.4 Europium-doped excited state calculations . . . 191
B.5 Atomic relaxation . . . 196
B.6 ZPR of undoped BSON compounds . . . 201

BIBLIOGRAPHY 203

LIST OF FIGURES

Figure 0.1 Experimental absorption and emission curve at 4 K for two Eu-doped BSON compounds. 3
Figure 0.2 The 5d-4f crossing decay model. 4
Figure 0.3 Experimental absorption (top) and emission (bottom) curves with temperature for the two Eu-doped BSON compounds. 5
Figure 0.4 The Dorenbos auto-ionization model. 7
Figure 0.5 Absorption and Emission model. 8
Figure 1.1 Feynman diagram of the Fan and Debye-Waller terms. 15
Figure 2.1 Relative differences Δ of the SGKK2 between ABINIT and QE. 54
Figure 2.2 Convergence with respect to the number of random $\mathbf{q}$-wavevetors included in the ZPR calculation. 58
Figure 3.1 Convergence study with respect to the $\mathbf{q}$-point grid density. 67
Figure 3.2 Temperature dependence of bandgaps in AlN. . . . 69
Figure 3.3 Electronic bandstructure of AlN compounds. 71
Figure 3.4 Temperature dependence of bandgaps in c-BN. . . 73
Figure 3.5 Electronic bandstructure of c-BN compound. 73
Figure 3.6 Temperature dependence of bandgaps in diamond. 75
Figure 3.7 Electronic bandstructure of diamond. 76
Figure 3.8 Temperature dependence of bandgaps in Silicon. . 79
Figure 3.9 Temperature dependence of bandgaps in Silicon. . 80
Figure 3.10 Electronic bandstructure of Si compound. 80
Figure 3.11 Convergence study of the integral with respect to the $\mathbf{q}$-point grid density. 82
Figure 3.12 Contribution of a $\mathbf{q} = [x, 0, 0]$ point to renormalization at $\mathbf{k} = \mathbf{\Gamma}$ for α-AlN. 83
Figure 3.13 Contribution of a $\mathbf{q} = [x, 0, 0]$ point to the renormalization at $\mathbf{k} = \mathbf{\Gamma}$ for Si. 84
Figure 3.14 Convergence study of the non-adiabatic integral with respect to the $\mathbf{q}$-point grid density. 85
Figure 3.15 Diamond electron-phonon coupling energies (EPCE) in DFT and *GW* 88

Figure 3.16 Temperature dependence of the direct bandgap computed in DFPT and with GW corrections. 90
Figure 4.1 Crystal structure of BSON host marterial after structural relaxation. 100
Figure 4.2 Crystalline environment of the two inequivalent barium atoms in BSON. 101
Figure 4.3 G_0W_0 host BSON quasiparticle bandstructure. . . . 103
Figure 4.4 Magnitude of G_0W_0 corrections to the DFT eigenergies for the host BSON materials. 105
Figure 4.5 Density of the first unoccupied band (84 th band) of BSON compounds. 106
Figure 4.6 Density of the first unoccupied band (84^{th} band) of BSON compounds 107
Figure 4.7 Density of the sum of the 85 to 90 th bands of BSON compounds 109
Figure 4.8 Comparison of the BSON electromagnetic absorption spectra. 110
Figure 5.1 The LDA+U methodology. 115
Figure 5.2 Comparison between PAW and all-electron calculation for the EuO case using Abinit and the Elk software. 117
Figure 5.3 Ground state of the europium-doped compounds. . 120
Figure 5.4 Configurational digaram. 124
Figure 5.5 Schematic of the crystal field splitting in europium-doped compounds. 126
Figure 5.6 The BSE in terms of Feynman diagrams. 128
Figure 5.7 G_0W_0 bandstructures of the europium-doped compounds in the core-hole approach at the undoped relaxed lattice parameters. 129
Figure 5.8 The different energy polyfit used for the europium-doped electronic bandstructure. 130
Figure 5.9 Brillouin zone of the hexagonal lattice. 131
Figure 5.10 Ground state of the europium-doped compounds in the rhombohedral supercell. 133
Figure 5.11 Electronic bandstructure in the depleted-shifted 4f approach with atomic relaxation and constrained lattice parameters. 136
Figure 5.12 Ground state of the europium-doped compounds. . 138
Figure 5.13 Electronic bandstructure of $Ba_3Si_6O_{12}N_2$:Eu_1 calculated with VASP. 140

Figure 5.14 Temperature dependence of the two undoped BSON compounds. 141
Figure 5.15 Absorption and Emission model. 144
Figure A.1 G. Antonius and S. Poncé in front of L. E. Boltzmann at the Vienna Zentralfriedhof (August 2011). 160
Figure A.2 Modeling of the G_0W_0 EPCE per **q**-point as a function of the DFT EPCE. 176
Figure A.3 Band structure of diamond from a self-consistent GW calculation and LDA. 177
Figure A.4 Electron-phonon coupling energies in GaAs. 179
Figure B.1 Convergence study with respect to the **q**-point grid density. 181
Figure B.2 Convergence study with respect to the **q**-point grid density. 182
Figure B.3 Convergence study with respect to the **q**-point grid density. 183
Figure B.4 Convergence study with respect to the **q**-point grid density. 184
Figure B.5 Ground state of the europium-doped compounds. . 187
Figure B.6 Ground state of the europium-doped compounds. . 190
Figure B.7 Electronic bandstructures of the 1x1x2 supercell calculations computed with the core-hole pseudopotentials at the undoped relaxed lattice parameters . 193
Figure B.8 Ground state of the europium-doped compounds . 194
Figure B.9 Ground state of the europium-doped compounds in the rhombohedral supercell. 195
Figure B.10 Excited state of the europium-doped compounds . 196
Figure B.11 Excited state of the europium-doped compounds in the rhombohedral supercell. 198
Figure B.12 Excited state of the europium-doped compounds . 199
Figure B.13 Excited state of the europium-doped compounds in the rhombohedral supercell. 200

LIST OF TABLES

Table 2.1 Comparison of diamond phonon frequencies computed from FP and from DFPT. 45
Table 2.2 Comparison between the AHC/DFPT and FP results for the contributions of specific **q**-points to the ZPR of several bands of diamond. 46
Table 2.3 Comparison of selected quantities related to the ground state and to phonon calculations for diamond. 52
Table 2.4 Comparison between Abinit and QE of the nine lower eigenenergies in eV. 53
Table 2.5 Comparison between Abinit (AB) and Quantum Espresso (QE) of absolute value of the SGKK2. . . . 55
Table 2.6 Comparison of the ZPR for different electronic states at **Γ**. 56
Table 2.7 Comparison inside Abinit of the ZPR (and its Fan + DW decomposition) for different pseudopotentials at **Γ**. 60
Table 3.1 Convergence and lattice parameters for the different studied compounds. 70
Table 3.2 Direct and indirect DFT electronic bandgaps. 77
Table 3.3 ZPR (meV) computed on a $4 \times 4 \times 4$ **q**-point grid in FP (finite differences) and in DFPT (perturbative DFT). 87
Table 3.4 ZPR (meV) computed on a $32 \times 32 \times 32$ **q**-point grid. The G_0W_0 and GW corrections are interpolated with the models discussed in the text. 89
Table 4.1 Selected bond lengths [in Bohr] of $Ba_3Si_6O_{12}N_2$ and $Ba_3Si_6O_9N_4$ compounds. 102
Table 4.2 Band positions [eV], bandwidth [eV] and the dominant band character of $Ba_3Si_6O_{12}N_2$ and $Ba_3Si_6O_9N_4$ compounds. 108
Table 5.1 Naming convention. 116
Table 5.2 Stokes shift table. 123
Table 5.3 ZPR for the different studied compounds. 142

Table A.1 Zero-point renormalization (meV) in GaAs computed on a $4 \times 4 \times 4$ q-point grid. 178
Table B.1 Selected bond lengths [in Bohr] and cell volume [in Bohr^3] of $Ba_3Si_6O_{12}N_2$ and $Ba_3Si_6O_9N_4$ compounds. 188
Table B.2 Selected bond lengths [in Bohr] and cell volume [in Bohr^3] of $Ba_3Si_6O_{12}N_2$ and $Ba_3Si_6O_9N_4$ compounds. 189
Table B.3 Band positions of the europium-doped compounds at different high symmetry points using the core-hole approach. 192
Table B.4 Selected bond lengths [in Bohr] and cell volume [in Bohr^3] of $Ba_3Si_6O_{12}N_2$ and $Ba_3Si_6O_9N_4$ compounds. 197
Table B.5 ZPR of the two undoped BSON compounds. 201

ACRONYMS

AHC Allen-Heine-Cardona

ASR Acoustic Sum Rule

BO Born-Oppenheimer

BSE Bethe-Salpeter equation

BZ Brillouin Zone

CBM Conduction Band Minimum

CECAM Centre Européen de Calcul Atomique et Moléculaire

DDW Diagonal Debye-Waller

DFPT Density Functional Perturbation Theory

DFT Density Functional Theory

DW Debye-Waller

EP Electron-Phonon

EPCE Electron-phonon coupling energies

FP Frozen Phonons

FWHM Full width at half maximum

GGA Generalized Gradient Approximation

GPU Graphics Processing Unit

Ha Hartree. Energy unit: 1 Ha = 27.211 eV

HPC High-Performance Computing

IBZ Irreducible Brillouin Zone

IFC Interatomic Force Constant

LDA Local Density Approximation

LED Light-Emitting Diode

MD Molecular Dynamics

NDDW Non-Diagonal Debye-Waller

pcLED Phosphor-converted white Light-Emitting Diode

PIMD Path-Integral Molecular Dynamics

QE Quantum Espresso

RIA Rigid-Ion Approximation

VBM Valence Band maximum

ZPR Zero-Point motion Renormalization

INTRODUCTION

White light-emitting diodes (WLEDs) are the subject of an intense world industrial research (Mitsubishi Chemicals, Philips Lumileds, Osram, Nichia, Cree, Seoul semiconductors ...) as they are seen as the most promising light sources to replace incandescent and neon lamps. Indeed the advantages of the WLEDs are numerous: low power consumption (more than 120 lumen/watt), extended lifetime (more than 50.000 working hours), large impact strength, eco-friendly (the WLEDs do not contain toxic mercury like fluorescent lamp) and increased safety (the WLEDs heat less therefore reducing the risk of burns). Some predicts an almost exclusive use of WLEDs as a light source by 2020 [1]. In fact, LEDs are so important that, on October 7, 2014, Professors Isamu Akasaki, Hiroshi Amano and Shuji Nakamura got the Nobel prize in physics for the invention of blue LEDs [2].

There are two primary ways of producing WLEDs. The first one is called the RGB system where individual LEDs that emit three primary colors (red, green and blue) are mixed and give the impression of white light. The other way is to use multiple layers of rare-earth doped luminescent materials called "phosphors" to convert the monochromatic UV or blue light from a diode (usually InGaN) into a broad-spectrum white light. This last type of LEDs are called phosphor-converted white LEDs (pcLEDs). In pcLEDs, part of the light goes through different phosphor layers unaltered whereas another fraction undergoes a Stokes shift (that is, a decrease of energy due to the emission of several phonons) and is down converted to longer wavelength visible light. Even though the pcLEDs working principles inevitably result into heat losses due to Stokes shifts, this type of WLEDs is the most manufactured today due to its simpler and cheaper design.

The radiative emission process in solid is called "luminescence". The study of phosphors with optimized luminescence properties for pcLEDs is the subject of a very active research [3]. Still, a detailed theoretical understanding of their electronic and temperature-dependent properties is lacking. A striking example is given by the two chemically close oxynitride materials, $Ba_3Si_6O_{12}N_2$:Eu and $Ba_3Si_6O_9N_4$:Eu (named generically BSON compounds). The hosts materials have very similar electronic and structural properties [4] but when doped with europium they

exhibit very different luminescence properties and temperature behavior. The $Ba_3Si_6O_{12}N_2$:Eu is a green phosphor with an intensity that stays almost constant with temperature up to its working temperature (around 100 °C) [5], while $Ba_3Si_6O_9N_4$:Eu is a bluish-green phosphor that exhibits an unfavorable decrease of the luminescence intensity with temperature.

When photons interact with a quantum system, they can transmit their energy to the system if this energy corresponds to an allowed quantum transition. This process is called "absorption". The quantum system is then in an excited state. Quantum systems emit light by spontaneous emission when the electrons in the excited state go down to lower level by radiative transitions. In the two-level model developed by Einstein, the rate at which such spontaneous emission occurs is determined by the Einstein coefficient A. The radiative emission rate if there is N excited electrons at time t is [6]

$$\left(\frac{dN}{dt}\right)_{\text{radiative}} = -AN. \tag{0.1}$$

Solving this rate equation gives

$$N(t) = N(0)e^{-At} = N(0)e^{\frac{-t}{\tau_R}}, \tag{0.2}$$

with $\tau_R = A^{-1}$ the radiative lifetime of the transition.

It can be shown (see for example Ref. [6]) that the Einstein coefficient A is directly linked with a similar coefficient for absorption. This means that the transition with large absorption coefficient will also have large emission coefficient. Nonetheless, The absorption and emission spectrum usually are very different from each other because of the Stoke shift, and also of the difference of population (there is usually much more electron in the ground state than in the excited state).

Unfortunately for the WLEDs industry, the radiative emission is not the only way by which an electron can relax to the ground state. Non-radiative process can also take place. For example, the electron can loose entirely its energy as heat by emitting phonons or transfer its energy to impurities or defects called "traps". The total rate equations thus reads

$$\left(\frac{dN}{dt}\right)_{\text{total}} = -N\left(\frac{1}{\tau_R} + \frac{1}{\tau_{NR}}\right). \tag{0.3}$$

The luminescence efficiency η_R (also called "quantum efficiency") is the ratio between the radiative Eq. (0.1) and the total Eq. (0.3) emission process

$$\eta_R = \left(\frac{dN}{dt}\right)_{\text{radiative}} / \left(\frac{dN}{dt}\right)_{\text{total}} = \frac{1}{1 + \frac{\tau_R}{\tau_{NR}}}. \tag{0.4}$$

This implies that the two BSON compounds must have different temperature dependence of their radiative and non-radiative lifetime ratio.

Coming back to the case of the two oxynitride materials, the experimental absorption and emission spectra at 4 K of the two europium-doped materials are superimposed in figure 0.1.

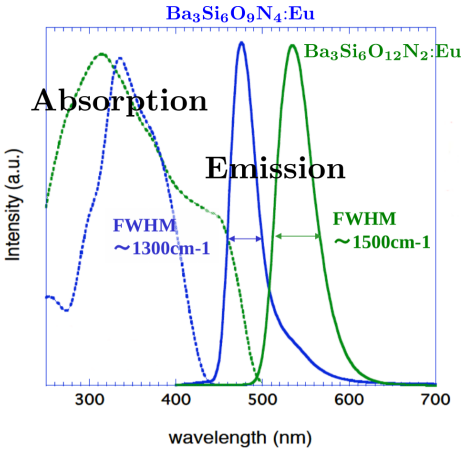
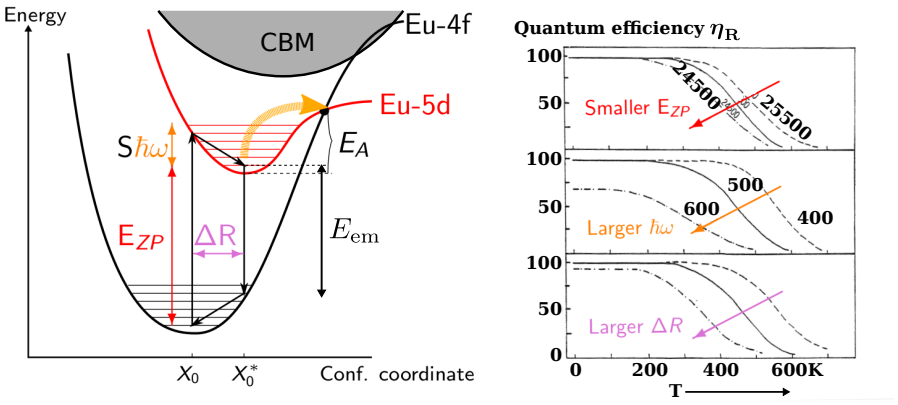


Figure 0.1: Experimental absorption (dashed line) and emission (plain line) curve at 4 K. The photoluminescence excitation (absorption) spectra are obtained by monitoring the 530 nm frequency for $Ba_3Si_6O_{12}N_2$:Eu and 480 nm for $Ba_3Si_6O_9N_4$:Eu. The photoluminescence (emission) spectra are obtained by shining light on the sample at 310 nm and 340 nm for $Ba_3Si_6O_{12}N_2$:Eu and $Ba_3Si_6O_9N_4$:Eu, respectively. Courtesy of M. Mikami.

When the two materials are doped, the europium atom can substitute a barium one at two inequivalent crystallographic positions in the case of $Ba_3Si_6O_{12}N_2$:Eu and at three inequivalent positions in the other material. From figure 0.1, we can measure the full width at half maximum (FWHM) of the two emission curves to 1500 cm^{-1} and 1300 cm^{-1} for $Ba_3Si_6O_{12}N_2$:Eu and $Ba_3Si_6O_9N_4$:Eu, respectively. These two FWHM are considered experimentally rather narrow and therefore it is expected that the luminescence in both compounds only comes from one luminescence centre (one non-equivalent crystallographic position). One of the goal of this thesis is to find out which is the luminescent crystallographic position in both compounds from *ab-initio* calculations.



(a) Configurational diagram model.

(b) Calculations on a model phosphor from Ref. [7].

Figure 0.2: The 5d-4f crossing decay model based on the configurational diagram. Stronger non-radiative decays occurs when the zero phonon line energy difference E_{ZP} is small and the parabola offset ΔR as well as the vibrational frequencies $\hbar\omega$ are large.

A very successful model for explaining luminescence and Stokes shift in phosphors is based on the configurational diagram (see figure 0.2a). In the case of Eu-doped phosphors, the electrons are excited from their 4f band into their excited 5d band by UV/blue photons coming from the InGaN diode. These excited electrons then relax to the bottom of the Eu_{5d} band making the average atomic position move from X_0 to X_0^*. The distance between the ground and excited states atomic position is called the parabola offset ΔR and the energy difference between this excited state level and the ground state level is called the zero-phonon line E_{ZP}. The excited parabola energy difference is the product of the vibrational, or phonon, frequency $\hbar\omega$ and the Huang-Rhys parameter S [3]. From the excited relaxed position, the electron can relax back to the 4f level by emitting a photon of lower energy. The energy difference between the incoming UV/blue photon and the outgoing (green for $Ba_3Si_6O_{12}N_2$:Eu) photon is called the Stokes shift. The change of emission (or absorption) spectra with temperature can be recorded and analyzed. In our case, the green phosphor $Ba_3Si_6O_{12}N_2$:Eu has an intensity that stays almost constant with temperature up to its working temperature (around 100 °C), while $Ba_3Si_6O_9N_4$:Eu is a bluish-green phosphor that exhibits an unfavorable decrease of the luminescence intensity with temperature as shown on figure 0.3.

Moreover, a blue shift with increasing temperature is observed in the emission spectrum for $Ba_3Si_6O_{12}N_2$:Eu, going from 535 nm at 4 K

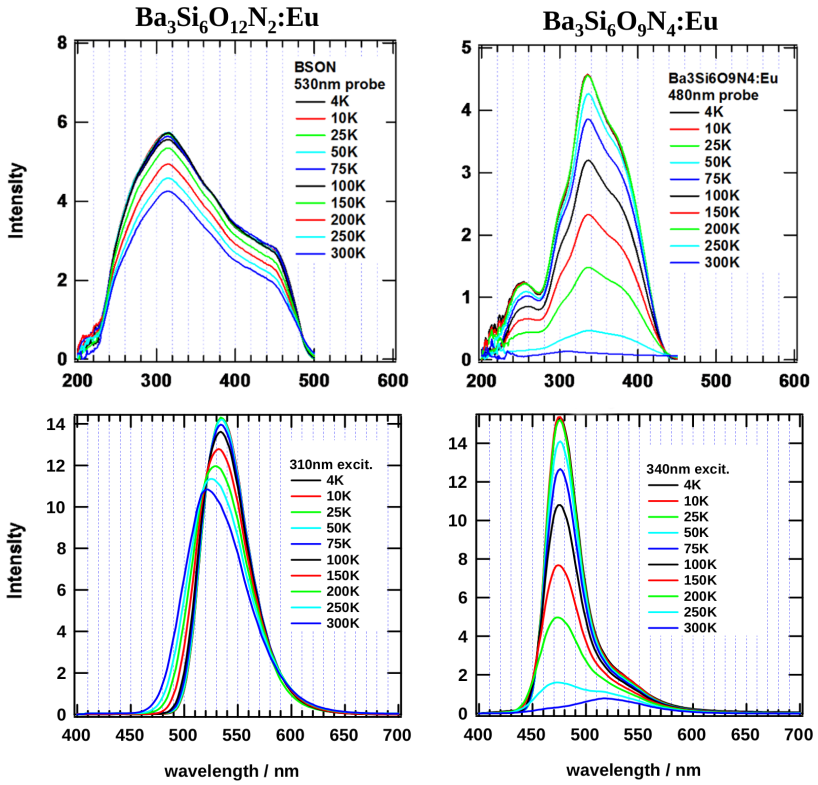


Figure 0.3: Experimental absorption (top) and emission (bottom) curve with temperature for the two Eu-doped BSON compounds from Ref. [8]. The intensity stays almost constant with increasing temperature in the $Ba_3Si_6O_{12}N_2$:Eu case whereas the other phosphor absorbs and emits almost not light at room temperature. Courtesy of M. Mikami.

to 520 nm at 300 K. For $Ba_3Si_6O_9N_4$:Eu almost no such shift is observed and the weak emission at 300 K is attributed to experimental $Ba_3Si_6O_{12}N_2$:Eu impurities in the sample.

The decrease of luminescence intensity with temperature, also called thermal quenching, can be explained by the so-called 5d-4f crossing decay model which is quite popular and is also based on the configurational diagram. In this model, it is believed that if the temperature is large enough, the excited electron of the 5d band can cross the activation energy barrier E_A and go from the 5d to the 4f state through this crossing point of the parabola and decay non-radiatively back into their ground state by simply dissipating heat (that is, emitting phonons).

Based on that model, Blasse and Grabmaier [7] made predictions about the thermal quenching. Stronger non-radiative decays occur when the zero phonon line energy difference E_{ZP} is small and the parabola offset ΔR as well as the vibrational frequencies $\hbar\omega$ are important (see figure 0.2b).

To see how this model applies to the two BSON compounds, let us review the experimental data on those two compounds. The Stokes shift is the energy difference between the absorption ($E_{ZP} + S\hbar\omega$) and the emission E_{em} energy. Both compounds have similar Stokes shifts ΔS of 2790 cm^{-1} and 3230 cm^{-1} for $Ba_3Si_6O_{12}N_2$:Eu and $Ba_3Si_6O_9N_4$:Eu, respectively [5, 9]. From figure 0.3, we can see that $Ba_3Si_6O_9N_4$:Eu has an emission peak that is at higher energy (larger E_{em}) than $Ba_3Si_6O_{12}N_2$:Eu. Finally, as already mentioned, the measured full width at half maximum (FWHM) of the two emission curves are 1500 cm^{-1} and 1300 cm^{-1} for $Ba_3Si_6O_{12}N_2$:Eu and $Ba_3Si_6O_9N_4$:Eu, respectively.

From this, we see that the 5d-4f crossing decay model predicts $Ba_3Si_6O_{12}N_2$:Eu to be more thermally quenched than $Ba_3Si_6O_9N_4$:Eu, in contradiction to the observed stronger thermal quenching in $Ba_3Si_6O_9N_4$:Eu (see figure 0.3). Indeed, $Ba_3Si_6O_{12}N_2$:Eu has a smaller E_{em} than $Ba_3Si_6O_9N_4$:Eu and therefore a smaller E_{ZP} (remember that both compounds have similar Stokes shifts). Since the compounds have similar Stokes shifts, they will have similar ΔR. Moreover, provided that the two parabola have similar curvature, the phonon frequency and the Huang-Rhys parameter S can be deduced from the following two formula [10, 11]

$$\mathrm{FWHM}(T) = \sqrt{8\ln 2}\hbar\omega\sqrt{S}\sqrt{\coth\frac{\hbar\omega}{2k_BT}} \tag{0.5}$$

$$\Delta S = (2S-1)\hbar\omega. \tag{0.6}$$

The solution of the two equations with two unknowns gives

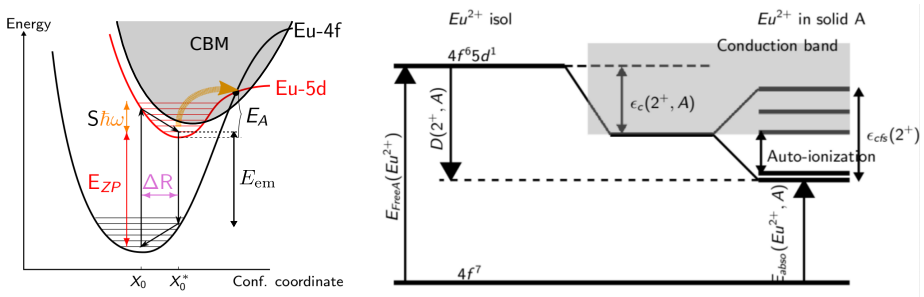
$$S \approx 5 \text{ and } \hbar\omega \approx 300\ cm^{-1} \text{ for } Ba_3Si_6O_{12}N_2\text{:Eu} \tag{0.7}$$

$$S \approx 11 \text{ and } \hbar\omega \approx 160\ cm^{-1} \text{ for } Ba_3Si_6O_9N_4\text{:Eu}. \tag{0.8}$$

where $Ba_3Si_6O_{12}N_2$:Eu has larger $\hbar\omega$ and is therefore expected to have a stronger thermal quenching than $Ba_3Si_6O_9N_4$:Eu, again in contradiction to the observed thermal quenching in the two BSON compounds. Note that the Huang-Rhys parameter S is related to the electron-phonon coupling strength with a value of $S < 1$ being often considered as a weak

coupling and a value of $S > 5$ as a strong coupling [7]. The electron-phonon coupling is therefore expected to be rather strong in both BSON compounds.

Another model, called the Dorenbos auto-ionization model, exists and is based on the fact that in some phosphors the conduction band from the host material is located below the 5d-4f crossing point. In that case, the excited electron from the europium 5d state can get auto-ionized to the conduction band of the host material and undergoes energy dissipation through other non-radiative mechanisms (trapping, defects, lattice vibration ...). This model is presented on figure 0.4 where the grey area represents the conduction band of the host material. Within this model, the phosphor with europium 5d bands that are the closest to the conduction band of its host compound will undergo the stronger thermal quenching.



(a) Configurational diagram model.

(b) Dorenbos auto-ionization model.

Figure 0.4: The Dorenbos auto-ionization model [12] predicts that the excited electron from the europium 5d state can get auto-ionized into the conduction band of the host material and undergoes non radiative energy dissipation.

The main goal of this thesis is to understand the origin of the remarkable difference between the temperature-dependence of the emission intensities of the two europium-doped barium silicate oxynitride compounds: $Ba_3Si_6O_{12}N_2$:Eu and $Ba_3Si_6O_9N_4$:Eu that are used in WLEDs.

From the Dorenbos model and the experimental observations, we propose in figure 0.5 an hypothetical band position for the absorption and emission phenomena in the two compounds. The horizontal band position are in black at 0 K and in green at 300 K (sometimes superimposed when there is no thermal effect). This model is based on the experimental observations mentioned above (the number in black in the figure) and some hypothetical value (in red in the figure). The bandgaps of 6.88 eV

and 6.45 eV of the host materials are obtained with G_0W_0 *ab-initio* calculation from Ref. [4]. It is expected that such bandgaps are almost unaffected by the local ionic relaxation when the europium is in its excited state. The lattice parameters should therefore also stay constant during the absorption-emission process. For the absorption, the 4f-5d gaps of 310 nm (4 eV) and 440 nm (2.8 eV) in $Ba_3Si_6O_{12}N_2$:Eu comes from the peak and shoulder positions of the experimental absorption spectrum of figure 0.3. The splitting of the 5d levels can be ascribed to the crystal field splitting due to the local environment and will be explained later in this thesis. The equivalent 4f-5d gap in $Ba_3Si_6O_9N_4$:Eu is located at 340 nm (3.65 eV). Similar consideration leads us to 5d-4f gaps of 535 nm (2.32 eV) and 480 nm (2.6 eV) for $Ba_3Si_6O_{12}N_2$:Eu and $Ba_3Si_6O_9N_4$:Eu, respectively. There is an additional blue shift of 0.06 eV at 300 K in the emission curve of figure 0.3 in the case of $Ba_3Si_6O_{12}N_2$:Eu. The hypo-

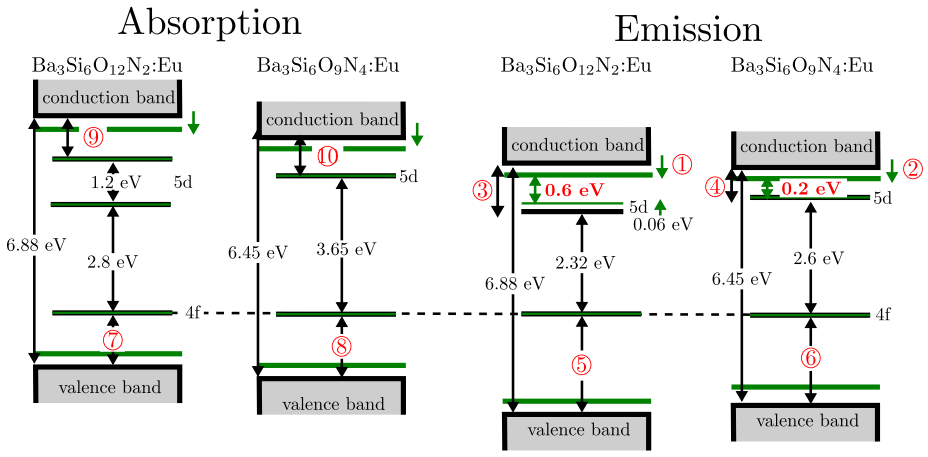


Figure 0.5: Proposed hypothetical band positions for the absorption and emission phenomena in $Ba_3Si_6O_{12}N_2$:Eu and $Ba_3Si_6O_9N_4$:Eu. The energy gap (in eV) are in black when it is experimental values (or G_0W_0 *ab-initio* value for the two band-gaps of the host materials for the absorption taken from Ref. [4]) and in red when the value are hypothetical. The horizontal band positions are in black at 0 K and in green at 300 K (sometimes superimposed when there is no thermal effect). We are interested by the numerical values of the 1-10 unknown gaps.

thetical values in red are based on the following set of assumptions: (i) the 4f levels being very local in space, they weakly react to their surrounding. As such it is expected that the position of the 4f states are the same in both compounds. (ii) The valence to 4f gap increase after ionic relaxation due to the europium atom being in its excited state. (iii) The

5d to CBM gap decrease due to temperature. (iv) From the Dorenbos' empirical formula

$$\Delta E = \frac{T_{0.5}}{680} eV, \tag{0.9}$$

where $T_{0.5}$ is the quenching temperature at which the emission intensity has dropped to 50% of the low temperature value and ΔE is the energy barrier [13], we can estimate the activation energy barrier. For $Ba_3Si_6O_9N_4$:Eu, the experimental $T_{0.5} \approx 150K$ (see figure 0.3). Such a quenching temperature leads to a 5d to CBM gap of approximatively 0.2 eV for $Ba_3Si_6O_9N_4$:Eu, in accordance with our hypothetical model of figure 0.5. The equivalent activation energy for $Ba_3Si_6O_{12}N_2$:Eu can be obtained thanks to additional experimental emission data in the temperature range 300-450 K. This leads to a 5d to CBM gap of approximatively 0.6 eV and is discussed in Ref. [9].

The hypothesis (i)-(ii) and (iv) are investigated in Part II of this thesis and the hypothesis (iii) is investigated in Chapter 1. The variations of the eigenenergies (bands) with the temperature within a purely *ab-initio* framework requires the use of theories based on the accurate description of the electron-phonon interaction and more specifically on the effect of the lattice vibrations on the electronic properties. In Part I of this thesis, we will first review the temperature-dependence of eigenenergies theory. The theory will then be validated, verified and applied to the case of simple semiconductors (α-AlN, β-AlN, c-BN, diamond and silicon). This work is based on the original implementation by Dr. Boulanger of the Allen-Heine-Cardona (AHC) temperature-dependence theory inside the Abinit software. This theory will be applied to the BSON host compounds at the end of the thesis, although computational capabilities will prevent the calculations to be fully converged.

More specifically, Chapter 1 compares in detail two of the three approaches still used today to calculate the zero-point motion renormalization (ZPR). An important contribution of this chapter is the clarification of the terms appearing beyond the rigid-ion approximation (RIA) made in the AHC theory. The extension of the theory to the dynamical case is also presented. The Chapter 2 validates the theory by comparing the results obtained for diamond with two methodologies that can be made equivalent. We compare such results obtained with the Abinit implementation of Dr. Boulanger with those from another *ab-initio* code (Yambo on top of Quantum Espresso). This crucial step resolves a discrepancy with previously published results on the value of the ZPR of the direct bandgap of diamond and sets it to -409 meV. The Chapter 3 presents the

application of the theory developed in the first two chapters to the case of five semiconductors and compares the results with the experiments when available.

Part II of this thesis presents the BSON host materials (Chapter 4) as well as its five europium-doped substitutions (Chapter 5). We will use different levels of theory as well as different approaches to predict the position of the europium 5d states with respect to the conduction band minimum (CBM) of the host materials. This will allow us to confirm or reject the Dorenbos auto-ionization model and gain more insight on the physical principles behind thermal quenching. Among the five possible europium-doped substitutions, the luminescent centers are clearly identified and characterized. Because the fully converged application of the temperature-dependence theory developed in Part I to the europium-doped BSON cases is unfortunately computationally out of reach at present, the thermal quenching is studied from *ab-initio* electronic structure calculations at zero temperature. We nonetheless show some preliminary results on the temperature-dependence of the two undoped BSON compounds in section 5.7.

Part I

THE TEMPERATURE DEPENDENCE OF ELECTRONIC EIGENENERGIES

The temperature dependence of electronic eigenenergies theory has a long and chaotic history that started in the fifties with Fan and Antončík [14, 15, 16]. They both developed independent theories that were only unified in 1974 by Baumann [17]. The first temperature-dependence calculation made using density functional theory (DFT) was performed by King-Smith in 1989 [18]. Since then, three popular *ab-initio* approaches have been used to compute the influence of lattice vibration on electronic eigenenergies.

Chapter 1 will review the history of the temperature dependence theory and present the state of the art approach to solve this problem. We will clarify the different terms entering into the perturbation based theory and briefly present its dynamical extension. The Chapter 2 will be dedicated to a careful numerical verification and validation of the theory within the Abinit software but also cross checking the implementation with the one of the Quantum Espresso and Yambo codes. Finally, in Chapter 3 we will apply the theory to semiconductors (α-AlN, β-AlN, c-BN, diamond and silicon). The electronic bandstructure, zero-point motion renormalization and phonon-induced lifetime broadening will be given for each of the studied semiconductors. The additional correction brought by many-body theories will also be shown for diamond and GaAs using the frozen-phonon approach.



1

THEORY OF THE TEMPERATURE DEPENDENCE

In this chapter, we will clarify or establish links between three different approaches of the temperature dependence within the adiabatic approximation at the first-principle level, for semiconductors and insulators. The theory does not apply to metals as the phonon frequencies cannot be neglected with respect to electronic excitations in this case. The same limitation is also encountered for semiconductors and insulators with a temperature sufficiently high to create a non-negligible population of holes and conduction electrons. So, provided the adiabatic approximation is valid, we establish Brook's theorem, and provide a detailed analysis of the difference between the Allen-Heine-Cardona (AHC) and the frozen phonons (FP) approach, elaborating on the brief results presented in Ref. [19].

The structure of the chapter is as follows. Section 1.2 examines Brooks theorem which relies, at the first-principle level, on Janak's theorem generalized to the case where the free energy including the vibrational entropy is used, instead of a purely electronic expression. Section 1.3 links the equations of section 1.2 with the AHC theory, in the periodic case (with notations suitable for later practical implementation) and also explores rigorously the rigid-ion approximation. In particular, one distinguishes the Fan contribution, the rigid-ion Debye-Waller (DW_{RIA}) contribution and the non rigid-ion Debye-Waller (DW_{NRIA}) contribution. The sum over a large number of bands, present in the AHC theory, can be reduced drastically, by complementing it with an expression based on the projection over high energy bands of the first-order wavefunctions, in the spirit of the Sternheimer equation. Section 1.4 establishes the connection between those equations and an equivalent finite-difference approach. Finally, section 1.5 extend the theory beyond the Rayleigh-Schrödinger perturbation theory to derive an expression for the phonon-induced lifetime.

All equations derived in this chapter are expressed in Hartree atomic unit where $m_e = \hbar = e = 1$.

The content of sections 1.1 to 1.4 has been submitted for publication [20].

1.1 HISTORICAL FRAMEWORK

Electronic properties of solids and nanostructures can be computed from first principles with varying accuracy. In particular, the widespread *GW* approximation [21] within many-body perturbation theory describes electronic bandgaps with errors in the range of 0.1-0.3 eV with respect to experiment [22]. Excitonic effects can be added based on the Bethe-Salpeter equation (BSE) [23]. However, a crucial ingredient is often disregarded: the electron-phonon interaction. Incidentally, the most advanced self-consistent *GW* calculations usually lead to overestimated bandgaps [22], and most of the remaining discrepancy might be due to the electron-phonon interaction. Indeed, the influence of the lattice vibration at 0 Kelvin, known as the zero-point motion renormalization (ZPR), can be as large as 0.37 eV for the indirect bandgap of diamond [24, 25]. This correction often leads to a reduction of the bandgap and hence might be crucial to correct the overestimation of self-consistent *GW* approximation.

The study of the direct effects of the electron-phonon interaction on the electronic structure has a long history. From the fifties to the late eighties, they were investigated and computed in a semi-empirical context. It was first recognized that the temperature dependence of the electronic energies has two different origins: the volume expansion (studied by Shockley and Bardeen [26]) and the electron-phonon interaction at constant volume. In fact, the effect of the electron-phonon interaction at constant volume is usually the major contribution, and proves to be the most difficult to compute from first principles. This contribution is the focus of this chapter[1]. In a pioneering work, Fröhlich introduced a model Hamiltonian that includes these interactions [28, 29, 30]. However, his approach leads to overscreening of phonon frequencies and involves empirical parameters [31].

In parallel, the self-energy contribution to electronic eigenenergy renormalization due to thermal vibrations was introduced by Fan [14, 15].

1 Although first-principle studies of thermal expansion are not very frequent, the formalism is well-established (at least for rather symmetric crystals, see e.g. Rignanese *et al* [27]).

His theory has no adjustable parameters and is based on the first-order perturbed Hamiltonian. Later, Cohen [32] used the Fan self-energy to compute the temperature dependence of the germanium bandgap. Also, ideas from electron diffraction theories based on thermally averaged nuclear potentials lead Antončík [16] and others [33, 34, 35] to develop empirical Debye-Waller (DW) corrections to the nuclear potential. As these two lines of thought (Fan and DW) were developed independently of each other, only one of them was usually included in calculations.

At about the same time as Antončík, Brooks [36] emphasized that the electronic gap is actually a free energy difference with respect to varying occupation numbers of electronic and phononic levels. Furthermore, Allen and Hui [37] highlighted the equivalence between the action of the phonon population (atomic position fluctuations) on the electronic eigenenergies and the action of the electronic occupations on the phonon eigenfrequencies. This equivalence, that was later called Brook's theorem, was used in the eighties by several authors to discuss the temperature dependence of eigenenergies [37, 18].

In 1974, Baumann [17] first suggested that both the Fan self-energy and DW terms were needed to describe the influence of lattice vibrations on the electronic eigenenergies (see figure 1.1 for the Feynman diagram representation of the two terms). Two years later, Allen and

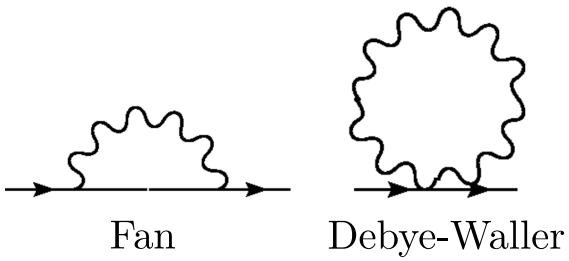


Figure 1.1: Feynman diagram of the Fan and Debye-Waller terms.

Heine [38] rigorously unified the theory and made the DW term translationally invariant. Their approach, combined with the rigid-ion approximation (RIA), which is valid for their semi-empirical model, allows for a re-writing of the problem in terms of first-order derivatives of the effective potential only. Calculations of electron-phonon renormalization were then led by Cardona and coworkers [39, 40, 41, 42], including Allen, based on physically motivated models [43, 44] or on rigid-ion pseudopotentials approximations and empirical phonon models. The resulting approach is now called the Allen-Heine-Cardona (AHC) theory.

Until then, none of the calculation were based on first principles. In 1989, King-Smith *et al* [18] computed the temperature-dependent bandgap of Silicon using Density Functional Theory (DFT) [45], by evaluating the change of phonon frequencies due to electronic occupations and invoking Brook's theorem.

It took more than one decade before other first-principles calculations were performed. Such studies relied on widely varying formalisms and methods, that can be broadly classified in three types, each with their distinct advantages and drawbacks. First, the temperature-dependent eigenenergies can be computed as a time average of the bandgap obtained using first-principles molecular dynamics (MD) simulations. Using this method, Franceschetti [46] studied Si nanocrystals, Kamisaka *et al* [47] studied CdSe and PbSe quantum dots and Ibrahim [48] the temperature dependence of the optical response of GaAs. Ramírez *et al* [49, 50] simulated the temperature dependence of diamond and 3C-SiC bandgap based on path-integral molecular dynamics (PIMD). This approach has the interesting characteristics that it includes effects beyond the harmonic approximation. Moreover, while normal molecular dynamics, which involves the harmonic approximation, wrongly gives a classical Boltzmann statistics for phonons, the more computationally demanding PIMD properly includes nuclear quantum effects and gives Bose-Einstein statistics for phonons. TThus, with PIMD, zero-point motion effects are observed. However, this MD (or PIMD) method is most suited for finite systems. Indeed, for solids, a supercell has to be used to sample the phonon wavevector space, with a corresponding increase of the computational time and memory.

A second method uses frozen phonons (FP): the computation of the change of eigenenergies due to atomic displacements along the normal modes is followed by a Bose-Einstein weighted sum of the contribution of each mode. In 2005, Capaz *et al* [51] studied the temperature dependence of carbon nanotube bandgap within the framework of a tight-binding method. Patrick *et al* [52] examined diamondoids, and Han and Bester [53] studied various semiconductor nanoclusters, still using the FP method but this time with DFT simulation. Anharmonic electron-phonon contributions to the temperature dependence of the indirect bandgap of diamond were also studied by Monserrat *et al* [54] with the same methodology. Recently, Antonius *et al* [55], still relying on the FP method, computed the renormalization of the diamond bandgap within the GW approximation and observed a large increase of the renormalization with respect to DFT, in better agreement with experimental values.

This result is in line with earlier estimations of many-body effects on electron-phonon coupling [56, 57, 58, 59, 60, 61].

As a third approach, the diagrammatic method of many-body perturbation theory (see figure 1.1), from which the AHC approach originates, allowed Giustino *et al* [62] to compute the ZPR and the temperature dependence of the diamond bandgap with Wannier functions in the Density-Functional perturbation theory (DFPT) [63, 64] framework. Marini *et al* [65, 66, 67, 68] focused on the dynamical effects, beyond the adiabatic approximation, which are absent from the two previous approaches (MD and FP).

There has been some confusion about the (non)-equivalence of these three approaches, in the first-principles context. Although the first (MD) and second (FP) ones are equivalent when considered within the adiabatic harmonic approximation, the third one (AHC) is equivalent to the MD and FP *only* when the rigid-ion approximation is valid, which is not the case in the first-principle context. Indeed, Gonze *et al* [19] pointed out that the FP and AHC formalisms differ by non-diagonal Debye-Waller terms, and computed these for simple diatomic molecules. In some cases, the non-diagonal Debye-Waller terms were as large as the direct terms. They also reformulated the AHC theory using Sternheimer equations instead of summations over empty states, which led to a significant speed-up of their calculations.

To complete this literature overview, the phonon-induced lifetime broadening of the electronic states derived from the imaginary part of the Fan self-energy was investigated by Lautenschlager [69, 70] in a semi-empirical context, and, more recently, by Giustino [71] and Restrepo [72, 73] with a first-principle implementation.

1.2 TEMPERATURE-DEPENDENT ELECTRONIC EIGENENERGIES IN THE ADIABATIC HARMONIC APPROXIMATION

Brook's theorem states that the shift in an electronic eigenenergy (labeled n) due to the electron-phonon interaction, when a phonon is added in a phononic mode (labeled m), is equivalent to the shift in the m phonon mode eigenfrequency when an electron is placed in the n level, also caused by the electron-phonon interaction. Namely, [36, 37, 18]

$$\frac{\partial \varepsilon_n}{\partial n_m} = \frac{\partial \omega_m}{\partial f_n}, \tag{1.1}$$

with ε_n and f_n being respectively the eigenenergy and the thermal average of the occupation of the electronic state n, while ω_m and n_m are

the eigenfrequency and the thermal average of the phononic occupation of the phonon mode m, respectively.

In this section, we detail this equality in a first-principles context: the phonons are obtained in the harmonic adiabatic approximation from the interatomic force constants, themselves second-order derivatives of the Born-Oppenheimer total energy in which the electronic occupations effects can be traced explicitly.

We decided, for pedagogical reasons, to work in this section with isolated systems but the extension to periodic systems is straightforward using the convention of appendices A.1 and A.2.

1.2.1 *Fluctuations of atomic positions*

The eigenfrequencies ω_m and unitless mass-scaled eigendisplacements $\xi_{m,\kappa\alpha}$ for the phonon mode m can be obtained from the dynamical equation [74] (also see Appendix A.3 for more informations)

$$\sum_{\kappa\alpha} D_{\substack{\kappa\alpha \\ \kappa'\gamma}} \xi_{m,\kappa\alpha} = \omega_m^2 \xi_{m,\kappa'\gamma}, \tag{1.2}$$

where κ and κ' label atoms in the unit cell, α and γ label the cartesian spatial dimensions, and $D_{\substack{\kappa\alpha \\ \kappa'\gamma}}$ are the mass-scaled interatomic force constants.

The mass-scaled quantities are expressed as follows:

$$\begin{aligned} \xi_{m,\kappa\alpha} &= \sqrt{M_\kappa} U_{m,\kappa\alpha}, \\ D_{\substack{\kappa\alpha \\ \kappa'\gamma}} &= \frac{1}{\sqrt{M_\kappa}} C_{\substack{\kappa\alpha \\ \kappa'\gamma}} \frac{1}{\sqrt{M_{\kappa'}}}, \end{aligned} \tag{1.3}$$

where M_κ is the mass of atom κ, $U_{m,\kappa\alpha}$ is the phonon eigendisplacements, and

$$C_{\substack{\kappa\alpha \\ \kappa'\gamma}} = \frac{\partial^2 E^{BO}}{\partial R_{\kappa\alpha} \partial R_{\kappa'\gamma}}, \tag{1.4}$$

are the inter-atomic force constants (IFC), where E^{BO} is the Born-Oppenheimer energy of the system (which excludes the kinetic energy of the nuclei), computed from first principles. Using the fact that the mass-scaled eigendisplacements $\xi_{m,\kappa\alpha}$ are orthonormal and complete, the phonon frequencies can be obtained from

$$\omega_m^2 = \sum_{\substack{\kappa\alpha \\ \kappa'\gamma}} U^*_{m,\kappa'\gamma} C_{\substack{\kappa\alpha \\ \kappa'\gamma}} U_{m,\kappa\alpha} \tag{1.5}$$

and the normalisation of phonon eigendisplacements is

$$\sum_{\kappa\alpha} M_\kappa U^*_{m,\kappa\alpha} U_{m',\kappa\alpha} = \delta_{mm'}. \tag{1.6}$$

Within the harmonic approximation, where normal modes are decoupled from each other, we express the static temperature dependence of the eigenenergies $\varepsilon_n(T)$ as a thermal average of the value of the position-dependent eigenenergies $\tilde{\varepsilon}_n[z\mathbf{U}]$, where $z\mathbf{U}$ denotes generically a displacement from the equilibrium atomic positions

$$\varepsilon_n(T) \triangleq \langle \tilde{\varepsilon}_n[z\mathbf{U}] \rangle (T) \tag{1.7}$$

$$= \sum_m^{3N} \frac{1}{\mathcal{Z}_m} \sum_{s_m} e^{\frac{-(s_m+1/2)\omega_m}{k_B T}} \int \chi^*_{m,s_m}(z) \tilde{\varepsilon}_n[z\mathbf{U}_{m,\kappa}] \chi_{m,s_m}(z) dz, \tag{1.8}$$

with N the number of atom, T the temperature, s_m the integer occupation of phonon mode m, $\mathcal{Z}_m = \sum_{s_m} e^{\frac{-(s_m+1/2)\omega_m}{k_B T}}$ the mode-partition function, k_B the Boltzmann's constant, $\chi_{m,s_m}(z)$ the phonon eigenfunctions, z the spatial coordinate associated with a phonon mode and where bold symbols like $\mathbf{U}_{m,\kappa}$ denote cartesian vectors.

We can expand the eigenenergies $\tilde{\varepsilon}_n[z\mathbf{U}_{m,\kappa}]$ of Eq. (1.7) in a Taylor series up to second order in z since we are working within the harmonic approximation

$$\tilde{\varepsilon}_n[z\mathbf{U}_{m,\kappa}] = \tilde{\varepsilon}_n[0] + z \frac{d}{dz} \tilde{\varepsilon}_n[z\mathbf{U}_{m,\kappa}]\Big|_{z=0} + \frac{1}{2} z^2 \frac{d^2}{dz^2} \tilde{\varepsilon}_n[z\mathbf{U}_{m,\kappa}]\Big|_{z=0}, \tag{1.9}$$

and insert it in Eq. (1.7). Using the properties of phononic wavefunctions in an harmonic potential (see appendix A.4 for more details), we obtain

$$\varepsilon_n(T) = \tilde{\varepsilon}_n[0] + \frac{1}{2} \sum_m^{3N} \frac{1}{\mathcal{Z}_m \omega_m} \frac{d^2}{dz^2} \tilde{\varepsilon}_n[z\mathbf{U}_{m,\kappa}]\Big|_{z=0} \sum_{s_m} e^{-(s_m+1/2)\alpha_m} \left(\frac{2s_m+1}{2}\right), \tag{1.10}$$

where we have defined $\alpha_m \triangleq \frac{\omega_m}{k_B T}$.

For sake of brevity, we introduce the notation $\Delta\varepsilon_n(T) \triangleq \varepsilon_n(T) - \tilde{\varepsilon}_n[0]$. Using the properties of geometrical series

$$\begin{aligned} \sum_{s_m} (e^{-\alpha_m})^{s_m} &= \frac{1}{1-e^{-\alpha_m}} = I(\alpha_m) \\ \sum_{s_m} (e^{-\alpha_m})^{s_m} s_m &= -\frac{dI(\alpha_m)}{d\alpha_m} = \frac{e^{-\alpha_m}}{(1-e^{-\alpha_m})^2} \end{aligned} \tag{1.11}$$

to evaluate the sum over s_m, we get

$$\Delta\varepsilon_n(T) = \frac{1}{2}\sum_m^{3N} \frac{1}{\frac{e^{-\alpha_m/2}}{1-e^{-\alpha_m}}\omega_m} \frac{d^2}{dz^2}\tilde{\varepsilon}_n[z\mathbf{U}_{m,\kappa}]\Big|_{z=0} e^{-\alpha_m/2}\left(\frac{e^{-\alpha_m}}{(1-e^{-\alpha_m})^2} + \frac{1}{2(1-e^{-\alpha_m})}\right), \tag{1.12}$$

which simplifies to

$$\Delta\varepsilon_n(T) = \sum_m^{3N} \frac{1}{2\omega_m} \frac{d^2}{dz^2}\tilde{\varepsilon}_n[z\mathbf{U}_{m,\kappa}]\Big|_{z=0} \left(n_m(T) + \frac{1}{2}\right), \tag{1.13}$$

where we have introduced the Bose-Einstein distribution

$$n_m(T) = \frac{1}{e^{\frac{\omega_m}{k_B T}} - 1}. \tag{1.14}$$

We can consider the phonon occupation number $n_m(T)$ as an independent variable in this expression, in which case

$$\frac{\partial\varepsilon_n}{\partial n_m} \triangleq \frac{\partial\varepsilon_n(T)}{\partial n_m(T)} = \frac{1}{2\omega_m} \frac{d^2}{dz^2}\tilde{\varepsilon}_n[z\mathbf{U}_{m,\kappa}]\Big|_{z=0}, \tag{1.15}$$

where we have defined the short-hand notation on the left hand side of the equation because each term in the central part of the equation depends on the temperature but their ratio does not. The slope of the eigenenergies with the phononic occupation is therefore independent of temperature and we will remove the explicit dependence of the terms when considering the slope. Eq. (1.13) can thus be written

$$\Delta\varepsilon_n(T) = \sum_m^{3N} \frac{\partial\varepsilon_n}{\partial n_m}\left(n_m(T) + \frac{1}{2}\right). \tag{1.16}$$

Then, the zero-point motion contribution (ZPR) is simply the shift of the eigenenergies at $T = 0$, that is

$$\Delta\varepsilon_n(T=0) = \frac{1}{2}\sum_m^{3N} \frac{\partial\varepsilon_n}{\partial n_m}, \tag{1.17}$$

highlighting that $\varepsilon_n(T=0) \neq \varepsilon_n[0]$. Additionally, from Eqs. (1.5) and (1.6) we can see that the phonon frequency goes as $M_\kappa^{-1/2}$. The $\mathbf{U}_{m,\kappa}$ goes as $M_\kappa^{-1/2}$ and the $z\mathbf{U}_{m,\kappa}$ must have the dimension of length because it is an ionic displacement (see Eq. (1.13)). Therefore, the z must have the dimension of $M_\kappa^{1/2}$ times length. All of this leads to the fact that the ZPR of Eq. (1.13) goes as $(\omega_m M_\kappa)^{-1}$, i.e. as $M_\kappa^{-1/2}$. This "isotopic effect" allows for experimental measurements of the zero-point renormalization by substituting atoms with heavier isotopes, as explained in the review paper of Cardona and Thewalt [25].

1.2.2 *Eigenenergies as derivatives with respect to electronic occupation numbers* f_n

Following Janak, we extend to fractional occupations the first-principle Born-Oppenheimer energy E^{BO}. Janak's theorem [75] then gives

$$\varepsilon_n = \frac{\partial E^{BO}}{\partial f_n}, \tag{1.18}$$

where it has to be noted that the Janak theorem breaks down, within DFT, if the exact exchange-correlation functional (or any non-analytic functional with respect to the occupation) is used. In that case, the total energy is not a continuous function of the electronic occupation anymore and eigenenergies must be defined as differences of total energies with integral occupations numbers.

We now complement the Born-Oppenheimer energy with phonon energy and entropy at the harmonic level. The energy becomes

$$\begin{aligned} E(T) &= E^{BO} + E_{vib}(T) \\ &= E^{BO} + \sum_m^{3N} \omega_m \left(n_m(T) + \frac{1}{2} \right), \end{aligned} \tag{1.19}$$

where E^{BO} is the total energy without phonon and electron-phonon contributions and where $E_{vib}(T)$ is derived in the Appendix A.5 (Eq. A.62). The Hamiltonian of an harmonic oscillator can also be obtained from second quantization (i.e. quantization of force fields by a quantized exchange of particle) $H = \sum_m \omega_m [a_m^\dagger a_m + 1/2]$ with the creation $a_m^\dagger$ and annihilation a_m operators. The mathematical development is given for example in chapter 1 of Mahan [76]. The total energy is the Helmholtz free energy [77] when the vibrational entropy is taken into account

$$F(T) \triangleq E(T) - TS_{vib}(T), \tag{1.20}$$

where S_{vib} is the vibrational entropy (see Eq. A.67 for more informations),

$$S_{vib}(T) = k_B \sum_m^{3N} \Big((1 + n_m(T)) \ln(1 + n_m(T)) - n_m(T) \ln(n_m(T)) \Big). \quad (1.21)$$

We now show that the temperature-dependent eigenenergies can be obtained from the extension of Janak's theorem to finite phonon temperature

$$\varepsilon_n(T) = \frac{\partial F(T)}{\partial f_n}. \quad (1.22)$$

For sake of simplicity, we neglect the dependence of the Born-Oppenheimer energy E^{BO} on electronic temperature. Actually, the explicit treatment of the electron system at finite temperatures (e.g. using the Mermin functional [78]), supposing (wrongly) the adiabatic approximation to be still valid. Using the definition of $\varepsilon_n(T)$ given in Eq. (1.22) and taking into account the dependence of the phonon frequencies on electronic occupation numbers as well as the dependence of phonon occupation numbers on electronic occupation numbers, the change of eigenenergies due to electron-phonon interaction becomes

$$\Delta\varepsilon_n(T) = \sum_m^{3N} \left(\frac{\partial \omega_m}{\partial f_n} \left(n_m(T) + \frac{1}{2} \right) + \omega_m \frac{\partial n_m(T)}{\partial f_n} - T \frac{\partial S_{vib}}{\partial n_m(T)} \frac{\partial n_m(T)}{\partial f_n} \right). \quad (1.23)$$

Substituting Eq. (1.21) for S_{vib} into Eq. (1.23) gives

$$\Delta\varepsilon_n(T) = \sum_m^{3N} \left(\frac{\partial \omega_m}{\partial f_n} \left(n_m(T) + \frac{1}{2} \right) + \omega_m \frac{\partial n_m(T)}{\partial f_n} - k_B T \frac{\partial n_m(T)}{\partial f_n} \ln \left(\frac{1 + n_m(T)}{n_m(T)} \right) \right). \quad (1.24)$$

Using Eq. (1.14), the last 2 terms in the sum cancel out. We thus obtain

$$\Delta\varepsilon_n(T) = \sum_m^{3N} \frac{\partial \omega_m}{\partial f_n} \left(n_m(T) + \frac{1}{2} \right). \quad (1.25)$$

This is a first important result of the present chapter. It was never derived starting from the free energy Eq. (1.20) and the finite temperature extension of Janak's theorem Eq. (1.22). Identification of Eq. (1.25) with Eq. (1.16) obviously yields

$$\frac{\partial \varepsilon_n}{\partial n_m} = \frac{\partial \omega_m}{\partial f_n}. \tag{1.26}$$

This link can be more rigorously established as follows. The derivative of the phonon frequency is retrieved from deriving Eq. (1.5) with respect to electronic occupation

$$2\omega_m \frac{\partial \omega_m}{\partial f_n} = \sum_{\substack{\kappa\alpha \\ \kappa'\gamma}} \frac{\partial C^{\kappa'\gamma}_{\kappa\alpha}}{\partial f_n} U^*_{m,\kappa'\gamma} U_{m,\kappa\alpha}, \tag{1.27}$$

where the derivative of the displacements $U_{m,\kappa\alpha}$ with respect to the electronic occupations f_n does not contribute thanks to the Hellmann-Feynman theorem [79, 80]. The temperature dependence of the eigenenergies is obtained by substituting the preceding result for $\frac{\partial \omega_m}{\partial f_n}$ into Eq. (1.25)

$$\Delta\varepsilon_n(T) = \sum_m^{3N} \frac{1}{2\omega_m} \sum_{\substack{\kappa\alpha \\ \kappa'\gamma}} U^*_{m,\kappa'\gamma} \frac{\partial C^{\kappa'\gamma}_{\kappa\alpha}}{\partial f_n} U_{m,\kappa\alpha} \left(n_m(T) + \frac{1}{2} \right). \tag{1.28}$$

Using Janak's theorem, we can reformulate the derivative of the IFC into derivatives of eigenenergies

$$\frac{\partial C^{\kappa'\gamma}_{\kappa\alpha}}{\partial f_n} = \frac{\partial}{\partial f_n} \left(\frac{\partial^2 E^{BO}}{\partial R_{\kappa\alpha} \partial R_{\kappa'\gamma}} \right) = \frac{\partial^2 \varepsilon_n}{\partial R_{\kappa\alpha} \partial R_{\kappa'\gamma}}. \tag{1.29}$$

Substituting the above expression into Eq. (1.28), we obtain

$$\Delta\varepsilon_n(T) = \sum_m^{3N} \frac{1}{2\omega_m} \sum_{\substack{\kappa\alpha \\ \kappa'\gamma}} U^*_{m,\kappa'\gamma} \frac{\partial^2 \varepsilon_n}{\partial R_{\kappa\alpha} \partial R_{\kappa'\gamma}} U_{m,\kappa\alpha} \left(n_m(T) + \frac{1}{2} \right). \tag{1.30}$$

The double sum over atomic position displacements is actually the second-order derivative of the eigenenergy with respect to the normal mode,

$$\sum_{\substack{\kappa\alpha \\ \kappa'\gamma}} U^*_{m,\kappa'\gamma} \frac{\partial^2 \varepsilon_n}{\partial R_{\kappa\alpha} \partial R_{\kappa'\gamma}} U_{m,\kappa\alpha} = \frac{d^2}{dz^2} \tilde{\varepsilon}_n [z\mathbf{U}_{m,\kappa}] \Big|_{z=0}, \tag{1.31}$$

so that we recover, from Eqs. (1.15), (1.26) and (1.31) the following relations

$$\frac{\partial \varepsilon_n}{\partial n_m} = \frac{1}{2\omega_m} \frac{d^2}{dz^2} \tilde{\varepsilon}_n[z\mathbf{U}_{m,\kappa}]\Big|_{z=0} \tag{1.32}$$

$$= \frac{1}{2\omega_m} \sum_{\substack{\kappa\alpha \\ \kappa'\gamma}} U^*_{m,\kappa'\gamma} \frac{\partial^2 \varepsilon_n}{\partial R_{\kappa\alpha} \partial R_{\kappa'\gamma}} U_{m,\kappa\alpha} = \frac{\partial \omega_m}{\partial f_n}, \tag{1.33}$$

where the quantity $\frac{\partial \varepsilon_n}{\partial n_m}$ is often called the electron-phonon coupling energies (EPCE). We thus obtain a demonstration of the Brook's theorem in the first-principle context.

1.2.3 *The Fan and Debye-Waller contributions*

In order to establish the links with the Fan, Debye-Waller (DW) and AHC approaches, we now analyse Eq. (1.30) in more detail, focusing on the second-order derivative of the eigenenergies with respect to two atomic displacements. We can obtain it from perturbation theory (see Annex A.2), starting from

$$\varepsilon_n = \langle \Psi_n | \hat{H} | \Psi_n \rangle , \tag{1.34}$$

and differentiate it, also using the Hellmann-Feynman theorem. At the equilibrium geometry,

$$\frac{\partial \varepsilon_n}{\partial R_{\kappa\alpha}} = \left\langle \Psi_n^{(0)} \right| \frac{\partial \hat{H}}{R_{\kappa\alpha}} \left| \Psi_n^{(0)} \right\rangle . \tag{1.35}$$

Eq. (1.35) can be derived a second time, with respect to another atomic displacement. An equivalent result can be obtained by switching the two atomic displacements. Both can be combined and deliver an expression that is real and explicitly symmetric with respect to the indices $\kappa\alpha$ and $\kappa'\gamma$

$$\frac{\partial^2 \varepsilon_n}{\partial R_{\kappa\alpha} \partial R_{\kappa'\gamma}} = \left\langle \Psi_n^{(0)} \right| \frac{\partial^2 \hat{H}}{\partial R_{\kappa\alpha} R_{\kappa'\gamma}} \left| \Psi_n^{(0)} \right\rangle + \frac{1}{2} \left[\left(\left\langle \frac{\partial \Psi_n}{\partial R_{\kappa\alpha}} \right| \frac{\partial \hat{H}}{\partial R_{\kappa'\gamma}} \left| \Psi_n^{(0)} \right\rangle + (\kappa\alpha) \leftrightarrow (\kappa'\gamma) \right) + (\text{c.c.}) \right], \tag{1.36}$$

where $(\kappa\alpha) \leftrightarrow (\kappa'\gamma)$ stands for the previous term where the indices $\kappa\alpha$ and $\kappa'\gamma$ have been exchanged and where (c.c.) stands for the complex conjugate of the previous term.

The contribution from the second-order perturbation of the Hamiltonian $\frac{\partial^2 \hat{H}}{\partial R_{\kappa\alpha} R_{\kappa'\gamma}}$ gives the DW term [16, 81] of the semi-empirical approach. The other bracketed term originates from the first-order modifications of the wavefunction and corresponds to the Fan term when considered in many-body perturbation theory. As mentioned in the introduction, the complementarity of the two terms for the description of the eigenenergy renormalization due to the electron-phonon interaction, although obvious in the present derivation, was first shown in 1974 by Baumann [17].

1.3 FROM THE ADIABATIC APPROXIMATION TO THE ALLEN-HEINE-CARDONA THEORY

In this section, we relate Eq. (1.30) to the AHC theory, as formulated[2] by Giustino *et al.* [62]. We also carefully treat the RIA and unveil the terms it neglects. Furthermore, we discuss the translational invariance and its consequences. In order to focus on solids (in view of the application and testing for diamond and solid-state systems in general), we work with periodic systems and introduce the related definitions. More information in this respect is provided in Appendix A.1 and A.2.

1.3.1 *Wavevectors and translational invariance*

We introduce a specific notation for the derivative of an arbitrary quantity X, that depends on the atomic coordinates, with respect to a collective displacement of atoms characterized by a wavevector $\mathbf{q}$

$$\frac{\partial X}{\partial R_{\kappa\alpha}(\mathbf{q})} = \frac{1}{N_{Bvk}} \sum_{l} e^{i\mathbf{q}\cdot\mathbf{R}_l} \frac{\partial X}{\partial R_{l\kappa\alpha}}, \tag{1.37}$$

where $R_{l\kappa\alpha}$ is the coordinate along the α axis of the atom κ in the cell l, and N_{Bvk} is the number of primitive cells of the periodic system defined by the Born-von Karman boundary conditions [82].

The eigendisplacement vectors are solution of the dynamical equation

$$\sum_{\kappa\alpha} \tilde{C}^{\kappa\alpha}_{\kappa'\gamma}(\mathbf{q}) U_{m,\kappa\alpha}(\mathbf{q}) = M_{\kappa'} \omega^2_{m\mathbf{q}} U_{m,\kappa'\gamma}(\mathbf{q}), \tag{1.38}$$

2 Although we agree with Eqs. (2-7) of Allen and Cardona [39], we think that their Eq. (8) is erroneous, since the polarization vectors in the DW term of this equation have different atomic indices κ and κ', which is not coherent with their Eq. (5) or with Ref. [62], where the polarization vectors have the same atomic index κ. On the contrary, we perfectly agree with the formulation of Giustino *et al.* [62].

where the Fourier transform of the IFC appears

$$\begin{aligned}\tilde{C}_{\substack{\kappa\alpha\\ \kappa'\gamma}}(\mathbf{q}) =& \frac{1}{N_{Bvk}} \sum_{ll'} C_{\substack{l\kappa\alpha\\ l'\kappa'\gamma}} e^{-i\mathbf{q}\cdot(\mathbf{R}_l-\mathbf{R}_{l'})} \\ =& \sum_{l'} C_{\substack{0\kappa\alpha\\ l'\kappa'\gamma}} e^{i\mathbf{q}\cdot\mathbf{R}_{l'}} \\ =& N_{Bvk} \frac{\partial^2 E^{BO}}{\partial R_{\kappa'\alpha}(-\mathbf{q})\partial R_{\kappa''\beta}(\mathbf{q})},\end{aligned} \tag{1.39}$$

where $\mathbf{R}_l$ is a translation vector of the Bravais lattice. As the solution of an eigenvalue problem with an hermitian matrix, the eigendisplacement vectors are normalized and complete

$$\sum_{\kappa\alpha} M_\kappa U^*_{m,\kappa\alpha}(\mathbf{q}) U_{m',\kappa\alpha}(\mathbf{q}) = \delta_{mm'} \tag{1.40}$$

$$\sum_{m} \sqrt{M_\kappa M_{\kappa'}} U^*_{m,\kappa\alpha}(\mathbf{q}) U_{m,\kappa'\gamma}(\mathbf{q}) = \delta_{\kappa\kappa'}\delta_{\alpha\gamma}. \tag{1.41}$$

All properties of a crystal, including its eigenenergies and their derivatives, must be invariant upon a uniform translation δ. Therefore,

$$\varepsilon_{n\mathbf{k}}[\{\mathbf{R}_{l\kappa}\}] = \varepsilon_{n\mathbf{k}}[\{\mathbf{R}_{l\kappa} + \delta\}] \tag{1.42}$$

$$\frac{\partial \varepsilon_{n\mathbf{k}}}{\partial R_{\kappa'\alpha}(\mathbf{\Gamma})}[\{\mathbf{R}_{l\kappa}\}] = \frac{\partial \varepsilon_{n\mathbf{k}}}{\partial R_{\kappa'\alpha}(\mathbf{\Gamma})}[\{\mathbf{R}_{l\kappa} + \delta\}]. \tag{1.43}$$

In Eq. (1.43), we have taken the derivative with respect to a collective displacement of atoms that does not break the translation symmetry ($\mathbf{q} = \mathbf{\Gamma}$) to avoid any problem with the Bloch theorem, and keep the Bloch notation $n\mathbf{k}$.

By Taylor expanding the right hand side of Eq. (1.43), we obtain

$$\begin{aligned}\frac{\partial \varepsilon_{n\mathbf{k}}}{\partial R_{\kappa'\alpha}(\mathbf{\Gamma})}[\{\mathbf{R}_{l\kappa} + \delta\}] =& \frac{\partial \varepsilon_{n\mathbf{k}}}{\partial R_{\kappa'\alpha}(\mathbf{\Gamma})}[\{\mathbf{R}_{l\kappa}\}] \\ &+ \sum_{\kappa''\beta} \delta_\beta \frac{\partial^2 \varepsilon_{n\mathbf{k}}}{\partial R_{\kappa'\alpha}(\mathbf{\Gamma})\partial R_{\kappa''\beta}(\mathbf{\Gamma})}[\{\mathbf{R}_{l\kappa}\}] + \mathcal{O}(\delta^2),\end{aligned} \tag{1.44}$$

where δ_β is the β component of the vector δ. Since, by Eq. (1.43), the left hand side cancels the first term of the right hand side in Eq. (1.44), we obtain that every term of order one and higher in the series must be identically zero

$$\begin{aligned}&\sum_\beta \delta_\beta \sum_{\kappa''} \frac{\partial^2 \varepsilon_{n\mathbf{k}}}{\partial R_{\kappa'\alpha}(\mathbf{\Gamma})\partial R_{\kappa''\beta}(\mathbf{\Gamma})}[\{\mathbf{R}_{l\kappa}\}] = 0 \quad \forall \delta_\beta \in \mathbb{R} \\ &\Rightarrow \sum_{\kappa''} \frac{\partial^2 \varepsilon_{n\mathbf{k}}}{\partial R_{\kappa'\alpha}(\mathbf{\Gamma})\partial R_{\kappa''\beta}(\mathbf{\Gamma})}[\{\mathbf{R}_{l\kappa}\}] = 0.\end{aligned} \tag{1.45}$$

1.3.2 *The temperature dependence in the adiabatic harmonic approximation for the solid periodic case*

The Eq. (1.30) can be generalized to the periodic case, with a discretized integral over $\mathbf{q}$ (N_q is the number of wavevectors used to sample the Brillouin zone)

$$\Delta\varepsilon_{n\mathbf{k}}(T) = \frac{1}{N_q}\sum_{\mathbf{q}}\sum_{m}^{3N}\frac{1}{2\omega_{m\mathbf{q}}}\sum_{\substack{\kappa\alpha\\ \kappa'\gamma}}\sum_{ll'}\frac{\partial^2\varepsilon_{n\mathbf{k}}}{\partial R_{l\kappa\alpha}\partial R_{l'\kappa'\gamma}} e^{-i\mathbf{q}\cdot(\mathbf{R}_l-\mathbf{R}_{l'})}U^*_{m,\kappa'\gamma}(\mathbf{q})U_{m,\kappa\alpha}(\mathbf{q})\left(n_{m\mathbf{q}}(T)+\frac{1}{2}\right). \quad (1.46)$$

Similarly, the generalization of Eq. (1.16) leads to

$$\Delta\varepsilon_{n\mathbf{k}}(T) = \frac{1}{N_q}\sum_{\mathbf{q}}\sum_{m}^{3N}\frac{\partial\varepsilon_{n\mathbf{k}}}{\partial n_{m\mathbf{q}}}\left(n_{m\mathbf{q}}(T)+\frac{1}{2}\right), \quad (1.47)$$

where

$$\frac{\partial\varepsilon_{n\mathbf{k}}}{\partial n_{m\mathbf{q}}} = \frac{1}{2\omega_{m\mathbf{q}}}\sum_{\substack{\kappa\alpha\\ \kappa'\gamma}}\sum_{ll'}\frac{\partial^2\varepsilon_{n\mathbf{k}}}{\partial R_{l\kappa\alpha}\partial R_{l'\kappa'\gamma}} e^{-i\mathbf{q}\cdot(\mathbf{R}_l-\mathbf{R}_{l'})}U^*_{m,\kappa'\gamma}(\mathbf{q})U_{m,\kappa\alpha}(\mathbf{q}) \quad (1.48)$$

and we will focus on the latter quantity, which represents the change of eigenenergy due to a specific phonon mode.

To split this expression in a Fan and a DW contribution, we substitute the extension to periodic system of Eq. (1.36) in it and retrieve

$$\frac{\partial\varepsilon_{n\mathbf{k}}}{\partial n_{m\mathbf{q}}} = \frac{1}{2\omega_{m\mathbf{q}}}\sum_{\substack{\kappa\alpha\\ \kappa'\gamma}}U^*_{m,\kappa'\gamma}(\mathbf{q})U_{m,\kappa\alpha}(\mathbf{q}) \left\{\left\langle u^{(0)}_{n\mathbf{k}}\right|\frac{\partial^2\hat{H}_{\mathbf{k},\mathbf{k}}}{\partial R_{\kappa\alpha}(-\mathbf{q})\partial R_{\kappa'\gamma}(\mathbf{q})}\left|u^{(0)}_{n\mathbf{k}}\right\rangle + \frac{1}{2}\left[\left(\left\langle\frac{\partial u_{n\mathbf{k}}}{\partial R_{\kappa\alpha}(\mathbf{q})}\right|\frac{\partial\hat{H}_{\mathbf{k},\mathbf{k}}}{\partial R_{\kappa'\gamma}(\mathbf{q})}\left|u^{(0)}_{n\mathbf{k}}\right\rangle + (\kappa\alpha)\leftrightarrow(\kappa'\gamma)\right) + (\text{c.c.})\right]\right\}, \quad (1.49)$$

where $\hat{H}_{\mathbf{k},\mathbf{k}}$ is defined through Eq. (A.4) applied to the Hamiltonian.

This allows us to introduce the following notation for the DW and Fan contributions related to band n and wavevector $\mathbf{k}$ (we skip the n and $\mathbf{k}$ indices, which should not be confusing in the present context)

$$\mathcal{D}_{\substack{\kappa\alpha\\ \kappa'\gamma}}(\mathbf{q}) \triangleq \left\langle u^{(0)}_{n\mathbf{k}}\right|\frac{\partial^2\hat{H}_{\mathbf{k},\mathbf{k}}}{\partial R_{\kappa\alpha}(-\mathbf{q})\partial R_{\kappa'\gamma}(\mathbf{q})}\left|u^{(0)}_{n\mathbf{k}}\right\rangle \quad (1.50)$$

$$\mathcal{F}^{\kappa\alpha}_{\kappa'\gamma}(\mathbf{q}) \triangleq \frac{1}{2}\Bigg[\Bigg(\Big\langle \frac{\partial u_{n\mathbf{k}}}{\partial R_{\kappa\alpha}(\mathbf{q})}\Big| \frac{\partial \hat{H}_{\mathbf{k},\mathbf{k}}}{\partial R_{\kappa'\gamma}(\mathbf{q})}\Big| u^{(0)}_{n\mathbf{k}}\Big\rangle + (\kappa\alpha) \leftrightarrow (\kappa'\gamma)\Bigg) + (\text{c.c.})\Bigg]. \quad (1.51)$$

The change of eigenenergy due to a specific phonon mode, Eq. (1.49), thus becomes

$$\frac{\partial \varepsilon_{n\mathbf{k}}}{\partial n_{m\mathbf{q}}} \triangleq \frac{\partial \varepsilon^{\text{FAN}}_{n\mathbf{k}}}{\partial n_{m\mathbf{q}}} + \frac{\partial \varepsilon^{\text{DW}}_{n\mathbf{k}}}{\partial n_{m\mathbf{q}}} \quad (1.52)$$

with the Fan contribution given by

$$\frac{\partial \varepsilon^{\text{FAN}}_{n\mathbf{k}}}{\partial n_{m\mathbf{q}}} \triangleq \frac{1}{2\omega_{m\mathbf{q}}} \sum_{\substack{\kappa\alpha \\ \kappa'\gamma}} \mathcal{F}^{\kappa\alpha}_{\kappa'\gamma}(\mathbf{q}) U^*_{m,\kappa'\gamma}(\mathbf{q}) U_{m,\kappa\alpha}(\mathbf{q}), \quad (1.53)$$

and the Debye-Waller contribution given by

$$\frac{\partial \varepsilon^{\text{DW}}_{n\mathbf{k}}}{\partial n_{m\mathbf{q}}} \triangleq \frac{1}{2\omega_{m\mathbf{q}}} \sum_{\substack{\kappa\alpha \\ \kappa'\gamma}} \mathcal{D}^{\kappa\alpha}_{\kappa'\gamma}(\mathbf{q}) U^*_{m,\kappa'\gamma}(\mathbf{q}) U_{m,\kappa\alpha}(\mathbf{q}). \quad (1.54)$$

With the same notations, the translational invariance Eq. (1.45) reads

$$\sum_{\kappa'} \mathcal{D}^{\kappa\alpha}_{\kappa'\gamma}(\mathbf{\Gamma}) + \mathcal{F}^{\kappa\alpha}_{\kappa'\gamma}(\mathbf{\Gamma}) = 0. \qquad \forall\, \alpha, \gamma, \kappa \quad (1.55)$$

In particular, one can multiply this expression by any expression independent of κ', and still get zero. This gives us some freedom to add terms which are chosen in such a way that $\mathcal{D}$ simplifies in the rigid-ion approximation (see next subsection). Moreover, these supplementary terms can be chosen in such a way that the resulting expression is Hermitian

$$\frac{\partial \varepsilon_{n\mathbf{k}}}{\partial n_{m\mathbf{q}}} = \frac{1}{2\omega_{m\mathbf{q}}} \sum_{\substack{\kappa\alpha \\ \kappa'\gamma}} \Bigg[\Big[\mathcal{D}^{\kappa\alpha}_{\kappa'\gamma}(\mathbf{q}) + \mathcal{F}^{\kappa\alpha}_{\kappa'\gamma}(\mathbf{q})\Big] U^*_{m,\kappa'\gamma}(\mathbf{q}) U_{m,\kappa\alpha}(\mathbf{q}) - \frac{1}{2}\Big[\mathcal{D}^{\kappa\alpha}_{\kappa'\gamma}(\mathbf{\Gamma}) + \mathcal{F}^{\kappa\alpha}_{\kappa'\gamma}(\mathbf{\Gamma})\Big] \Big(U^*_{m,\kappa\gamma}(\mathbf{q}) U_{m,\kappa\alpha}(\mathbf{q}) + U^*_{m,\kappa'\gamma}(\mathbf{q}) U_{m,\kappa'\alpha}(\mathbf{q})\Big)\Bigg]. \quad (1.56)$$

Without loss of generality, taking advantage of the translational invariance, the Debye-Waller term is equivalently given by

$$\frac{\partial \varepsilon^{DW}_{n\mathbf{k}}}{\partial n_{m\mathbf{q}}} = \frac{1}{2\omega_{m\mathbf{q}}} \sum_{\substack{\kappa\alpha \\ \kappa'\gamma}} \Bigg[\mathcal{D}_{\substack{\kappa\alpha \\ \kappa'\gamma}}(\mathbf{q}) U^*_{m,\kappa'\gamma}(\mathbf{q}) U_{m,\kappa\alpha}(\mathbf{q}) - \frac{1}{2}\Big[\mathcal{D}_{\substack{\kappa\alpha \\ \kappa'\gamma}}(\mathbf{\Gamma}) + \mathcal{F}_{\substack{\kappa\alpha \\ \kappa'\gamma}}(\mathbf{\Gamma})\Big] \Big(U^*_{m,\kappa\gamma}(\mathbf{q}) U_{m,\kappa\alpha}(\mathbf{q}) + U^*_{m,\kappa'\gamma}(\mathbf{q}) U_{m,\kappa'\alpha}(\mathbf{q}) \Big) \Bigg]. \quad (1.57)$$

At this point, the only approximations we have used are the adiabatic and the harmonic approximations. The Debye-Waller term that we have obtained, Eq. (1.50), involves the second-order derivative of the first-principle Hamiltonian. In most DFPT procedures, calculations of the phonon band structure rely only on the evaluation of the *first-order* derivative of the self-consistent DFT Hamiltonian and wavefunctions. Indeed, while the expression leading to such phonon band structure calculations include a second-order derivative with respect to the non-self-consistent electron-ion potential, the latter term does not depend on *second-order* derivative of the wavefunction and Hamiltonian [64]. Thus, the Debye-Waller term is not a by-product of a phonon band structure calculation. We will now show how the rigid-ion approximation allows us to compute the Debye-Waller term without computing the second-order derivative of the self-consistent first-principle Hamiltonian.

1.3.3 *The rigid-ion Hamiltonian*

In the case of semi-empirical potentials, it is natural to suppose that the Hamiltonian depends on potentials created *independently* by each nucleus, screened by electrons attached to them. In this case, as pointed by Allen and Heine [38], the numerical burden of computing a second-order derivative of the Hamiltonian can be completely avoided. A rigid-ion Hamiltonian has the following form

$$\hat{H}^{ri} = \hat{T} + V^{ionic}(\hat{\mathbf{r}}), \quad (1.58)$$

where

$$V^{ionic}(\hat{\mathbf{r}}) = \sum_{l\kappa} V_{l\kappa}(\hat{\mathbf{r}} - \mathbf{R}_{l\kappa}). \quad (1.59)$$

The mixed (off-site) second-order derivatives of such Hamiltonian vanish

$$\frac{\partial^2 \hat{H}^{ri}}{\partial R_{l\kappa\alpha}\partial R_{l'\kappa'\gamma}} = 0 \qquad \text{if } \kappa \neq \kappa' \text{as well as if } l \neq l'. \tag{1.60}$$

Using the notation of Eq. (1.50), the DW term constructed with a rigid-ion Hamiltonian has the following property

$$\mathcal{D}^{ri}_{\substack{\kappa\alpha \\ \kappa'\gamma}}(\mathbf{q}) = \mathcal{D}^{ri}_{\substack{\kappa\alpha \\ \kappa'\gamma}}(\Gamma)\delta_{\kappa,\kappa'}. \tag{1.61}$$

Enforcing Eq. (1.61) to the DW terms of Eq. (1.57) for a rigid-ion Hamiltonian leads to

$$\frac{\partial \varepsilon^{DW^{ri}}_{n\mathbf{k}}}{\partial n_{m\mathbf{q}}} = \frac{-1}{4\omega_{m\mathbf{q}}} \sum_{\substack{\kappa\alpha \\ \kappa'\gamma}} \mathcal{F}^{ri}_{\substack{\kappa\alpha \\ \kappa'\gamma}}(\Gamma) \Big(U^*_{m,\kappa\gamma}(\mathbf{q}) U_{m,\kappa\alpha}(\mathbf{q}) + U^*_{m,\kappa'\gamma}(\mathbf{q}) U_{m,\kappa'\alpha}(\mathbf{q}) \Big), \tag{1.62}$$

which is the AHC expression of the DW contribution.

1.3.4 *The rigid-ion approximation*

In a DFT approach (GW behaves similarly, with an electronic self-energy replacing the DFT exchange-correlation potential), the Hamiltonian is the sum of the kinetic energy operator $\hat{T}$ and the Kohn-Sham potential $V_{KS}[\rho](\hat{\mathbf{r}})$. The latter term can further be split in the sum of potentials generated by each ion $V_{l\kappa}(\hat{\mathbf{r}} - \mathbf{R}_{l\kappa})$ and the Hartree and exchange-correlation (Hxc) potential $V_{Hxc}[\rho](\hat{\mathbf{r}})$ generated by the electronic density of the system

$$\hat{H} = \hat{T} + V_{KS}[\rho](\hat{\mathbf{r}}) = \hat{T} + V_{ionic}(\hat{\mathbf{r}}) + V_{Hxc}[\rho](\hat{\mathbf{r}}). \tag{1.63}$$

Thus, the change of the Hamiltonian is related to the change of the density only through $V_{Hxc}[\rho](\hat{\mathbf{r}})$. The change of the density due to the displacement of one atom being in general affected by the displacement of another atom, the second order derivative of the Hamiltonian with respect to the displacement of two different atoms will contain contributions from $V_{Hxc}[\rho](\hat{\mathbf{r}})$, but not from $\hat{T}$ and $V_{l\kappa}(\hat{\mathbf{r}} - \mathbf{R}_{l\kappa})$ since they have the form of Eq. (1.58). This can be seen as a consequence of the fact that, unlike the bare ionic potential, the Hxc potential is screened (see Appendix A.6 for an alternative view of the DW term expressed in term of the dielectric function).

The numerical evaluation of the Debye-Waller term is difficult since it requires the evaluation of the second functional derivative of the Hamiltonian with respect with atomic positions. A popular approximation, called the rigid-ion approximation, is to apply Eq. 1.62, exact for a rigid-ion Hamiltonian, to a DFT Hamiltonian

$$\frac{\partial \varepsilon_{nk}^{DW_{RIA}}}{\partial n_{mq}} = \frac{-1}{4\omega_{mq}} \sum_{\substack{\kappa\alpha \\ \kappa'\gamma}} \mathcal{F}_{\substack{\kappa\alpha \\ \kappa'\gamma}}(\Gamma) \left(U^*_{m,\kappa\gamma}(q) U_{m,\kappa\alpha}(q) + U^*_{m,\kappa'\gamma}(q) U_{m,\kappa'\alpha}(q) \right). \quad (1.64)$$

With the rigid-ion approximation, the change of electronic energies reads

$$\frac{\partial \varepsilon_{nk}^{RIA}}{\partial n_{mq}} = \frac{\partial \varepsilon_{nk}^{FAN}}{\partial n_{mq}} + \frac{\partial \varepsilon_{nk}^{DW_{RIA}}}{\partial n_{mq}}. \quad (1.65)$$

This rewriting makes the calculations easier to perform, since only first-order derivative of the DFT Hamiltonian have to be computed.

All Fan-like contributions can be derived from DFPT, as explained in the appendix A.2. In practice, in the AHC theory as formulated by Giustino *et al* [62], $\mathcal{F}_{\substack{\kappa\alpha \\ \kappa'\gamma}}(q)$ is obtained using Eq. (1.51) and

$$\left\langle \frac{\partial u_{nk}}{\partial R_{\kappa\alpha}(q)} \middle| \frac{\partial \hat{H}_{k,k}}{\partial R_{\kappa'\gamma}(q)} \middle| u^{(0)}_{nk} \right\rangle = \sum_{n'=1}^{\infty}{}' \frac{\left\langle u^{(0)}_{nk} \middle| \frac{\partial \hat{H}_{k,k}}{\partial R_{\kappa\alpha}(-q)} \middle| u^{(0)}_{n'k+q} \right\rangle \left\langle u^{(0)}_{n'k+q} \middle| \frac{\partial \hat{H}_{k,k}}{\partial R_{\kappa'\gamma}(q)} \middle| u^{(0)}_{nk} \right\rangle}{\varepsilon^{(0)}_{nk} - \varepsilon^{(0)}_{n'k+q}}, \quad (1.66)$$

where the infinite sum over bands is truncated in numerical calculations, while the prime after the sum symbol indicates that the terms with a vanishing denominator (such situation always occurs at Γ when $n = n'$) have to be excluded.

In the resulting expression, one needs to sum over a large number of empty bands since the first-order wavefunction is expressed in the sum-over-states form. As shown by Sternheimer [83], the summation over highly energetic bands can be replaced by the solution of a linear equation. This equation can then be solved iteratively with the same techniques as the ones of the DFPT approach used to calculate phonon eigenvectors and eigenenergies [63, 84, 64, 85]. The resulting expression for the first-order wavefunction is detailed in appendix A.2 of this thesis

(Eq. (A.19)) and leads to an alternative form of Eq. (1.66), proposed in Ref. [19]

$$\left\langle \frac{\partial u_{n\mathbf{k}}}{\partial R_{\kappa\alpha}(\mathbf{q})} \middle| \frac{\partial \hat{H}_{\mathbf{k},\mathbf{k}}}{\partial R_{\kappa'\gamma}(\mathbf{q})} \middle| u^{(0)}_{n\mathbf{k}} \right\rangle = \sum_{n'=1}^{M}{}' \frac{\left\langle u^{(0)}_{n\mathbf{k}} \middle| \frac{\partial \hat{H}_{\mathbf{k},\mathbf{k}}}{\partial R_{\kappa\alpha}(-\mathbf{q})} \middle| u^{(0)}_{n'\mathbf{k}+\mathbf{q}} \right\rangle \left\langle u^{(0)}_{n'\mathbf{k}+\mathbf{q}} \middle| \frac{\partial \hat{H}_{\mathbf{k},\mathbf{k}}}{\partial R_{\kappa'\gamma}(\mathbf{q})} \middle| u^{(0)}_{n\mathbf{k}} \right\rangle}{\varepsilon^{(0)}_{n\mathbf{k}} - \varepsilon^{(0)}_{n'\mathbf{k}+\mathbf{q}}} + \left\langle \hat{P}_{c\mathbf{k}+\mathbf{q}} \frac{\partial u_{n\mathbf{k}}}{\partial R_{\kappa\alpha}(\mathbf{q})} \middle| \frac{\partial \hat{H}_{\mathbf{k},\mathbf{k}}}{\partial R_{\kappa'\gamma}(\mathbf{q})} \middle| u^{(0)}_{n\mathbf{k}} \right\rangle. \quad (1.67)$$

This formulation is independent of the value of M, which is usually taken to be slightly larger than the number of bands for which the electron-phonon renormalization is sought. It removes the cumbersome sum over states, and results in a significant speed up of the calculations [19] as well as the elimination of the convergence study on the truncation of the sum. The complete expression for the change of eigenenergies due to electron-phonon interactions, in the RIA, is obtained from the combination of Eqs. (1.47), (1.51), (1.53), (1.64), (1.65) and (1.67).

1.3.5 *Beyond the rigid-ion approximation*

We can now analyze the term that were neglected by enforcing the rigid-ion approximation to a general Hamiltonian. We decompose the full Debye-Waller term as follows

$$\frac{\partial \varepsilon^{\mathrm{DW}}_{n\mathbf{k}}}{\partial n_{m\mathbf{q}}} = \frac{\partial \varepsilon^{\mathrm{DW_{RIA}}}_{n\mathbf{k}}}{\partial n_{m\mathbf{q}}} + \frac{\partial \varepsilon^{\mathrm{DW_{NRIA}}}_{n\mathbf{k}}}{\partial n_{m\mathbf{q}}}. \quad (1.68)$$

The second term, which we call the non-rigid-ion approximation to the Debye-Waller term, is composed of the terms neglected by the RIA

$$\frac{\partial \varepsilon^{\mathrm{DW_{NRIA}}}_{n\mathbf{k}}}{\partial n_{m\mathbf{q}}} \triangleq \frac{1}{2\omega_{m\mathbf{q}}} \sum_{\substack{\kappa\alpha \\ \kappa'\gamma}} \Big[\mathcal{D}^{\kappa\alpha}_{\kappa'\gamma}(\mathbf{q}) U^*_{m,\kappa'\gamma}(\mathbf{q}) U_{m,\kappa\alpha}(\mathbf{q}) - \frac{1}{2} \mathcal{D}^{\kappa\alpha}_{\kappa'\gamma}(\Gamma) \Big(U^*_{m,\kappa\gamma}(\mathbf{q}) U_{m,\kappa\alpha}(\mathbf{q}) + U^*_{m,\kappa'\gamma}(\mathbf{q}) U_{m,\kappa'\alpha}(\mathbf{q}) \Big) \Big]. \quad (1.69)$$

It may be noted that the present convention differs from the one of Ref. [19]. While our FAN term is the same as Eq. (16) of this reference, our $\mathrm{DW_{RIA}}$ term is instead called *diagonal* Debye-Waller by them (see their Eq. (16)). However, such a term is not diagonal in atom index nor

in cell site, hence the new naming convention proposed here. Similarly, we may note that our DW_{NRIA} term is called *non-diagonal* Debye-Waller by them (see their Eq. (22)), although it possesses diagonal components.

This apparent discrepancy can be explained by noting that Ref. [19] studied isolated molecules, for which the only wavevector to be considered was $\mathbf{q} = \mathbf{\Gamma}$. In this context, the contribution beyond the Fan and DW_{RIA} was indeed purely non-diagonal. However, this is not true in the general case. Thus, we believe that the updated definitions presented in this paper are more general and lifts some possible confusion.

1.4 TEMPERATURE DEPENDENCE FROM FINITE DIFFERENCES OVER ATOMIC DISPLACEMENTS

The temperature dependence can also be computed through a FP approach where, in a supercell, a set of self-consistent first-principles calculations are done with atoms displaced slightly from their equilibrium positions. The change of force due to atomic displacements allows one to construct the IFC, from which the phonon frequencies and eigenvectors can be deduced.

Since the FP formalism does not include the RIA (see Eq. (1.64)), it becomes interesting to obtain the contributions neglected by it from FP calculations, to assess its validity.

1.4.1 *The frozen-phonon approach*

When performing DFPT calculations, the problem lies in the fact that the term beyond the rigid-ion approximation (Eq. (1.69)) requires the direct evaluation of the second-order derivative of the Hamiltonian with respect to atomic positions. Such terms might be computed by higher-order DFPT, but would require the computation of the second-order derivatives of the Hamiltonian with respect to all pairs of atomic displacements, which is prohibitive from a computational point of view. Indeed, to the author's knowledge, no solid state computer code is nowadays able to compute such terms. For this reason, we will rely on finite-difference calculations to have access to all the quantities beyond the RIA terms.

Although the IFC of Eq. (1.4), expressed in real space, is a symmetric matrix, the dynamical matrix $\tilde{C}_{\substack{\kappa\alpha \\ \kappa'\gamma}}(\mathbf{q})$ defined in Eq. (1.39) can be com-

plex. First, we notice that such quantity at $\mathbf{q}$ and $-\mathbf{q}$ are linked through time-reversal symmetry

$$\begin{aligned}\tilde{C}_{\substack{\kappa\alpha\\ \kappa'\gamma}}(-\mathbf{q}) &= \sum_{l} C_{\substack{0\kappa\alpha\\ l\kappa'\gamma}} e^{-i\mathbf{q}\cdot\mathbf{R}_l} \\ &= \Big(\sum_{l} C_{\substack{0\kappa\alpha\\ l\kappa'\gamma}} e^{+i\mathbf{q}\cdot\mathbf{R}_l}\Big)^* = \tilde{C}^*_{\substack{\kappa\alpha\\ \kappa'\gamma}}(\mathbf{q}). \end{aligned} \tag{1.70}$$

Therefore the dynamical equation for $-\mathbf{q}$ can be written as

$$\sum_{\kappa\alpha} \tilde{C}^*_{\substack{\kappa\alpha\\ \kappa'\gamma}}(\mathbf{q}) U_{m,\kappa\alpha}(-\mathbf{q}) = M_{\kappa'}\omega^2_{m-\mathbf{q}} U_{m,\kappa'\gamma}(-\mathbf{q}). \tag{1.71}$$

Taking the complex conjugate of the previous equation gives

$$\sum_{\kappa\alpha} \tilde{C}_{\substack{\kappa\alpha\\ \kappa'\gamma}}(\mathbf{q}) U^*_{m,\kappa\alpha}(-\mathbf{q}) = M_{\kappa'}\omega^2_{m-\mathbf{q}} U^*_{m,\kappa'\gamma}(-\mathbf{q}). \tag{1.72}$$

Therefore, by direct comparison with Eq. (1.38), we can see that, for all modes m, we have $\omega^2_{m\mathbf{q}} = \omega^2_{m-\mathbf{q}}$ and $U_{m,\kappa\alpha}(\mathbf{q}) = U^*_{m,\kappa\alpha}(-\mathbf{q})$. Taking advantage of these time-reversal symmetry properties, we can define a real displacement that is the sum of a displacement at $\mathbf{q}$ and another at $-\mathbf{q}$

$$v_{lm,\kappa\alpha}(\mathbf{q}) = \frac{1}{2}\Big[U_{m,\kappa\alpha}(\mathbf{q}) e^{i\mathbf{q}\cdot\mathbf{R}_l} + U_{m,\kappa\alpha}(-\mathbf{q}) e^{-i\mathbf{q}\cdot\mathbf{R}_l}\Big] \tag{1.73}$$

and we can also define another real displacement that is the difference of a displacement at $\mathbf{q}$ and another at $-\mathbf{q}$

$$w_{lm,\kappa\alpha}(\mathbf{q}) = -\frac{1}{2}i\Big[U_{m,\kappa\alpha}(\mathbf{q}) e^{i\mathbf{q}\cdot\mathbf{R}_l} - U_{m,\kappa\alpha}(-\mathbf{q}) e^{-i\mathbf{q}\cdot\mathbf{R}_l}\Big]. \tag{1.74}$$

1.4.2 *Frozen-phonon expression of the different terms entering into the ZPR*

Using the notation introduced in the previous section, we start from Eq. (1.48) and compute the second-order derivative of the eigenenergies through a FP approach based on second-order finite differences

$$\begin{aligned}\frac{\partial \varepsilon_{n\mathbf{k}}}{\partial n_{m\mathbf{q}}} &= \frac{1}{2\omega_{m\mathbf{q}}} \sum_{\substack{l\kappa\alpha\\ l'\kappa'\gamma}} \frac{\partial^2 \varepsilon_{n\mathbf{k}}}{\partial R_{l\kappa\alpha}\partial R_{l'\kappa'\gamma}} e^{-i\mathbf{q}\cdot(\mathbf{R}_l - \mathbf{R}_{l'})} U^*_{m,\kappa'\gamma}(\mathbf{q}) U_{m,\kappa\alpha}(\mathbf{q}) \\ &= \frac{1}{2\omega_{m\mathbf{q}}}\Bigg[\frac{\partial^2}{\partial h^2}\varepsilon_{n\mathbf{k}}\Big[\Big\{R_{l\kappa'\alpha} + h v_{lm,\kappa'\alpha}(\mathbf{q})\Big\}\Big]\Big|_{h=0} \\ &\qquad + \frac{\partial^2}{\partial h^2}\varepsilon_{n\mathbf{k}}\Big[\Big\{R_{l\kappa'\alpha} + h w_{lm,\kappa'\alpha}(\mathbf{q})\Big\}\Big]\Big|_{h=0}\Bigg], \end{aligned} \tag{1.75}$$

where $\hbar$ sets the amplitude of the FP displacement along real vector $v_{l m,\kappa\alpha}(\mathbf{q})$ or $w_{l m,\kappa\alpha}(\mathbf{q})$, $R_{l\kappa\alpha}$ are the equilibrium positions of the atoms, the eigenvalues $\varepsilon_{n\mathbf{k}}$ are evaluated with the atoms displaced along the real vector $v_{l m,\kappa\alpha}(\mathbf{q})$ or $w_{l m,\kappa\alpha}(\mathbf{q})$, and $\{\}$ denotes the set of values obtained by iterating upon l, κ and α.

We also compute, from a FP approach, the NRIA contribution to the eigenenergies renormalization, that is, the DW_{NRIA} contribution (see Eq. (1.69))

$$\begin{aligned}\frac{\partial \varepsilon_{n\mathbf{k}}^{DW_{NRIA}}}{\partial n_{m\mathbf{q}}} = \frac{1}{2\omega_{m\mathbf{q}}}\Bigg(&\frac{\partial^2}{\partial \hbar^2}\left\langle u_{n\mathbf{k}}^{(0)}\middle|\hat{H}_{\mathbf{k},\mathbf{k}}\left[\left\{R_{l\kappa'\alpha}+\hbar v_{l m,\kappa'\alpha}(\mathbf{q})\right\}\right]\right.\\ &\left.+\hat{H}_{\mathbf{k},\mathbf{k}}\left[\left\{R_{l\kappa'\alpha}+\hbar w_{l m,\kappa'\alpha}(\mathbf{q})\right\}\right]\middle|u_{n\mathbf{k}}^{(0)}\right\rangle\Big|_{\hbar=0}\\ &-\sum_{\gamma}\frac{\partial^2}{\partial S_\gamma \partial T_\gamma}\left\langle u_{n\mathbf{k}}^{(0)}\middle|\hat{V}_{Hxc}\left[\left\{R_{l\kappa'\alpha}+S_\gamma U^{*}_{m,\kappa'\gamma}(\mathbf{q})U_{m,\kappa'\alpha}(\mathbf{q})\right.\right.\right.\\ &\left.\left.\left.+T_\gamma\delta_{\alpha\gamma}\right\}\right]\middle|u_{n\mathbf{k}}^{(0)}\right\rangle\Big|_{S_\gamma,T_\gamma=0}\Bigg), \quad (1.76)\end{aligned}$$

where S_γ and T_γ are scalars introduced for finite differences purposes. The term $T_\gamma\delta_{\alpha\gamma}$ computed through finite differences is a collective displacement of the atoms in a primitive cell. The derivative of this term with respect to T_γ is non-zero because the expectation value of the displaced potential is evaluated at fixed equilibrium ion position which is taken with respect to the unperturbed periodic part of the wavefunction $u_{n\mathbf{k}}^{(0)}$. More details on this equation can be found in Appendix A.7.

Antonius *et al* [55] computed the temperature dependence of diamond using finite differences (Eq. (1.75)) in the many-body *GW* framework, which led to an additional 200 meV ZPR of the diamond bandgap with respect to the AHC value, closer to the experimental bandgap. This *GW* correction will be discussed in Section 3.3 of the present thesis.

Finally, for practical calculations, the interested reader might look into appendix A.8 for a discussion over the symmetry properties of ground-state and electron-phonon matrix elements.

1.5 BEYOND THE RAYLEIGH-SCHRÖDINGER PERTURBATION THEORY

Phonons alter the one-electron energy bands $\varepsilon_{n\mathbf{k}}$ in two ways: there is a shift $\Delta\varepsilon_{n\mathbf{k}}$ and a lifetime broadening $1/\tau_{n\mathbf{k}}$. As seen in the previous section, the adiabatic approximation leads to a real renormalization of the eigenstates. The study of the lifetime broadening requires a dynamical theory.

In 1978, Allen generalized his earlier work derived within the standard Rayleigh-Schrödinger perturbation theory to include finite phonon frequencies using many-body perturbation techniques and obtained a complex energy $\varepsilon_{n\mathbf{k}}(T)$ [86]

$$\varepsilon_{n\mathbf{k}}(T) \triangleq \tilde{\varepsilon}_{n\mathbf{k}}[0] + \Delta\varepsilon_{n\mathbf{k}}(T) + \frac{i}{2\tau_{n\mathbf{k}}} \tag{1.77}$$

$$= \tilde{\varepsilon}_{n\mathbf{k}}[0] + \frac{1}{N_q}\sum_{\mathbf{q}}\sum_{m}^{3N}\frac{1}{2\omega_{m\mathbf{q}}}\sum_{\substack{\kappa\alpha\\ \kappa'\gamma}}\Big[\mathcal{D}_{\substack{\kappa\alpha\\ \kappa'\gamma}}(\mathbf{q})\Big(n_{m\mathbf{q}}(T)+\frac{1}{2}\Big) + \tilde{\mathcal{F}}_{\substack{\kappa\alpha\\ \kappa'\gamma}}(\mathbf{q},\omega)\Big]U^{*}_{m,\kappa'\gamma}(\mathbf{q})U_{m,\kappa\alpha}(\mathbf{q}) \tag{1.78}$$

where the Debye-Waller correction to the unperturbed energy of the initial state $\varepsilon^{(0)}_{n\mathbf{k}}$ is purely real (Hermitian matrix at $\mathbf{q} = \Gamma$) and therefore has the same definition as Eq. (1.50). The dynamical Fan self-energy can be defined as (see Refs. [86, 87, 67] as well as reference therein for an in depths derivation)

$$\tilde{\mathcal{F}}_{\substack{\kappa\alpha\\ \kappa'\gamma}}(\mathbf{q},\omega) = \frac{1}{2}\sum_{n'=1}^{\infty}{}' \Big\langle u^{(0)}_{n\mathbf{k}}\Big|\frac{\partial\hat{H}_{\mathbf{k},\mathbf{k}}}{\partial R_{\kappa\alpha}(-\mathbf{q})}\Big|u^{(0)}_{n'\mathbf{k}+\mathbf{q}}\Big\rangle \Big\langle u^{(0)}_{n'\mathbf{k}+\mathbf{q}}\Big|\frac{\partial\hat{H}_{\mathbf{k},\mathbf{k}}}{\partial R_{\kappa'\gamma}(\mathbf{q})}\Big|u^{(0)}_{n\mathbf{k}}\Big\rangle \Big(\frac{n_{m\mathbf{q}}(T)+f_{n'\mathbf{k}+\mathbf{q}}}{\omega-\varepsilon^{(0)}_{n'\mathbf{k}+\mathbf{q}}+\omega_{m\mathbf{q}}+i\delta\mathrm{sgn}(\omega)} + \frac{n_{m\mathbf{q}}(T)+1-f_{n'\mathbf{k}+\mathbf{q}}}{\omega-\varepsilon^{(0)}_{n'\mathbf{k}+\mathbf{q}}-\omega_{m\mathbf{q}}+i\delta\mathrm{sgn}(\omega)}\Big), \tag{1.79}$$

where $\mathrm{sgn}(\omega) = 1$ if $\omega > 0$ and -1 if $\omega < 0$ and where we can see that $\tilde{\mathcal{F}}_{\substack{\kappa\alpha\\ \kappa'\gamma}}(\mathbf{q},\omega)$ is not Hermitian and so its eigenvalues are not pure real numbers and its eigenstates are not absolutely stationary states. This means that we have a spectral function instead of a well defined state. Nonetheless the $\mathbf{k}$-vector, Brillouin zone and periodicity in $\mathbf{k}$-space remain clearly defined if one performs ensemble averaging (periodicity in $\mathbf{r}$ space is then restored).

Within the many-body perturbation theory, the Green function for the electron can be written [87]

$$G_{n\mathbf{k}}(\omega,T) = \frac{1}{\omega-\varepsilon^{(0)}_{n\mathbf{k}}-\Sigma^{\mathrm{Fan}}_{n\mathbf{k}}(\omega,T)-\Sigma^{\mathrm{DW}}_{n\mathbf{k}}(T)}, \tag{1.80}$$

with

$$\Sigma^{\text{Fan}}_{n\mathbf{k}}(\omega, T) = \frac{1}{N_q}\sum_{\mathbf{q}}\sum_{m}^{3N}\frac{1}{2\omega_{m\mathbf{q}}} \sum_{\substack{\kappa\alpha \\ \kappa'\gamma}} \tilde{\mathcal{F}}^{\kappa\alpha}_{\kappa'\gamma}(\mathbf{q}, \omega) U^{*}_{m,\kappa'\gamma}(\mathbf{q}) U_{m,\kappa\alpha}(\mathbf{q}), \quad (1.81)$$

and

$$\Sigma^{\text{DW}}_{n\mathbf{k}}(T) = \frac{1}{N_q}\sum_{\mathbf{q}}\sum_{m}^{3N}\frac{1}{2\omega_{m\mathbf{q}}} \sum_{\substack{\kappa\alpha \\ \kappa'\gamma}} \mathcal{D}^{\kappa\alpha}_{\kappa'\gamma}(\mathbf{q}) U^{*}_{m,\kappa'\gamma}(\mathbf{q}) U_{m,\kappa\alpha}(\mathbf{q}) \left(n_{m\mathbf{q}}(T) + \frac{1}{2}\right). \quad (1.82)$$

The spectral function $A_{n\mathbf{k}}(\omega, T)$ for electrons interacting with phonons is defined as the imaginary part of the electronic Green's function

$$A_{n\mathbf{k}}(\omega, T) \triangleq \frac{1}{\pi}\left|\Im G_{n\mathbf{k}}(\omega, T)\right|, \quad (1.83)$$

with the spectral function obeying the following sum rules (the proof can be found for example in Eq. (5.33) of Ref. [87])

$$\int_{-\infty}^{\infty} A_{n\mathbf{k}}(\omega, T) d\omega = 1, \quad (1.84)$$

which is equivalent to the conservation of the number of electrons as the electron-phonon interaction is turned on.

Note that the electron Green's function in the limit of $(\Sigma^{\text{Fan}}_{n\mathbf{k}}(\omega, T) - \Sigma^{\text{DW}}_{n\mathbf{k}}(T)) \to i\delta$, with an infinitesimal δ, can be re-written as

$$G^{0}_{n\mathbf{k}}(\omega) = \frac{1}{\omega - \varepsilon^{(0)}_{n\mathbf{k}} + i\delta}. \quad (1.85)$$

The spectral function corresponding to this non-interacting Green's function $G^{0}_{n\mathbf{k}}(\omega)$ is a delta function at the single-particle electron energy

$$A_{n\mathbf{k}}(\omega) = \delta(\omega - \varepsilon^{(0)}_{n\mathbf{k}}). \quad (1.86)$$

This non-interacting case satisfies trivially the sum rule of Eq. (1.84).

The Eq. (1.83) can also be re-written as

$$A_{nk}(\omega, T) = \frac{1}{\pi} \frac{\left|\Im\Sigma^{\text{Fan}}_{nk}(\omega, T)\right|}{\left[\omega - \varepsilon^{(0)}_{nk} - \Re\Sigma^{\text{Fan}}_{nk}(\omega, T) - \Sigma^{\text{DW}}_{nk}(T)\right]^2 + \left[\Im\Sigma^{\text{Fan}}_{nk}(\omega, T)\right]^2}. \quad (1.87)$$

To get the real and imaginary part of the Fan self-energy, we can use the Dirac identity, also called the Sokhotski-Plemelj theorem for singular integrand

$$\Re \int_a^b \frac{f(x)}{x - x_0 + i\delta} dx = \lim_{\delta \to 0} \left[\int_a^{x_0 - \delta} + \int_{x_0 + \delta}^b \right] \frac{f(x)}{x - x_0} dx \quad (1.88)$$

$$= P \int_a^b \frac{f(x)}{x - x_0} dx, \quad (1.89)$$

and

$$\Im \int_a^b \frac{f(x)}{x - x_0 + i\delta} dx = -i\pi f(x_0) \text{ if } a < x_0 < b \text{ and } 0 \text{ otherwise,} \quad (1.90)$$

where P means the principal value of the integrand. The real and imaginary part of the Fan self-energy therefore are

$$\Re\Sigma^{\text{Fan}}_{nk}(\omega, T) = \frac{1}{N_q} \sum_{\mathbf{q}} \sum_{m}^{3N} \frac{1}{2\omega_{m\mathbf{q}}} \sum_{\substack{\kappa\alpha \\ \kappa'\gamma}} U^*_{m,\kappa'\gamma}(\mathbf{q}) U_{m,\kappa\alpha}(\mathbf{q})$$

$$\frac{1}{2} \sum_{n'=1}^{\infty}{}' \left\langle u^{(0)}_{nk} \middle| \frac{\partial \hat{H}_{\mathbf{k},\mathbf{k}}}{\partial R_{\kappa\alpha}(-\mathbf{q})} \middle| u^{(0)}_{n'\mathbf{k}+\mathbf{q}} \right\rangle \left\langle u^{(0)}_{n'\mathbf{k}+\mathbf{q}} \middle| \frac{\partial \hat{H}_{\mathbf{k},\mathbf{k}}}{\partial R_{\kappa'\gamma}(\mathbf{q})} \middle| u^{(0)}_{nk} \right\rangle$$

$$\left(\frac{n_{m\mathbf{q}}(T) + f_{n'\mathbf{k}+\mathbf{q}}}{\omega - \varepsilon^{(0)}_{n'\mathbf{k}+\mathbf{q}} + \omega_{m\mathbf{q}}} + \frac{n_{m\mathbf{q}}(T) + 1 - f_{n'\mathbf{k}+\mathbf{q}}}{\omega - \varepsilon^{(0)}_{n'\mathbf{k}+\mathbf{q}} - \omega_{m\mathbf{q}}} \right) \quad (1.91)$$

and

$$\Im\Sigma^{\text{Fan}}_{nk}(\omega, T) = \frac{\pi}{N_q} \sum_{\mathbf{q}} \sum_{m}^{3N} \frac{1}{2\omega_{m\mathbf{q}}} \sum_{\substack{\kappa\alpha \\ \kappa'\gamma}} U^*_{m,\kappa'\gamma}(\mathbf{q}) U_{m,\kappa\alpha}(\mathbf{q})$$

$$\frac{1}{2} \sum_{n'=1}^{\infty}{}' \left\langle u^{(0)}_{nk} \middle| \frac{\partial \hat{H}_{\mathbf{k},\mathbf{k}}}{\partial R_{\kappa\alpha}(-\mathbf{q})} \middle| u^{(0)}_{n'\mathbf{k}+\mathbf{q}} \right\rangle \left\langle u^{(0)}_{n'\mathbf{k}+\mathbf{q}} \middle| \frac{\partial \hat{H}_{\mathbf{k},\mathbf{k}}}{\partial R_{\kappa'\gamma}(\mathbf{q})} \middle| u^{(0)}_{nk} \right\rangle$$

$$\Big(\Big(n_{m\mathbf{q}}(T) + f_{n'\mathbf{k}+\mathbf{q}} \Big) \delta(\omega - \omega_{m\mathbf{q}} - \varepsilon^{(0)}_{n'\mathbf{k}+\mathbf{q}})$$

$$+ \Big(n_{m\mathbf{q}}(T) + 1 - f_{n'\mathbf{k}+\mathbf{q}} \Big) \delta(\omega + \omega_{m\mathbf{q}} - \varepsilon^{(0)}_{n'\mathbf{k}+\mathbf{q}}) \Big). \quad (1.92)$$

These two equations verify the Kramers-Kronig relation [87]

$$\Re\Sigma^{\text{Fan}}_{n\mathbf{k}}(\omega, T) = \frac{1}{\pi}\int_{-\infty}^{\infty} \frac{\left|\Im\Sigma^{\text{Fan}}_{n\mathbf{k}}(\omega, T)\right|}{\omega - \nu} d\nu. \tag{1.93}$$

By taking the adiabatic limit ($\omega_{m\mathbf{q}} << \omega - \varepsilon_{n'\mathbf{k}+\mathbf{q}}$) of Eq. (1.91), we can recover the Fan term introduced earlier

$$\Re\Sigma^{\text{Fan}}_{n\mathbf{k}}(\omega = \varepsilon^{(0)}_{n\mathbf{k}}, T) = \frac{1}{N_q}\sum_{\mathbf{q}}\sum_{m}^{3N} \frac{1}{2\omega_{m\mathbf{q}}} \sum_{\substack{\kappa\alpha \\ \kappa'\gamma}} \mathcal{F}^{\kappa\alpha}_{\kappa'\gamma}(\mathbf{q}) U^{*}_{m,\kappa'\gamma}(\mathbf{q}) U_{m,\kappa\alpha}(\mathbf{q}), \tag{1.94}$$

as well as the phonon-induced lifetime broadening in the adiabatic limit as presented by Lautenschlager *et al.* [69]

$$\Im\Sigma^{\text{Fan}}_{n\mathbf{k}}(\omega = \varepsilon^{(0)}_{n\mathbf{k}}, T) = \frac{\pi}{N_q}\sum_{\mathbf{q}}\sum_{m}^{3N} \frac{1}{2\omega_{m\mathbf{q}}} \sum_{\substack{\kappa\alpha \\ \kappa'\gamma}} {\sum_{n'=1}^{\infty}}' \left\langle u^{(0)}_{n\mathbf{k}} \middle| \frac{\partial \hat{H}_{\mathbf{k},\mathbf{k}}}{\partial R_{\kappa\alpha}(-\mathbf{q})} \middle| u^{(0)}_{n'\mathbf{k}+\mathbf{q}} \right\rangle \left\langle u^{(0)}_{n'\mathbf{k}+\mathbf{q}} \middle| \frac{\partial \hat{H}_{\mathbf{k},\mathbf{k}}}{\partial R_{\kappa'\gamma}(\mathbf{q})} \middle| u^{(0)}_{n\mathbf{k}} \right\rangle \delta(\varepsilon^{(0)}_{n\mathbf{k}} - \varepsilon^{(0)}_{n'\mathbf{k}+\mathbf{q}}). \tag{1.95}$$

1.6 CONCLUSIONS

The renormalization of eigenenergies due to electron-phonon coupling can be computed by different methods. In the introduction of this chapter, we have mentioned three of them: the first-principle molecular dynamics method, the frozen-phonon (FP) method and the Allen-Heine-Cardona (AHC) method based on Density-Functional Perturbation Theory. The two first methods are equivalent within the adiabatic harmonic approximation while the third is only equivalent when the non-rigid-ion (NRIA) terms are included or when the rigid-ion approximation (RIA) is valid.

The theory's key ingredient is the second-order derivative of the eigenenergies with respect to two atomic displacements. This derivative gives rise to a term stemming from the first-order modification of the wavefunction, called the Fan term, and a term corresponding to a second-order perturbation of the Hamiltonian, called the Debye-Waller (DW) term. Although the two terms were discovered separately in the 50's,

there was a lot of confusion in the litterature until Baumann realised in 1974 the complementarity of these two terms for the computation of the zero-point motion renormalization (ZPR).

The present first chapter compared in detail two (AHC/DFPT and FP) of the three approaches still used today to calculate the ZPR. We considered the first for its efficiency in the computation of the ZPR at arbitrary **q**-points, crucial for periodic system, and the later, to go beyond the RIA and study its impact on the calculated ZPR.

Also, we derived Brook's theorem in the first-principle context and obtained an expression for the eigenenergy renormalization from the finite temperature extension of Janak's theorem (see Eqs. (1.32) and (1.25)).

We also rederived how, within the RIA, the translational invariance (Eq. (1.45)) allows to express the DW contribution in terms of first-order derivatives of the Hamiltonian only.

A major contribution of this chapter is the clarification of the term appearing beyond the RIA made in the AHC theory. This allows all the definitions to be coherent with their respective names (see Eqs. (1.53), (1.64) and (1.69)).

Nevertheless, due to the computational limitation related to the evaluation of the second-order derivative of the Hamiltonian, the NRIA terms could not be computed from the second-order response of the wavefunctions. Therefore we derived the equations related to the FP approach, which will allow us to numerically evaluate the NRIA terms in the case of bulk diamond in Chapter 2 using Eqs. (1.75) and (1.76).

Finally, we presented an extension of the static theory to the dynamical case (going beyond the Rayleigh-Schrödinger perturbation theory) in order to derive the phonon induced lifetime broadening of the electronic states. The next chapter will be dedicated to the verification and validation of the theory developed in this first chapter.

2

VERIFICATION AND VALIDATION OF FIRST-PRINCIPLES CODES

The need for better verification of electronic structure codes and better validation of the methods they implement is crucial to have credibility toward industry and as a community in general.

Verification (i.e. of the correctness of computer codes) is crucial due to the ever increasing complexity of software, resulting from the implementation of more refined and sophisticated methods and theory. Moreover, the need to adapt to new computer architectures that take advantage of Graphics Processing Unit (GPU) or the fact that the codes can take advantage of massively-parallel High-Performance Computing (HPC) centres increases the likelihood of bugs or instabilities of the code.

Validation (i.e. of the correctness of theoretical methods) is a process that can be carried on with the accumulation of computed results. Indeed, most advanced theoretical methods rely on approximation and are usually based on ground-state calculations that are themselves based on other approximations. The goal of validation is to account for the reliability of the final result.

After an introduction to the verification and validation (V&V) framework in section 2.1, the section 2.2 presents the numerical validation of the theory developed in Chapter 1 and applied to the case of diamond. The validity of the theory is assessed by direct comparison between the AHC theory and the equivalent finite-difference scheme. The importance of the rigid-ion approximation in the case of periodic solids is also analysed. Section 2.3 introduces additional equations required by the verification study. The section 2.4 presents the computational details and the numerical comparison between the software applications Abinit and Yambo on top of Quantum Espresso.

The content of sections 2.1, 2.3, 2.4 and 2.5 has been published in Ref. [88]. The content of section 2.2 has also been submitted for publication [20].

2.1 THE VERIFICATION AND VALIDATION FRAMEWORK

First-principles electronic-structure codes develop and evolve : they adapt to increasing computational capabilities and also include new formalisms, approximations, and numerical methods. In addition to the validation of new formalisms and approximations, the verification of implementations is of utmost importance if one wants to deliver reliable new results or compare them to existing ones. This concern has been the subject of increased attention in the recent years, as witnessed by the set up of ES-TEST, a framework for the validation and verification of electronic structure codes [89], and the organization of several related activities under the auspices of the "Centre Européen de Calcul Atomique et Moléculaire" (CECAM) [90].

In particular, the first-principles computation of electronic properties, quasiparticles band structures and optical spectra of crystalline solids has reached an unprecedented level of sophistication. Many-body GW calculations [21], dynamical-mean-field theory [91] and Bethe-Salpeter [23] calculations, that includes excitonic effects, sometimes claim to agree with experimental data at the level of 0.1-0.2 eV. However, the influence of lattice vibrations on electronic properties is usually neglected because it is assumed to lead only to minor corrections, on the order of a few tens of meV. Actually, as reviewed in Ref. [92], for materials that contain light atoms like diamond, the inclusion of the influence of lattice vibration is non-negligible, since the renormalization is larger than the claimed accuracy of quasiparticle methods.

For the case of diamond, the closing of the electronic gap has been measured experimentally at different temperatures, and an Einstein oscillator fit has been used to extrapolate the data at zero Kelvin [25], giving a value of 0.37 eV for the renormalization of the indirect band-gap due to the ZPR of atoms. The temperature dependence of the direct band-gap of diamond was also studied experimentally [93].

The direct band-gap renormalization has been studied from first-principles approaches. Ramírez obtained 0.7 eV using path-integral Monte Carlo simulations [49] and more recently Giustino *et al.* [62] obtained a value of 0.615 eV using the Allen-Heine-Cardona (AHC) [38, 39] theory, with the Local Density Approximation (LDA) [94, 95] of Density Functional Theory (DFT) [45], a basis of plane waves, and norm-conserving pseudopotentials [45].

However, the first-principles computation of such a quantity is particularly delicate, because it is the outcome of several layers of consec-

utive first-principles calculations: computation of the total energy (and associated relaxation of cell geometry), computation of the phonon frequencies and eigenvectors, computation of the electron-phonon (EP) coupling, and finally, computation of the zero-point motion effect. Not only the choice of a mathematical formalism, with associated approximations (like the above-mentioned Monte Carlo versus DFT possibility), might deliver different values, but the implementation of one well-defined mathematical formalism, with given approximations, needs to be carefully verified.

At variance with the 0.615 eV result of Giustino *et al.* [62], calculations made by us lead to a smaller value, on the order of 0.4 eV, on the basis of the implementation of AHC described in Chapter 1. However, the mathematical formalism and numerical approximations were, to our understanding, equivalent to that of Ref. [62]. This raised the question on whether the accumulation of layers of calculations could yield numerical errors that are as large as 0.2 eV, or whether there might be a problem in the implementations.

In this chapter, we present a rigorous and careful study of all the quantities that enters into the calculation of the ZPR of the direct bandgap of diamond due to EP coupling, on the basis of two different implementations, and provide the values of the numerical discrepancies. We work within the AHC formalism with exactly the same numerical approximations, as implemented in ABINIT [96], on one side, and in Yambo [97] on top of Quantum Espresso (QE) [98], on the other side. These implementations have been done completely independently by two different groups. The ABINIT implementation was used earlier to study zero-point motion effects on the electronic structure in the above-mentioned Ref. [19], while the YAMBO+QE implementation has been used, independently, in Ref. [65, 66, 67, 99]. Unfortunately, we did not have access to the code used by Giustino *et al.* [62].

We found only small numerical discrepancies between the ABINIT and QE+YAMBO results: less than 10^{-5}Ha/at on the total energy, 0.07 cm^{-1} on the phonon frequencies, 0.005 on the electron-phonon matrix elements squared (relative difference), and less than 4 meV on the ZPR. Given our choice of formalism, and associated approximations, the numerically converged value for the renormalization of the direct bandgap in diamond due to electron-phonon coupling in the AHC formalism is -0.409 eV (reduction of the bandgap), from both implementations. Changing the pseudopotential can lead to larger differences, in any case not larger than 50 meV.

2.2 INTERNAL CROSS-VALIDATION OF THE THEORY WITHIN THE ABINIT SOFTWARE

Before doing the verification between the two sets of *ab-initio* codes to understand the observed discrepancy between our results and those of Ref. [62], we start by an internal validation inside the software ABINIT. We compare AHC and FP results for some chosen $\mathbf{q}$-wavevector contributions to the ZPR of the diamond bandgap. We study the $\mathbf{q}$-wavevector contributions to the ZPR instead of the full ZPR since the converged $\mathbf{q}$-point integration required by the full ZPR is computationally out of reach for FP. For the full $\mathbf{q}$-point integration within AHC, please see Ref. [88].

The calculation of structural properties in this work are based on Density-Functional Theory (DFT) [45] within the local density approximation (LDA) [94, 95]. We use a planewave basis set to represent the wavefunctions and account for the core-valence interaction using norm-conserving pseudopotentials [100]. The $2s^2 2p^2$ valence electrons of carbon are treated explicitly in our ab-initio calculations. All the calculations are done using the ABINIT software package [96].

Convergence studies with a tolerance of 0.5 mHa per atom on the total energy led to the use of a $6 \times 6 \times 6$ Γ-centered Monkhorst-Pack sampling [101] of the Brillouin zone and an energy cut-off of 30 Hartree for the truncation of the planewave basis set. A lattice parameter of 6.675 Bohr was obtained by structural optimization.

The phonon frequencies were calculated using Eq. (1.5) for the DFPT method and a second-order derivative of the total energy with respect to atomic displacements converged with a Richardson interpolation of order 4, for the finite-difference method. Also, for the latter method and the $\mathbf{q} = \mathrm{L}$ point, a $2 \times 2 \times 2$ supercell with a $3 \times 3 \times 3$ Γ-centered Monkhorst-Pack sampling were used to ensure the $\mathbf{k}$-point sampling remained equivalent to the one used for the DFPT calculation on the primitive cell. The comparison between FP and DFPT for the phonon frequencies is given in Table 2.1. The discrepancies between the two methods remain within 0.2% for the two $\mathbf{q}$-points considered, which demonstrates both the equivalence of the two methods and the convergence of our calculations with respect to the finite difference parameter.

We now assess the accuracy of our AHC implementation and quantify the impact of the RIA. The contribution of the same two $\mathbf{q}$-points to the ZPR at $\mathbf{k} = \mathbf{\Gamma}$ and $\mathbf{k} = \mathbf{L}$ is given in Table 2.2. This table presents the

q-point	Mode	ω DFPT [Ha]	ω FP [Ha]	diff. [%]
Γ	LO+TO	0.006 064 74	0.006 052 26	0.2058
L	TA	0.002 502 56	0.002 501 11	0.0580
	LA	0.004 941 58	0.004 943 44	0.0376
	TO	0.005 647 86	0.005 652 44	0.0810
	LO	0.005 775 97	0.005 770 16	0.1007

Table 2.1: Comparison of diamond phonon frequencies computed from FP and from DFPT.

renormalization of the different eigenenergies due to electron-phonon coupling for the 4 first distinguishable bands of diamonds. The $\mathbf{\Gamma}_{25'}$ valence band maximum is three-fold degenerate as well as the $\mathbf{\Gamma}_{15}$ conduction band. In diamond, the conduction band minimum is located between the $\mathbf{k} = \mathbf{\Gamma}$ and $\mathbf{k} = \mathbf{X}$ points. At the $\mathbf{k} = \mathbf{L}$, the valence $\mathbf{L}_1$ and conduction $\mathbf{L}_{3'}$ bands are only doubly degenerate. It can also be noted that our results show the contribution of some **q**-points to the ZPR with values in very close agreements (within 2 meV) with Figure 1 of Ref. [55] that shows the electron-phonon coupling energies (there is therefore a conversion factor of 1/2).

The AHC results are split into Fan and $\mathrm{DW}_{\mathrm{RIA}}$ contributions that are computed using Eq. (1.53) and Eq. (1.64), respectively. The importance of the rigid-ion approximation can be deduced by computing the $\mathrm{DW}_{\mathrm{NRIA}}$ term through finite difference calculations using Eq. (1.76).

The impact of the RIA remains below 23% and is usually much smaller for wavevectors other than the zone-center one. To assess completely the validity of the approximation, we should do a full **q**-point integration on the BZ. However, since the ZPR converges extremely slowly with the number of **q**-points [88], this would require huge supercell calculations, which are currently computationally out of reach.

Finally, the sum of the AHC and NRIA contributions can be compared to the finite difference calculations done using Eq. (1.75). All the FP calculations are also converged with a Richardson interpolation of order 4. The discrepancies remain below 7 μeV in absolute value. Such discrepancies can be attributed to numerical noise or anharmonicity. Indeed, the finite displacements selected in the FP method (0.02 to 0.0025 Bohr) ensure a good compromise between these two sources of error, so that both are present, but as small as allowed by our convergence criterion.

q-point	**k**-point	AHC [meV]			NRIA [meV]		sum all	FP	diff.
		Fan	DW_{RIA}	sumAHC	DW_{NRIA}	% NRIA	[meV]	[meV]	[μeV]
Γ	Γ_1	−32.8174	20.2868	−12.5306	1.4500	13.09	−11.0806	−11.0809	0.308
	$\Gamma_{25'}$	−332.4265	357.2564	24.8300	3.5982	12.66	28.4282	28.4289	−0.638
	Γ_{15}	−330.4363	316.2021	−14.2342	0.3848	2.78	−13.8494	−13.8497	0.338
	$\Gamma_{2'}$	−63.3087	32.3760	−30.9327	0.2998	0.98	−30.6328	−30.6335	0.748
	$L_{2'}$	−67.8598	46.8783	−20.9814	2.2820	12.20	−18.6993	−18.6999	0.554
	L_1	−146.0806	129.4769	−16.6037	1.1326	7.32	−15.4710	−15.4714	0.367
	$L_{3'}$	−311.2306	321.3287	10.0981	2.9610	22.67	13.0590	13.0592	−0.307
	L_3	−473.0115	292.4656	−180.5458	0.1558	0.09	−180.3900	−180.3937	6.977
L	Γ_1	−116.4278	62.6966	−53.7312	0.9068	1.72	−52.8256	−52.8245	1.104
	$\Gamma_{25'}$	−922.8240	1104.1052	181.2812	2.2949	1.25	183.5761	183.5771	−1.017
	Γ_{15}	−1250.8082	977.2263	−273.5819	−1.0060	0.37	−274.5878	−274.5881	0.244
	$\Gamma_{2'}$	−407.6022	100.0584	−307.5438	−1.8483	0.60	−309.3921	−309.3973	5.131
	$L_{2'}$	−234.2353	144.8781	−89.3572	1.4860	1.69	−87.8712	−87.8728	1.542
	L_1	−620.7070	400.1500	−220.5570	0.5069	0.23	−220.0501	−220.0525	2.359
	$L_{3'}$	−1018.9788	993.0698	−25.9090	1.7417	7.21	−24.1674	−24.1672	−0.210
	L_3	−740.6821	903.8683	163.1862	−1.0928	0.67	162.0934	162.0935	−0.142

Table 2.2: Comparison between the AHC/DFPT and FP results for the contributions of specific **q**-points to the ZPR of several bands of diamond. The column "diff." is the sum of the AHC and the NRIA contributions minus the FP result.

It is therefore concluded that the internal validation within the ABINIT software is successful and could not yield the witness discrepancy of ~50%. We can then proceed to the verification of the two set of codes: ABINIT versus Yambo on top of QE.

2.3 VERIFICATION METHODOLOGY

The decomposition of the total energy differs between ABINIT and QE, such that a comparison of energy components needs to be done with care. The expression for the total ground-state energy per unit cell of a periodic insulator at zero Kelvin, within DFT is [45, 64]

$$E_{\text{Total}} = \frac{1}{N_k} \sum_{\mathbf{k}} \sum_{n}^{\text{occ}} \left\langle \Psi^{(0)}_{n\mathbf{k}} \middle| \hat{T} + \hat{V}_{\text{psp}} \middle| \Psi^{(0)}_{n\mathbf{k}} \right\rangle + E_{\text{Hxc}} + E_{\text{Ew}} + E_{\text{psp-core}}, \quad (2.1)$$

where n is the band number, $\mathbf{k}$ the wavevector, N_k the number of $\mathbf{k}$-points, $\Psi^{(0)}_{n\mathbf{k}}$ represents a Kohn-Sham orbital, $\hat{T}$ the kinetic energy operator, $\hat{V}_{\text{psp}}$ the operator corresponding to the external potential of the electronic system (composed by a local and a non-local part when the implementation is based on the pseudopotential concept), the n-summation is over the occupied bands and the $\mathbf{k}$-summation over a discretization of the Brillouin zone. E_{Hxc} is the Hartree and exchange-correlation energy functional of the electronic density (expressed per unit cell), E_{Ew} is the Ewald energy per unit cell (periodic positively charged particles placed in a negatively charged homogeneous background), and finally $E_{\text{psp-core}}$ is the pseudo-core energy per unit cell. It is also possible to define a one-electron contribution per unit cell as

$$E_{\text{One-el}} = \frac{1}{N_k} \sum_{\mathbf{k}} \sum_{n}^{\text{occ}} \left\langle \Psi^{(0)}_{n\mathbf{k}} \middle| \hat{T} + \hat{V}_{\text{psp}} \middle| \Psi^{(0)}_{n\mathbf{k}} \right\rangle + E_{\text{psp-core}}. \quad (2.2)$$

See the appendix A.11 for more details concerning the Ewald energy, the pseudocore energy and the one-electron contribution.

The phonon frequencies and eigenvectors can be obtained from Density Functional Perturbation Theory (DFPT) following Refs. [63, 102, 64, 84, 85] or Eq. (1.5)

$$\omega^2_{m\mathbf{q}} = \sum_{\substack{\kappa\alpha \\ \kappa'\gamma}} U^*_{m,\kappa'\gamma}(\mathbf{q}) \tilde{C}^{\kappa\alpha}_{\kappa'\gamma}(\mathbf{q}) U_{m,\kappa\alpha}(\mathbf{q}), \quad (2.3)$$

with $\tilde{C}_{\substack{\kappa\alpha \\ \kappa'\gamma}}(\mathbf{q})$ being the interatomic force constant matrix in reciprocal space defined Eq. (1.39) and $U_{m,\kappa\alpha}(\mathbf{q})$ the eigendisplacement vectors defined as solution of the dynamical equation Eq. (1.38).

The computation of the *ab-initio* temperature dependence implies the calculation of the electron-phonon interaction. Following Ref. [99] the first-order electron-phonon matrix elements can be computed thanks to DFPT as

$$g^{m\mathbf{q}}_{nn'\mathbf{k}} = \sum_{\kappa\alpha} \frac{1}{\sqrt{2\omega_{m\mathbf{q}}}} \left\langle u^{(0)}_{n\mathbf{k}} \middle| \frac{\partial \hat{H}_{\mathbf{k},\mathbf{k}}}{\partial R_{\kappa\alpha}(-\mathbf{q})} \middle| u^{(0)}_{n'\mathbf{k}+\mathbf{q}} \right\rangle U_{m,\kappa\alpha}(\mathbf{q}), \quad (2.4)$$

where $\hat{H}_{\mathbf{k},\mathbf{k}}$ is the self-consistent Hamiltonian felt by the electrons (which depends on the atomic positions, see Eq. (A.4) applied to the Hamiltonian operator)

The first-order electron-phonon matrix element, $g^{m\mathbf{q}}_{nn'\mathbf{k}}$, that will be referred to as the "GKK" matrix element, describes the probability amplitude for an electron to be scattered from $\mathbf{k}$ to $\mathbf{k}+\mathbf{q}$, with the emission or the absorption of a phonon with crystalline momentum $\mathbf{q}$ belonging to the phonon branch m.

The second-order electron-phonon matrix element is

$$\Lambda^{m\mathbf{q}m'\mathbf{q}'}_{nn'\mathbf{k}} = \frac{1}{2} \sum_{\substack{l\kappa\alpha \\ l'\kappa'\gamma}} \frac{U^{*}_{m,\kappa\alpha}(\mathbf{q}) U_{m',\kappa'\gamma}(\mathbf{q}')}{2(\omega_{m\mathbf{q}}\omega_{m'\mathbf{q}'})^{1/2}} \times \left\langle u^{(0)}_{n\mathbf{k}} \middle| \frac{\partial^2 \hat{H}_{\mathbf{k},\mathbf{k}}}{\partial R_{l\kappa\alpha}(-\mathbf{q}) \partial R_{l'\kappa'\gamma}(\mathbf{q}')} \middle| u^{(0)}_{n'\mathbf{k}+\mathbf{q}+\mathbf{q}'} \right\rangle. \quad (2.5)$$

The AHC theory [39] allows to calculate the temperature-dependent change in the electronic eigenenergies, as well as their zero-point renormalization, as the sum of a Fan [14, 15] and a Debye-Waller (DW) self-energy term. These two terms can be deduced from the more general many-body formalism [99] as

$$\Sigma^{\mathrm{FAN}}_{n\mathbf{k}}(i\omega, T) = \frac{1}{N_q} \sum_{n'm\mathbf{q}} \left| g^{m\mathbf{q}}_{nn'\mathbf{k}} \right|^2 \times \left(\frac{n_{m\mathbf{q}}(T) + f_{n'\mathbf{k}+\mathbf{q}}}{\omega - \varepsilon^{(0)}_{n'\mathbf{k}+\mathbf{q}} + \omega_{m\mathbf{q}}(T) + i\delta} + \frac{n_{m\mathbf{q}}(T) + 1 - f_{n'\mathbf{k}+\mathbf{q}}}{\omega - \varepsilon^{(0)}_{n'\mathbf{k}+\mathbf{q}} - \omega_{m\mathbf{q}}(T) + i\delta} \right), \quad (2.6)$$

which is a slightly different form of Eq. (1.79) where the summation over modes and $\mathbf{q}$-points is performed and the eigendisplacement vectors are included. The second term is

$$\Sigma^{\mathrm{DW}}_{n\mathbf{k}}(T) = \frac{1}{N_q}\sum_{m\mathbf{q}} \Lambda^{m\mathbf{q},m-\mathbf{q}}_{nnk}(n_{m\mathbf{q}}(T)+\frac{1}{2}), \tag{2.7}$$

where N_q is the number of $\mathbf{q}$ points, $n_{m\mathbf{q}}(T)$ is the Bose-Einstein distribution function for the phonon mode $m\mathbf{q}$ at temperature T, and $f_{n'\mathbf{k}+\mathbf{q}}(T)$ is the electronic occupation.

The ZPR of the traditional AHC theory [39] is recovered by using the following approximations for the Fan term: $\omega \approx \varepsilon_{n\mathbf{k}}$ (the on-the-mass-shell (OMS) limit), $|\varepsilon_{n\mathbf{k}} - \varepsilon_{n'\mathbf{k}+\mathbf{q}}| \gg \omega_{m\mathbf{q}}$ (the adiabatic limit) and by considering only the real part of the self energy

$$\Delta\varepsilon^{\mathrm{AHC}}_{n\mathbf{k}}(T) = \Sigma^{\mathrm{DW}}_{n\mathbf{k}}(T) + \frac{1}{N_q}\sum_{n'm\mathbf{q}} \frac{\left|g^{m\mathbf{q}}_{nn'\mathbf{k}}\right|^2 (n_{m\mathbf{q}}(T)+\frac{1}{2})}{\varepsilon_{n\mathbf{k}} - \varepsilon_{n'\mathbf{k}+\mathbf{q}}}. \tag{2.8}$$

From a practical point of view, the DW term is very difficult to calculate, as one needs access to the second derivative of the self-consistent potential (that is not provided by a DFPT calculation of phonons). Making use of the translational invariance (if all atoms are displaced by the same amount in the same direction, all physical quantities should be conserved) [39] and the RIA, the $\mathrm{DW}_{\mathrm{RIA}}$ contribution can be retrieved as the product of first-order electron-phonon matrix elements that is easy to calculate with Eq. (1.64).

The NRIA contribution comes from the modification of the screening due to atomic motion. By opposition with the case of small molecules [19], the effect of the NRIA terms is expected to be small in extended system, thanks to the screening of the periodic lattice.

From a numerical point of view, the term with an energy denominator in Eq. (2.8) is omitted when the difference of eigenenergies is smaller than 10^{-6} or is smoothed by introducing a small imaginary component.

Finally, following Sternheimer [83], we can largely speed up the calculation of the sum over states appearing in the Fan and $\mathrm{DW}_{\mathrm{RIA}}$ terms. In that case, they are rewritten in terms of a sum limited to an active space (spanning the occupied state with a few extra bands over the valence band maximum) as written in Eq. (1.67). The result of such a projection re-writing is an outcome of a phonon DFPT calculation, and, as such it is available at no additional cost.

2.4 DIAMOND: CALCULATIONS DETAILS

The ABINIT, QE and Yambo software applications are described in Refs. [96, 98, 97], respectively.

The calculation of structural properties in this work is based on DFT [103, 104, 45] using the LDA [94, 95]. A norm-conserving pseudopotential [100] accounts for the core-valence interaction and a plane-wave basis set is then used to expand the electronic wavefunctions. The pseudopotential was generated using the `fhi98PP` code [105] with a 1.5 atomic unit cut-off radius for pseudization. The valence electrons of Carbon, treated explicitly in the *ab-initio* calculations, are generated for the $2s^2 2p^2 3d^0$ configuration. Quite importantly for the comparison between codes, the same pseudopotential file was used by ABINIT and QE. Moreover this pseudopotential is the same as the one used in Ref. [62]. We refer to this pseudopotential as our "reference" pseudopotential.

Careful convergence checks (error below 0.5 mHa per atom on the total energy) lead to the use of a 6x6x6 Γ-centered Monkhorst-Pack $\mathbf{k}$-point sampling [101] of the Brillouin zone and an energy cut-off of 30 Hartree for the truncation of the plane wave basis set. The lattice parameter of 6.652 Bohr was obtained by structural relaxation of the diamond system.

Additional tests were performed to assess the influence of the pseudopotential choice. In addition to our "reference" pseudopotential, we considered five other ones. We will refer to the first one as `06-C.LDA.fhi` also generated using the `fhi98PP` code. It is a Troullier-Martins pseudopotential with the Perdew/Wang [106] parametrization of LDA, an atomic cut-off radius of 1.0247 atomic unit and a maximum angular channel of $l = 3$. The second one is the `6c.pspnc` Troullier-Martin [100] pseudopotential with a 1.4851 atomic unit cut-off radius and a maximum angular channel of $l = 1$. The third one is the `06-C.GGA.fhi` Troullier-Martin pseudopotential with the GGA Perdew/Burke/Ernzerhof [107] parametrization and a 1.0247 atomic unit cut-off radius. The maximum angular channel used is $l = 3$ for this pseudopotential. The required cut-off energy for the truncation of the basis set for those three pseudopotential was also 30 Hartree. The fourth one is the `6c.4.hgh` Hartwigsen-Goedecker-Hutter pseudopotential [108] with a 1.2284 atomic unit cut-off radius and a maximum angular channel of $l = 1$. An energy cut-off of 60 Ha was required for this pseudopotential. The last one is the `C.pz-vbc.UPF` VonBarth-Car pseudopotential with a maximum angular channel of l=1 and an energy cut-off of 45 Ha and 1.5 atomic unit cut-off radius. The lattice parameters of the five additional pseudopotentials

after structural relaxation were 6.648, 6.694, 6.729, 6.675 and 6.663 Bohr, respectively. All the calculations with these pseudopotentials were also done with the 6x6x6 unshifted Monkhorst-Pack **k**-point grid.

In order to converge the ZPR below 1 meV, in the original AHC formulation, around 300 unoccupied bands needs to be explicitly included in the summation present in the Fan and DW_{RIA} terms for diamond. In contrast, only 12 bands were needed to describe the active space when the Sternheimer re-writing is used.

To avoid high symmetry points that might slow down the convergence study (some EP matrix elements might be zero by symmetry and are not representative of the discretization of an integral) we computed the ZPR correction on a random **q**-wavevector grid, as described in Ref. [99]. The rate of convergence of homogeneous wavevector grid will also be discussed. The statistical analysis to converge the results is explained in the next section. The Sternheimer implementation, which speeds up significantly the calculation, is only present in the ABINIT software. Therefore we did the statistical analysis only with ABINIT.

2.5 VERIFICATIONS RESULTS FOR DIAMOND

2.5.1 *Ground-state and phonons*

We started by comparing DFT ground-state total energies between ABINIT and QE using the same "reference" norm-conserving pseudopotential and the same numerical parameters (plane wave kinetic energy cut-off and wavevector sampling). The total energy in ABINIT and QE is decomposed in different terms detailed in Eqs. (2.1) and (2.2). The comparison between the terms and the total energy is given in the upper panel of Table 2.3. The agreement is excellent: one gets a discrepancy on the order of 10^{-5} Ha/atom between the total energies computed using the two codes. The disagreement is even smaller for selected contributions : on the order of 10^{-7} Ha/atom for the exchange-correlation and Hartree contributions, and about 10^{-9} Ha/atom for the Ewald energy. We did not try to track down the origin of the total energy discrepancy, the agreement being beyond practical needs.

Table 2.3 also shows the agreement between the two codes on the phonon frequencies at some high symmetry points obtained from the DFPT Eq. (2.3). The agreement is also rather good, with less than 0.07 cm^{-1} differences after imposition of the acoustic sum rule (ASR) at Γ. The imposition of the ASR is discussed e.g. in Ref. [74]. Without the impo-

	ABINIT 7.3.2	QE 4.0.5
Kinetic energy	8.450 310 501	-
One-electron energy	-	4.135 925 595
Hartree energy	0.943 336 981	0.943 337 120
XC energy	−3.567 609 861	−3.567 609 935
Ewald energy	−12.955 782 342	−12.955 782 345
Psp-core energy	0.581 222 385	-
Loc. psp. energy	−5.093 200 787	-
NL psp. energy	0.197 606 844	-
Total energy	−11.444 116 277	−11.444 129 565
Phonon frequency at		
$q = \Gamma_1$ /with ASR	3.335/0.000 (x3)	8.832 /0.000 (x3)
$q = \Gamma_{25'}$ /with ASR	1330.408/1330.403(x3)	1330.428 /1330.400 (x3)
$q = L_3$	555.305 (x2)	555.319 (x2)
$q = L_{2'}$	1076.250	1076.268
$q = L_1$	1235.429 (x2)	1235.440 (x2)
$q = L_{3'}$	1273.840	1273.860
$q = X_3$	795.900 (x2)	795.964 (x2)
$q = X_4$	1098.461 (x2)	1098.489 (x2)
$q = X_1$	1224.570 (x2)	1224.590 (x2)

Table 2.3: Comparison of selected quantities related to the ground state and to phonon calculations, for diamond, with a 6x6x6 unshifted **k**-point grid and a kinetic energy cutoff of 30 Hartree for the plane wave basis set. The same norm-conserving LDA pseudopotential is used. The lattice parameter is 6.652 Bohr. All the energies are in Hartree, are expressed per cell (two atoms per cell) and the phonon frequencies are in cm^{-1}.

sition of the ASR, the frequency of acoustic modes at Γ are small, but non-negligible : 3.335 cm^{-1} for ABINIT, and 8.832 cm^{-1} for QE. Such a variation between codes is however sufficient to lead to significant differences in the absolute value of the Fan and DW_{RIA} terms computed separately, as we shall see later. Concerning the electronic properties, the nine lower eigenenergies, relative to the top of the valence band at Γ are compared for the two codes in Table 2.4. One can see that there is less than 0.0003 eV differences between the two codes.

Sym.	Band	Eigenergies in Abinit	Eigenergies in QE
Γ_1	1	−21.7959	−21.7957
$\Gamma_{25'}$	2-3-4	0.0000	0.0000
Γ_{15}	5-6-7	5.6698	5.6699
$\Gamma_{2'}$	8	14.3020	14.3023
Γ_1	9	19.4714	19.4716

Table 2.4: Comparison between Abinit and QE of the nine lower eigenenergies in eV, relative to the top of the valence band at Γ.

2.5.2 *Electron-phonon coupling and zero-point motion renormalization*

We now move forward and compare the GKK electron-phonon matrix elements given in Eq. (2.4). This quantity is actually subject to an arbitrary dependence on the phase factors of the wavefunctions, and cannot be compared directly between codes. We have therefore compared the square norm of the GKK (the GKK times its complex conjugate). Such a quantity, termed "GKK2" is relevant in the present context, since the square of GKK is used to build the ZPR, see Eq. (2.6). When wavefunctions are degenerate, we also sum them inside the degenerate space, to remove any arbitrariness. Moreover, to decrease the number of handled data, we sum the GKK2 over the six phonon modes, giving SGKK2

$$\mathrm{SGKK2} = \sum_{m}^{3N} g^{m\mathbf{q}*}_{nn'\mathbf{k}} g^{m\mathbf{q}}_{nn'\mathbf{k}}. \tag{2.9}$$

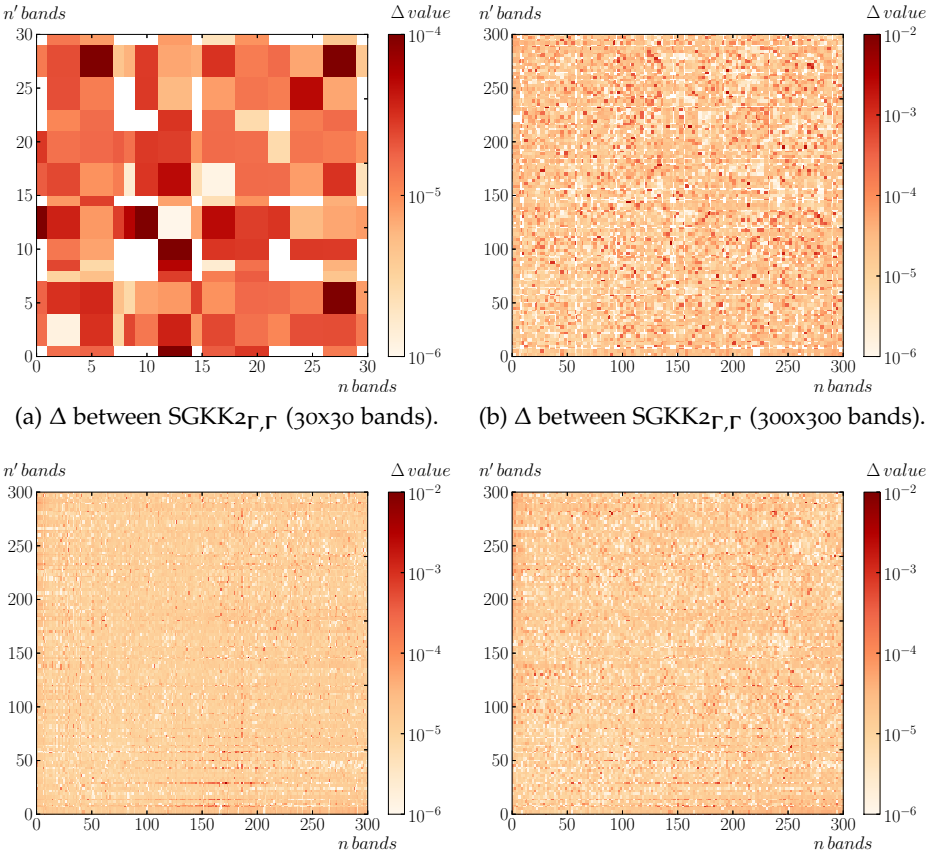
A measure of the relative difference between the two codes for SGKK2, for different high symmetry $\mathbf{q}$-wavevectors is displayed in Fig. 2.1. We plot, for each pair of electronic state (or degenerate state) the difference of the SGKK2 divided by their sum :

$$\Delta = \left| \frac{\mathrm{SGKK2(ABINIT)} - \mathrm{SGKK2(QE)}}{\mathrm{SGKK2(ABINIT)} + \mathrm{SGKK2(QE)}} \right|. \tag{2.10}$$

The absolute values of SGKK2 are reported in Table 2.5 for the two codes.

One can see that the relative differences are in all three cases lower than 0.005 for all matrix elements on the 300x300 matrix bands.

Finally, we compared the ZPR computed with ABINIT and Yambo using the GKKs of QE in the AHC framework of Eq. (2.8). The energy



(a) Δ between SGKK2$_{\Gamma,\Gamma}$ (30x30 bands).

(b) Δ between SGKK2$_{\Gamma,\Gamma}$ (300x300 bands).

(c) Δ between SGKK2$_{\Gamma,L}$ (300x300 bands).

(d) Δ between SGKK2$_{\Gamma,X}$ (300x300 bands).

Figure 2.1: Relative differences Δ of the SGKK2 between ABINIT and QE, at $\mathbf{k} = \Gamma$ and $\mathbf{q} = \Gamma$ for 20x20 pairs of bands, $\mathbf{q} = \Gamma$, $\mathbf{q} = L$ or $\mathbf{q} = X$ for 300x300 pairs of bands.

denominator was smoothened by introducing a small imaginary component of 100 meV, following Ref. [42, 62]. We first compared the two codes without the Sternheimer rewriting and then, in the case of ABINIT, we used the Sternheimer rewriting of Eq. (1.67) and we summed over 300 bands in the case of Yambo. In Table 2.6 we show a comparison between ABINIT and YAMBO for different number of $\mathbf{q}$-wavevectors. The 47 $\mathbf{q}$-wavevector case corresponds to a homogeneous, non-shifted 10x10x10 grid, folded in the irreducible part of the Brillouin zone. For the 1000 and 2000 $\mathbf{q}$-wavevector cases, the wavevectors are randomly generated once and then used in both codes. In the last two columns of Table 2.6, we can see that the disparity between the two codes on the ZPR is lower than 4 meV.

Band	Soft.	1	2-3-4	5-6-7	8	9
1	AB	0.0				
	QE	0.0				
2-3-4	AB	1.530 449	5.803 074			
	QE	1.530 401	5.803 088			
5-6-7	AB	0.493 950	0.292 491	4.495 984		
	QE	0.493 932	0.292 472	4.496 296		
8	AB	0.0	4.635 255	2.430 641	0.0	0.0
	QE	0.0	4.635 284	2.430 665	0.0	0.0
9	AB	0.0	1.565 383	4.002 821	0.0	0.0
	QE	0.0	1.565 460	4.002 843	0.0	0.0

Table 2.5: Comparison between Abinit (AB) and Quantum Espresso (QE) of absolute value of the SGKK2, at $\mathbf{k} = \Gamma$ and $\mathbf{q} = \Gamma$ in 10^{-6} Ha. Matrix elements with values lower than 10^{-11} Ha have been put to 0.

We have imposed in both codes the phonon frequencies to be 0 for the acoustic modes at $\mathbf{q} = \Gamma$ (ASR). One can nevertheless see that the absolute value of the Fan (last term in Eq. (2.8)) and DW_{RIA} (Eq. (1.64)) terms display more variation between both codes than the total ZPR (which is the sum of both terms). The reason for this is that the acoustic modes tends to have a larger relative difference than the optical ones between the two codes. Their separate contributions in the Fan and DW_{RIA} tend to the same value, with opposite signs, when the limiting behaviour for vanishing wavevector is considered. There is thus a cancellation of error between the Fan and DW_{RIA} terms, that allows one to obtain a much better accuracy on the sum of these terms. Indeed, due to the presence of the phonon frequency in the denominator of Eqs. (1.53) and (1.64), the acoustic modes will be the ones that contribute mostly to the Fan and DW_{RIA} terms. It can be shown that, due to translational invariance, the eigendisplacement vectors of Fan and DW_{RIA} will tend to cancel out for acoustic modes (especially those close to Γ). As a result, mostly the optical modes will contribute to the ZPR. This explains why the discrepancy is larger on the absolute value of Fan and DW_{RIA} terms separately, than on the total ZPR between the two codes. Note that the Fan and DW_{RIA} terms are not observable quantities separately. They come from a perturbation series, whose sum is an observable.

		Fan		DW_{RIA}		Fan+DW_{RIA}	
Set of **q**-wavevectors	Band	ABINIT 7.3.2 SEq / 300 bands	Yambo 3.4.0 300 bands	ABINIT 7.3.2 SEq / 300 bands	Yambo 3.4.0 300 bands	ABINIT 7.3.2 SEq / 300 bands	Yambo 3.4.0 300 bands
47	1	−120.76 /-116.54	117.30	59.23 /55.23	55.69	−61.53 /-61.30	−61.65
	2-3-4	−981.61 /-969.44	−978.00	1119.92 /1107.28	1116.53	138.30 /137.84	138.50
	5-6-7	−1332.55 /-1318.55	−1329.10	1005.15 /994.69	1002.88	−327.40 /-323.86	−326.20
	8	−555.40 /-541.89	−543.70	60.42 /50.32	50.76	−494.98 /-491.57	−492.90
	9	−33.72 /-28.50	−28.49	−34.89 /-39.91	−40.24	−68.61 /-68.41	68.73
1000	1	−121.13	−117.70	59.46	55.90	−61.67	−61.79
	2-3-4	−983.51	−979.90	1124.21	1120.82	140.70	140.90
	5-6-7	−1272.74	−1269.20	1009.01	1006.74	−263.73	−262.50
	8	−284.45	−272.80	60.64	50.96	−223.80	−221.80
	9	−9.83	−4.55	−35.03	−40.39	−44.85	−44.95
2000	1	−121.20	−117.80	59.45	55.90	−61.75	−61.87
	2-3-4	−983.56	−980.00	1124.11	1120.72	140.54	140.70
	5-6-7	−1269.55	−1266.00	1008.92	1006.65	−260.63	−259.40
	8	−293.01	−281.30	60.64	50.95	−232.37	−230.40
	9	−8.83	−3.56	−35.02	−40.39	−43.86	−43.95

Table 2.6: Comparison of the ZPR for different electronic states at **Γ**, for a 6x6x6 unshifted **k**-point grid with an energy cutoff of 30 Hartree for the plane wave basis set, using the same norm-conserving LDA pseudopotential. In the case of YAMBO, 300 bands were explicitly included into the calculation. In the case of ABINIT, the Sternheimer equation (SEq) was used to limit the computational effort (12 active bands were needed). Moreover, for the set of 47 **q**-wavevectors, the value obtained without the Sternheimer equation and with a summation over 300 bands, is also displayed. The energies are in meV.

2.5.3 *Analysis of the convergence with respect to the number of* **q**-*wavevectors*

We have just provided an analysis of the level of agreement that one can expect from two different codes that implement the same physics. We now turn ourselves to a careful convergence study of the ZPR within the AHC formalism. Since the calculations are heavy in YAMBO due to the band summations we decided to make that convergence study in ABINIT only, with the Sternheimer rewriting.

We performed DFPT calculations on 20,000 randomly generated **q**-wavevectors in the full Brillouin Zone. We then performed a statistical analysis of these results. We computed the ZPR over N (N=250, 500, 750, 1000, 2000, 3000, 4000, 5000, 6000, 10000) **q**-wavevectors taken randomly in the 20,000 set and we have performed such a calculation 100 times for each N. This gave us, for each N, a set of 100 different ZPR values whose statistical characteristics are given in figure 2.2. We can see that the ZPR converges smoothly towards 409 meV, the mean of the ZPR for the 20,000 set.

Since the rate of convergence of the variance of a normal distribution goes as $1/N_q$ with N_q the number of random **q**-wavevectors, the rate of convergence of the associated standard deviation goes as $1/\sqrt{N_q}$. We can see on Fig. 2.2 that the $1/\sqrt{N_q}$ of the continuous line follow neatly the lower 25% and upper 75%.

The drawback of the random **q**-points methods is that one is forced to test a sufficiently large set of random **q**-wavevectors. The homogeneous grid approaches might be more appealing. The green dots on Fig. 2.2 corresponds to non shifted homogeneous Monkhorst-Pack grids closest to the random points number we have chosen to analyse (e.g. the last grid is a 70x70x70 unshifted **q**-point grid that lead to 8112 **q**-wavevectors in the irreducible Brillouin-Zone.). As we can see, the green dots are always well inside the 50% windows.

One can set an upper limit on the convergence rate if one does not use an imaginary component to smooth the function.

In this case, when the difference of eigenenergies in the denominator of Eq. (2.8) vanishes, the integrand to be considered over the whole Brillouin zone diverges. This happens around Γ, with a divergence that behaves like $\frac{1}{q^2}$. Treating separately a small volume around Γ, set aside of the regular discretization, one can estimate its contribution by replacing it by the integral over a sphere with a cut-off radius q_c whose length is inversely proportional to the linear density of **q**-wavevectors. The contribution of this small sphere is $\propto \int_0^{q_c} \frac{1}{q^2} q^2 dq$ so that the rate of conver-

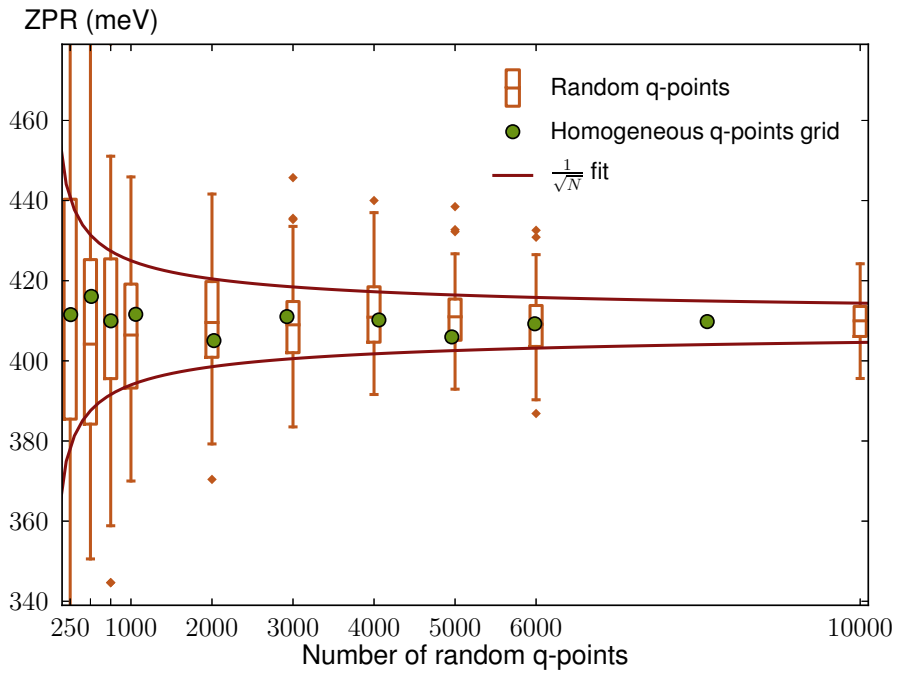


Figure 2.2: Convergence with respect to the number of random **q**-wavevetors included in the ZPR calculation using the software ABINIT in the static AHC formulation. 100 ZPR calculations have been performed for each subset of **q**-wavevectors taking N_q **q**-wavevectors among 20,000 (the total number of computed **q**-wavevectors). The upper and lower bars are the maximal and minimal values in each set. The top and bottom of the boxes represent 25% and 75% of all the data in the set. The middle line is the median and the red diamonds are outliers. The green dots come from non shifted homogeneous Monkhorst-Pack grids, for which the number of **q**-wavevectors corresponds to those in the irreducible Brillouin zone

gence of these integrals goes as $q_c \propto N_q^{-1/3}$, slightly worse than in the case of the random sampling.

Moreover, there are also regions distant from Γ, but where the eigenenergies of the **q**-wavevectors are very close to the one at Γ (diamond is indeed an indirect gap semiconductor). On the surface $S(\epsilon_\Gamma)$ where the eigenenergy is exactly equal to the Γ eigenenergy, the denominator also vanishes. In the neighborhood of the surface, the divergence is inversely proportional to the linear difference between the energy at Γ and the actual eigenenergy in its neighborhood. To estimate the rate of convergence with respect to the number of **q**-wavevectors of the discretized integral, we have to consider the discretization of an integral in the Brillouin zone, in a zone of width q_c around $S(\epsilon_\Gamma)$, in which the distance with respect to the surface is denoted as $q_\perp$ giving a behaviour

$\propto S(\epsilon_\Gamma) \times \int_{-q_c}^{+q_c} \frac{1}{q_\perp} dq_\perp$. Although the principal value of this integral vanishes identically, fluctuations due to the discretization will not be small, and hence the convergence is non-monotonic.

Nonetheless, in practice, the small imaginary component at the denominator is present. One can observe, in Fig. 2.2, that the fluctuations, in the case of the homogeneous grid, are quite acceptable. The error with respect to the **q**-wavevector sampling might be estimated at 5 meV, for the set of 20,000 **q**-wavevectors.

After this careful comparison between codes, and this convergence analysis, we obtain that the ZPR converges smoothly towards 409 meV.

This value disagrees with the one (0.615 eV) provided by Ref. [62]. The latter was actually first confirmed using QE+YAMBO, see e.g. Ref. [67]. However, while performing the cross verification between ABINIT and QE+YAMBO for the present study, we found a misuse of the symmetries at **Γ** in the interfacing between QE and YAMBO, affecting only the DW_{RIA} term. After correction, we obtain the results provided in this work, with the numerical uncertainty being much smaller than 0.2 eV. Documentation describing how to generate data at **Γ** with the same standard meaning as data at other **k**-points appeared in QE version later than 4.0.5 (input variable `nogg`). Work relying on such data might have been affected by this ambiguity.

2.5.4 *Pseudopotential choices*

We will now assess the influence of the pseudopotential choices. Such a study would not be mandatory in the present context of comparison between codes for the same pseudopotential (the reference pseudopotential has indeed been used with ABINIT, YAMBO, and also in the study of Ref. [62]). This comparison will be performed only using the Abinit software. We tested all the norm-conserving pseudopotentials available on the Abinit website as well as two UPF pseudopotentials, one of which is the reference pseudopotential. In the Table 2.7, we give a comparison of the ZPR using different pseudopotentials for carbon. The calculations are made on an homogeneous 10x10x10 **q**-point grid (47 **q**-points in the IBZ), for a 6x6x6 unshifted **k**-point grid with the energy cut-off reported in section 2.4 for the plane wave basis set, and 12 bands were used (with the Sternheimer equation). The low density **q**-wavevector grid used in this study allows for a fair comparison between pseudopotentials, but does not yield converged final results.

Pseudo	Band	Fan	DW_{RIA}	Fan+DW_{RIA}	ZPR
`reference`	2-3-4	−981.61	1119.92	138.30	465.70
	5-6-7	−1332.56	1005.16	−327.40	
`06-C.LDA.fhi`	2-3-4	−980.90	1119.42	138.52	467.73
	5-6-7	−1333.64	1004.44	−329.20	
`6c.pspnc`	2-3-4	−938.85	1074.14	135.28	468.32
	5-6-7	−1286.04	953.00	−333.03	
`06-C.GGA.fhi`	2-3-4	−952.12	1090.20	138.09	477.12
	5-6-7	−1324.85	985.82	−339.03	
`6c.4.hgh`	2-3-4	−1512.58	1649.55	136.97	450.35
	5-6-7	−1791.63	1478.25	−313.38	
`C.pz-vbc.UPF`	2-3-4	−1027.72	1167.13	139.41	419.22
	5-6-7	−1303.42	1023.61	−279.81	

Table 2.7: Comparison inside Abinit of the ZPR (and its Fan + DW_{RIA} decomposition) for different pseudopotentials at Γ. Homogeneous 10x10x10 $\mathbf{q}$-point grid (47 $\mathbf{q}$-points in the IBZ), for a 6x6x6 unshifted $\mathbf{k}$-point grid with the adapted energy cut-off for the plane wave basis set, 12 bands with were used (with the Sternheimer equation). The energies are in meV. Due to the low sampling on the $\mathbf{q}$-wavevector, these value are not converged one, although the comparison between different pseudopotentials is meaningful.

One can see that although the pseudopotentials are very different (various exchange-correlation functional, different angular momentum channel included and different atomic cut-off radius) the spread on the ZPR is only around 50 meV. Fluctuations for the Fan and DW_{RIA} terms, treated separately, are much larger. As emphasized earlier, the decomposition is indeed non-physical, and prone to large numerical uncertainties.

2.6 CONCLUSIONS

In this chapter, we have undertaken a validation and verification study to understand the source of discrepancy between the ABINIT and Yambo software for the value of the ZPR within the static adiabatic AHC theory, taking diamond as a test case.

The validation study (performed with ABINIT) leads, for the diamond phonon frequencies, to a discrepancy between the FP and AHC approaches below 0.2%. The differences of ZPR between the two methods are always below 7 μeV in absolute value, which strengthens our confidence in the theory and numerical implementation within the ABINIT

software. These small differences are attributed to the unavoidable numerical noise and anharmonicity in the FP calculations. The impact of the RIA is also evaluated for two **q**-points ($\mathbf{\Gamma}$ and **L**) and is found to be as large as 23% for the $\mathbf{\Gamma}$ zone center contribution to the ZPR but is usually much smaller for other **q**-points contributions.

For the verification study, we carefully compared all the quantities entering into the calculation of the ZPR in the AHC formalism in two different software applications: ABINIT and Yambo on top of QE. We show that one can get less than 10^{-5} Ha/atom discrepancy on the total energy, 0.07 cm^{-1} on the phonon frequencies, 0.005 on the electron-phonon matrix elements squared (relative discrepancy) and less than 2 meV on the zero-point motion renormalization. We also discussed the absolute value of the Fan and DW_{RIA} terms taken separately. We presented the converged result of the band-gap reduction due to electron-phonon renormalization, that is 409 meV at 0 Kelvin and discussed its discrepancy with previously published result. We also performed an analysis of the convergence rate of **q**-wavevector samplings.

Finally we discussed the impact of the pseudopotential choices and shown that it was relatively small (around 10% of the total ZPR) thus increasing our confidence in the results and methodology.

This chapter shows promising results for the *ab-initio* developer community as it was shown here that two different codes implemented separately with different algorithms would lead to the above mentioned level of agreement on physical observable.

The next chapter will be dedicated to the study of the temperature dependence of important semiconductors as well as the computation of the temperature dependence relying on many-body perturbation theory (GW).



3

CALCULATIONS OF THE TEMPERATURE DEPENDENCE OF α-ALUMINUM NITRIDE, β-ALUMINIUM NITRIDE, BORON NITRIDE, DIAMOND AND SILICON

In this last chapter of Part I, we apply the theory developed in Chapter 1 and validated in Chapter 2, to five relatively simple semiconductors (maximum 4 atoms per unit cells). This important chapter will help us to assess the strength of the AHC theory as well as its limitations in describing electron-phonon induced renormalization by direct comparison with experiment whenever possible.

Section 3.1 investigates two phases of aluminium nitride (wurtzite and zincblende), boron nitride, diamond and silicon within the static and non-adiabatic AHC theory and also discusses the phonon-induced lifetime broadening in the adiabatic limit.

The section 3.2 analyses in more depth the convergence rate of the static and non-adiabatic ZPR with respect to the $\mathbf{q}$-point sampling for α-AlN and silicon.

Section 3.3 shows that the G_0W_0 and GW treatments of the electron-electron interaction enhance the ZPR in diamond by more than 40% with respect to DFT in the LDA, and that these corrections allow us to obtain the correct temperature dependence of the band gap. To do this, we combine the FP method and DFPT to compute the direct bandgap renormalization. This allows us to revise an important approximation of the AHC theory, namely the rigid-ion approximation (see section 1.3.4). In all perturbative calculations, the Debye-Waller interaction term is simplified to allow for its computation from linear response. The approximation is known to break down in the case of diatomic molecules [19], but its reliability in solids had not been verified so far to our knowledge. In this section, we assert the validity of the rigid-ion approximation in diamond, and in general for three-dimensional systems. To complement the study with another material, the case of GaAs will also be discussed.

The content of section 3.3 has been published in Ref. [55].

3.1 STUDY OF THE TEMPERATURE DEPENDENCE OF SOME SEMICONDUCTORS IN LDA

In this section, we study the temperature-dependent properties of α-AlN, β-AlN, c-BN, diamond and silicon within LDA.

The calculations of structural and electronic properties are based on DFT [103, 104, 45] using norm-conserving pseudopotential [100] to account for the core-valence interaction. A planewave basis set is then used to expand the electronic wavefunctions. The LDA [94, 95] to the exchange-correlation functional is used for all the semiconductors. We will investigate the static renormalization of the eigenenergies using Eq. (1.47) in the rigid-ion approximation where $\frac{\partial \varepsilon_{nk}}{\partial n_{mq}} = \frac{\partial \varepsilon^{RIA}_{nk}}{\partial n_{mq}}$, with $\frac{\partial \varepsilon^{RIA}_{nk}}{\partial n_{mq}}$ defined in Eq. (1.65). The calculation on the active space (the "nband" Abinit input parameter) is performed using Eq. (1.66) with an additional $i\delta$ parameter in the denominator to smooth the divergence. The calculation on the space orthogonal to it is made using a Sternheimer re-writing given by Eq. (1.67). Using those equations, the static temperature-dependent renormalization in the RIA can be written as

$$\begin{aligned}
\Delta\varepsilon^{(\text{static,RIA})}_{nk}(T) = \frac{1}{N_q}\sum_{\mathbf{q}}\sum_{m}^{3N}\left(n_{m\mathbf{q}}(T)+\frac{1}{2}\right)\frac{1}{2\omega_{m\mathbf{q}}}\sum_{\substack{\kappa\alpha\\ \kappa'\gamma}}
\Bigg[\sum_{n'=1}^{M}{}' \frac{\left\langle u^{(0)}_{n\mathbf{k}}\middle|\frac{\partial\hat{H}_{\mathbf{k},\mathbf{k}}}{\partial R_{\kappa\alpha}(-\mathbf{q})}\middle|u^{(0)}_{n'\mathbf{k}+\mathbf{q}}\right\rangle\left\langle u^{(0)}_{n'\mathbf{k}+\mathbf{q}}\middle|\frac{\partial\hat{H}_{\mathbf{k},\mathbf{k}}}{\partial R_{\kappa'\gamma}(\mathbf{q})}\middle|u^{(0)}_{n\mathbf{k}}\right\rangle}{\varepsilon^{(0)}_{n\mathbf{k}}-\varepsilon^{(0)}_{n'\mathbf{k}+\mathbf{q}}+i\delta} \\
+\left\langle P_{c\mathbf{k}+\mathbf{q}}\frac{\partial u_{n\mathbf{k}}}{\partial R_{\kappa\alpha}(\mathbf{q})}\middle|\frac{\partial\hat{H}_{\mathbf{k},\mathbf{k}}}{\partial R_{\kappa'\gamma}(\mathbf{q})}\middle|u^{(0)}_{n\mathbf{k}}\right\rangle\Bigg] U^{*}_{m,\kappa'\gamma}(\mathbf{q})U_{m,\kappa\alpha}(\mathbf{q}) \\
-\frac{1}{2}\Bigg[\sum_{n'=1}^{M}{}' \frac{\left\langle u^{(0)}_{n\mathbf{k}}\middle|\frac{\partial\hat{H}_{\mathbf{k},\mathbf{k}}}{\partial R_{\kappa\alpha}(\Gamma)}\middle|u^{(0)}_{n'\mathbf{k}}\right\rangle\left\langle u^{(0)}_{n'\mathbf{k}}\middle|\frac{\partial\hat{H}_{\mathbf{k},\mathbf{k}}}{\partial R_{\kappa'\gamma}(\Gamma)}\middle|u^{(0)}_{n\mathbf{k}}\right\rangle}{\varepsilon^{(0)}_{n\mathbf{k}}-\varepsilon^{(0)}_{n'\mathbf{k}}+i\delta} \\
+\left\langle P_{c\mathbf{k}}\frac{\partial u_{n\mathbf{k}}}{\partial R_{\kappa\alpha}(\Gamma)}\middle|\frac{\partial\hat{H}_{\mathbf{k},\mathbf{k}}}{\partial R_{\kappa'\gamma}(\Gamma)}\middle|u^{(0)}_{n\mathbf{k}}\right\rangle\Bigg]\Big(U^{*}_{m,\kappa\gamma}(\mathbf{q})U_{m,\kappa\alpha}(\mathbf{q}) \\
+U^{*}_{m,\kappa'\gamma}(\mathbf{q})U_{m,\kappa'\alpha}(\mathbf{q})\Big). \qquad (3.1)
\end{aligned}$$

We will also study the non-adiabatic ZPR going beyond the adiabatic approximation but still within the RIA. The non-adiabatic ZPR is retrieved by taking the real part of the Fan self-energy of Eq. (1.79). By

evaluating the frequency ω at the KS eigenenergies $\varepsilon_{n\mathbf{k}}$, the formulation of the renormalization is still non-adiabatic but not dynamical anymore. We will therefore refer to it as the "non-adiabatic" extension to the AHC equations. This gives the following lengthy equation that is based on electron-phonon matrix elements already calculated for the static renormalization

$$
\begin{aligned}
\Delta\varepsilon_{n\mathbf{k}}^{(\text{non-adiabatic,RIA})}(T) = \Re\frac{1}{N_q}\sum_{\mathbf{q}}\sum_{m}^{3N}\frac{1}{2\omega_{m\mathbf{q}}}\sum_{\substack{\kappa\alpha\\ \kappa'\gamma}}
&\Bigg[\sum_{n'=1}^{M}\left\langle u_{n\mathbf{k}}^{(0)}\middle|\frac{\partial\hat{H}_{\mathbf{k},\mathbf{k}}}{\partial R_{\kappa\alpha}(-\mathbf{q})}\middle|u_{n'\mathbf{k}+\mathbf{q}}^{(0)}\right\rangle\left\langle u_{n'\mathbf{k}+\mathbf{q}}^{(0)}\middle|\frac{\partial\hat{H}_{\mathbf{k},\mathbf{k}}}{\partial R_{\kappa'\gamma}(\mathbf{q})}\middle|u_{n\mathbf{k}}^{(0)}\right\rangle\\
&\left(\frac{n_{m\mathbf{q}}(T)+f_{n'\mathbf{k}+\mathbf{q}}}{\omega-\varepsilon_{n'\mathbf{k}+\mathbf{q}}^{(0)}+\omega_{m\mathbf{q}}(T)+i\delta\,\mathrm{sgn}(\varepsilon_{n\mathbf{k}})}\right.\\
&\left.+\frac{n_{m\mathbf{q}}(T)+1-f_{n'\mathbf{k}+\mathbf{q}}}{\omega-\varepsilon_{n'\mathbf{k}+\mathbf{q}}^{(0)}-\omega_{m\mathbf{q}}+i\delta\,\mathrm{sgn}(\varepsilon_{n\mathbf{k}})}\right)\\
&+\left\langle P_{c\mathbf{k}+\mathbf{q}}\frac{\partial u_{n\mathbf{k}}}{\partial R_{\kappa\alpha}(\mathbf{q})}\middle|\frac{\partial\hat{H}_{\mathbf{k},\mathbf{k}}}{\partial R_{\kappa'\gamma}(\mathbf{q})}\middle|u_{n\mathbf{k}}^{(0)}\right\rangle\left(n_{m\mathbf{q}}(T)+\frac{1}{2}\right)\Bigg]\\
&U_{m,\kappa'\gamma}^{*}(\mathbf{q})U_{m,\kappa\alpha}(\mathbf{q})\\
&-\frac{1}{2}\Bigg[\sum_{n'=1}^{M}\frac{\left\langle u_{n\mathbf{k}}^{(0)}\middle|\frac{\partial\hat{H}_{\mathbf{k},\mathbf{k}}}{\partial R_{\kappa\alpha}(\Gamma)}\middle|u_{n'\mathbf{k}}^{(0)}\right\rangle\left\langle u_{n'\mathbf{k}}^{(0)}\middle|\frac{\partial\hat{H}_{\mathbf{k},\mathbf{k}}}{\partial R_{\kappa'\gamma}(\Gamma)}\middle|u_{n\mathbf{k}}^{(0)}\right\rangle}{\varepsilon_{n\mathbf{k}}^{(0)}-\varepsilon_{n'\mathbf{k}}^{(0)}+i\delta}\\
&+\left\langle P_{c\mathbf{k}}\frac{\partial u_{n\mathbf{k}}}{\partial R_{\kappa\alpha}(\Gamma)}\middle|\frac{\partial\hat{H}_{\mathbf{k},\mathbf{k}}}{\partial R_{\kappa'\gamma}(\Gamma)}\middle|u_{n\mathbf{k}}^{(0)}\right\rangle\Bigg]\\
&\qquad\left(U_{m,\kappa\gamma}^{*}(\mathbf{q})U_{m,\kappa\alpha}(\mathbf{q})+U_{m,\kappa'\gamma}^{*}(\mathbf{q})U_{m,\kappa'\alpha}(\mathbf{q})\right),
\end{aligned}
\tag{3.2}
$$

where a convergence study on M is required for the Fan term due to the fact that the Sternheimer projection does not contain the same denominator as the active space in the non-adiabatic case.

Additionally, we will also calculate the phonon-induced lifetime broadening in the static limit by using Eq. (1.95)

$$\frac{1}{2\tau_{n\mathbf{k}}^{(\text{static,RIA})}} = \frac{\pi}{N_q}\sum_{\mathbf{q}}\sum_{m}^{3N}\frac{1}{2\omega_{m\mathbf{q}}}\left(n_{m\mathbf{q}}(T)+\frac{1}{2}\right)\sum_{\substack{\kappa\alpha\\ \kappa'\gamma}}\sum_{n'=1}^{M}{}' \left\langle u_{n\mathbf{k}}^{(0)}\middle|\frac{\partial\hat{H}_{\mathbf{k},\mathbf{k}}}{\partial R_{\kappa\alpha}(-\mathbf{q})}\middle|u_{n'\mathbf{k}+\mathbf{q}}^{(0)}\right\rangle\left\langle u_{n'\mathbf{k}+\mathbf{q}}^{(0)}\middle|\frac{\partial\hat{H}_{\mathbf{k},\mathbf{k}}}{\partial R_{\kappa'\gamma}(\mathbf{q})}\middle|u_{n\mathbf{k}}^{(0)}\right\rangle \delta(\varepsilon_{n\mathbf{k}}^{(0)}-\varepsilon_{n'\mathbf{k}+\mathbf{q}}^{(0)})U_{m,\kappa'\gamma}^{*}(\mathbf{q})U_{m,\kappa\alpha}(\mathbf{q}). \quad (3.3)$$

Though rather straightforward, the non-adiabatic phonon-induced lifetime broadening of Eq. (1.92) is not yet coded inside Abinit but should be in the forthcoming months. This task was not judged mandatory as the static limit of the lifetime does not have a divergence and therefore does not depend on a sensible $i\delta$ parameter.

We will now use these three equations to compute the different physical quantities in five relevant semiconductors.

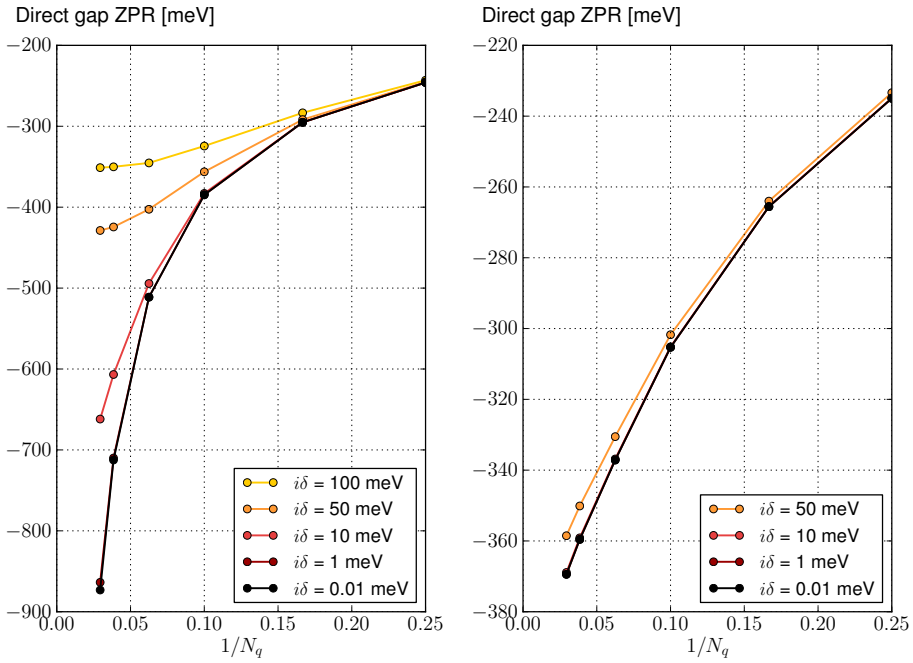
3.1.1 *Aluminum Nitride*

Aluminum nitride in the wurtzite structure (α-AlN) is one of the widest bandgap nitride semiconductor. It has a $P6_3mc$ (hexagonal, 186) space group. α-AlN is used for high-temperature electronics and opto-electronic applications [109] with a melting temperature of 3273 K [110]. The zincblende form of aluminum nitride (β-AlN) has a $F\bar{4}3m$ (cubic, 216) space group and has been reported to be experimentally metastable [111]. We will study the temperature-dependence properties of these two phases using the equations mentioned above to compute the ZPR.

Concerning the numerical details of the calculations, the aluminium and nitrogen pseudopotentials were generated using the `fhi98PP` code [105] with a 1.0247 atomic unit cut-off radius for pseudization and a maximum angular channel of $l = 2$. Both of them are Troullier-Martins pseudopotentials with the Perdew/Wang [106] parametrization of LDA. The valence electrons of aluminum and nitrogen, treated explicitly in the *ab-initio* calculations, are generated for the $3s^2 3p^1$ and $2s^2 2p^3$ configuration, respectively.

Convergence checks (error below 0.5 mHa per atom on the total energy) lead to the use of a 6x6x6 Γ-centered Monkhorst-Pack $\mathbf{k}$-point sampling [101] of the Brillouin zone and an energy cut-off of 35 Hartree for the truncation of the plane wave basis set.

The relaxed lattice parameters are calculated to be a=5.783 and c=9.255 Bohr for α-AlN and a=8.130 Bohr for β-AlN. These values are at maximum 2.3% below the experimental one (see table 3.1).



(a) Static ZPR of α-AlN

(b) Non-adiabatic ZPR of α-AlN

Figure 3.1: Convergence study for the direct bandgap of α-AlN with respect to the **q**-point grid density integration for different values of iδ going to 0 for the (a) static and (b) non-adiabatic renormalization. For the non-adiabatic case, the curves for iδ=10 to iδ=0.01 meV are almost on top of each other.

The electronic bandstructures were computed at the LDA level. For α-AlN, there is a direct gap at **Γ** of 4.691 eV. This is quite over the 4.056 eV bandgap computed within the Material's Project using GGA [112] but well in the range of other LDA bandgaps (see table 3.2). These DFT values naturally underestimate the experimental bandgap of 6.28 eV at 5K [113, 114]. The zincblende β-AlN turns out to have an indirect $\mathbf{\Gamma} - \mathbf{X}$ bandgap of 3.308 eV, almost identical to the Materials Project value (see table 3.2). The direct gap at **Γ** of 4.677 eV is a bit above most the the LDA values reported in the Table. We have nonetheless to bare in mind that the 4.2 eV LDA direct gap calculation performed in Ref. [109] is done at the experimental lattice parameter.

For the calculations of the ZPR we used 18 bands to describe the active space in Eqs. (3.1) and (3.2).

The convergence with respect to **q**-point integration for α-AlN is shown on figure 3.1. The two graphs show the static and non-adiabatic renormalization of the smallest direct Γ-Γ bandgap with the densification of the **q**-point grid along one direction (N_q is the number of **q**-points along one direction so that the **q**-point grid is N_qxN_qxN_q). Convergence studies for β-AlN are shown in the Appendix, figure B.1 for the direct and indirect $\Gamma - \mathbf{X}$ bandgap. We have pushed the convergence up to a 34x34x34 **q**-grid (2052 **q**-points in the IBZ) for α-AlN and up to a 63x63x63 **q**-grid (5984 **q**-points in the IBZ) for β-AlN.

From the Eqs. (3.1) and (3.2), we expect the static and non-adiabatic ZPR to converge linearly with $1/N_q$ for the top of the valence and the bottom of the conduction bands (a discussion on the convergence rate is given in the next section). Nonetheless, we see on figure 3.1 that the static case diverges for vanishing $i\delta$. We believe that such divergence also occurs in the non-adiabatic case, although for larger **q**-point grid. This divergence is ascribed to numerical errors for small **q**-wavevectors that make the electron-phonon matrix elements diverge as $1/\mathbf{q}^2$ for $\mathbf{q} \to 0$ (a more detailed explanation is provided in section 3.2). We therefore present here values for finite $i\delta$. Moreover, the convergence of the direct bandgap of β-AlN is given in figure B.1 and shows a more difficult convergence as the lowest conduction band of the direct bandgap diverges when another state at a different **k**-point has an eigenenergy close to the energy of the lowest conduction band at Γ.

The non-adiabatic equation for vanishing $i\delta$ (0.01 meV) gives a ZPR of -369$\pm$58 meV for the direct bandgap of α-AlN and -311$\pm$54 meV for the indirect bandgap of β-AlN (see Table 5.3 for more information). Note that the numbers after the symbol $\pm$ are the values of phonon-induced lifetime broadening in the static limit given by Eq. (3.3). As explained before, we did not compute the non-adiabatic phonon-induced lifetime broadening.

The temperature dependence of the three gaps is reported on figure 3.2 and give a slope at high temperature of -0.74, -0.49 and -0.73 meV/K for the direct gap of α-AlN, the indirect bandgap of β-AlN and the direct bandgap of β-AlN, respectively.

The experimental ZPR for α-AlN has been obtained from linear extrapolation to 0 K of the change of the direct bandgap with temperature and yield a value of -239 meV with a linear slope at high temperature of -0.83 meV/K [115, 116, 25], in relatively good agreement with our -0.74 meV/K value. The obvious disagreement with our theoretical value for the direct bandgap ZPR (-369 meV versus -239 meV) can be attributed

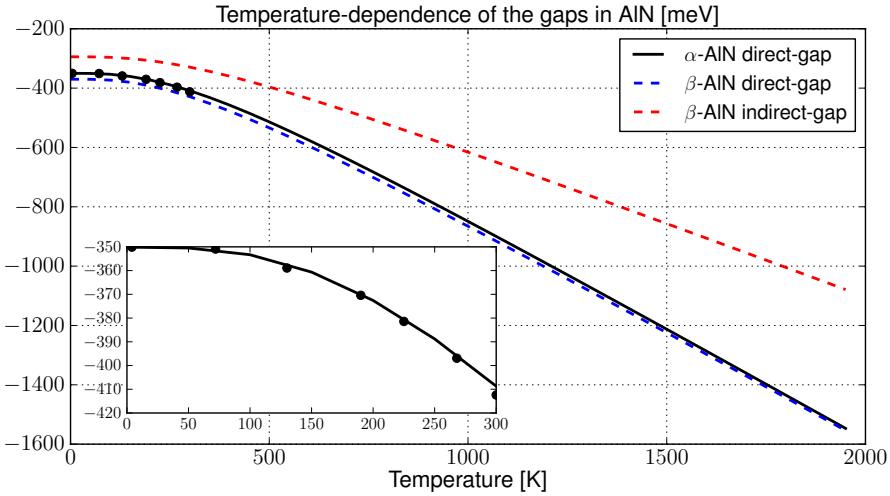


Figure 3.2: Temperature dependence of the AlN gaps using the non-adiabatic temperature dependence and a $i\delta$ parameter of 50 meV. The slopes at high temperature are -0.74, -0.49 and -0.73 meV/K for the direct gap of α-AlN, the indirect bandgap of β-AlN and the direct bandgap of β-AlN, respectively. The inset shows a zoom on the 0-300K temperature range for α-AlN where the experimental values (black dots) from Ref. [115] are shifted to match with the theoretical one at 4 K.

to the fact that the experimental data set measured by Brunner *et al.* [115] are very scarce and on a narrow temperature range (4-298 K). As pointed out by Pässler [116] for this compounds, *"this illustrates the great importance of extending experimental measurements in wide bandgap materials far beyond room temperature"*.

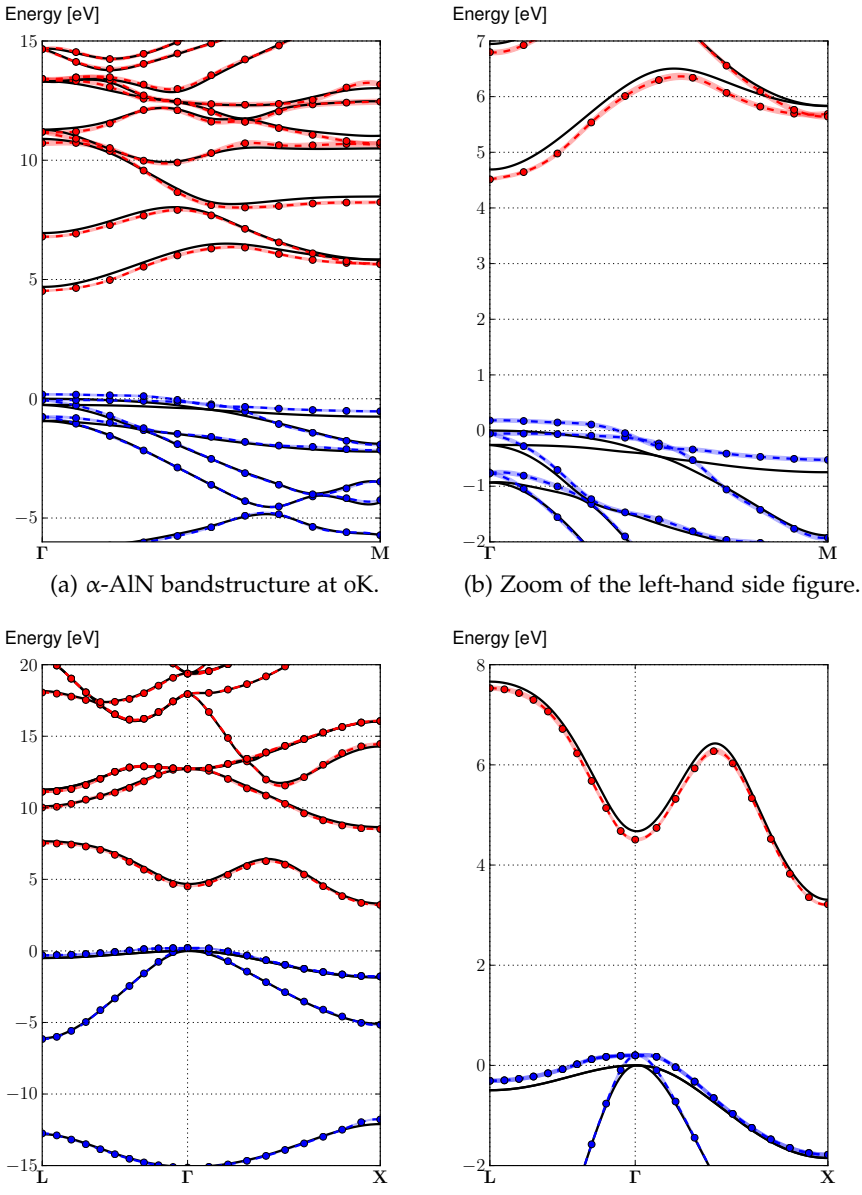
Finally, we show on figure 3.3 the non-adiabaticly renormalized electronic bandstructure at 0 K along the highest symmetry $\mathbf{\Gamma} - \mathbf{M}$ path for α-AlN and along the $\mathbf{L} - \mathbf{\Gamma} - \mathbf{X}$ path of the β phase of AlN. The thickness of the lines is associated with the lifetime of the electronic state computed with Eq. (3.3).

3.1.2 *Boron Nitride*

Boron nitride (BN) exists in various crystalline forms. The hexagonal form corresponding to the graphite stacking is the most stable among them. It used as a lubricant and an additive to cosmetic products. The cubic boron nitride (c-BN) has a zincblende structure and is isoelectronic to diamond. It is the second hardest material below diamond, but its chemical stability is far superior with high thermal conductivity and low dielectric constant [133]. Boron nitride is not found in nature and is

	space group	Ecut [Ha]	**k**-grid	this work	lattice parameters [Bohr] other DFT	experiment (300K)
α-AlN	$P6_3mc$ [186]	35	6x6x6	5.783/9.255	5.913/9.481* [112]	5.881/9.415 [117]
					5.820/9.335 [118]	5.880/9.409 [111]
						5.877/9.411 [119]
β-AlN	$F\bar{4}3m$ [216]	35	6x6x6	8.130	8.317* [112]	8.258 [120]
					8.164 [121]	8.277 [111]
					8.205 [118]	
					8.303* [122]	
c-BN	$F\bar{4}3m$ [216]	35	8x8x8	6.746	6.852* [112]	6.833 [123]
					6.754 [124]	6.831 [125]
					6.752 [126]	
					6.814 [127]	
					6.833 [128]	
C-d	$Fd\bar{3}m$ [227]	30	6x6x6	6.652	6.652 [62]	6.740 [129]
					6.756* [130]	
Si	$Fd\bar{3}m$ [227]	20	6x6x6	10.170	10.335* [112]	10.26 [131]
					10.223 [132]	

Table 3.1: Convergence parameters for the different studied compounds. The space groups are given in Hermann-Mauguin notation with the number in bracket being the crystallographic index number in international tables and the homogeneous **k**-points sampling are **Γ**-centered. All the pseudopotentials in this work use the LDA exchange-correlation functional. A star * is used when other DFT work used GGA exchange-correlation functional and no star when LDA is used.



(a) α-AlN bandstructure at 0K.

(b) Zoom of the left-hand side figure.

(c) β-AlN bandstructure at 0K.

(d) Zoom of the left-hand side figure.

Figure 3.3: Electronic bandstructure (plain black line), renormalisation (dashed line) and phonon-induced broadening (envelope around the dashed line) at 0 K for the AlN phases, where the dots are the actual renormalization calculation. A spline function is used to connect the renormalization dots. The non-adiabatic ZPR is integrated on a (a) 26x26x26 **q**-point grid (iδ=10 meV) and on a (c) 63x63x63 **q**-point grid (iδ=50 meV).

therefore produced synthetically from boric acid or boron trioxide. We will only study the c-BN polymorph here.

The boron and nitrogen pseudopotentials were also generated using the `fhi98PP` code [105] with a 1.0247 atomic unit cut-off radius for pseudization and a maximum angular channel of $l = 2$. Both of them are Troullier-Martins pseudopotential with the Perdew/Wang [106] parametrization of LDA. The valence electrons of boron and nitrogen, treated explicitly in the *ab-initio* calculations, are the $2s^2 2p^1$ and $2s^2 2p^3$ orbitals, respectively.

Careful convergence checks (error below 0.5 mHa per atom on the total energy) lead to the use of a 8x8x8 Γ-centered Monkhorst-Pack $\mathbf{k}$-point sampling [101] of the Brillouin zone and an energy cut-off of 35 Hartree for the truncation of the plane wave basis set.

The relaxed lattice parameter is calculated to be 6.746 Bohr, 1.3% below the experimental value of 6.833 Bohr [123] (see table 3.1 for more information on the structural properties).

The electronic bandstructure was computed at the DFT level and gave a direct gap at Γ of 8.890 eV and an indirect $\Gamma - \mathbf{X}$ bandgap of 4.446 eV, intrinsically below the experimental bandgap of 6.4 eV at 300K [134] (see table 3.2).

For the calculations of the ZPR, we used 18 bands to describe the active space in Eqs. (3.1) and (3.2).

The convergence with respect to $\mathbf{q}$-point integration for the direct and indirect bandgap of c-BN are shown in the appendix on figure B.2. The densest grid computed is a 63x63x63 $\mathbf{q}$-grid (5984 $\mathbf{q}$-points in the IBZ) and the non-adiabatic equation for vanishing $i\delta$ (0.01 meV) gives a ZPR of -385±67 meV for the indirect $\Gamma - \mathbf{X}$ bandgap of c-BN (see Table 5.3 for more information).

The non-adiabatic temperature dependence of direct and indirect bandgaps are reported on figure 3.4 for a 63x63x63 $\mathbf{q}$-grid with an $i\delta = 10\ meV$ and give a slopes at high temperature of -0.59 and -0.50 meV/K, respectively.

Finally, the non-adiabatic renormalized electronic bandstructure of c-BN at 0K along the $\mathbf{L} - \Gamma - \mathbf{X}$ high symmetry line is shown on figure 3.5 for a 63x63x63 $\mathbf{q}$-point grid with a $i\delta$=10 meV.

3.1.3 *Diamond*

Diamond is a metastable allotrope of carbon where the C atoms are arranged into two interpenetrating face-centered cubic lattices shifted

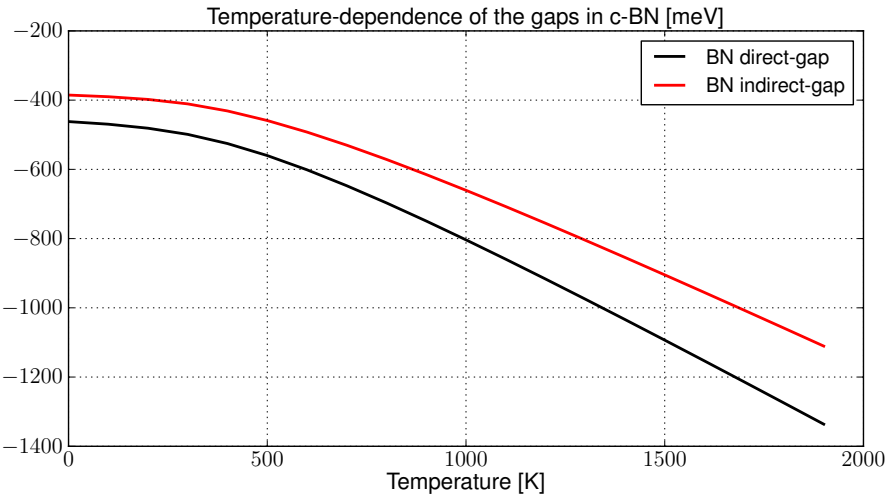
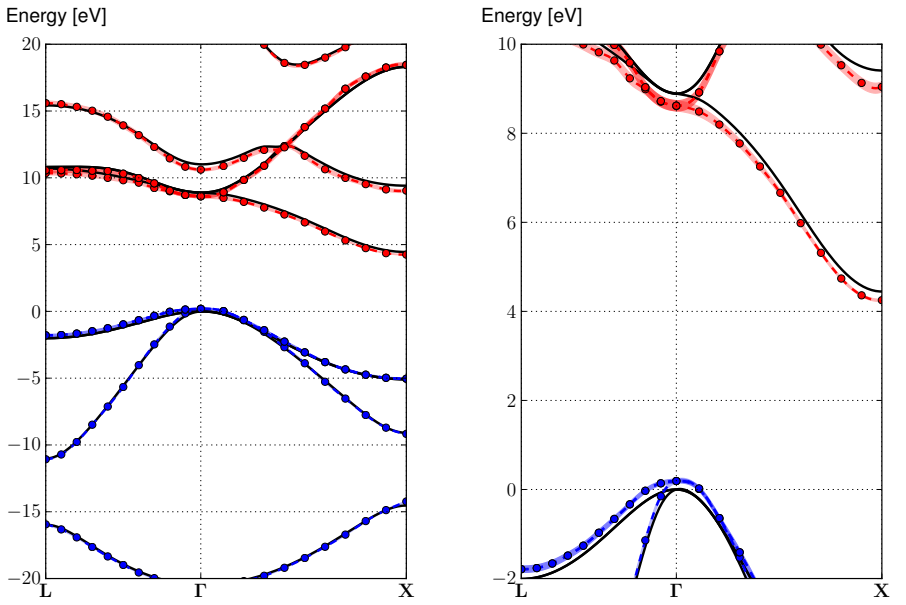


Figure 3.4: Temperature dependence of the c-BN gaps using the non-adiabatic temperature dependence and an iδ parameter of 10 meV on a 63x63x63 **q**-grid. The slopes at high temperature is -0.59 meV/K for the direct gap of c-BN and -0.50 meV/K for the indirect one.



(a) c-BN bandstructure at 0K.

(b) Zoom of the left-hand side figure.

Figure 3.5: Electronic bandstructure (plain black line), renormalisation (dashed line) and phonon-induced broadening (envelope around the dashed line) at 0K using the non-adiabatic ZPR integrated on a 63x63x63 **q**-point grid (iδ=10 meV) for c-BN, where the dots are the actual renormalization calculation. A spline function is used to connect the renormalization dots.

along the body diagonal by $\frac{1}{4}^{\text{th}}$ of its length. The space group associated with this spatial arrangement is $Fd\bar{3}m$ (cubic, 227). The word "diamond" comes from the ancient Greek αδάμας which means "unbreakable" and stems from the strong covalent bonds that the carbon atoms form in this phase. Diamond has the highest hardness and thermal conductivity of any bulk material [135]. It is therefore used as cutting and polishing tool in the industry. The stable phase of bulk carbon under normal condition is graphite but we are going to study the diamond phase.

The pseudopotential was generated using the `fhi98PP` code [105] with a 1.5 atomic unit cut-off radius for pseudization. The valence electrons of carbon, treated explicitly in the *ab-initio* calculations, are the $2s^2 2p^2 3d^0$ orbitals.

Careful convergence checks (error below 0.5 mHa per atom on the total energy) lead to the use of a 6x6x6 Γ-centered Monkhorst-Pack $\mathbf{k}$-point sampling [101] of the Brillouin zone and an energy cut-off of 30 Hartree for the truncation of the plane wave basis set. The relaxed lattice parameter is calculated to be 6.652 Bohr, 1.3% below the experimental value of 6.740 Bohr, measured at room temperature [129] (see table 3.1 for more information on the structural properties).

The electronic bandstructure was computed at the DFT level and gave a direct bandgap at Γ of 5.67 eV and an indirect $\Gamma - (0.361, 0.0, 0.361)$ bandgap of 4.25 eV intrinsically below the experimental bandgap of 5.48 eV at ~0K [92] (see table 3.2).

For the calculations of the ZPR we used 12 bands to describe the active space in Eqs. (3.1) and (3.2).

The convergence with respect to $\mathbf{q}$-point integration for the direct and indirect bandgap of diamond are shown on figure B.3. Note that the indirect position has been taken to be the (0.33,0.0,0.33) $\mathbf{k}$-point of the 6x6x6 grid in place of the (0.361,0.0,0.361), averaged on the six equivalent positions (related by symmetry operations).

The densest grid computed is a 125x125x125 $\mathbf{q}$-grid (436800 $\mathbf{q}$-points in the IBZ) and it is clear from figure figure B.3(d) that the non-adiabatic indirect gap diverges for vanishing $i\delta$ (see the next section for the discussion on this divergence stemming from a numerical cancellation error). The static indirect bandgap ZPR is -366±61 meV and the non-adiabatic one is -334 meV with $i\delta = 50$ meV in both cases (see Table 5.3 for more information).

The temperature dependence of the direct and indirect bandgaps is reported on figure 3.6 on a 55x55x55 $\mathbf{q}$-grid and show that the slope at high temperature for the non-adiabatic ZPR with an $i\delta$ parameter of

10 meV is -0.49 meV/K for the direct bandgap and -0.44 meV/K for the indirect one.

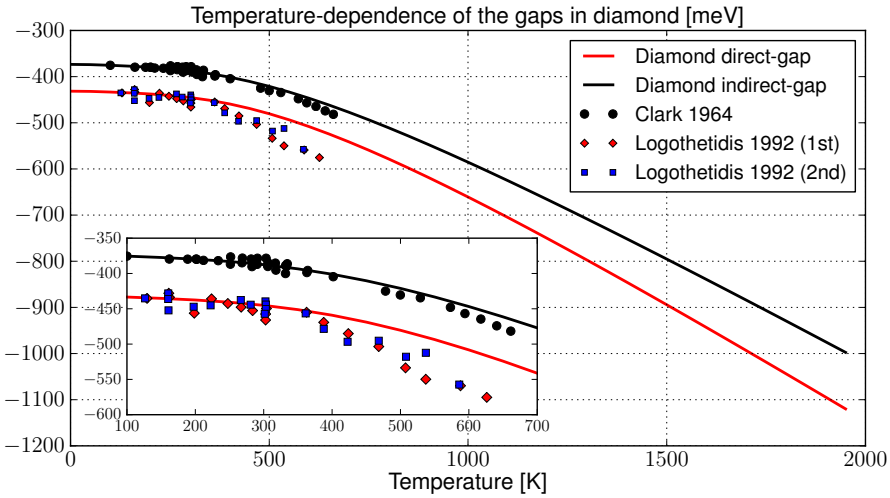


Figure 3.6: Temperature dependence of the diamond gaps using the static temperature dependence and an $i\delta$ parameter of 10 meV on a 55x55x55 $\mathbf{q}$-grid. The slopes at high temperature is -0.49 meV/K for the direct gap of diamond and -0.44 meV/K for the indirect one. The experimental points from Clark *et al.* [24] and Logothetidis *et al.* [93] (using first or second-derivative line-shape analysis) are shifted so that the lowest temperature point matches the theoretical line.

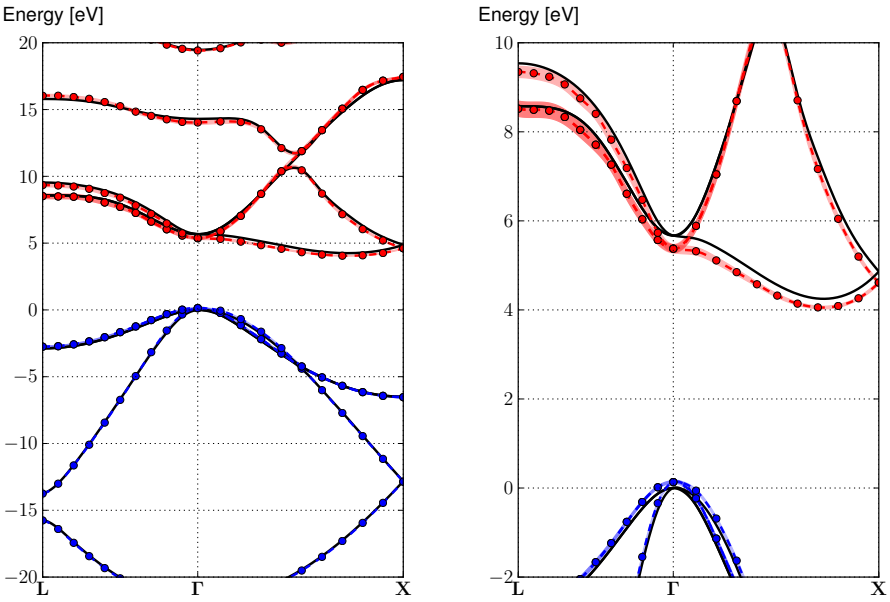
Our result underestimates the experimental zero-point motion renormalization of the diamond indirect bandgap of -364 meV [25] by 7.1%. Since our calculation neglects several effects like anharmonic effects, non-rigid-ion terms or many-body G*W* correction, we are rather close to the experimental value. The measured linear slope at high temperature for the indirect bandgap of diamond is -0.54 meV/K [25]. The measured linear slope at high temperature for the direct bandgap is -0.60 or -0.69 meV/K [93], depending on the analysis[1]. Our theoretical value underestimates the experimental one by ~18% for both the indirect and direct bandgap. We hypothesize that this underestimation of the linear slope at high temperature for the direct bandgap of diamond is due to the fact that the ZPR is quite overestimated within DFT. Indeed, as it will be discussed in section 3.3, the correction brought by G*W* to the ZPR is quite substantial (-209 meV, see Table 3.4). Since the ZPR is directly linked with the slope at high temperature, it is not surprising that we witness such an underestimation with respect to the experimental

1 Logothetidis *et al.* deduced the temperature dependence of the direct bandgap of diamond from first and second-derivative line-shape analysis, see Ref. [93] for more details.

results. We did not compute such GW correction for ZPR of the indirect bandgap of diamond but expect from the results of figure 3.6 to have a much smaller correction.

It is worthy to note that the complete lack of experimental data for low temperature (T < 100 K) and the relatively large error bars (up to ±10 meV) between 200 K and 350 K generate an uncertainty of several meV on the experimental ZPR [116]. This calls for new, reliable and wide range temperature measurement of the evolution of the bandgap with temperature in diamond. We hope that our theoretical study will stimulate such experimental interest.

Finally, the non-adiabatically renormalized electronic bandstructure of diamond at 0K along the $\mathbf{L}-\mathbf{\Gamma}-\mathbf{X}$ high symmetry line is shown on figure 3.7 for a 55x55x55 $\mathbf{q}$-point grid with a $i\delta$=10 meV.



(a) Diamond bandstructure at 0K. (b) Zoom of the left-hand side figure.

Figure 3.7: Electronic bandstructure (plain black line), renormalisation (dashed line) and phonon-induced broadening (envelope around the dashed line) at 0K using the non-adiabatic ZPR integrated on a 55x55x55 $\mathbf{q}$-point grid ($i\delta$=10 meV) for diamond, where the dots are the actual renormalization calculation. A spline function is used to connect the renormalization dots.

	direct gap [eV]			indirect gap [eV]		
	this work	other DFT	exp.	this work	other DFT	exp.
α-AlN	4.691	4.056* [112]	6.28* [113]	-	-	-
		4.2 [136]	6.28* [114]	-	-	-
		4.3 [109]	6.3 [120]	-	-	-
		4.41 [118]		-	-	-
		4.52 [137]		-	-	-
		4.74 [122]		-	-	-
β-AlN	4.677	3.995* [112]	-	3.308	3.306* [112]	-
		4.2 [109]	-		3.2 [109]	-
		4.35 [118]	-		3.2 [136]	-
		4.75 [122]	-			-
		4.2 [138]	-			-
c-BN	8.890	8.6 [139]	14.5 [125]	4.446	4.450* [112]	6.4 [140]
		8.7 [128]	-		5.18 [128]	6.4 [134]
		8.8 [126]	-		4.4 [126]	
C-d	5.670	5.571* [112]	7.3* [92]	4.250	4.113* [112]	5.48* [92]
					4.12* [130]	
Si	2.567	2.52 [141]	3.378* [142]	0.463	0.45 [141]	1.17* [142]
		2.557* [112]			0.612* [112]	

Table 3.2: The direct and indirect (when relevant) DFT electronic bandgaps are compared with other references (theoretical or experimental). The star * sign denotes low temperature experiment (below 10K) or GGA calculations and no star means room temperature or LDA calculations.

3.1.4 *Silicon*

Silicon is a tetravalent metalloid widely used in integrated circuit and semiconductor electronics. It has a diamond cubic crystal structure with a $Fd\bar{3}m$ (cubic, 227) space group. Pure silicon is usually not found in nature but manufactured to get monocrystalline silicon for use in computer microchips. Although the manufacturing process is rather expansive, this material is so important that about 50.000 metric tons are produced per year worldwide [143].

The pseudopotential used for silicon was generated using the `fhi98PP` code [105] with a 1.0247 atomic unit cut-off radius for pseudization. The valence electrons of silicon, treated explicitly in the *ab-initio* calculations, are the $3s^2 3p^2$ orbitals.

Careful convergence checks (error below 0.5 mHa per atom on the total energy) lead to the use of a 6x6x6 Γ-centered Monkhorst-Pack **k**-point sampling [101] of the Brillouin zone and an energy cut-off of 20 Hartree for the truncation of the plane wave basis set. The relaxed lattice parameter is calculated to be 10.170 Bohr, 0.9% below the experimental value, measured at room temperature [131] (see table 3.1 for more information on the structural properties).

The electronic bandstructure was computed at the DFT level and gave a direct gap at Γ of 2.567 eV and an indirect $\Gamma - (0.4, 0.0, 0.4)$ bandgap of 0.463 eV intrinsically below the experimental bandgaps of 3.378 and 1.17 eV at ~10K [142] for the direct and indirect bandgap, respectively. (see table 3.2). Many *ab-initio* simulations have been performed on silicon and give similar value to ours. For example, Ref. [141] got a direct bandgap of 2.52 eV and an indirect one of 0.45 eV, also using the Abinit software.

For the calculations of the ZPR, we used 12 bands to describe the active space in Eqs. (3.1) and (3.2). Note that the indirect position has been taken to be the $(0.33, 0.0, 0.33)$ **k**-point of the 6x6x6 grid in place of the true minimum, located close to the $(0.4, 0.0, 0.4)$ **k**-point, averaged on the six equivalent positions (related by symmetry operations).

The convergence with respect to **q**-point integration for the direct and indirect bandgaps of silicon is shown on figure B.4. The densest grid computed is a 63x63x63 **q**-grid (5984 **q**-points in the IBZ) and the non-adiabatic equation for an $i\delta$ of 50 meV gives a ZPR of -59±30 meV for the indirect bandgap and -42±26 meV for the direct one. Such values can be compared with those mentioned in the recently published paper by Patrick and Giustino [132] who got values of -57 and -22 meV for the indirect and direct bandgap renormalization of silicon using a 4x4x4 supercell within the AHC framework. It should be noted that with such supercell, the results are not converged in **q**-grid. Actually, our unconverged values for the static 4x4x4 **q**-grid are much closer to theirs with -54 and -29 meV for the indirect and direct bandgaps, respectively (as can also be seen on figure B.4). The non-adiabatic temperature dependence of direct and indirect $(0.4, 0.0, 0.4)$ bandgaps integrated over a 55x55x55 **q**-grid with an $i\delta$ parameter of 10 meV is reported on figure 3.8 and gives slopes at high temperature of -0.19 and -0.30 meV/K, respectively. The computed variation of the indirect bandgap renormalization with temperature matches closely the experimental one of Refs. [144] and [145].

The experimental zero-point motion renormalization of the silicon indirect bandgap is -62 meV obtained from mass derivative of the gap and

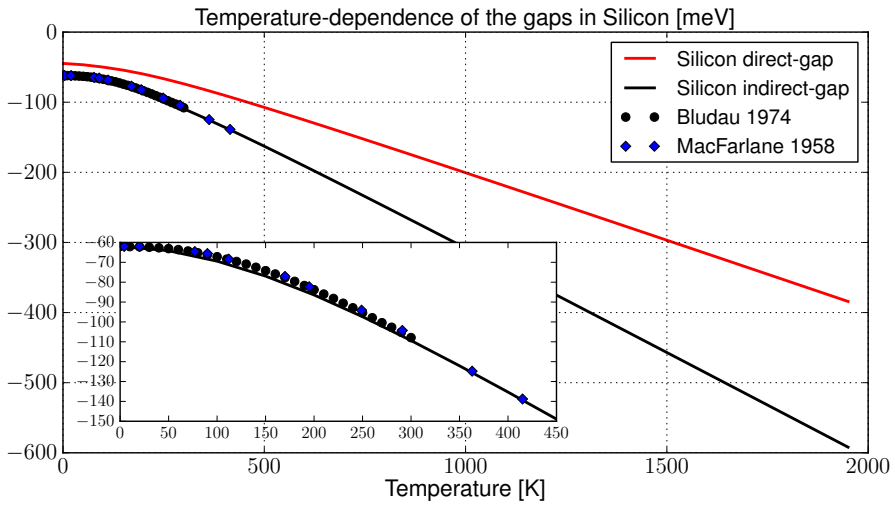


Figure 3.8: Temperature dependence of the silicon gaps using the static temperature dependence and an $i\delta$ parameter of 10 meV on a 55x55x55 $\mathbf{q}$-grid. The slopes at high temperature is -0.19 meV/K for the direct gap of silicon and -0.30 meV/K for the indirect one. The experimental data from Ref. [144] (black circles) and [145] (blue diamond).

-64 meV obtained from linear extrapolation to 0 K [25]. The measured linear slope at high temperature is -0.32 meV/K. Those experimental results are quite close to our theoretical ones using the non-adiabatic extension to the AHC equations and give us confidence in this method.

Additionally, for silicon, we present on figure 3.9 the phonon-induced broadening of the direct and indirect bandgap of silicon with temperature. The experimental broadening, measured with spectroscopic ellipsometry in Ref. [69] (red dots), is attributed to the broadening of the E_1=$\mathbf{\Lambda}_{3v} - \mathbf{\Lambda}_{1c}$ direct transition with temperature. In Ref. [69], they also mentioned that the measured values at higher temperature (black dots) are difficult to attribute to the broadening of one particular transition because the E_1 gap is nearly degenerate with the $E_0' = \mathbf{\Gamma}_{25'v} - \mathbf{\Gamma}_{15c}$. Since the ellipsometry measurement is a spectroscopic measurement, it can only probe direct transition. At such, we should compare the broadening results (both black and red dots) with the silicon red line (direct-gap E_0').

Finally, the non-adiabatically renormalized electronic bandstructure of silicon at 0 K along the $\mathbf{L} - \mathbf{\Gamma} - \mathbf{X}$ high symmetry line is shown on figure 3.10 for a 55x55x55 $\mathbf{q}$-point grid with a $i\delta$=10 meV.

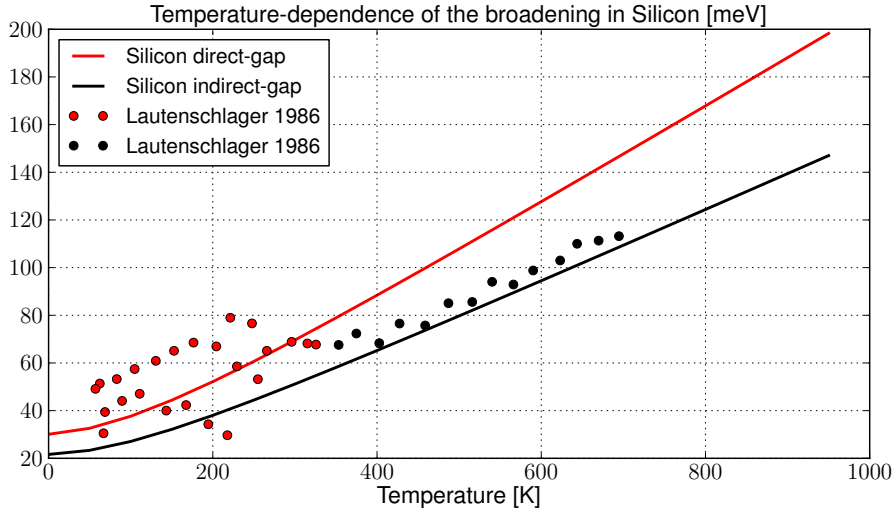
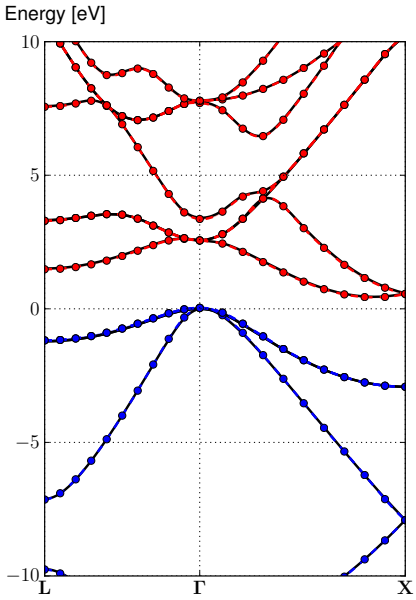
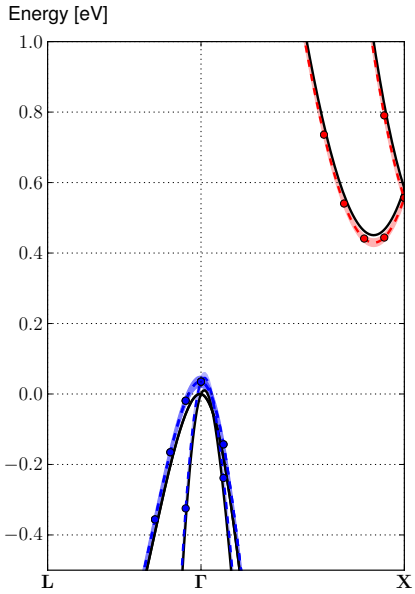


Figure 3.9: Temperature dependence of the silicon broadening of the direct and indirect bandgap using the static temperature dependence and an $i\delta$ parameter of 50 meV on a 55x55x55 **q**-grid. The experimental data (red and black dots) are from Ref. [69]. See additional discussion in the text.



(a) Silicon bandstructure at 0K.



(b) Zoom of the left-hand side figure.

Figure 3.10: Electronic bandstructure (plain black line), renormalisation (dashed line) and phonon-induced broadening (envelope around the dashed line) at 0K using the non-adiabatic ZPR integrated on a 55x55x55 **q**-point grid ($i\delta$=10 meV) for silicon, where the dots are the actual renormalization calculation. A spline function is used to connected the renormalization dots.

3.2 ANALYSIS OF THE CONVERGENCE RATE OF ALUMINIUM NITRIDE AND SILICON

When performing temperature-dependence calculations, the convergence with respect to the density of the **q**-point grid is crucial.

We can analyze the theoretical rate of convergence of Eq. (3.1) with densification of the **q**-point grid at the extrema of a parabolic eigenenergies **k**-point dispersion (relevant for the calculation of the renormalization due to electron-phonon coupling of the smallest electronic bandgap) using the GKKs of α-AlN or silicon as an example.

The **q**-dependence should come from the energy denominator and we can study it as already done in section 2.5.3. This corresponds to the integration of the divergence in a sphere of radius q_c around it

$$\iiint_0^{q_c} \frac{1}{q^2 + i\delta} dq^3 = \int_0^{q_c} \int_0^{\pi} \int_{-\pi}^{\pi} \frac{q^2 \sin\theta d\theta d\phi dq}{q^2 + i\delta}. \tag{3.4}$$

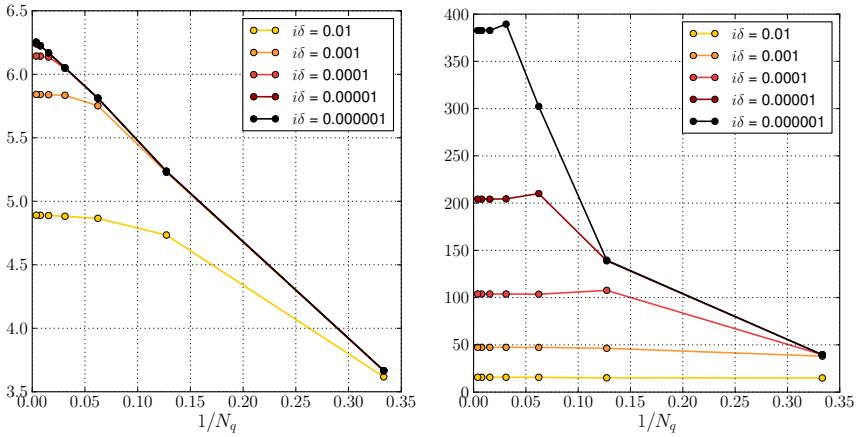
If we take $q_c = 0.5$ as the zone border, this integral is well defined and integrate itself to 2π for $i\delta \to 0$. To see the rate of convergence with the $i\delta$ parameter tending to 0, we numerically integrate this function on a three dimensional grid of **q**-points

$$\frac{1}{N_q^3} \sum_q \frac{1}{q^2 + i\delta}, \tag{3.5}$$

where the element of volume is the number of **q**-points N_q^3 needed to discretized the grid. The numerical integral of Eq. (3.5) is shown on figure 3.11a and converges toward 2π as expected.

However, as see in the previous section, the ZPR diverges with increasing **q**-point grid integration for vanishing $i\delta$. This is due to the fact that the SGKK2 (introduced in Eq. (2.9)) in α-AlN, for example, behaves as $1/q^2$ as can be seen on figure 3.12 for the renormalization of the LUMO band at Γ (the HOMO band behaves similarly). We have computed the same **q**-points on a denser 8x8x8 **k**-point grid. The maximum deviation on the 18 **q**-points between Γ and **M** shown on figure 3.12 is of 0.9% with respect to the 6x6x6 **k**-point grid. This leads us to believe that there is no cross-convergence phenomenon happening here.

To test whether this behaviour of the GKKs was linked to the fact that α-AlN is a polar material, we also studied the SGKK2 of silicon and the results are shown on figure 3.13. That figure shows the averaged value over the three degenerate bands of the HOMO at Γ and it seems that the SGKK2 also behaves as $1/q^2$ in this non-polar material.



(a) The numerical integral of Eq. (3.5) converges toward 2π as expected. We can see that the convergence in $\mathbf{q}$ points and $i\delta$ is rather slow.

(b) The numerical integral of Eq. (3.9) diverges.

Figure 3.11: Convergence study of the integral with respect to the $\mathbf{q}$-point grid density and $i\delta$ parameter.

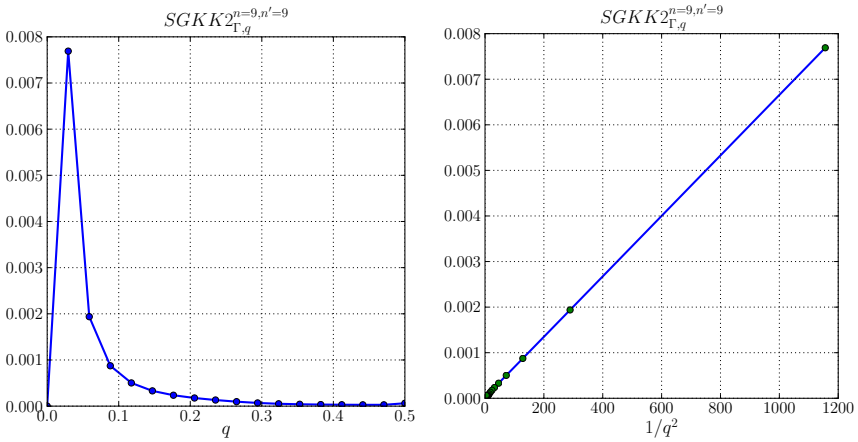
The SGKK2 contains three elements: the phonon frequency at the denominator, the first-order matrix elements and the eigendisplacement vectors. From our numerical tests, we realized that although the acoustic phonon frequencies behave linearly with $\mathbf{q}$ for $\mathbf{q} \to 0$, they do not contribute to the observed $1/q^2$ behaviour as such modes are cancelled by the translational invariance. The eigendisplacement vectors being normalized, we conclude that the $1/q^2$ behaviour must come from the first-order matrix elements squared.

The perturbed Hamiltonian to first-order can be written as (see Eq. (61) of Ref. [64])

$$H^{(1)}_{\mathbf{k}+\mathbf{q},\mathbf{k}} = v^{(1)}_{\text{sep},\mathbf{k}+\mathbf{q},\mathbf{k}} + v^{(1)}_{\text{loc},\mathbf{q}} + v^{(1)}_{\text{H},\mathbf{q}} + v^{(1)}_{\text{xc},\mathbf{q}}, \tag{3.6}$$

where $v^{(1)}_{\text{sep}}, v^{(1)}_{\text{loc}}, v^{(1)}_{\text{H}}$ and $v^{(1)}_{\text{xc}}$ are the first-order perturbation to the non-local, local, Hartree and exchange-correlation potential. Out of these four terms, the Hartree and local potential diverges with $\mathbf{q} \to 0$. They can be written as

$$v^{(1)}_{\text{H},\mathbf{q}}(\mathbf{G}) = 4\pi \frac{n^{(1)}_{\mathbf{q}}(\mathbf{G})}{|\mathbf{G}+\mathbf{q}|^2}, \tag{3.7}$$



(a) Electron-phonon matrix element squared $SGKK2^{n=9,n'=9}_{\Gamma,q}$ as a function of $q = [x, 0, 0]$.

(b) Electron-phonon matrix element squared $SGKK2^{n=9,n'=9}_{\Gamma,q}$ as a function of $1/q^2$.

Figure 3.12: The contribution of a $\mathbf{q} = [x, 0, 0]$ point to the renormalization at $\mathbf{k} = \Gamma$ of the LUMO state due to the same band behaves as $1/q^2$ in α-AlN (direct bandgap semiconductor).

where the density perturbed at first-order is proportional to $\mathbf{q}$ and therefore $v^{(1)}_{H,\mathbf{q}}$ diverges as $1/\mathbf{q}$ and

$$v^{(1)}_{loc,\mathbf{q}}(\mathbf{G}) = \frac{1}{\Omega_0}(-i)(\mathbf{G}+\mathbf{q})_\alpha e^{-i(\mathbf{G}+\mathbf{q})\cdot\tau_\kappa} v^{loc}_\kappa(\mathbf{G}+\mathbf{q}), \tag{3.8}$$

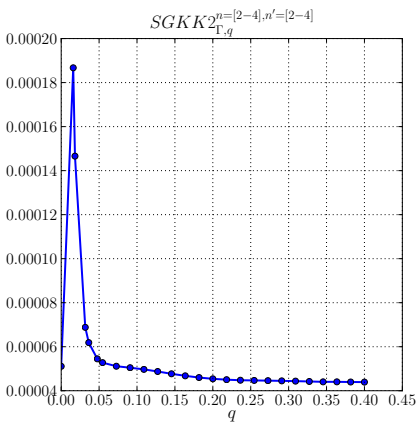
where Ω_0 is the volume of the unit cell and $v^{loc}_\kappa(\mathbf{G}+\mathbf{q})$ can be expressed in term of a real space potential. Such potential has a $1/\mathbf{r}$ dependence and therefore a $1/\mathbf{q}^2$ in reciprocal space. Since $v^{(1)}_{loc,\mathbf{q}}$ is multiplied by $\mathbf{q}$ it also diverges as $1/\mathbf{q}$.

Based on physical consideration discussed in Ref. [64], these two potentials should diverges as $1/\mathbf{q}$ but with opposite sign and should perfectly cancels out.

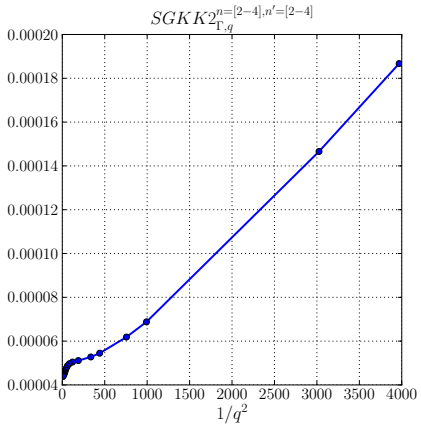
Numerical studies on these potentials for silicon have shown however that the cancellation was not exact and that the resulting sum Eq. 3.6 still diverges as $1/\mathbf{q}$.

With such a $1/q^2$ divergence of the GKKs in α-AlN and Si, the total ZPR behaves as

$$\frac{1}{N_q^3}\sum_q \frac{1}{q^2(q^2+i\delta)} \approx \frac{1}{N_q^3}\sum_q \frac{1}{q^4+i\delta}. \tag{3.9}$$



(a) Electron-phonon matrix element squared $SGKK2^{n=[2-4],n'=[2-4]}_{\Gamma,q}$ as a function of $q = [x, 0, 0]$.



(b) Electron-phonon matrix element squared $SGKK2^{n=[2-4],n'=[2-4]}_{\Gamma,q}$ as a function of $1/q^2$.

Figure 3.13: The contribution of a $\mathbf{q} = [x, 0, 0]$ point to the renormalization at $\mathbf{k} = \Gamma$ of the HOMO state due to the same band (the degeneracices are averaged) also behaves as $1/q^2$ in silicon.

Such integral is ill defined and diverges as shown on figure 3.11b. It is therefore expected that the static ZPR of such compounds will diverge with $i\delta \to 0$ but will converge for a given value of $i\delta$. If such value is physically motivated (for example by taking it equal to the experimental lifetime of the material), then the resulting static ZPR can be physically relevant. We should nonetheless warn that the ZPR is rather sensitive to the $i\delta$ parameter and therefore we would advice the use of more refined theories.

For that reason, we will also study the non-adiabatic ZPR of Eq. (3.2), going beyond the adiabatic approximation. The non-adiabatic equation can be approximated with the following formula

$$\frac{1}{N_q^3} \sum_q \frac{1}{q^2(q^2 + \omega + i\delta)}, \tag{3.10}$$

where ω is a constant average phonon frequency that we here arbitrarily choose to be 0.01. When $\mathbf{q}$ is very small, the q^2 in the parenthesis vanishes and we recover a $\frac{1}{q^2}$ behaviour that converges smoothly as shown on figure 3.14.

However, the Eq. (3.2) also have the same GKKs that diverges for the materials that we have considered. This ZPR calculated with this equa-

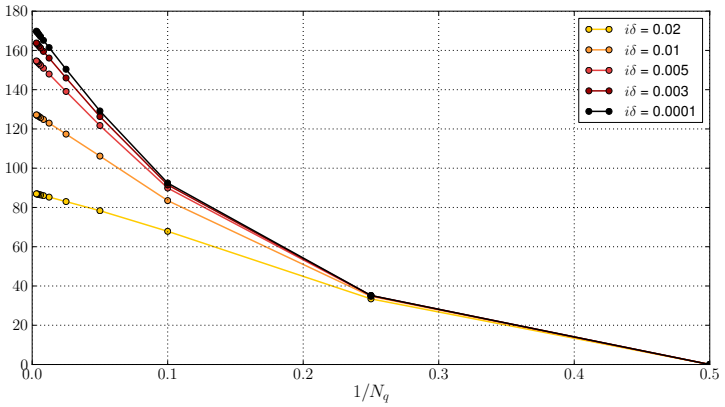


Figure 3.14: Convergence study of the non-adiabatic integral of Eq. 3.10 with respect to the **q**-point grid density and iδ parameter.

tion will therefore also diverge but for denser **q**-grid because the phonon frequencies in the denominator lower the divergence.

3.3 MANY-BODY EFFECTS ON THE ZERO-POINT RENORMALIZATION OF THE BAND STRUCTURE OF DIAMOND AND GAAS

The reliability of DFT for the electron-phonon coupling has been questioned in recent years [56, 58, 59]. Since the scattering of an electron by a phonon probes the excited states of a system, a theory describing this process should rely on an accurate unrenormalized band structure, unlike the one of DFT. This has motivated the use of non-local DFT functionals [56, 58, 59, 61]. These studies have shown that, as well as correcting the bandgap, exact exchange functionals are also necessary to accurately describe the electron-phonon coupling. A truly *ab-initio* scheme however would rely on many-body perturbation theory. As such, it was reported that G_0W_0 [146] corrections lead to a significant increase of the electron-phonon coupling in C_{60} fullerene and in graphene [59, 56]. We now study this effect for diamond.

As explained in Chapter 1, the temperature dependence of the electronic eigenvalues originates from the phonon population and the thermal expansion of the lattice [147, 92], the latter effect being relatively small. The important quantity entering into the calculation of the temperature dependence is the electron-phonon coupling energies (EPCE). Within the FP method, and in the harmonic approximation, the EPCEs

are obtained from the second-order derivatives of the eigenvalues at equilibrium (see Eq. (1.32)).

Each EPCE requires a supercell calculation to account for the wavelength of the phonon. Although this makes the technique more computationally demanding than DFPT, it offers several theoretical advantages. It makes no approximation for the Debye-Waller term, and it gives complete liberty on the method to compute the electronic structure.

3.3.1 *DFPT calculations*

The DFPT scheme allows for a fine sampling of the Brillouin zone (BZ), as shown on Fig. 3.15a. Diamond being an indirect gap insulator, a divergence occurs in the Γ_{15c} EPCE when a phonon wavevector connects this state to another one with close energy. This is handled by adding a small imaginary part to the energy differences (0.1 eV)[2]. Although most of the divergences cancel out after integration, the broad peak at $\mathbf{\Gamma}$ gives an important contribution to the energies renormalization. The central region covering one eighth of the BZ, accounts for 45% of the Γ'_{25v} ZPR and 20% of the Γ_{15c} ZPR.

The rigid-ion approximation is not present in the FP approach. Remarkably, using small displacements ($\sim$ 0.01% of the bond length), the coupling energies computed from Eq. (1.32) fall closely on the DFPT curve. The total ZPR obtained with the FP method differs by less than 3% from the DFPT value (see Table 3.3), a discrepancy we attribute to the rigid-ion approximation. Since the neglected non-rigid-ion Debye-Waller term is a short-ranged interaction between neighboring atomic sites, it does not become any stronger near $\mathbf{\Gamma}$ than it is at the BZ boundary. Therefore, this term should be of negligible importance in any three-dimensional crystal, where the BZ center area accounts for a significant portion of the ZPR.

3.3.2 *Many-body corrections*

Displacing the atoms by 0.1% of the bond length causes the electrons to move from the contracting bonds to the stretching bonds, in favor of lower kinetic energy. This charge transfer pushes the Γ'_{25v} energy upward, causing a renormalization of 119 meV in LDA. With the G_0W_0

2 See the calculation details in annex A.9.

	Γ'_{25v}	Γ_{15c}	Gap
	Rigid-ion approximation		
Perturbative DFT	113	−314	−427
Finite differences harmonic[(a)]	117	−320	−437
	Many-body effects		
Finite differences DFT[(b)]	119	−318	−437
Finite differences G_0W_0[(b)]	145	−477	−622

Phonon displacements: (a) ~ 0.01% (b) ~ 0.1% of the bond length.

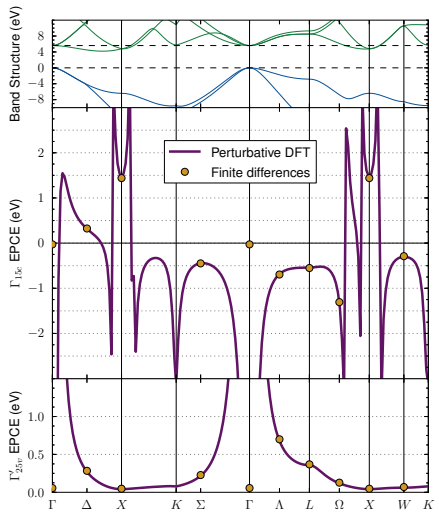
Table 3.3: ZPR (meV) computed on a $4 \times 4 \times 4$ **q**-point grid in FP (finite differences) and in DFPT (perturbative DFT).

corrections[3], the EPCE is uniformly increased all over the Brillouin zone by about 50 meV per **q**-point, as shown on Fig. 3.15b. Although the Γ_{15c} state shows a negative renormalization of −318 meV in LDA, the EPCE elements are positive in the $\mathbf{\Gamma} - \mathbf{X}$ direction, where the lowest conduction band reaches its minimum. The G_0W_0 corrections increase the amplitude of the negative EPCE elements while reducing the positive elements, bringing the Γ_{15c} ZPR to −477 meV, and increasing the bandgap renormalization by more than 40%, as reported in Table 3.3. We observed the same trend in gallium arsenide, which is a direct bandgap semiconductor. Whereas the LDA predicts a bandgap renormalization of −23 meV in this material, the ZPR is increased by −10 meV when G_0W_0 corrections are applied.

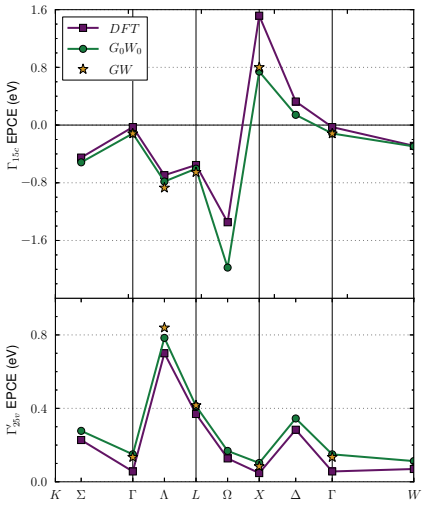
The self-energy is thus more sensitive to the perturbation than the LDA exchange-correlation potential. This reflects the fact that LDA is based on the jellium model. The electron-electron interaction is overly screened in the bonding region, where the charge density packs up. In contrast, retaining only the bare exchange corresponds to a Hartree-Fock calculation with the DFT wavefunctions. Such a calculation overestimates the renormalization of the Γ'_{25v} (207 meV), which is located in the bonds, while the Γ_{15c} ZPR (−473 meV) does not suffer from the lack of correlation. This illustrates the importance of proper screening in the high density region. The same feature was reported in graphene to a higher extent, due to the shorter sp^2 bonds [56].

Quasiparticle *GW* [148] calculations of the EPCE were performed on a subset of our **q**-point grid ($\mathbf{\Gamma}$, $\mathbf{\Lambda}$, **L**, **X**). The self-consistency increases

3 See annex A.9 for computational details on DFPT calculations, G_0W_0 and *GW* calculations, finite differences calculations, interpolation scheme, and detailed results for GaAs.



(a) EPCE for the top of the valence band (lower panel) and the bottom of the conduction band at **Γ** (middle panel), calculated in DFPT (solid line) and with the frozen-phonon method (circles).



(b) EPCE for the top of the valence band (lower panel) and the bottom of the conduction band at **Γ** (top pannel), in DFT (squares), in G_0W_0 (circles) and in GW (stars).

Figure 3.15: Diamond electron-phonon coupling energies (EPCE) in DFT and GW. The top panel in (a) shows the band structure with dashed lines indicating the Γ'_{25v} and Γ_{15c} energies. Courtesy of G. Antonius.

slightly the EPCE of the Γ'_{25v} ($\sim$ 8 meV, on average) and the Γ_{15c} ($\sim$ -22 meV). Such a small change results from two canceling effects. While the self-energy allows for a greater interstitial charge density, it also reduces the electron mobility by opening the bandgap much more than G_0W_0 does[3]. Overall, the LDA+G_0W_0 calculation seems to agree well with the electron-phonon coupling obtained from self-consistent GW.

3.3.3 *Temperature dependence of the bandgap*

Our coarse sampling of the Brillouin zone might not capture the relative importance of the strongly coupling modes. Hence, we interpolate the many-body corrections on a dense **q**-point grid using a cubic polynomial fit for the G_0W_0 corrections to the EPCE[3]. We obtain the bandgap renormalization and its temperature dependence from a DFPT calculation on a $32 \times 32 \times 32$ **q**-point grid, as reported in Table 3.4. This fine sampling reveals a bigger G_0W_0 correction to the Γ_{15c} ZPR due to the strong positive contributions near **X** being reduced and those near **Γ** be-

	Γ'_{25v}	Γ_{15c}	Gap
DFPT	141	−263	−404
Δ G_0W_0	+26	−183	−209
Δ GW- G_0W_0	+4	−11	−15
Total	171	−457	−628

Table 3.4: ZPR (meV) computed on a $32 \times 32 \times 32$ **q**-point grid. The G_0W_0 and GW corrections are interpolated with the models discussed in the text.

ing enhanced. As a result, the bandgap ZPR is increased from −404 meV to −628 meV when many-body corrections are applied.

Figure 3.16 shows the temperature dependence of the direct bandgap of diamond computed in DFPT and with many-body corrections. In this figure, the bare bandgap (7.732 eV) was obtained from a full-frequency G_0W_0 calculation starting from an LDA band structure with a scissor shift of 1.5 eV which reproduces the *renormalized* gap[3]. Clearly, the DFPT method underestimates the ZPR, and the many-body corrections are critical to restore the agreement with experiments. The high-temperature slope is also increased from −0.42 meV/K to −0.67 meV/K with many-body corrections, in good agreement with experimental data (−0.60 and −0.69 meV/K [93]).

The correspondence between theoretical and experimental results is remarkable, given that several approximations were made. On the one hand, our calculations were performed in the adiabatic approximation, whereas the full treatment should include non-adiabatic effects as well. We checked, using the non-adiabatic AHC theory and the same $i\delta$, that those effects have a small impact, changing the direct bandgap ZPR by +5 meV. However, it was reported that the non-adiabatic electron-phonon self-energy causes a spreading of the main quasiparticle peak in the Γ_{15c} spectral function, reducing further the optical gap by about 50 meV [67]. On the other hand, the harmonic approximation was used throughout the study, whereas anharmonic effects are believed to reduce the renormalization of the bandgap (in absolute value) [54]. Hence, it would seem that those effects we neglected tend to cancel each other, leading to the agreement of the static harmonic DFPT+GW scheme to within 50 meV of the experimental data.

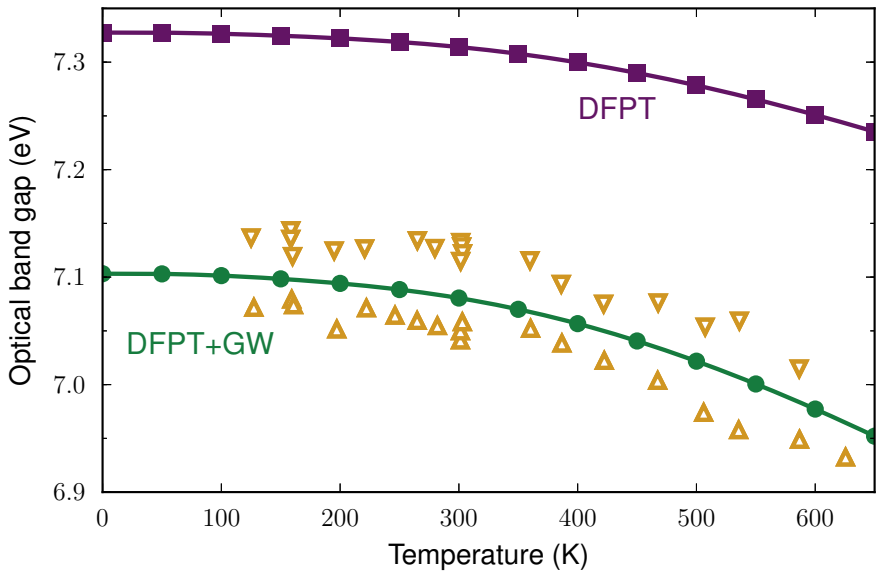


Figure 3.16: Temperature dependence of the direct bandgap computed in DFPT (squares) and with GW corrections (circles). The bandgap (7.732 eV) is computed in G_0W_0, and the two experimental data sets (upper and lower triangles) are from [93]. Courtesy of G. Antonius.

3.4 CONCLUSION

In this chapter, we studied the temperature dependence and zero-point renormalization of five semiconductors and showed that the static and non-adiabatic AHC could be computed routinely. We should nonetheless emphasize that some additional development is required for those type of calculations to be widespreadly used. The main route for improvement lies especially at the level of symmetries. For the moment all the calculations were done using no **k**-point symmetries but using **q**-point symmetries (the opposite can also be done). Additionally, all the **k**-points related by symmetry had to be averaged because the phonon perturbation breaks some **k**-point symmetry (see annex A.8 for more information).

The results are quite satisfactory when compared with experimental results and the maximal discrepancy arise for α-AlN with a ZPR for the direct bandgap of -369 meV compared to the -239 meV experimental value.

We also analyzed the rate of convergence for a polar (α-AlN) and non polar (silicon) material and conclude that the non-adiabatic ZPR was more adapted to describe correctly the ZPR.

Finally, the frozen-phonon method allowed us to go beyond the DFPT framework for the zero-point renormalization of the optical bandgap of diamond and gallium arsenide. We validated the rigid-ion approximation for crystals, showing that the DFPT scheme is a reliable way to calculate the EPCE. The electron self-energy as obtained from G_0W_0 corrections revealed to be much more sensitive to ionic displacements than the LDA exchange-correlation potential. Bringing GW calculations to self-consistency further increased the coupling, but the G_0W_0 approximation captures most of the many-body corrections. Those corrections increase the zero-point renormalization of the bandgap as well as its high-temperature slope by more than 40%. Overall, we find that the DFPT+GW scheme reproduces accurately the temperature dependence of the direct bandgap of diamond. While DFPT remains the most efficient method to treat the electron-phonon interaction, our results call for a more accurate scheme. Ideally, an improvement of the linear response would include non-local exchange and non-adiabatic screening in the ways of the many-body perturbation theory. We hope this work motivates such development.



Part II

EU-DOPED BA-SI OXYNITRIDES FOR WLEDS APPLICATIONS

As mentioned in the introduction of this thesis, this second part focuses on the description of the undoped BSON compounds and on the validation of the Dorenbos auto-ionization model to describe thermal quenching in the two europium-doped oxynitride compounds ($Ba_3Si_6O_{12}N_2$ and $Ba_3Si_6O_9N_4$). The evolution of the conduction band minimum of the host with temperature is also discussed. The end goal of this second part is to estimate the unknown gaps in figure 0.5.

Europium is one of the few lanthanides that commonly exists in stable divalent and trivalent states. In most of them the only stable oxidation state is the +3. The peculiarity of europium is due to the fact that the +2 oxidations state is stabilized by the half-filled 4f shell. The Eu^{2+} is often used (like in the BSON cases) as dopant in luminescent materials due to its dipole allowed optical transition from the lowest $4f^65d^1$ excited state to the $4f^75d^0$ ground state so that this transition occurs with high probability [149].

Chapter 4 deals with the two undoped BSON host materials where the many-body G_0W_0 bandstructure of the two hosts is presented.

When doped, the europium atoms can substitute a barium one in two inequivalent positions for the $Ba_3Si_6O_{12}N_2$:Eu^{2+} case and in three inequivalent positions in the $Ba_3Si_6O_9N_4$:Eu^{2+} cases, leading to the study of five non-equivalent systems. The Chapter 5 is dedicated to the study of the absorption of those five cases through the core-hole and depleted-shifted 4f methods. The emission properties are investigated by means of excited state structural relaxation.



4

BSON HOST MATERIAL

$Ba_3Si_6O_{12}N_2$:Eu^{2+} and $Ba_3Si_6O_9N_4$:Eu^{2+} have strikingly similar atomistic structures, but the former is an efficient green phosphor at working temperature while the latter is a bluish-green phosphor whose luminescence decreases quite fast with temperature. Aiming at the understanding of such a different behavior, we compute the quasiparticle electronic band structure of the two hosts, $Ba_3Si_6O_{12}N_2$ and $Ba_3Si_6O_9N_4$, thanks to many-body perturbation theory in the G_0W_0 approximation. The gap differs by about 0.43 eV. We analyze the eigenfunctions at the top of valence band, at the bottom of the conduction band, and also the chemical shifts for the Ba site in the two hosts. The valence bands, directly impacted by the different stoichiometric ratio, are not thought to play a large role in the luminescence. Deceivingly, the dispersive bottom of conduction band, directly related to luminescent properties, is similar in both compounds. The spatial topology of the probability density of the bottom of the conduction bands differs, as well as the location of the 5d peak, with a much higher energy in $Ba_3Si_6O_{12}N_2$ than in $Ba_3Si_6O_9N_4$ (well above the bottom of the conduction band in both cases). Electromagnetic absorption spectra are also computed for both compounds.

The content of this chapter has been published in Ref. [4].

4.1 HISTORICAL CONTEXT

After the recent invasion of compact fluorescent lamps, white LED lighting is becoming a major contender in eco-friendly light sources, with a combination of green- and red-emitting phosphors partly absorbing the blue light emitted by an InGaN LED [150, 3]. Phosphors with optimized luminescence properties (i.e. with an optical spectrum close to the solar one and low thermal quenching) are coveted by industry and subject of very active development. A detailed theoretical understanding

of their electronic structure is still lacking and might aid experimental researchers in finding more efficient phosphors.

In this spirit, we have studied two chemically close oxynitride materials, in which rare-earth europium doping lead to different luminescence properties. The recently discovered green phosphor $Ba_3Si_6O_{12}N_2$:Eu^{2+} offers very good luminescence properties and weak thermal quenching [8, 5] at working temperature (around 100°C), while $Ba_3Si_6O_9N_4$:Eu^{2+} is a bluish-green phosphor that exhibits unfavourable decrease of the luminescence intensity with temperature [8, 5, 151]. The crystal structure of $Ba_3Si_6O_9N_4$:Eu^{2+} was reported by Stadler *et al.* [152]. The original result of Uheda *et al.* [8] for $Ba_3Si_6O_{12}N_2$:Eu^{2+} was confirmed and studied in more depth by further experimental studies [153, 154, 155, 156, 157, 158, 151]. In particular, Braun *et al.* [154] evaluated the $Ba_3Si_6O_{12}N_2$ bandgap to be 7.05 eV by means of X-ray emission spectroscopy (XES) and X-ray absorption near edge spectroscopy (XANES).

The crystalline structure of these two materials is very similar: Si-O-N layers alternate with barium layers. The Si-O-N layers are made of tetrahedra with silicon at their center, and oxygen or nitrogen at their apices, connected through Si-O-Si or Si-N-Si bonds. The lattice parameters are similar as well. The barium environment is more subject to variations, not only in the two materials, but also for different crystalline positions within one material: although predominantly surrounded by oxygen atoms, some barium are not close to any nitrogen atom, while some have one, two or three nitrogen neighbors. The europium dopant might substitute any of these sites. With such apparently similar materials, one can wonder why the quenching temperature is so different. In particular, this might indicate the extent to which a search for good luminescent materials has to take into account small details of the crystalline structure of the host.

Despite their similar structure and chemical formula, the different optical characteristics as a function of temperature might enable one to single out basic factors influencing their fluorescence properties. Empirical hypotheses were brought up by Mikami *et al.* [5]. They postulated that $Ba_3Si_6O_9N_4$:Eu^{2+} experienced a stronger thermal quenching because the lowest Eu-d states are closer to the conduction bands than in the $Ba_3Si_6O_{12}N_2$:Eu^{2+} case. The photo-excited 5d-electrons of Eu^{2+} would then be thermally ionized to the conduction bands at room temperature following the Dorenbos model [13] (auto-ionization). In general, it is difficult to experimentally determine bandgaps of phosphors, because phosphor samples are usually obtained as powder, so this assertion can

only be verified through comprehensive numerical analysis with sufficient accuracy, on the order of a few sub-eV for the thermal quenching temperature[1].

The hosts and doped materials have been studied from the *ab-initio* point of view as well. Mikami *et al.* [5] obtained an electronic bandgap of 4.63 eV and 4.37 eV for $Ba_3Si_6O_{12}N_2$ and $Ba_3Si_6O_9N_4$, respectively. They used generalized-gradient approximation (GGA) within the density functional theory (DFT) [45, 159]. Such an approach is subject to the well-known DFT *bandgap problem*: the gap is usually underestimated, sometimes strongly. Braun *et al.* [154] found an indirect bandgap ($\mathbf{A} - \mathbf{\Gamma}$) of 4.8 eV for $Ba_3Si_6O_{12}N_2$ using GGA and went further by also using a modified Becke-Johnson potential (mBJ-GGA), known to give a much better global agreement with true gap values, albeit wrong bandwidth [160], leading to a value of 6.93 eV. Tang *et al.* [155] performed DFT+U calculations for the Eu-doped compounds using a supercell ($Ba_{11}Si_{24}O_{48}N_8Eu$). They obtained a direct gap of 1.3 eV between the europium 4f states and the excited europium 5d state. Still, the accuracy of DFT+U computation for such 4f-5d gap is also questionable.

Unlike previous DFT-based studies, we compute the band structure of these materials by state-of-the-art many-body perturbation theory in the G_0W_0 approximation [21], which is much more computationally demanding than DFT, but reliably gives bandgaps within 10% of the experimental value, usually underestimating it [161]. To our knowledge, it has not yet been used for LED phosphors (neither Eu-based ones nor Ce-based ones). Our G_0W_0 bandgap is indeed very close to the experimental bandgap for $Ba_3Si_6O_{12}N_2$. The narrowing of the gap between $Ba_3Si_6O_{12}N_2$ and $Ba_3Si_6O_9N_4$ is confirmed. We then perform different analyses to characterize the differences in electronic structure and optical properties in both compounds, and find that the opening of the gap is more related to valence bands modifications than to conduction bands ones, while the reverse would be expected in order to establish the link to different luminescent behavior. Thus, calculations on doped hosts are needed to clarify the situation. The fact that such detailed calculation might be needed is somehow problematic, in view of rapid first-principles screening of materials in large databases, which is an emerging technique to explore the huge variety of materials [162].

1 The accuracy of band gap evaluation is necessary for the discussion on thermal quenching, by considering Dorenbos' empirical formula: $\Delta E = T_{0.5}/680$ eV, where $T_{0.5}$ is the quenching temperature at which the emission intensity has dropped to 50% of the low temperature value and ΔE is the energy barrier [13].

After the present introduction, we detail our numerical approach in section 4.2. In section4.3, we analyses successively the crystallographic structure, the quasiparticle band structures and density of states, the effective masses, and then discuss energy shifts, electrostatic potential and absorption spectra in both materials, before concluding.

4.2 NUMERICAL APPROACH

We have used projector augmented wave (PAW) [163] pseudopotentials with the Perdew-Burke-Ernzerhof parametrization of the generalized gradient approximation [107] for the exchange-correlation functional. Due to the precise nature of the PAW numerical method, which includes information about rapidly varying wavefunctions in atomic core regions, the quality of the results should be very close to that of all-electron calculations, despite the fact that the PAW methodology assumes a selected set of core electrons to be frozen and a finite number of projectors on valence states (or semi-core states) replacing a formally infinite one, as detailed below.

Crucially, we have found that a reliable computation of the G_0W_0 corrections to the GGA bandgap requires the explicit treatment and relaxation of semi-core states in the PAW atomic data for barium.

We have generated a PAW atomic dataset for barium taking the $4d^{10}5s^2$ $5p^6 6s^2$ orbitals as valence states, and considering the states below as frozen. The PAW sphere radius is 2.45 Bohr with 3 projectors per occupied angular momentum channel. A large number of projectors is sometimes required for perturbative calculations, where the unoccupied states are used as a basis and therefore need to be accurately described. Increasing the number of projectors improves the flexibility of the basis and hence allows for an accurate reproduction of the all-electron wavefunction. We have used the software ATOMPAW [164] to generate the barium PAW pseudopotential. The other PAW pseudopotentials were taken from the ABINIT website `http://www.abinit.org/downloads/PAW2`. The silicon PAW data-set with $3s^2 3p^2$ valence electrons has a 1.71 Bohr sphere radius and 2 projectors per angular momentum channel. Oxygen with $2s^2 2p^4$ valence electrons has a 1.2 Bohr sphere radius and 3 projectors per angular momentum channel. The nitrogen with $2s^2 2p^3$ valence electrons has a 1.3 Bohr radius and 2 projectors per angular channel.

With these pseudopotentials we made a structural relaxation of the cell geometry and atoms positions using a Broyden-Fletcher-Goldfarb-Shanno (BFGS) minimization scheme [165] at the DFT level. We com-

puted the quasiparticle correction on a 6x6x4 Monkhorst-Pack sampling [101] of the Brillouin zone half-shifted along the z direction. The quasiparticle bandstructure was then obtained using an energy-dependent polynomial fit of the G_0W_0 eigenenergies [160]. This approach is significantly better than the cruder usual method of using a constant scissor-shift for all unoccupied bands, and leads to similar results as provided by a Wannier interpolation[2] but is easier to use and less computationally demanding. A cut-off energy of 25 Ha was used for the planewave basis set to describe the wavefunctions, and a converged cut-off energy of 6 Ha was chosen for the planewave set representing the independent-particle susceptibility and the dielectric matrix for the calculation of the screening. A number of efficient approaches to the calculation of the GW self-energy have recently been developed such that only a small number of unoccupied states are required for the perturbation expansion summation. Among them, the *extrapolar method* [167] consists in introducing an average pole energy to replace the poles arising from the eigenvalues of empty states beyond an arbitrary energy level. This allows for the truncation of the sum-over-states in the screening or self-energy calculation and improves convergence with respect to the number of unoccupied bands, while keeping unmodified the final converged value. We have chosen an extrapolar energy of 2.5 Ha for the screening calculation (and 2 Ha for the self-energy). This reduces by a factor of five the number of empty states required for a convergence of the gap to within 0.01 eV for both screening and self-energy calculations. In both cases, 340 unoccupied bands were explicitly treated in the sums.

We have used a Godby-Needs [168] plasmon-pole model to evaluate the self-energy operator $\Sigma(\omega)$. A computationally more demanding fully frequency-dependent numerical integration by the contour deformation (CD) technique [169] was also undertaken to assess the quality of the plasmon-pole model. The CD calculation was made only at the Γ point for $Ba_3Si_6O_{12}N_2$ and reveals a discrepancy of the bandgap of less than 0.4% with respect to the plasmon-pole model approach. We have consequently chosen to make all further calculations with this plasmon-pole model. After a careful convergence analysis, the estimated numerical error (within the chosen approximations, as explained above) is about 0.1 eV.

We also have computed the electromagnetic (optical + UV) absorption spectra (imaginary part of the macroscopic dielectric function $\varepsilon(\omega)$) of the two materials in the independent particle sum-over-states approxi-

2 See for example Ref. [166] for a description of the Wannier interpolation scheme.

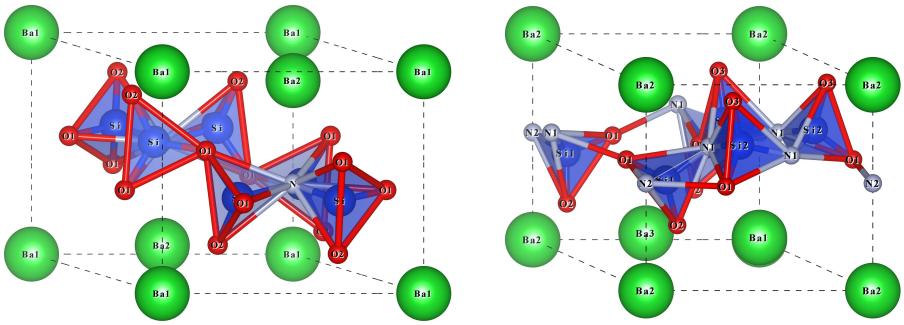
mation, also called Random Phase Approximation (RPA) [170]. The relative convergence below 1% of the absorption spectrum in the energy range considered required a 6x6x6 **k**-point grid. The convergence on the number of bands included in the calculations is crucial for RPA calculation. The transition between the 38 highest valence bands and the 67 lowest conduction bands were taken explicitly into account for the case of $Ba_3Si_6O_{12}N_2$. For $Ba_3Si_6O_9N_4$ the 44 highest valence band and the 71 lowest conduction bands were needed. We used a scissor of 2.258 eV for $Ba_3Si_6O_{12}N_2$ and 2.07 eV for $Ba_3Si_6O_9N_4$ to account for the opening of the quasiparticle bandgap between DFT and G*W*.

All calculations have been done using the ABINIT software [96].

4.3 RESULTS AND DISCUSSION

4.3.1 *Crystallographic structure*

The space group of $Ba_3Si_6O_{12}N_2$ is $P\bar{3}$ (trigonal, 147). The DFT structural relaxation leads to lattice constants a = 14.377 Bohr and c = 12.383 Bohr. This theoretical result is slightly above the experimental values given by Braun *et al* [154] of 14.214 Bohr and 12.223 Bohr, although well within the expectations of GGA functionals, which tend to overestimate slightly the bond lengths.

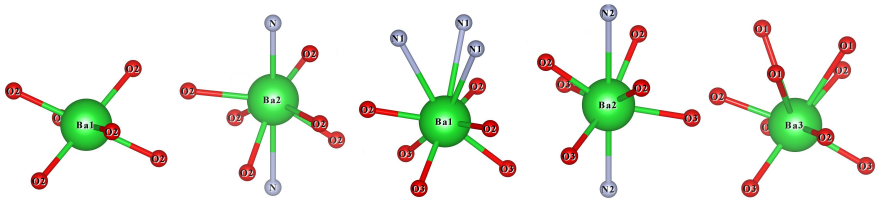


(a) $Ba_3Si_6O_{12}N_2$ (b) $Ba_3Si_6O_9N_4$

Figure 4.1: (a) Crystal structure of $Ba_3Si_6O_{12}N_2$ after structural relaxation. There are two inequivalent barium atoms. The first one is labeled Ba_1 and occupies the 1a Wyckoff-position and the other labeled Ba_2 is in the 2d Wyckoff-position. Figure (b) shows the crystal structure of $Ba_3Si_6O_9N_4$ after structural relaxation. There are three inequivalent barium atoms. The first one is labeled Ba_1 and occupies the 1c Wyckoff-position, the second one labeled Ba_2 is in the 1a Wyckoff-position and the last one named Ba_3 is in the 1b Wyckoff-position.

As shown in Fig. 4.1, $Ba_3Si_6O_{12}N_2$ is built up of corner-sharing SiO_3N tetrahedra forming corrugated layers between which the Ba^{2+} ions are located [5]. The latter ions occupy two different crystallographic sites: (1) one barium atom denoted by Ba_1 occupies Wyckoff position 1a and is surrounded by six symmetrically equivalent oxygen atoms forming a trigonal anti-prism (distorted octahedron); (2) two barium atoms denoted by Ba_2 occupy Wyckoff positions 2d and are surrounded by six oxygen atoms forming a trigonal anti-prism, further capped with two nitrogen atom.

The space group of $Ba_3Si_6O_9N_4$ is P3 (trigonal,143). As described by Stadler *et al.* [152] the Ba^{2+} ions occupy three different crystallographic sites in the crystal structure of $Ba_3Si_6O_9N_4$. In the latter reference, it is mentioned that two of them are trigonal anti-prisms with six oxygen atoms (Ba_1 and Ba_3) while the other is a trigonal anti-prism with six oxygen atoms, further capped with a nitrogen atom (Ba_2). However, a look at neighbors in a slightly larger environment reveals that Ba_1 is also close to three nitrogen atoms forming a triangle perpendicular to the z axis, while there exist another nitrogen atom close to the Ba_2, opposite to the first one, along the z direction, as shown in Fig. 4.2. The DFT structural relaxation for this second host gives two lattice constants of a=13.838 Bohr and c=12.969 Bohr also somewhat larger than the experimental value by Stadler *et al.* [152] of 13.699 Bohr and 12.820 Bohr. The crystallographic figures are made using the VESTA software [171].



(a) Ba_1 (b) Ba_2 (c) Ba_1 (d) Ba_2 (e) Ba_3

Figure 4.2: (a) and (b) show the crystalline environment of the two inequivalent barium atoms in $Ba_3Si_6O_{12}N_2$. (c), (d) and (e) show the crystalline environment of the three inequivalent barium atoms in $Ba_3Si_6O_9N_4$. Bond lengths are reported in Table 4.1

The selected bond lengths and bond angles of the two host materials are shown in Table 4.1 and compared with experiment and previous GGA calculations using NC pseudopotentials. The O-(O,N)-O angles of $Ba_3Si_6O_{12}N_2$ range from 135-161° and correspond well with experimental data from Braun *et al.* [154] that range from 135-160°. The Si-N-Si

angles of $Ba_3Si_6O_9N_4$ range from 117-121° and also match the experimental results of Stadler *et al.* [152] that range from 116-121°.

	$Ba_3Si_6O_{12}N_2$		
	GGA-PAW	GGA-NC[3]	Experimental[4]
Ba_1-O_2 (6x)	5.2149	5.2421	5.185(6)
Ba_2-O_2 (3x)	5.5917	5.5936	5.484(6)
-O_2 (3x)	5.3141	5.3555	5.327(6)
-N (1x)	5.7712	5.7467	5.663(12)
-N (1x)	6.6121	6.1624	6.559(12)
Si -N (1x)	3.3165	3.3070	3.279(4)
-O_1 (1x)	3.1589	3.1426	3.116(6)
-O_1 (1x)	3.1636	3.1445	3.118(8)
-O_2 (1x)	3.0476	3.0236	2.999(6)
	$Ba_3Si_6O_9N_4$		
Ba_1-O_2 (3x)	5.1287	5.1608	5.080(8)
-O_3 (3x)	5.3347	5.3593	5.337(8)
-N_1 (3x)	6.6103	6.5762	6.450(10)
Ba_2-O_2 (3x)	5.1079	5.1533	5.110(8)
-O_3 (3x)	5.4046	5.4197	5.354(8)
-N_2 (1x)	6.2059	6.1076	5.963(14)
-N_2 (1x)	6.7633	6.8937	6.854(14)
Ba_3-O_2 (3x)	5.1589	5.1797	5.121(8)
-O_3 (3x)	5.1608	5.2081	5.148(8)
-O_1 (3x)	6.3778	6.3891	5.920(8)
Si_1 -O_2 (1x)	3.0765	3.0519	3.033(8)
-O_1 (1x)	3.1596	3.1426	3.107(10)
-N_1 (1x)	3.3089	3.2995	3.277(10)
-N_2 (1x)	3.3335	3.3240	3.299(4)
Si_2 -O_3 (1x)	3.0670	3.0425	3.014(8)
-O_1 (1x)	3.1634	3.1483	3.116(8)
-N_1 (1x)	3.3184	3.3070	3.284(10)
-N_1 (1x)	3.3486	3.3391	3.315(10)

Table 4.1: Selected bond lengths [in Bohr] of $Ba_3Si_6O_{12}N_2$ and $Ba_3Si_6O_9N_4$ compounds.

3 See Ref. [5] for $Ba_3Si_6O_{12}N_2$ and $Ba_3Si_6O_9N_4$
4 See Ref. [154] for $Ba_3Si_6O_{12}N_2$ and Ref. [152] for $Ba_3Si_6O_9N_4$

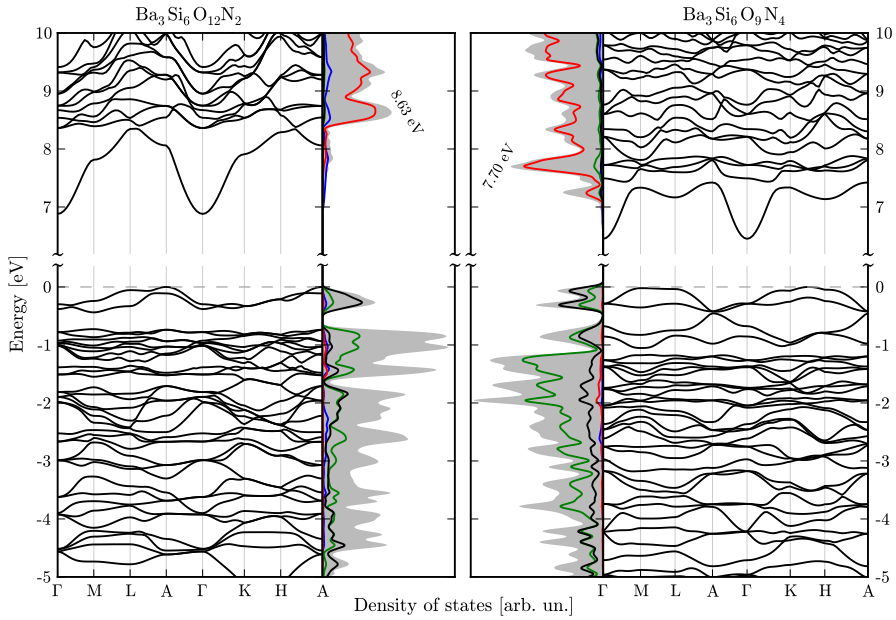


Figure 4.3: Quasiparticle bandstructure of $Ba_3Si_6O_{12}N_2$ (left side) and $Ba_3Si_6O_9N_4$ (right side) calculated within the G_0W_0 approximation. The corresponding density of states (DOS) are reported in the middle panels (grey area). It is decomposed into the partial density of states (PDOS) of the Ba_d level (red line), the Ba_s level (blue line), the O_p level (green line) and the N_p level (black line).

4.3.2 *Quasiparticle band structure and density of states*

The computed quasiparticle electronic bandstructures based on the one-shot G_0W_0 approximation with PAW pseudopotentials are given in Fig. 4.3. Using the theoretical structure, $Ba_3Si_6O_{12}N_2$ shows an indirect **Γ-A** fundamental gap of 6.88 eV, slightly underestimating the experimental gap value of 7.05±0.25 eV [154]. Such slight underestimation is often observed within the G_0W_0 approximation [161]. It is actually in better agreement when the experimental structure is used. In this case, the obtained bandgap is 7.00 eV. $Ba_3Si_6O_9N_4$ has an indirect **Γ-M** bandgap of 6.45 eV when the theoretical structure is used.

The fundamental gap of $Ba_3Si_6O_9N_4$ is thus 0.43 eV smaller than the one of $Ba_3Si_6O_{12}N_2$. This is in agreement with the phenomenological interpretation of the quenching mechanism according to the Dorenbos's scheme [172, 13]. We will now discuss the narrowing of the gap in terms of factors related to valence band differences and conduction band dif-

ferences. Note, however, that we did not attempt to compute accurate band offsets between the two hosts, as an accurate prediction would need larger supercells.

The density of states, and the partial density of states for the Ba_d, Ba_s, O_p and N_p states are also presented in Fig. 4.3. The top of the valence bands is dominated by the N_p states in both compounds. Two bands clearly emerge from the block of valence bands in $Ba_3Si_6O_{12}N_2$, while four bands emerge for $Ba_3Si_6O_9N_4$. These numbers of bands can be correlated with the existence of non-bonding N_p states, one for each nitrogen atom. The appearance of the two extra valence nitrogen states in $Ba_3Si_6O_9N_4$ pushes the two other nitrogen states higher in energy. This is clearly a factor leading to lowering of the bandgap.

The analysis of the conduction bands complex is particularly relevant as well, as in both cases, one strongly dispersive band is observed, originating from a combination of Ba_s and O_p states. The electrons excited in this dispersive band will have a rather high mobility, and thus might approach a luminescence killer defect, regardless of its origin. We will analyse these orbitals, and associated effective mass later. Above the strongly dispersive band, a large set of flatter bands is observed, 8.63 eV higher than the valence band maximum in the case of $Ba_3Si_6O_{12}N_2$, and 7.70 eV higher in the case of $Ba_3Si_6O_9N_4$. They arise mainly from the Ba_d channel, albeit mixed with other orbitals. The large difference between the two hosts for the dominant peak in the conduction DOS will have to be investigated.

Before performing this analysis, the G_0W_0 corrections to the DFT eigenergies for the two hosts are presented in Fig. 4.4. The relatively large range of corrections (up to 0.5 eV spread) for the DFT conduction states between 6 and 7 eV corresponding to G_0W_0 energies between 10 and 11 eV above the valence band maximum) is to be related to the strong hybridization between the 5d and 6s levels of barium. On the other hand, the narrow dispersion of corrections below 6 eV is related to the well defined 6s states of barium. This illustrates the validity of our interpolation scheme for the valence bands and the lowest conduction band, but also its limit for the higher bands.

4.3.3 *Effective masses*

The effective mass at a given $\mathbf{k}$-point and band index n is defined as

$$m^*_{n\mathbf{k}} = \hbar^2 \left(\frac{\partial^2 \varepsilon_{n\mathbf{k}}}{\partial \mathbf{k}^2} \right)^{-1}, \tag{4.1}$$

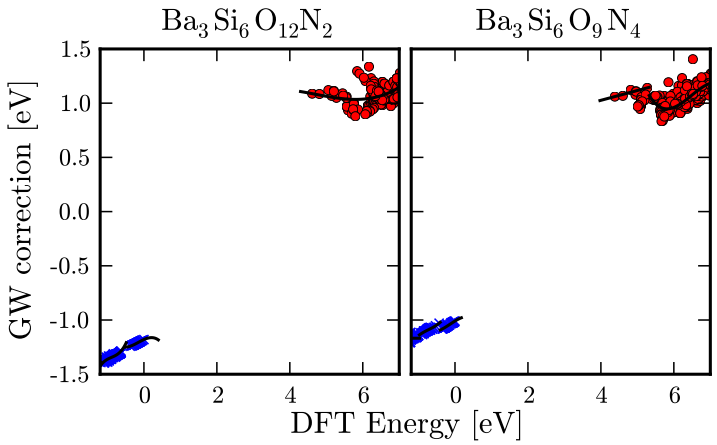
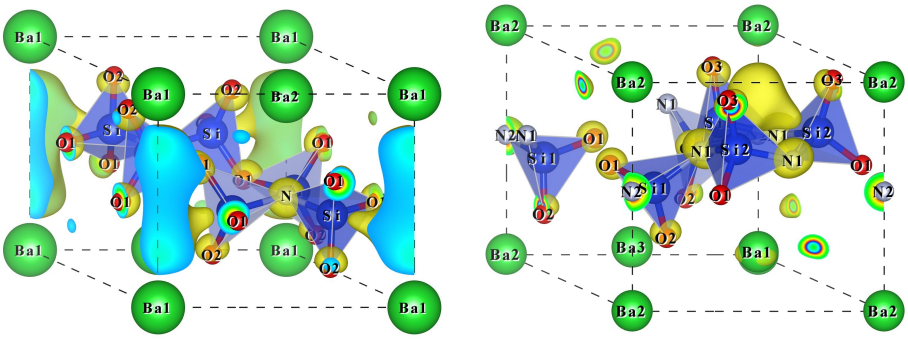


Figure 4.4: Magnitude of G_0W_0 corrections to the DFT eigenergies for $Ba_3Si_6O_{12}N_2$ on the left side and $Ba_3Si_6O_9N_4$ on the right side. The negative corrections (blue crosses) are for the occupied states and the positive (red dots) for the unoccupied states. The full line shows the energy polyfit that was used to generate the quasi-particle bandstructure in Fig. 4.3.

with $\varepsilon_{n\mathbf{k}}$ the eigenenergy at a given **k**-point and band index n. The effective masses of the electrons at the bottom of the conduction band in the direction **Γ**-**A** and **Γ**-**K** are 0.481 and 0.503 for $Ba_3Si_6O_{12}N_2$ in DFT, respectively. For $Ba_3Si_6O_9N_4$ in the direction **Γ**-**A** and **Γ**-**K** we have 0.446 and 0.491 at the DFT level, respectively (effective masses from the polyfit interpolation scheme do not include **k**-dependent corrections [173], and it is preferable to stay at the DFT level). The effective masses are smaller in the direction **Γ**-**A**. In Fig. 4.5, the square of the wavefunction at the bottom of the conduction band is presented. For $Ba_3Si_6O_{12}N_2$, one sees that in this direction (along the z axis and perpendicular to the barium plane) the density creates a channel linking the Ba_1. An other view from the top in Fig. 4.6 shows that in $Ba_3Si_6O_{12}N_2$ the density has a sixfold symmetry that points towards the six silicon atoms (three are in the upper plane and three are in the down plane). The states in that direction will be more delocalized and hence the energy dispersion will be steeper, with a smaller effective mass in that direction. In contrast which what one may think, it is not the Ba_2 close to the nitrogen that conducts the electrons of the unoccupied band but the Ba_1.

The main difference between the two compounds, for the conduction band, thus lies in the fact that the barium atom that has the biggest weight in the first unoccupied state is the one surrounded only by oxygen in the case of $Ba_3Si_6O_{12}N_2$ (Ba_1) and the one close to three nitrogen



(a) $Ba_3Si_6O_{12}N_2$ (b) $Ba_3Si_6O_9N_4$

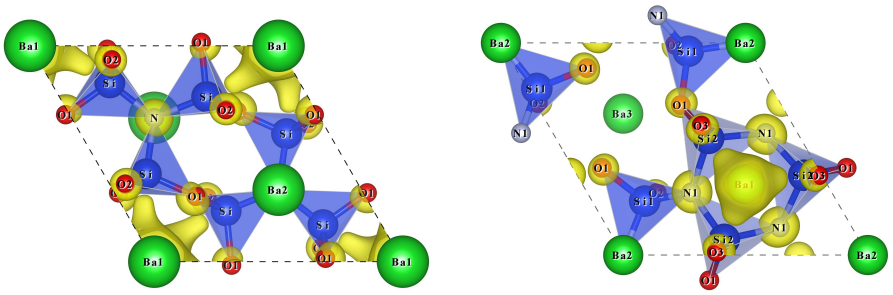
Figure 4.5: (a) Density of the first unoccupied band (84^{th} band) of $Ba_3Si_6O_{12}N_2$ at the Γ point, that is $\Psi^*_{84\Gamma}\Psi_{84\Gamma}$. The channel density corresponds mainly to the 6s state of barium. (b) Density of the first unoccupied band (80^{th} band) of $Ba_3Si_6O_9N_4$ at the Γ point, that is $\Psi^*_{80\Gamma}\Psi_{80\Gamma}$. Both iso-density are at 10% of the maximum density of that state. Large values are located around nitrogen and oxygen atoms.

in the case of $Ba_3Si_6O_9N_4$ (Ba_1). We will also see later in Chapter 5 that those are the two luminescent centres.

4.3.4 *Energy shifts and electrostatic potential*

We now turn to the analysis of the DOS peaks, attributed to Ba_{5d} states. The fact that the 5d states are 0.93 eV lower in energy in $Ba_3Si_6O_9N_4$ (7.70 eV) than in $Ba_3Si_6O_{12}N_2$ (8.63 eV), and closer to the conduction band minimum, might be important to explain the thermal quenching. Indeed, in the europium-doped material, the europium is substitutional to some of the barium atoms. If the local electrostatic potential at the barium site is lower in one (or another) site of one of the host materials, it should also be lower when the europium replaces the barium. Obviously, a further shift due to the substitution might be present as well, but is expected to be similar in the two materials. Also, the lowering of the 5d states might not be due to the electrostatic potentials, but to different hybridization with orbitals from neighboring atoms.

In order to analyze the local electrostatic potential and in addition to the analysis performed at the vicinity of the bandgap, we have gathered informations on the electronic structure for a larger range of energies in table 4.2, including band edges, bandwidths and the dominant band characters for both hosts.



(a) $Ba_3Si_6O_{12}N_2$ (b) $Ba_3Si_6O_9N_4$

Figure 4.6: Top view of the (a) density of the first unoccupied band (84^{th} band) of $Ba_3Si_6O_{12}N_2$ at the Γ point and (b) density of the first unoccupied band (80^{th} band) of $Ba_3Si_6O_9N_4$ at the Γ point. Both iso-density are at 10% of the maximum density of that state.

$Ba_3Si_6O_{12}N_2$				
Position DFT	Bandwidth DFT	Position G_0W_0	Bandwidth G_0W_0	Band character
6.130	1.508(1)	8.350	1.470(1)	Ba_{6s}
4.622		6.880		Ba_{6s}
0.000	0.377(2)	0.000	0.437(2)	N_{2p}
−0.377		−0.437		N_{2p}
−0.623	5.417(35)	−0.742	5.756(35)	Ba_{4d} N_{2p}
−6.040		−6.498		Si_{3p} O_{2p}
−6.342	0.860(2)	−6.803	0.863(2)	N_{2p}
−7.202		−7.666		Si_{3s} O_{2p}
−7.363	1.231(3)	−7.833	1.280(3)	Si_{3s}
−8.594		−9.112		Si_{3s}
−9.798	0.479(9)	−10.303	0.523(9)	Ba_{5p}
−10.277		−10.826		Ba_{5p}
−14.285	0.302(2)	−14.402	0.296(2)	N_{2s}
−14.587		−14.698		N_{2s}
−16.437	0.382(6)	−16.680	0.371(6)	O_{2p} Si_{3p}
−16.819		−17.051		O_{2p} Si_{3p}
−17.935	1.589(6)	−18.079	1.514(6)	O_{2s} Si_{3s}
−19.524		−19.593		O_{2s} Si_{3s}
−24.656	0.270(3)	−23.610	0.426(3)	Ba_{5s}
−24.926		−24.036		Ba_{5s}
−80.508	0.040(5)	-	-	Ba_{4d}
−80.548		-		Ba_{4d}

Continued on next page

Table 4.2 – continued from previous page

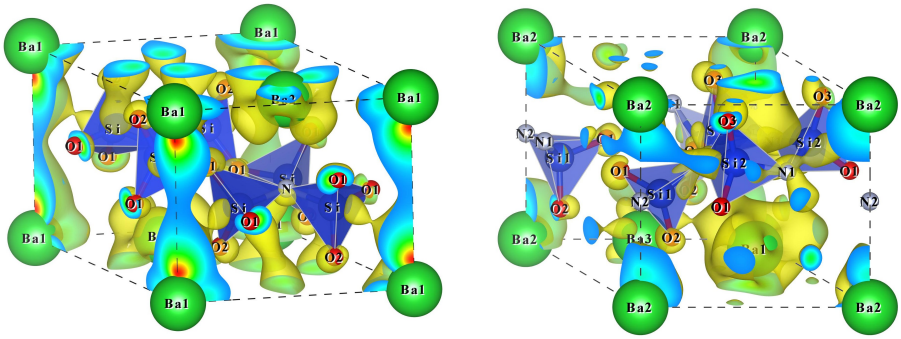
−80.821	0.011(10)	-	-	Ba_{4d}
−80.832		-		Ba_{4d}
		$Ba_3Si_6O_9N_4$		
Position DFT	Bandwidth DFT	Position G_0W_0	Bandwidth G_0W_0	Band character
5.271	0.890(1)	7.421	0.970(1)	Ba_{6s}
4.381		6.451		Ba_{6s}
0.000	0.352(4)	0.000	1.053(4)	N_{2p}
−0.352		−1.053		N_{2p}
−0.435	6.504(32)	−1.171	5.601(32)	N_{2p} O_{2p}
−6.939		−6.772		Si_{3p}
−7.367	0.984(3)	−7.229	1.078(3)	N_{2p} O_{2p}
−8.351		−8.307		Si_{3s}
−10.051	0.128(3)	−9.985	0.175(3)	Ba_{5p}
−10.179		−10.160		Ba_{5p}
−10.282	0.263(6)	−10.206	0.324(6)	Ba_{5p}
−10.530		−10.545		Ba_{5p}
−13.934	1.172(4)	−13.920	1.171(4)	Ni_{2s} Si_{3p}
−15.106		−15.091		Ni_{2s} Si_{3p}
−16.892	0.411(6)	−16.878	0.410(6)	O_{2s} Si_{3s}
−17.303		−17.288		O_{2s} Si_{3s}
−18.909	0.391(3)	−18.892	0.392(3)	O_{2s} Si_{3s}
−19.300		−19.285		O_{2s} Si_{3s}
−24.894	0.274(3)	−24.879	0.274(3)	Ba_{5s}
−25.168		−25.153		Ba_{5s}
−80.716	0.025(5)	-	-	Ba_{4d}
−80.741		-		Ba_{4d}
−80.976	0.027(10)	-	-	Ba_{4d}
−81.003		-		Ba_{4d}

Table 4.2: Band positions [eV], bandwidth [eV] and the dominant band character of $Ba_3Si_6O_{12}N_2$ and $Ba_3Si_6O_9N_4$ compounds. The number in parenthesis for the bandwidth is the number of bands in that group.

Directly influenced by the local electrostatic potential at the atomic site, the 4d core levels of barium are located lower in energy in $Ba_3Si_6O_9N_4$ than in $Ba_3Si_6O_{12}N_2$, with respect to the top of the valence band. However, the difference is not very large (about 0.2 eV). We note that the local electrostatic potential is not the same in the different locations for each host. The Ba_{4d} levels at the Ba_2 site in $Ba_3Si_6O_{12}N_2$ are about 0.3 eV lower than the Ba_{4d} level at the Ba_1 site. Similarly, the Ba_{4d} levels at the Ba_1 and Ba_2 sites are about 0.26 eV lower than at the Ba_3

site for $Ba_3Si_6O_9N_4$. The spread of the Ba_{5s} bands, combining contributions from the three sites is on the order of 0.27 eV, for both hosts, with a chemical shift between the two hosts that is similar to the one of the Ba_{4d} states. From this analysis, the local electrostatic potential only explains a fraction of the 0.93 eV shift of the 5d states.

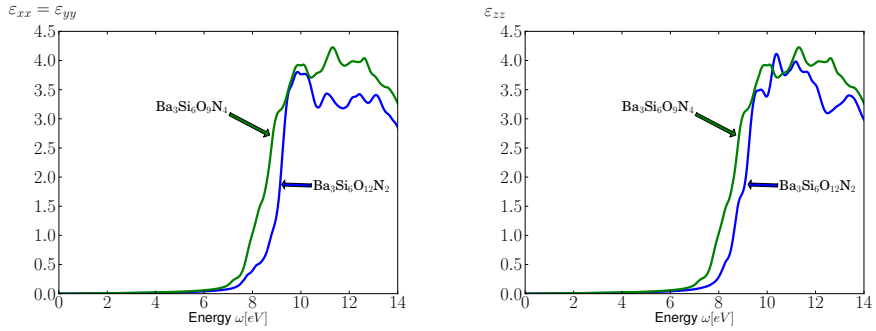
In order to understand the hybridization, the probability density for wavefunctions in the zone of energies corresponding to the peak in the DOS, attributed to the 5d states of barium, are also shown in Fig. 4.7. For $Ba_3Si_6O_{12}N_2$, one clearly sees a large probability density in the region between the Ba_1 atoms, along the z direction, with also some localized d states around Ba_2. For $Ba_3Si_6O_9N_4$ a large probability density is observed around the Ba_1 atoms, with an additional protrusion along the z axis, downwards, (so seen through the upper face of Fig. 4.7(b)). This protrusion is similar in shape to the one seen in Fig. 4.5(b). In this region, there is no atom, but three Si tetrahedra building blocks face it directly, as can be seen in Fig. 4.1(b). No such structure is present in $Ba_3Si_6O_{12}N_2$, see Fig. 4.1(a).



(a) $Ba_3Si_6O_{12}N_2$ (b) $Ba_3Si_6O_9N_4$

Figure 4.7: (a) Density of the sum of the 85 to 90 th bands of $Ba_3Si_6O_{12}N_2$ at the Γ point that corresponds mainly to the 5d states of barium. (b) Density of the sum of the 81 to 83 th bands of $Ba_3Si_6O_9N_4$ at the Γ point that corresponds mainly to the 5d states of barium. Both iso-density are at 10% of the maximum density of that state.

On the basis of the electronic structure of the undoped hosts only, one can hardly progress further. Careful analysis of the different thermal quenching models requires an in-depth study including the phononic behavior of the host as done by Mikami [11]. The vibrational analysis performed there indicate no significant difference between the two hosts suggesting that the difference in thermal quenching may be explained by the auto-ionization model rather than the traditional configurational



(a) Absorption spectra in the $xx = yy$ direction.

(b) Absorption spectra in the zz direction.

Figure 4.8: Comparison of the $Ba_3Si_6O_{12}N_2$ and $Ba_3Si_6O_9N_4$ electromagnetic absorption spectra at the RPA level for electric field polarizarion in the two non trivial directions.

coordinate diagram. The nephelauxetic effect (electronic cloud delocalization) of the 5d europium state in the phosphors will therefore be investigated in Chapter 5.

4.3.5 *Absorption spectra at the RPA level*

The last analysis made on the two materials is the computation of the macroscopic dielectric function in the independent particle sum-over-states approximation (RPA), whose imaginary part is directly linked to the electromagnetic (optical and UV) absorption spectrum. Since both materials have an hexagonal lattice structure, the only two non trivial components of the dielectric function, probed by the electric field polarization, are $\varepsilon_{xx} = \varepsilon_{yy}$ and ε_{zz}. Both components are compared for the two materials on Fig. 4.8.

As anticipated from the G_0W_0 bandstructure, the onset of absorption occurs at a lower energy in the $Ba_3Si_6O_9N_4$ case. In the quasi-plateau region, where the imaginary part of the dielectric function is between 3.0 and 4.5 for both materials and in both directions, we observe a smaller average value for $Ba_3Si_6O_{12}N_2$, although for selected energies, the value observed for $Ba_3Si_6O_{12}N_2$ can be bigger than the one for $Ba_3Si_6O_9N_4$.

The real part of the macroscopic dielectric function at zero electronic frequencies gives a value of 2.38 and 2.80 for $\varepsilon^{\infty}_{xx} = \varepsilon^{\infty}_{yy}$ in $Ba_3Si_6O_{12}N_2$ and $Ba_3Si_6O_9N_4$, respectively. The $\varepsilon^{\infty}_{zz}$ component has a value of 2.41 and 2.74 for $Ba_3Si_6O_{12}N_2$ and $Ba_3Si_6O_9N_4$, respectively. These results

are made at the RPA level without local field effect. The inclusion of local fields effects at the density functional perturbation level (the Hartree and exchange-correlation kernels are included - calculations are done at the GGA level), with the computational parameters detailed in Mikami and Kijima [174], gives 3.10 and 3.30 for $\varepsilon^{\infty}_{xx} = \varepsilon^{\infty}_{yy}$ in $Ba_3Si_6O_{12}N_2$ and $Ba_3Si_6O_9N_4$, respectively, and 3.07 and 3.21 for $\varepsilon^{\infty}_{zz}$ in $Ba_3Si_6O_{12}N_2$ and $Ba_3Si_6O_9N_4$, respectively. The anisotropy of these materials, although non-negligible, is thus quite weak, as was already reported in the case of the effective masses.

Some excitonic effects are anticipated (but are outside the scope of this study). We can hypothesize Frenkel excitons will be observed, in view of the relatively low dielectric constants. Indeed a low value for the dielectric constant means a weak screening and, as a result, a tightly bound exciton. Based on this fact, we can deduce that the $Ba_3Si_6O_{12}N_2$ would have a somewhat more strongly bound exciton than $Ba_3Si_6O_9N_4$. The difference between quasiparticle energy gaps, previously shown to be on the order of 0.43 eV, might thus be increased when considering optical energy gaps (although the optical gaps will be smaller than the electronic gaps).

4.4 CONCLUSION BSON

The temperature-dependent luminescent properties of $Ba_3Si_6O_{12}N_2$:Eu^{2+} and $Ba_3Si_6O_9N_4$:Eu^{2+} are quite different, despite similar crystallographic structures. In order to understand whether small details, related to the coordination of the Eu ions in the two hosts, are at the heart of the different behaviour, we have performed an in-depth analysis of the electronic structure of $Ba_3Si_6O_{12}N_2$ and $Ba_3Si_6O_9N_4$.

The determination of the indirect electronic bandgaps of $Ba_3Si_6O_{12}N_2$ with state of the art G_0W_0 techniques, not subject to the well-known DFT bandgap problem, gives an electronic bandgap of 6.88 eV. This agrees with the experimental results obtained by Braun *et al.* [154] of 7.05 ± 0.25 eV. Such technique could be used for other phosphors, because it is not straightforward to experimentally evaluate bandgaps of powdered phosphor samples, often with Ce or Eu luminescent centres and (possible) unintentional impurities/defects.

Moreover, the difference in the quasiparticle bandgap between $Ba_3Si_6O_{12}N_2$ and $Ba_3Si_6O_9N_4$ as calculated with G_0W_0 correction is of 0.43 eV in agreement with the phenomenological interpretation of the quenching mechanisms according to the Dorenbos' scheme (auto-ionization).

The fact that the 5d states of barium are located closer to the conduction band minimum in the $Ba_3Si_6O_9N_4$ compounds also strengthens that argument. We also have computed the macroscopic dielectric function in the sum-over-state approximation for both materials. In addition to the straight quasiparticle band structure study, we have also analysed in detail the characteristics of (1) the valence band edge, directly linked to the nitrogen non-bonding states, two for $Ba_3Si_6O_{12}N_2$ and four for $Ba_3Si_6O_9N_4$, explaining in part the reduction of the bandgap in the latter material, (2) the conduction band edge, similarly dispersive for both materials, although the associated spatial distribution exhibits striking differences, (3) the nature of the main peak in the DOS of the conduction band, mainly made of Ba_{5d} states, however hybridizing differently in both materials, (4) the chemical shift at the different barium atomic sites, showing that the large lowering of the energy of the Ba_{5d} peak in $Ba_3Si_6O_9N_4$ with respect to $Ba_3Si_6O_{12}N_2$ is also present for the barium core states, albeit strongly reduced, and (5) the absorption spectrum in the visible-UV range and dielectric constant, showing again strong similarities in both materials, except for the the 0.43 eV energy bandgap difference.

The present study highlights that the contribution of the valence band modification cannot be neglected in the reduction of the bandgap of $Ba_3Si_6O_9N_4$ with respect to $Ba_3Si_6O_{12}N_2$. Actually, the modification of the energy difference between the luminescent level (an excited state) and the conduction band cannot be determined in the present scheme. Thus, our accurate bandstructure calculations of the host two materials may not be conclusive because the auto-ionization model (introduced in figure 0.4) seems to be the explanation for the different thermal quenching behaviour. The analysis of the europium-doped models is needed to provide the definite answer to this puzzling behaviour.

5

EUROPIUM-DOPED BSON

This chapter is dedicated to the study of europium-doped $Ba_3Si_6O_{12}N_2$ and $Ba_3Si_6O_9N_4$. Because of the numerical complexity of computing the *ab-initio* temperature dependence of such compounds using the theory developed in Part I of this thesis, we will try to validate the Dorenbos auto-ionization model by studying the electronic properties and more specifically the position of the Eu_{5d} bands with respect to the conduction band minimum (CBM) of the host crystal. The goal is to estimate the different unknown bandgaps presented in red in figure 0.5 of the introduction.

For this, a reliable europium pseudopotential is required and section 5.1 will be dedicated to such assessment. Section 5.3 presents an estimation of the Stokes shift developed in the introduction. Section 5.2 investigates the electronic properties of the five inequivalent doping sites in the two BSON compounds when relaxed to their ground-state position. The excited states properties, required to describe the absorption process, will be studied in section 5.4.1 and 5.4.2 using two methods: the core-hole and the depleted-shifted 4f approach, respectively.

The section 5.5 is dedicated to the study of the luminescence (emission) and therefore the excited state crystallographic position of section 5.4.1 and 5.4.2 needs to be relaxed in that excited electronic configuration.

Section 5.6 investigates whether the spin-orbit coupling effect is important in BSON materials.

Finally, section 5.7 is our most advanced trial to bring results of Part I in the realm of phosphor materials: the application of AHC formalism to the undoped materials using norm-conserving pseudopotentials (the AHC theory is not yet implemented within the PAW formalism in the Abinit software).

5.1 ASSESSMENT OF THE QUALITY OF THE EUROPIUM PSEUDOPOTENTIAL

One of the most severe problems of DFT is that no systematic way has been found to improve the exchange and correlation functionals[1]. This issue is particularly critical in materials in which the electrons are localized and strongly correlated, such as transition metal oxides and rare earth compounds. Various methods have been developed to extend the functional approach by adding physically relevant terms like self-interaction corrections (SIC) methods or LDA+U [45]. Europium being such a rare-earth element, we choose to use the LDA+U methodology and introduce it in the next section. The quality of our europium PAW pseudopotential is then assessed using EuO as a test case.

5.1.1 *The LDA+U methodology*

Approximation to the exchange-correlation functional such as the Local Density Approximation (LDA) or Generalized Gradient Approximation (GGA) are mean-field theories based on parametrization of (nearly) homogeneous electron gas that usually fail to describe strong Coulomb correlations. For example, both the local spin-density approximation (LSDA) and spin-polarized generalized gradient approximation (σ-GGA) fail to predict the insulating behavior of many simple transition metal oxides, producing a qualitatively wrong metallic ground state [176].

One of the methods proposed to overcome this problem is the LDA+U approach, first introduced by Anisimov and co-worker [177, 178, 179] in the nineties. The term "LDA+U" stands for methods that involve LDA- or GGA-type calculations coupled with an additional orbital-dependence of the Coulomb and exchange interaction [177, 180, 45]. The LDA+U energy functional is adapted from model Hamiltonians like the Anderson-Hubbard model [181] (the +U terminology comes from the second letter of Hubbard last name). The Anderson-Hubbard model integrates an energy penalty to the model Hamiltonian associated with adding an electron on an occupied site (with opposite spin to the existing particle in that site). The total energy penalty for a specific angular momentum l

1 Exact Kohn-Sham scheme based on perturbation theory exists but cannot be used practically, for the moment, to create an exact exchange-correlation functional. See for example Ref. [175] for such exact Kohn-Sham scheme.

from this additional coulombic repulsion between the two electrons can be given by [181]

$$U = \int |\phi_l(\mathbf{r})|^2 \frac{e^2}{|\mathbf{r}-\mathbf{r}'|} |\phi_l(\mathbf{r}')|^2 d\mathbf{r} d\mathbf{r}'. \tag{5.1}$$

Therefore the energy spectrum of this system has a gap of value U between the N- and $(N+1)$-particle states. For transition metal oxides, this gives an insulating system where the gap arises from the coulomb interaction, as expected from experiment. A sketch of the total energy profile as a function of the number of electrons in a generic atomic system is presented in figure 5.1. More information on the LDA+U methodology

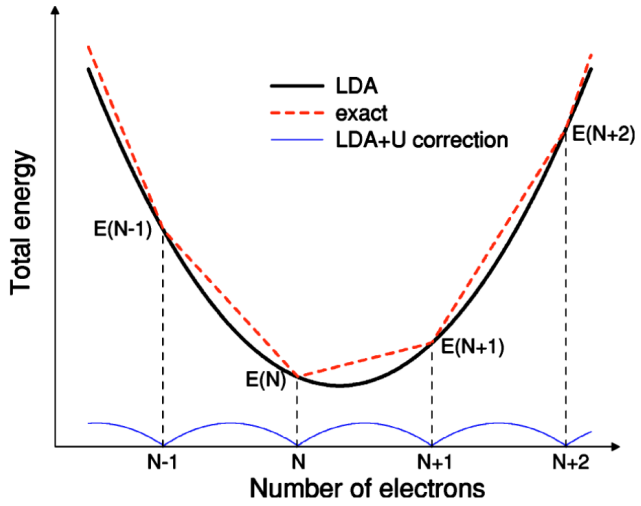


Figure 5.1: Drawing of the total energy profile as a function of the number of electrons. The LDA and the LDA+U correction yield a curve close to the exact discontinuous total energy line. The drawing is from Ref. [176].

and its different flavors can be found in section B.2 of the Annex.

5.1.2 *EuO as a test case*

For the study of the europium-doped cases, we have generated a PAW pseudopotential with the Perdew-Burke-Ernzerhof (PBE) parametrization of the generalized gradient approximation [107] for the exchange-correlation functional. The $4d^{10}5s^2\ 5p^6 4f^7 6s^2$ orbitals were taken as valence states in the PAW atomic dataset, considering the states below as frozen. The PAW sphere radius is 2.57 Bohr with 3 projectors on the s

and d occupied angular momentum channel and 2 projectors on the p and f ones. We have used the software ATOMPAW [164] to generate the europium PAW pseudopotential.

To assess the quality of this new pseudopotential, we decided to compare it against an all-electron full-potential augmented plane-wave plus local orbitals (FP-APW+lo) [182, 183] calculation as implemented in the Elk code[2] and we chose the face-centred cubic ($Fm\bar{3}m$, 225) EuO as a test case. For the Abinit calculations, a cut-off energy of 25 Ha and a 8x8x8 Monkhorst-Pack sampling of the Brillouin zone shifted four times in the (0.5,0.5,0.5),(0.5,0.0,0.0),(0.0,0.5,0.0),(0.0,0.0,0.5) directions was needed to reach a convergence on the total energy below 5 mHa/atom. The Elk calculation reached the same level of accuracy with a 6x6x6 **k**-points grid shifted once in the (0.5,0.5,0.5) direction. The muffin-tin radii of europium and oxygen are set, respectively, to $R_{MT}^{Eu} = 2.0$ a.u. and $R_{MT}^{O} = 1.45$ a.u. The basis set cut-off $R_{MT}^{Eu}|\mathbf{G}+\mathbf{k}|_{max}$ is set to be 8.

The Teter 93 [184] parametrization of LDA was used for the Elk calculation and led to a relaxed cell parameter of 9.765 Bohr with a bulk modulus of 86.04 GPa. The same lattice parameter was used for the Abinit calculation. This value is close to the experimental lattice parameter of 9.71 Bohr [185].

	Elk [eV]					Abinit [eV]			
U	gap 1	gap 2	gap3	gap 4	U	gap 1	gap 2	gap3	gap 4
6.72	0.038	0.722	1.918	2.642	6.0	0.019	0.714	2.049	2.717
7.26	0.178	0.741	1.773	2.646	6.5	0.161	0.715	1.921	2.737
7.54	0.247	0.756	1.703	2.653	7.5	0.452	0.753	1.616	2.761
8.16	0.436	0.778	1.504	2.661	8.0	0.599	0.771	1.448	2.767
9.52	0.813	0.857	1.076	2.688	8.5	0.762	0.796	1.277	2.782
10.01	0.865	0.875	1.001	2.682	9.0	0.899	0.835	1.106	2.783
10.88	1.069	0.942	0.737	2.697	9.5	1.061	0.873	0.930	2.799
13.60	1.630	1.264	0.212	2.803	10.0	1.201	0.915	0.753	2.792

Table 5.1: Values of the different bandgaps in Abinit and Elk for different values of U. The gaps obtained for a U value of 9.5 eV and 10.88 eV (Abinit and Elk) are given in figure 5.2.

Both calculations are spin-polarized but do not include spin-orbit corrections because the version 1.4.18 of Elk did not lead to the correct

2 The Elk code is an all-electron full-potential linearized augmented planewave plus local orbitals FP-LAPW+lo code, available for free at http://elk.sourceforge.net.

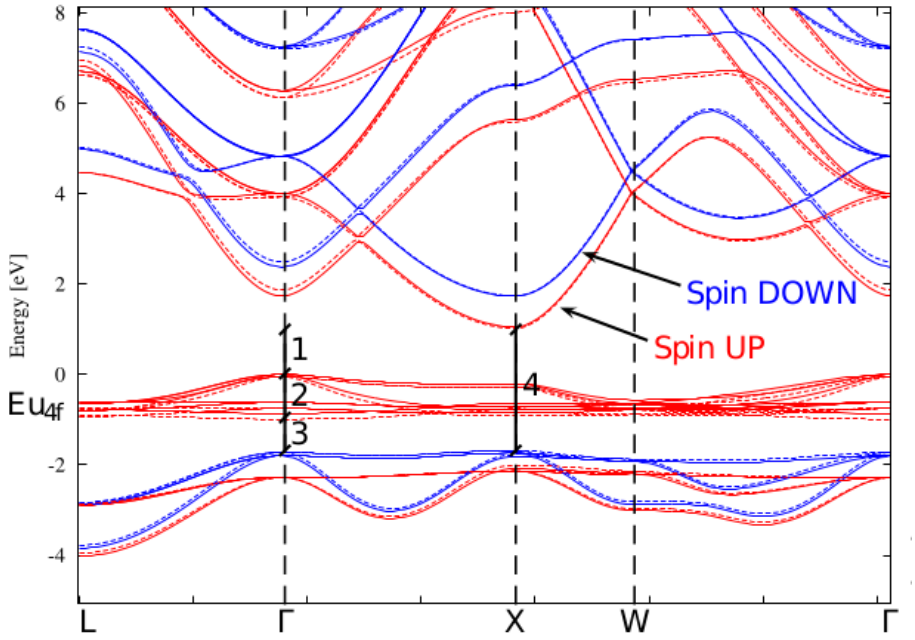


Figure 5.2: Comparison between PAW and all-electron calculation for the EuO case using Abinit (plain lines) and the Elk (dashed lines) software. The Abinit calculations are performed using PAW pseudopotential with GGA-PBE functional and the Elk ones are full-potential augmented plane-wave plus local orbitals with LDA functional. Both calculations are done using the FLL limit for the double-counting term. A U value of 9.5 eV and 10.88 eV were chosen for the Abinit and Elk software, respectively.

magnetization for such system. The 4f states of europium are localised with the LDA+U methods in the FLL limit for both software. The implementation of the LDA+U scheme in the Elk software is exemplified in Ref. [186].

We then vary the U parameter (taking J=0.1U) to fit the experimental optical gap (labelled "1" in figure 5.2) of 0.95 eV measured at ~0K [187, 188]. The table 5.1 shows that a U value of 10.88 eV and 9.5 eV reproduced this experimental gap for Elk and Abinit, respectively. The fact that the U values are different in Abinit and Elk comes from the fact that the muffin-tin spheres in Elk have different radii from the PAW sphere in Abinit.

The figure 5.2 presents the electronic bandstructure of EuO computed with Abinit (plain lines) and Elk (dashed line) with the U values mentioned above. This leads to an average difference between the two codes

for the spin up component of 0.02134 eV and 0.08525 eV for spin down, computed on 32 bands.

The agreement between our PAW pseudopotential and all-electron calculation is convincing and we have decided to use it for the more involved europium-doped BSON calculations.

5.2 EUROPIUM-DOPED BSON GROUND STATE CALCULATIONS

Chapter 4 was dedicated to the study of the two undoped BSON compounds and showed the need for studying their europium doping to understand the strong thermal quenching in $Ba_3Si_6O_9N_4:Eu^{2+}$ with respect to $Ba_3Si_6O_{12}N_2:Eu^{2+}$. When doped, the europium atom can substitute a barium one in two inequivalent positions for the $Ba_3Si_6O_{12}N_2$-$:Eu^{2+}$ case and in three inequivalent positions in the $Ba_3Si_6O_9N_4:Eu^{2+}$ case, leading to the study of five non-equivalent systems (see figure 4.2). We have studied those five cases using the Abinit software package and used the PAW GGA-PBE pseudopotentials described in section 4.2 for barium, silicon, oxygen and nitrogen. The europium pseudopotential with 27 valence electrons was validated against an all-electron code and described in the previous section.

This being said, we have performed structural relaxation of the five europium-doped compounds on a 4x4x4 Monkhorst-Pack sampling [101] of the Brillouin zone half-shifted along the z direction. Energy cut-off of 30 Ha and 35 Ha on the planewave basis set were used for the two europium-doped $Ba_3Si_6O_{12}N_2$ and the three europium-doped $Ba_3Si_6O_9$-N_4 situations, respectively.

This structural relaxation leads to the relaxed lattice parameters of $a = 14.273$ Bohr and $c = 12.381$ Bohr for $Ba_3Si_6O_{12}N_2:Eu_1$ where Eu_1 is the position surrounded by 6 oxygen atoms, following the convention adopted in figure 4.2. The other non-equivalent substitution position leads to lattice parameters of $a = 14.346$ Bohr and $c = 12.204$ Bohr for $Ba_3Si_6O_{12}N_2:Eu_2$. The europium-doped structures are contracted with respect to the undoped compounds. This seems reasonable given that the experimental atomic radius of europium is 185 pm, smaller than the 215 pm atomic radius of barium [189]. The relaxed values for the europium-doped $Ba_3Si_6O_9N_4$ compounds are $a = 13.755$, 13.806, 13.736 Bohr and $c = 12.939$, 12.789, 12.925 Bohr for the Eu_1, Eu_2 and Eu_3 substitutions, respectively. The selected bond lengths of the five inequivalent europium-doped cases are presented in table B.1 and have to be compared with the selected bond lengths of the two undoped com-

pounds taken from table 4.1. As expected, we can see a rather strong contraction of the bonds around the substituted europium atoms (colored in red in the table). The overall cell volume is contracted by 1.5% and 1.9% with respect to the undoped case for the Eu_1 and Eu_2 substitution in $Ba_3Si_6O_{12}N_2$. An equivalent contraction of 1.5%, 1.9% and 1.8% happens for Eu_1, Eu_2 and Eu_3 in $Ba_3Si_6O_9N_4$, respectively.

Unfortunately, the use of the 27 valence electrons pseudopotential for europium also bears along quite an additional computational cost. Indeed, the description of the 4f orbitals means that the simulations have to be spin-polarized. To overcome this limitation, we have created another pseudopotential with only 10 valence electrons ($5s^2 5p^6 6s^2$) where the $4d^{10}$ and $4f^7$ orbitals have been considered as frozen in the core of the pseudopotentials. We have used the same ATOMPAW input parameters as for the 27 electrons pseudopotential described in section 5.1.2 except for the change of valence to core state for the d and f orbitals. The structural unpolarized DFT relaxation using such 10 electrons pseudopotential is calculated to be $a = 14.139$ and $c = 12.329$ Bohr for the Eu_1 substitution of $Ba_3Si_6O_{12}N_2$ and $a = 14.316$ and $c = 11.985$ Bohr for the Eu_2 ones. The relaxed values for the europium-doped $Ba_3Si_6O_9N_4$ compounds are $a = 13.659$, 13.774, 13.618 Bohr and $c = 12.863$, 12.570, 12.814 Bohr for the Eu_1, Eu_2 and Eu_3 substitutions, respectively. These lattice parameters are below 2% away from the one computed with the 27 electrons pseudopotential. The selected bond lengths of the five inequivalent europium-doped cases are presented in table B.2.

The electronic bandstructure of the five europium-doped compounds were computed at the relaxed atomic positions using the 10 electrons pseudopotential and are shown on figure B.5.

The $\mathbf{A} - \mathbf{\Gamma}$ bandgaps have a value of 4.566 eV (4.596 eV for $\mathbf{\Gamma} - \mathbf{\Gamma}$) and 4.765 eV (4.870 eV for $\mathbf{\Gamma} - \mathbf{\Gamma}$) for $Ba_3Si_6O_{12}N_2$:Eu_1 and $Ba_3Si_6O_{12}N_2$:Eu_2, respectively. The $\mathbf{M} - \mathbf{\Gamma}$ gaps are 4.245 eV (4.499 eV for $\mathbf{\Gamma} - \mathbf{\Gamma}$), 4.421 eV (4.616 eV for $\mathbf{\Gamma} - \mathbf{\Gamma}$) and 4.323 eV (4.670 eV for $\mathbf{\Gamma} - \mathbf{\Gamma}$) for the three $Ba_3Si_6O_9N_4$ substitutions.

From the five electronic bandstructures, it is clear that the 5d electrons of europium are not correctly localized inside the bandgap of the host material, in contradiction to both the 5d-4f crossing decay model and the Dorenbos auto-ionization model presented in the introduction of this thesis. This is not an uncommon result and has been also acknowledged for example by Tang *et al.* [190]. In their publication, they studied the $Ba_3Si_6O_{12}N_2$:Eu^{2+} crystal and have also shown that within the GGA+U (as implemented within the CASTEP code [191]) framework,

the 5d states were lying much higher in energy than the bandgap of the host material.

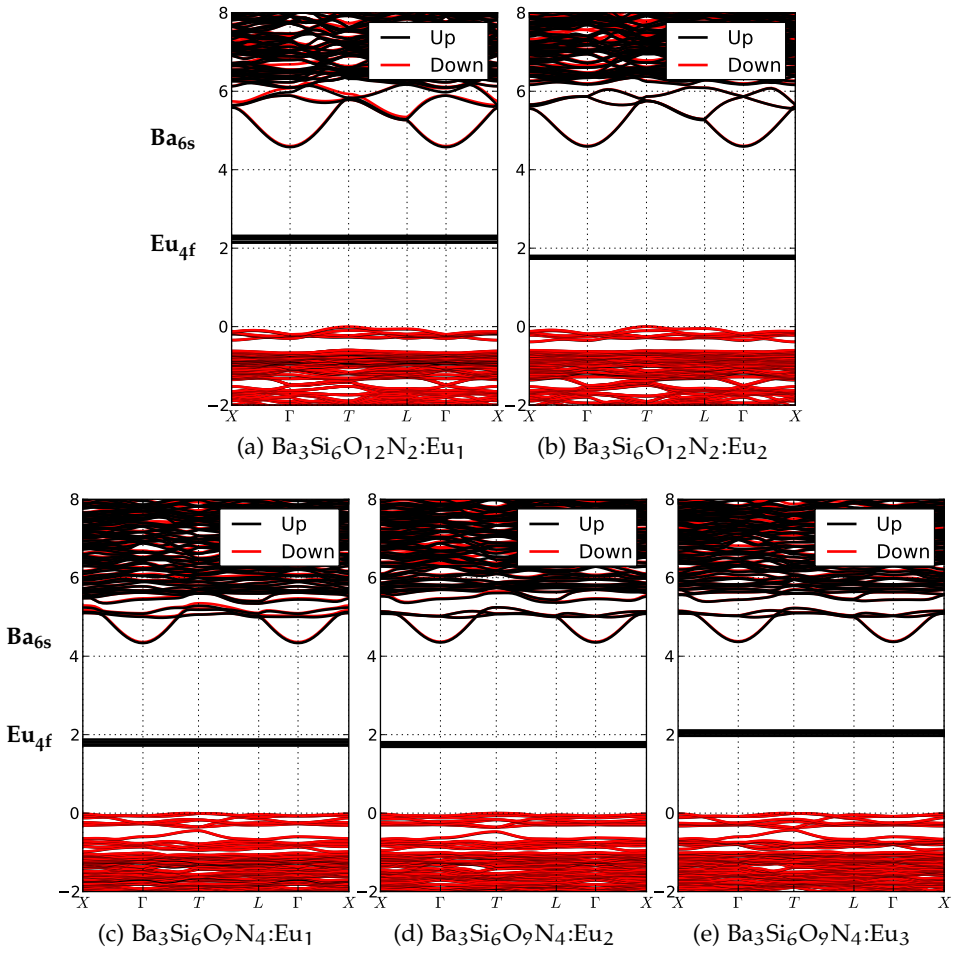


Figure 5.3: **[GS]** The ground-state electronic bandstructure of the europium-doped elements are computed at the *ab-initio* relaxed parameter with the 10 valence electrons pseudopotential in the rhombohedral supercell. The black line shows the spin up component and the red line the spin down.

To conclude this section, we will investigate the effect of reducing the doping concentration. The doping concentration in the above-mentioned primitive cells is 33% (one of the three barium is replaced by an europium) whereas the experimental doping for such compounds is between 2 to 10% [154]. An europium-doping concentration of 11% could be obtained by using a rhombohedral supercell that is three times larger than the primitive cell. The structural relaxation of these supercells are

extremely computationally demanding due to the large configurational space and took months on recent supercomputers (~75k cpu hours per compounds). Such relaxation could therefore only be done for this 10 electrons pseudopotential and not for the 27 electrons ones.

The relaxation leads to a lattice parameter of 18.900 Bohr with a rhombohedral angle of 81.889° for $Ba_3Si_6O_{12}N_2$:Eu_1 and a lattice parameter of 18.882 Bohr with a rhombohedral angle of 82.456° for $Ba_3Si_6O_{12}N_2$:Eu_2. The three europium substitution Eu_1, Eu_2 and Eu_3 in $Ba_3Si_6O_9N_4$ have lattice parameters that are calculated to be 18.894 Bohr, 18.870 Bohr and 18.878 Bohr with rhombohedral angles of 78.371°, 78.680° and 78.339°.

As seen on table 5.2, the rhombohedral total energy of $Ba_3Si_6O_{12}N_2$:Eu_1 is 0.145 eV lower than in $Ba_3Si_6O_{12}N_2$:Eu_2. This means that the europium atom will preferably substitute the barium that is octahedrally surrounded by six oxygen atoms. Indeed, as seen on table B.2, the Ba-O bond lengths are smaller at this site than in the other non-equivalent sites. As a result, the europium substitution will naturally go inside the smaller site that will generate the least distortion of the global crystal. As a matter of fact, we will see later in this thesis that the luminescent active center is indeed $Ba_3Si_6O_{12}N_2$:Eu_1.

For the other BSON compound, $Ba_3Si_6O_9N_4$:Eu_3 has the lowest energy with a 0.063 eV lower than $Ba_3Si_6O_9N_4$:Eu_1, which has the second lowest energy. This energy difference is rather small and amounts to 1.453 kcal/mol which is above the chemical accuracy of 1 kcal/mol but can still be considered rather close. It is therefore somewhat difficult to discuss the stability of the three substitutions and we will see later that the only luminescence center occurs in $Ba_3Si_6O_9N_4$:Eu_1.

The rhombohedral supercell electronic bandstructures, computed at these relaxed ground-state lattice parameters, are shown on figure B.6. The $\mathbf{T}-\mathbf{\Gamma}$ bandgap is 4.587 eV and 4.596 eV with an additional 0.197 eV and 0.184 eV for the $\mathbf{\Gamma}-\mathbf{\Gamma}$ bandgap of the Eu_1 and Eu_2 substitution of $Ba_3Si_6O_{12}N_2$, respectively. The $\mathbf{T}-\mathbf{\Gamma}$ bandgaps in $Ba_3Si_6O_9N_4$ are calculated to be 4.342 eV, 4.354 eV and 4.478 eV with an additional 0.072 eV, 0.068 eV and 0.084 eV for the Eu_1, Eu_2 and Eu_3 substitution, respectively. Those bandgaps are very close to the primitive cell ones (within ~3%) as expected. Equally expected, there are 6 valence nitrogen bands, three times more than the primitive cell shown on figure B.5.

Keeping in mind that our goal is to provide quantitative first-principles based answer to the unknown gaps presented in figure 0.5 of the introduction, we would like to describe the 4f states as well. To do that, we have performed another rhombohedral electronic bandstructure cal-

culation with the 27 electrons pseudopotential but at the lattice and atomic position obtained with the 10 electrons pseudopotential. The electronic bandstructure of the five ferromagnetic ($7\mu_B$) europium-doped compounds were computed using spin-polarized GGA+U calculation by applying a U value of 7.5 eV and a J value of 0.6 eV on the 4f states only. They are shown on figure 5.3. The only purpose of these two fitting parameters U and J are to localize the 4f states enough so that they lie within the bandgap of the host materials, as expected from experiment. We have checked that significant deviation ($\pm 1eV$) around the U value had no noticeable effect on all the other bands.

The electronic bandstructure corresponding to the absorption of light is the one obtained by making an electronic bandstructure calculation at the relaxed atomic position computed here and by promoting one of the seven electrons from the 4f band to the 5d conduction band. The natural way to achieve this goal is by solving the Bethe-Salpeter equation (BSE) [23] that correctly treats the electron-hole interaction in a many-body framework. Unfortunately, such a refined theory is computationally out of reach. We therefore have used an alternative schemes to try to reproduce such result at a cheaper computational cost. This scheme is called the core-hole approach and will be described in section 5.4.1.

Finally, the electronic structure corresponding to the luminescence process (emission) is obtained by letting the atomic position and/or lattice parameters relaxed in their excited state. This will be presented in section 5.5.

5.3 STOKES SHIFT

The Stokes shift, named after Irish physicist George G. Stokes, is *the difference (in wavelength or frequency units) between positions of the band maxima of the absorption and emission spectra (fluorescence and Raman being two examples) of the same electronic transition* [192]. When a system absorbs a photon, it increases its energy and goes into an excited state. This excited system can relax by emitting a photon or through vibrations (heat energy losses). If the emitted photon has less energy than the absorbed one, this energy difference is called the Stokes shift.

In our case, the Stokes shift is the energy difference between the center of Eu^{2+} 4f→5d absorption peak and the 5d→4f emission peak at the excited state atomic coordinate [193]. This can be seen using the single configurational coordinate model depicted in figure 5.4. This diagram shows the total energy (electronic and ionic) of the BSON compounds

	Total energy of the hexagonal primitive cell [Ha]				
	$Ba_3Si_6O_{12}N_2$:Eu^{2+}		$Ba_3Si_6O_9N_4$:Eu^{2+}		
Case	Eu_1	Eu_2	Eu_1	Eu_2	Eu_3
GS	−604.320 652	−604.308 028	−575.846 798	−575.847 903	−575.851 566
Exc	−609.685 594	−609.543 707	−581.204 068	−581.188 567	−581.198 239
Exc*	−609.691 848	−609.647 431	−581.220 338	−581.219 972	−581.233 987
GS*	−604.313 463	−604.284 122	−575.828 274	−575.799 952	−575.802 215
ΔE^{stokes}	2950 cm^{-1}	28011 cm^{-1}	7636 cm^{-1}	17416 cm^{-1}	18677 cm^{-1}
$\Delta E^{stokes*}$	3156 cm^{-1}	5247 cm^{-1}	8131 cm^{-1}	21048 cm^{-1}	21663 cm^{-1}
	Total energy of the rhombohedral supercell [Ha]				
GS	−2408.536 901	−2408.531 555	−2323.139 501	−2323.138 339	−2323.141 829
Exc	−2406.826 520	−2406.801 030	−2321.443 511	−2321.439 384	−2321.451 666
Exc*	−2406.844 042	−2406.818 158	−2321.460 989	−2321.456 574	−2321.469 623
GS*	−2408.493 067	−2408.495 914	−2323.098 646	−2323.101 977	−2323.103 974
ΔE^{stokes}	13466 cm^{-1}	11581 cm^{-1}	12803 cm^{-1}	11753 cm^{-1}	12249 cm^{-1}
$\Delta E^{stokes*}$	19241 cm^{-1}	15644 cm^{-1}	17933 cm^{-1}	15961 cm^{-1}	16616 cm^{-1}
ΔE^{exp}	2790 cm^{-1}		3230 cm^{-1}		

Table 5.2: Total energy of the different cases reported on figure 5.4. The Stokes shift ΔE^{stokes} is computed using Eq. (5.2) and $\Delta E^{stokes*}$ using Eq. (5.3). For the hexagonal primitive cell, the 10 electrons pseudopotential for europium is used both to compute the relaxed atomic positions and the total energy while for the rhombohedral supercell, the 10 electrons pseudopotential is used to compute the relaxed atomic positions but the total energy is computed with the 27 electrons pseudopotential. The experimental Stokes shifts are from Refs [5, 9]. More information is available in the text.

with the Eu^{2+} in their ground state (curved labeled "4f") and the BSON compounds with the Eu^{2+} in their first excited state (labelled "5d"), as a function of the generalized configurational coordinate X. This coordinate is made of any relevant combination of ionic degrees of freedom of the BSON system. The horizontal lines in the 4f and 5d curves indicates allowed phonon states of the system.

The fact that the equilibrium configuration of the BSON system depends on the state (ground-state or excited) of the electronic configuration of the compounds is represented by the two equilibrium configurations X_0 and X_0^*. After the rapid (~0.1 fs) excitation of the europium ion, $E_0 \rightarrow E_1$, the system will be out of thermal equilibrium and will relax quickly (~1 ps) from configuration X_0 toward X_0^*.

The system will then undergo a radiative transition from $E_2 \rightarrow E_3$. This transition occurs on a longer time scale (~>1 ns) that allows the

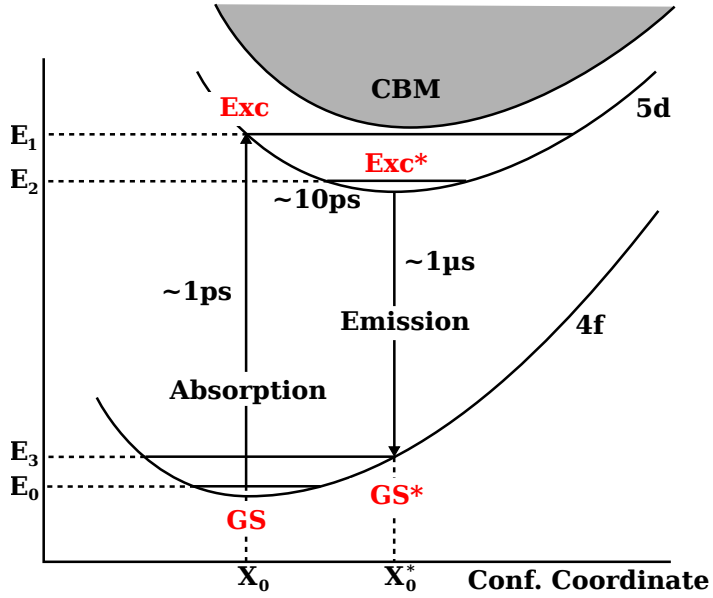


Figure 5.4: Single configurational diagram where the different cases (ground-state (GS), excited-state (Exc), excited-state at relaxed atomic position (Exc*) and ground-state at the relaxed excited atomic position (GS*)) treated in this chapter are presented.

ions to move in this excited state. It is nonetheless usually admitted that such a time scale is not long enough to have a change of the full lattice parameters (the crystal volume will stay almost constant).

Finally, after the radiative transition, the system will be once again out of thermal equilibrium in E_3 and relax from X_0^* back to the initial configuration X_0. From this global process, the Stokes shift is

$$\Delta E^{\text{stokes}} = (E_1 - E_0) - (E_2 - E_3). \tag{5.2}$$

Since the *ab-initio* excited state calculations have additional approximations with respect to the ground-state ones, we can use an approximated formula that does not use these states and assume that the ground state and excited state parabola have the same curvature

$$\Delta E^{\text{stokes*}} = 2(E_3 - E_0). \tag{5.3}$$

We have already studied the GS in section 5.2 and will now study the other three cases in the two next sections.

Before studying in detail all the different cases using the Abinit software, we will estimate the Stokes shift for the five non-equivalent BSON substitutions. The total energy of the different cases, computed with

Abinit after structural relaxation, are reported together with the Stokes shift in table 5.2.

As mentioned in the introduction of the thesis, the experimental Stokes shifts for $Ba_3Si_6O_{12}N_2$:Eu^{2+} and $Ba_3Si_6O_9N_4$:Eu^{2+} are 2790 cm^{-1} and 3230 cm^{-1}, respectively. As can be seen on table 5.2, the calculated Stokes shift overestimate the experimental one quite substantially. At this stage (we will come back to it later), it is difficult to discuss the comparison of our theoretical results with the experimental ones.

5.4 EUROPIUM-DOPED EXCITED STATE CALCULATIONS

The absorption process occurs through the Eu^{2+} parity-allowed electronic dipole transition ($4f^7 \rightarrow 4f^6 5d^1$). The excited electron goes from a very spatially localized 4f states to a more delocalized 5d level. Since the 5d are more delocalized, they will react more strongly to the electric field of the point charges around the europium atom. If the negative charges around the europium atom were spherically symmetric, all the five orbitals would be equally affected. In a real crystal, this is never the case since the negative charges occupy specific positions. As already mentioned previously, the substitutional Eu_1 atom in $Ba_3Si_6O_{12}N_2$ is surrounded by six oxygen atoms that form an octahedron (O_h point group). The substitutional Eu_2 atom is surrounded by six oxygen atoms and a nitrogen atom that form a monocapped octahedron (C_{3v} point group).

In the case of the octahedral position of the charges around the europium atom, there is a splitting of the d levels into a doublet E_g (d_{z^2} and $d_{x^2-y^2}$ orbitals) and a triplet T_{2g} (d_{xy}, d_{yz} and d_{xz} orbitals). The E_g and T_{2g} refer to symmetry associated with the orbitals. The E and T mean a doubly or triply degenerated representation and g means an even (from the German *gerade*) parity of the wavefunction through an inversion centre. Finally, the 2 refers to the fact that the orbital is symmetric with respect to a C_2 axis perpendicular to the highest symmetry axis.

For the monocapped octahedron case, there is a splitting of the d levels into one singlet with A_1 symmetry (d_{z^2}) and two doublet with E symmetry (d_{xy} and d_{yz} for the first doublet, d_{xz} and $d_{x^2-y^2}$ for the second). The A symmetry denotes that the wavefunction is symmetrical upon a rotation of the principal axis and the index 1 refers to the fact that the wavefunction has an even parity upon mirror reflection.

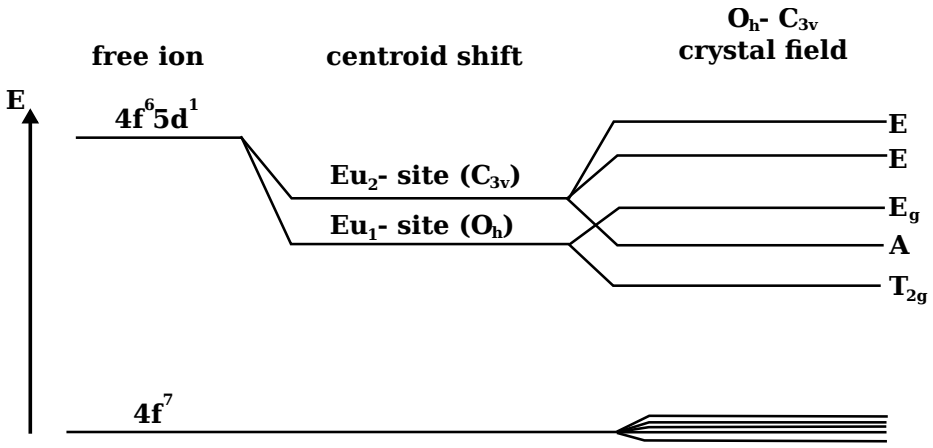


Figure 5.5: Schematic (adapted from Ref. [194]) of the Eu_{5d} level splitting due to the crystal field of the two inequivalent substitutions in the $Ba_3Si_6O_{12}N_2$:Eu^{2+} compound. The centroid shift is the barycentre of the slitted states.

A schematic drawing of this splitting is provided on figure 5.5. Since group theory does not provide information about the value of the energy difference between split levels or the order of the levels, we decide to order them according to the result of the *ab-intio* calculations made in section 5.4.1 (the A_1 band has lower energy). As will be seen in the next section, the substitutional Eu_1 atom in $Ba_3Si_6O_{12}N_2$ is not exactly surrounded by atoms that preserve the octahedral symmetry (long ranged interactions with other atoms, positioned around the oxygen cage). Therefore this substitution also shows C_{3v} point group symmetry and therefore leads to one A_1 and two doubly degenerate E states.

The case of $Ba_3Si_6O_9N_4$:Eu^{2+} is rather similar. If we take the closest atom around the europium substitution, the Eu_1 and Eu_3 are surrounded by an oxygen octahedron and the Eu_2 by a monocapped octahedron. Due to atoms located slightly further, the pure octahedral symmetry is lost and the three cases have C_{3v} point group symmetry with A_1 and two doubly degenerate E states.

5.4.1 *The core-hole approach*

The idea of the so-called "core-hole" approach is to mimic the effect of a core-hole interaction (exciton) through the creation of a pseudopotential where the 4f electrons are frozen in the core state with a hole. This means that one electron from the 4f core states was removed and that a unitary

homogeneous negative charge must be added during the calculation to preserve charge neutrality. Such a pseudopotential was generated by X. Gonze using ATOMPAW [164] with the same input parameters as for the previously used PAW GGA-PBE pseudopotentials (also including the 4d states as core states to lower the computational cost of such pseudopotential). This new PAW atomic dataset has the following valence states: $5s^2 5p^6 6s^2$ but is different from the 10 electrons pseudopotential presented in section 5.2 as one 4f core electron is removed from the pseudopotential.

Such core-hole approach is not new and has been used by other groups to estimate the effect of core-hole interaction (see for example Ref. [195]). As a matter of fact, the core-hole approach is an approximation to the BSE. Indeed, without going too deep into the detail of the BSE (for that, see for example the review of G. Onida *et al.* [23]), the key quantity to compute the two-particle excited-states is the polarizability L

$$L(1234) = L_0(1234) + L_0(1256)\Xi(5678)L(7834), \tag{5.4}$$

where L is the four-point polarization and L_0 is the independent particle polarizability. Also, the Bethe-Salpeter kernel Ξ contains the electron-hole exchange contribution v and the electron-hole attraction $-W$

$$\Xi(5678) = v(57)\delta(56)\delta(78) - W(56)\delta(57)\delta(68), \tag{5.5}$$

where the associated graphical representation in terms of Feynman diagram is given in figure 5.6.

As seen in Eq. (5.4), the Bethe-Salpeter kernel Ξ is made of two terms that can be written, within the Tamm-Dancoff approximation where only positive energy electron-hole pairs (vc), $(v'c')$ contributes [196], as a non-screened exchange repulsion term (here written in the transition space with the factor "2" due to spin degeneracy)

$$v_{(vc\mathbf{k})(v'c'\mathbf{k})} = \frac{2}{V}\sum_{\mathbf{G}\neq 0} v(\mathbf{G})\left\langle \Psi_{c\mathbf{k}}\middle| e^{i\mathbf{G}\cdot\mathbf{r}}\middle|\Psi_{v\mathbf{k}}\right\rangle\left\langle \Psi_{v'\mathbf{k}'}\middle| e^{-i\mathbf{G}\cdot\mathbf{r}}\middle|\Psi_{c'\mathbf{k}'}\right\rangle, \tag{5.6}$$

where $v = \frac{4\pi}{|\mathbf{G}^2|}$ is the bare Coulomb interaction, v denotes the valence bands and c the conduction ones. The second term in the Bethe-Salpeter kernel describes the electron and hole interaction through a screened Coulomb attraction interaction

$$W_{(vc\mathbf{k})(v'c'\mathbf{k})} = \frac{2}{V}\sum_{\mathbf{G}_1\mathbf{G}_2} W_{\mathbf{G}_1\mathbf{G}_2}(\mathbf{q}) \left\langle \Psi_{v'\mathbf{k}'}\middle| e^{i(\mathbf{q}+\mathbf{G}_1)\cdot\mathbf{r}}\middle|\Psi_{v\mathbf{k}}\right\rangle\left\langle \Psi_{c\mathbf{k}}\middle| e^{-i(\mathbf{q}+\mathbf{G}_2)\cdot\mathbf{r}}\middle|\Psi_{c'\mathbf{k}'}\right\rangle\delta_{\mathbf{q},\mathbf{k}-\mathbf{k}'}, \tag{5.7}$$

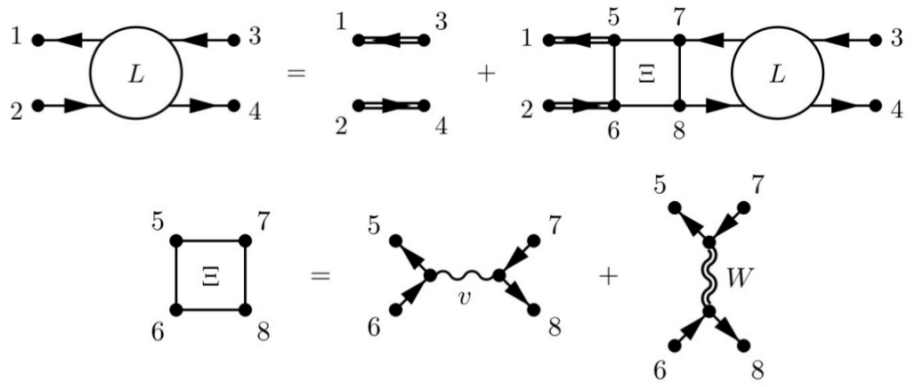


Figure 5.6: The Bethe-Salpeter equation (BSE) in terms of Feynman diagrams. The Bethe-Salpeter kernel Ξ is the sum of a bare exchange repulsion term and a screened Coulomb interaction. Courtesy of M. Gatti (TDDFT school).

where $W_{G_1G_2}(\mathbf{q}) = \frac{4\pi\varepsilon^{-1}_{G_1G_2}(\mathbf{q})}{|\mathbf{q}+\mathbf{G}_1||\mathbf{q}+\mathbf{G}_1|}$ is the screened Coulomb interaction and $\varepsilon^{-1}_{G_1G_2}(\mathbf{q})$ the inverse dielectric constant.

This second term is correctly accounted for in the core-hole technique because the change of the electronic potential resulting from the hole in the pseudopotential is computed self-consistently within DFT (screened electron-hole interaction). In contrast, the exchange term V_{xc} within DFT is only a one-point function and therefore does not have the good form to reproduce the four-point kernel function of the BSE.

To evaluate the crudeness of the core-hole approach, we have performed a BSE calculation on the $Ba_3Si_6O_{12}N_2$:Eu_1 compounds only, using a modified version of Abinit[3] that neglects the screened Coulomb term and only computes the exchange one. This calculation showed that the effect of the exchange could be as large as 0.25 eV but the lowest transitions are nearly unaffected (0.02 eV). This result was considered satisfactory and validates the core-hole approach.

Firstly, we decided to make an europium-doped calculation at the undoped lattice parameters and atomic positions to be able to compare the bandstructures with the undoped ones. Additionally, we have computed the G_0W_0 corrections to the DFT eigenenergies using the same convergence criteria and energy-dependent polynomial fit to the G_0W_0 eigenenergies as described in section 4.2.

3 This modified version is a courtesy of M. Giantomassi, to whom we are indebted.

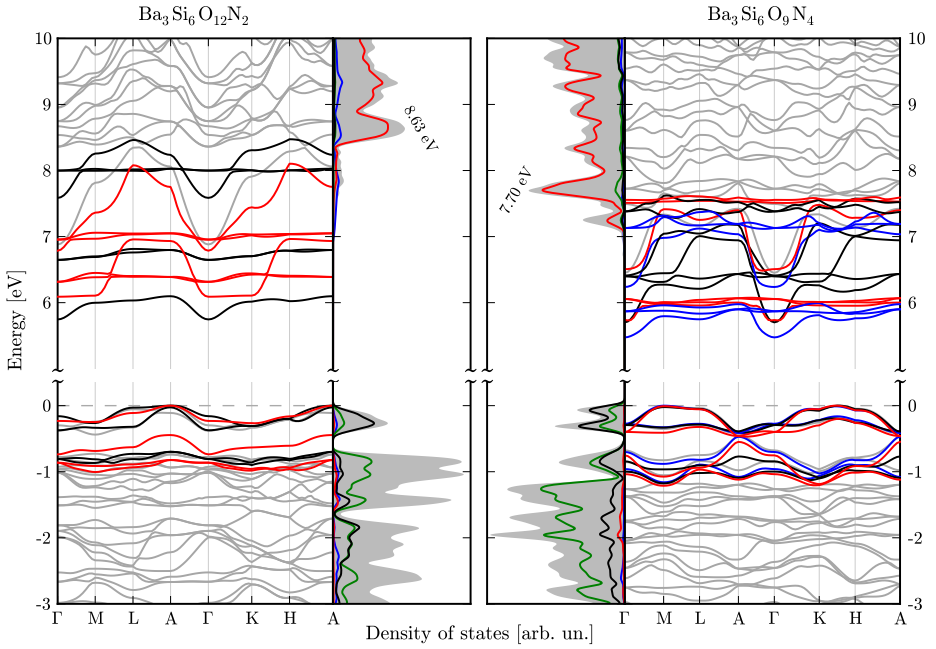
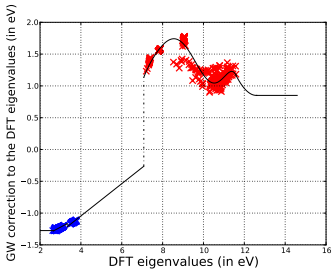


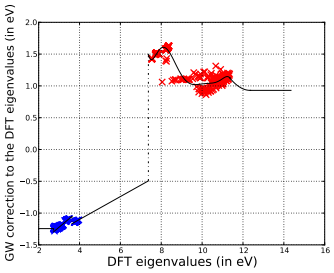
Figure 5.7: **[Exc]** G_0W_0 electronic bandstructures of the $Ba_2Si_6O_{12}N_2$ and $Ba_2Si_6O_9N_4$ compounds as well as the doped ones in the core-hole approach. All the calculations are made at the undoped relaxed lattice parameters. The grey lines correspond to the undoped cases, the black lines correspond to the $Ba_3Si_6O_{12}N_2$:Eu_1 and $Ba_3Si_6O_9N_4$:Eu_2 cases, the red lines to the $Ba_3Si_6O_{12}N_2$:Eu_2 and $Ba_3Si_6O_9N_4$:Eu_3 cases, finally the blue lines correspond to the $Ba_3Si_6O_9N_4$:Eu_1.

We happily found out that the core-hole methods correctly localized the 5d state inside the bandgap of the host materials. The resulting bandstructure can be seen on figure 5.7 along with the undoped cases (grey lines), already presented in figure 4.3. The different energy polyfits used to make the five bandstructures are presented in figure 5.8.

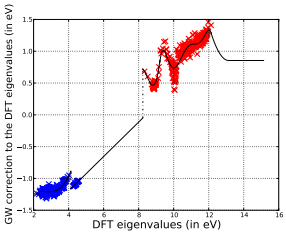
The black G_0W_0 bandstructures in figure 5.7 correspond to the $Ba_3Si_6O_{12}N_2$:Eu_1 and $Ba_3Si_6O_9N_4$:Eu_2 cases, the red lines to the $Ba_3Si_6O_{12}N_2$:Eu_2 and $Ba_3Si_6O_9N_4$:Eu_3 cases and finally the blue lines correspond to the $Ba_3Si_6O_9N_4$:Eu_1 case. The exact G_0W_0 band positions as well as their DFT values are given in table B.3 using the same color code. A first important result that we can draw from this sets of bandstructures is the fact that $Ba_3Si_6O_{12}N_2$:Eu_1 and $Ba_3Si_6O_9N_4$:Eu_1 seem to have the lowest 5d state and therefore be the luminescence centers. From the introduction and specifically figure 0.3, it was experimentally expected from the rather small FWHM that both compounds only had one luminescence center.



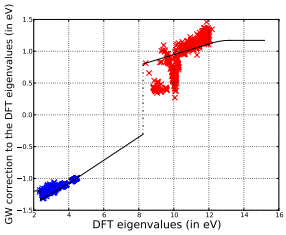
(a) $Ba_3Si_6O_{12}N_2$:Eu_1.



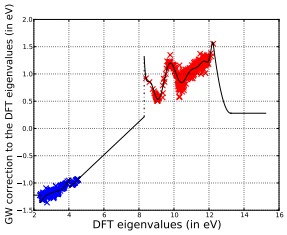
(b) $Ba_3Si_6O_{12}N_2$:Eu_2.



(c) $Ba_3Si_6O_9N_4$:Eu_1.



(d) $Ba_3Si_6O_9N_4$:Eu_2.



(e) $Ba_3Si_6O_9N_4$:Eu_3.

Figure 5.8: The different energy polyfit used for the europium-doped electronic band-structure of figure 5.7.

Some experimentalists hypothesized that the $Ba_3Si_6O_{12}N_2$:Eu_2 case might be the luminescent one due to its proximity to a nitrogen atom. This prediction relies on the conventional idea that oxynitride/nitride materials may be advantageous for long wavelength excitations (by blue or nUV light) owing to their stronger covalency than ordinary oxides. It is believed that the strong covalency due to ligand N^{-3} ions may induce large centroid shift of the 5d levels. A large centroid shift is related to a strong nephelauxetic effect or in other word a strong electronic cloud expansion. Actually, as shown by M. Mikami and N. Kijima [174], the meaning of "covalency" is rather vague due to the lack of a quantitative definition and having strong covalent bonds does not necessarily mean having a large electronic cloud expansion.

Confirming the findings of M. Mikami and N. Kijima, the first set of *ab-initio* core-hole calculations made here seems to point out that the position of the Eu_{5d} states are strongly dependent on the Eu-O bond length: the closer the oxygen atoms, the stronger the potential felt by the europium. The Eu_{5d} bands are higher in energy in the $Ba_3Si_6O_{12}N_2$:Eu_2 case because the nitrogen tends to repel the oxygen atoms.

Concerning the effect of the doping concentration, we first studied a 1x1x2 supercell (17% doping) at the undoped relaxed atomic position

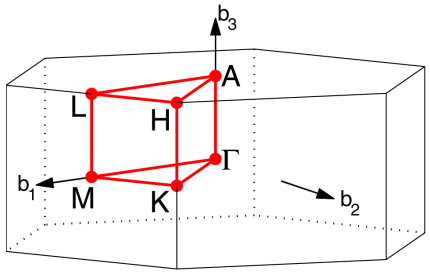


Figure 5.9: Brillouin zone of the hexagonal lattice with the **Γ-M-L-A-Γ-K-H-A** high symmetry path highlighted.

and the associated electronic bandstructures are shown on figure B.7. From these calculations, we make the following observations:

- the Eu_{5d} bands flatten with respect to the primitive cell calculation.
- The correct folding behavior of the supercell is observed (e.g. the segment A-L of the primitive cell figure 5.7 is correctly folded in Γ-M taking into account slight changes due to the change of europium concentration, also see the Brillouin zone of the hexagonal lattice figure 5.9 for more information).
- There are only two nitrogen bands at the valence band level in the 1x1x2 supercell. These two nitrogen bands are the one located far from the europium atom and therefore do not feel it. The other two bands close to the europium atom are deeper in energy in the valence bands. This explains why the valence band to Eu_{5d} gap appears to decrease in the supercell calculation.
- The increased gap between the Eu_{5d} states and the bottom of the conduction band could be explained by the fact that the electrons in the conduction states feel an average periodic potential from the europium atoms that interact with each other in the primitive cell. In the supercell calculations, the europium atoms are further apart and this generates a larger energy difference and therefore experience a stronger potential.

The second natural step is to make the core-hole calculations at the europium-doped ground-state relaxed lattice parameters and atomic positions as described in the previous section 5.2.

These calculations lead to the electronic bandstructures presented in figure B.8. With respect to the calculations made at the host atomic position, the fact that the Eu_{5d} states in $Ba_3Si_6O_{12}N_2$:Eu_1 are lower in

energy than $Ba_3Si_6O_{12}N_2$:Eu_2 is less clear. We hypothesized that this could be due to the too high doping.

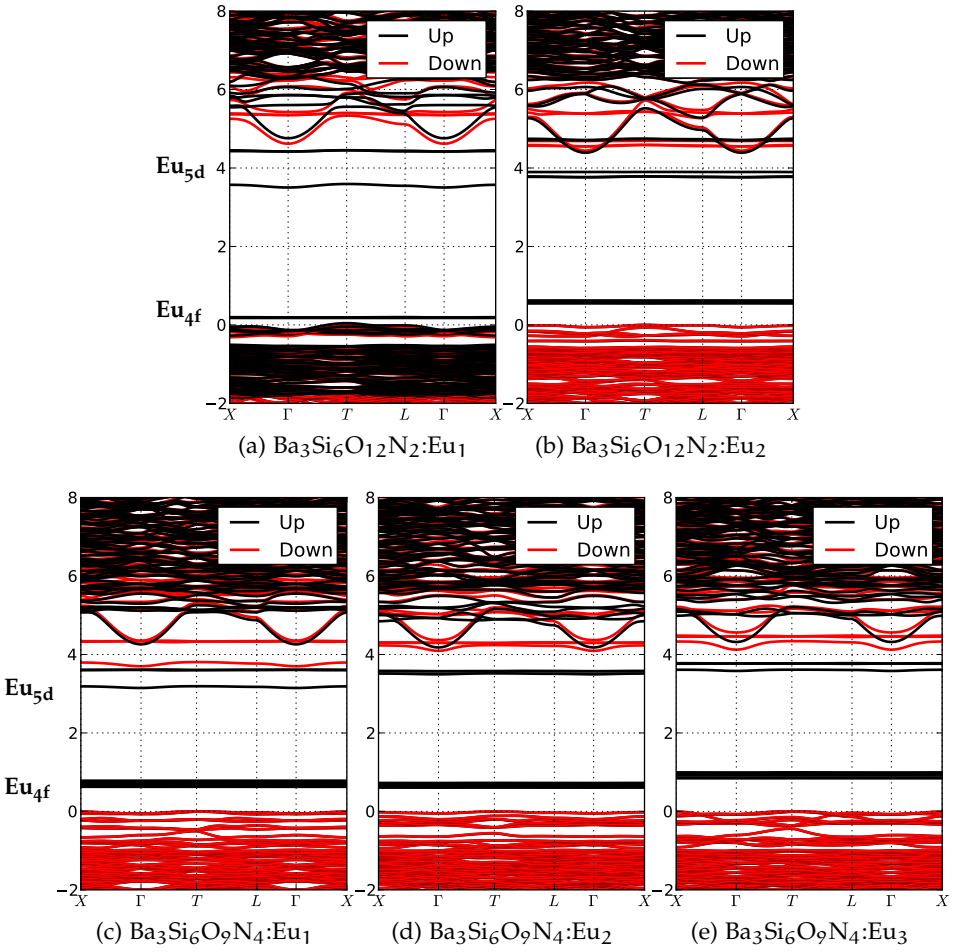
We therefore decided here to make a rhombohedral supercell calculation (11% doping). The advantage of such a supercell is that the europium is far from any other europium replica (in opposition to a 1x1x2 supercell). The corresponding electronic bandstructures are presented on figure B.9 where the two luminescent centers can be clearly identified (the two Eu_1 doped compounds). We therefore deduced that indeed the fact that Eu_{5d} had almost the same energy in $Ba_3Si_6O_{12}N_2$:Eu_1 and $Ba_3Si_6O_{12}N_2$:Eu_2 in figure B.8 was due to the too high doping. We also observed the expected flattening of the Eu_{5d} bands within the rhombohedral supercell and the expected number of nitrogen bands at the valence band level (three times more than the primitive case).

One of the main drawbacks from the core-hole approach is the fact that we loose all the information about spin. Due to the ferromagnetic nature of the europium-doped BSON compounds, such description might be important.

5.4.2 *The depleted-shifted* 4f *approach*

As done in section 5.2, we can use the pseudopotential with 27 valence electrons and a GGA+U methodology with the same value and compute the electronic bandstructure with the relaxed lattice and atomic parameters of the ground-state with the 10 electrons pseudopotentials. Since we now treat the 4f states explicitly in the calculations, we can remove one of the seven electrons from the 4f states and place it in the Eu_{5d} state. This approach is based on constrained DFT (CDFT) that has been applied successfully to a wide range of materials [197, 198, 199, 200]. The idea behind CDFT is that we can create a density functional with a given desired constrain on the charge density (like localizing an electron in a particular orbital). Such constrain can be obtained by introducing an appropriate external potential in the Kohn-Sham equations [201]. For rare-earth doped solid-state compounds, the group of Canning were the first to use successfully CDFT to study the luminescence in Ce-doped [202, 203] and Eu-doped [204] inorganic scintillators. They studied a family of Ce- or Eu-doped scintillators to see whether their (Ce^{3+})* excited states[4] were lying below the conduction band minimum (CBM) or not.

4 The (Ce^{3+})* excited state usually have an atom-like Eu_{5d} shape if not hybridized with the conduction band of the host material.



(a) $Ba_3Si_6O_{12}N_2$:Eu_1 (b) $Ba_3Si_6O_{12}N_2$:Eu_2

(c) $Ba_3Si_6O_9N_4$:Eu_1 (d) $Ba_3Si_6O_9N_4$:Eu_2 (e) $Ba_3Si_6O_9N_4$:Eu_3

Figure 5.10: **[Exc]** Electronic bandstructure of the rhombohedral supercell calculations computed with the 27 electrons pseudopotential at the ground-state atomic position computed with the 10 electrons pseduopotential. The doped elements are computed on the cell and atoms relaxed in the ground-state. They all are calculated on a 2x2x2 shifted 1/2 in all direction **k**-points grid and with a 30 Ha energy cut-off for the $Ba_3Si_6O_{12}N_2$ and 35 Ha for the $Ba_3Si_6O_9N_4$ compounds. An additional potential energy shift of 0.3 Ha was added to the 4f states (applied to both the spin up and spin down channels).

For stability of the self-consistent cycle in the Abinit software, we have removed one seventh of an electron on each of the seven 4f states and added only 6/7 of an electron to the lowest Eu_{5d} band and twice 1/14 in the two degenerate next ones. In this way, the occupation of the bands always decreases with increasing energy of the europium bands. The problem with such approach is that this kind of calculation suffers from

non-physical self-interaction of the excited electron. This will overscreen the electronic properties and push the 5d too high in energy.

We therefore propose an hybrid method trying to mimic the core-hole approach. In this approach, we remove one electron from the 4f states and place it as a homogeneous background compensation charge. This corresponds to an ionization of the totally delocalized electron as in the core-hole approach. In this way, we do not suffer from the spurious self-interaction but we are missing the force acting on the atoms coming from the electron in the Eu_{5d} state[5]. Moreover, the use of GGA+U was not enough to localize the Eu_{4f} states inside the bandgap when an electron is removed. An additional atomic potential energy shift of 0.3 Ha had to be applied on the Eu_{4f} states (through the Abinit input variable `atvshift`). This fitting parameter is not *ab-initio* but nor is the +U term already applied to these states. Since this additional atomic potential is applied in the same way for the five cases, we can still discuss the relative difference between them. We propose the name *depleted-shifted 4f approach* for our hybrid method as we remove one electron from the 4f states (depleted) and we apply an additional atomic potential energy (shifted) to those 4f states.

The electronic bandstructures of the rhombohedral europium-doped supercell computed at the ground-state atomic positions with the electron put as a uniform background compensation charge are shown on figure 5.10. We can see that these results, for the spin-up channel, are extremely similar to those obtained in the core-hole approach in figure B.9 with the additional advantage of having the spin information. This follows from the fact that depleted-shifted 4f approach with the electron uniformly delocalized as a background compensation charge is equivalent to the core-hole methodology, except for the spin-polarization and the fact that in this case the hole in the Eu_{4f} is explicitly calculated and could depend on the chemical surrounding whereas in the core-hole case, the hole was frozen in the pseudopotential. As we have just seen comparing figure 5.10 and B.9, this effect is weak because the Eu_{4f} states are very localized and therefore depend weakly on their surrounding.

Finally, it must be noted that Yan *et al.* [205] have also successfully localized the 5d states below the conduction band minimum of the host using yet another approach: hybrid functionals. This interesting route was not studied here but would be worth investigating in a future work.

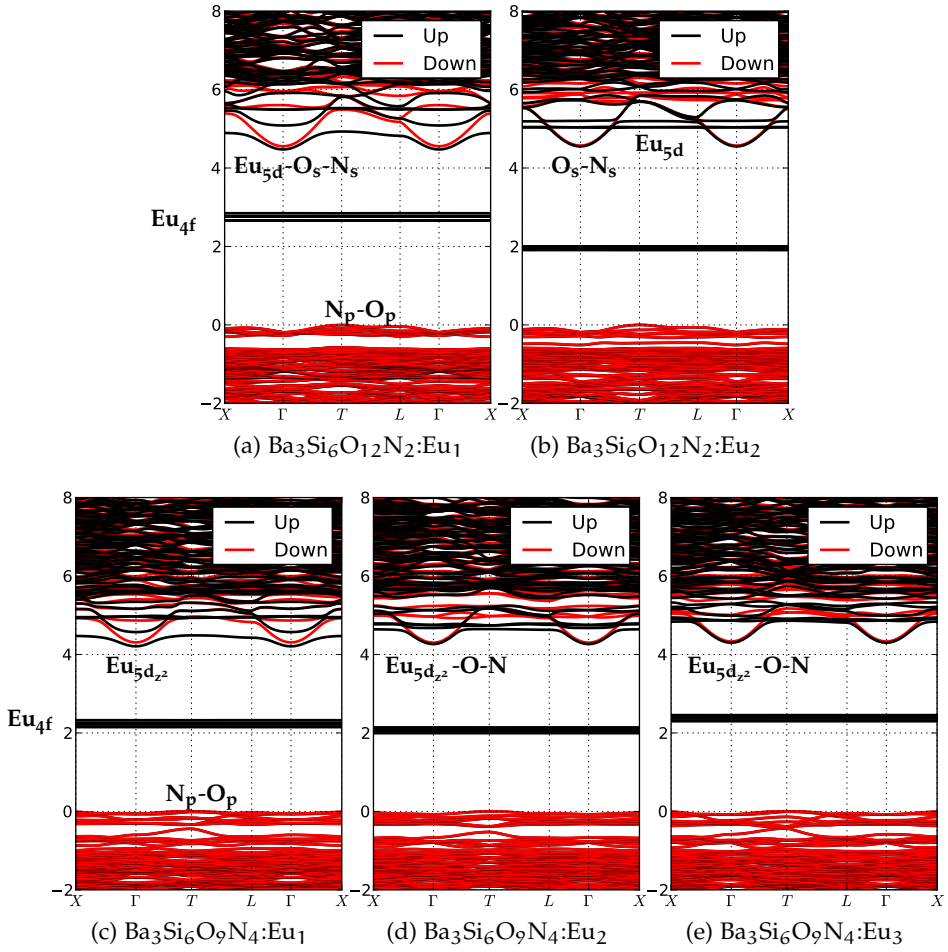
5 After different tests, it was concluded that this missing force acting on the atom was a less stringent approximation than the self-interaction issue from CDFT.

5.5 IMPORTANCE OF THE ATOMIC RELAXATION

When a photon interacts with an electron from the Eu_{4f} states, it can transfer its energy to it and promote the electron into an excited Eu_{5d} state. The electronic transition is an absorption of one photon and has been described in the two preceding sections. The excited electron will impact its surrounding and atoms will move as the result of electrostatic interaction. The electron will then re-emit a photon and go back to its ground state. If the electron stays a very short amount of time in its excited state, it will only affect the atoms around him and the lattice parameters of the crystal will not change very strongly. We will therefore only consider atomic relaxation at fixed lattice parameters.

The electronic bandstructures computed with the core-hole pseudopotential at fixed lattice parameters but relaxed atomic positions (see the Exc* position on figure 5.4) is given in figure B.10 for the hexagonal primitive cell. Important changes with respect to the Exc position of figure B.8 indicates that an excited state structural relaxation is crucial. For that reason, the analysis of selected bond-lengths is presented in table B.4. The table shows that the contraction of the oxygen cage around the europium can be for some bonds extremely important with up to 16% contraction of the Eu-O bond length with respect to the undoped case. This level of additional contraction is well in line with the change of cation radii associated with the change of oxidation state for the europium atom that we describe. Indeed, the experimental europium cation radii goes from 131 pm for Eu^{2+} to 108.7 pm for Eu^{3+} [206].

The analysis of the wavefunctions squared (density) at Γ for different bands revels the character of the bands. For example, the density of the lowest conduction band at Γ for $Ba_3Si_6O_{12}N_2$:Eu_1 in figure B.10 forms clear channels along the c axis between all the Eu_1 equivalent atoms in a manner very similar to figure 4.5a. Some of the density is also spherically located around the oxygen and nitrogen atoms, hence the denomination $\mathbf{Eu_{5d}}$-$\mathbf{O_s}$-$\mathbf{N_s}$ for this (europium dominant) hybridized state in figure B.10. The bottom of this hybridized state to the CBM gap is 1.23 eV. In contrast, the lowest dispersive band in $Ba_3Si_6O_{12}N_2$:Eu_2 is an hybridized $\mathbf{O_s}$-$\mathbf{N_s}$ state with no europium character. The almost flat band above it is an almost atomic like europium 5d state. This clearly shows that this europium substitution is not luminescent because the radiative emission from the europium 5d→4f transition will not occur as the excited electron will relax in the bottom of the conduction band



(a) $Ba_3Si_6O_{12}N_2$:Eu_1 (b) $Ba_3Si_6O_{12}N_2$:Eu_2

(c) $Ba_3Si_6O_9N_4$:Eu_1 (d) $Ba_3Si_6O_9N_4$:Eu_2 (e) $Ba_3Si_6O_9N_4$:Eu_3

Figure 5.11: **[Exc*]** Spin-polarized rhombohedral electronic bandstructure supercell in the depleted-shifted 4f approach with the removed electron put as background compensation charge. The europium-doped compounds are computed at the ground-state relaxed lattice parameters presented in section 5.2 but with the atomic position relaxed in the excited states. An additional atomic potential energy shift of 0.3 Ha had to be applied on the Eu_{4f} states.

or will, preferably, transfer to the Eu_1 substitution with a much lower energy for the lowest 5d state.

A very similar argument holds for the Eu_1 substitution in $Ba_3Si_6O_9N_4$ versus the two others. In this case, the lowest state is strongly atom-like with a clear $Eu_{5d_{z^2}}$ character. Such band is not completely flat because this hexagonal primitive cell has a large doping concentration of 33% and the europium replicas interact with each other. The $Eu_{5d_{z^2}}$ to CBM gap is smaller with a value of 0.74 eV.

We therefore conclude that the two Eu_1 substitutions in $Ba_3Si_6O_{12}N_2$ and $Ba_3Si_6O_9N_4$ are the only luminescent centers, as expected from the small FWHM from experiment (see figure 0.1). The fact that the 5d to CBM gap is 0.49 eV smaller in the $Ba_3Si_6O_9N_4$ case agrees with the Dorenbos model and indicate a stronger thermal quenching in this compound. Nonetheless, from the Dorenbos empirical formula, we expect the gap to be around 0.6 eV for $Ba_3Si_6O_{12}N_2$:Eu_1 and 0.2 eV for $Ba_3Si_6O_9N_4$. It is reasonable to expect a flattening of the localized states with decreasing europium doping.

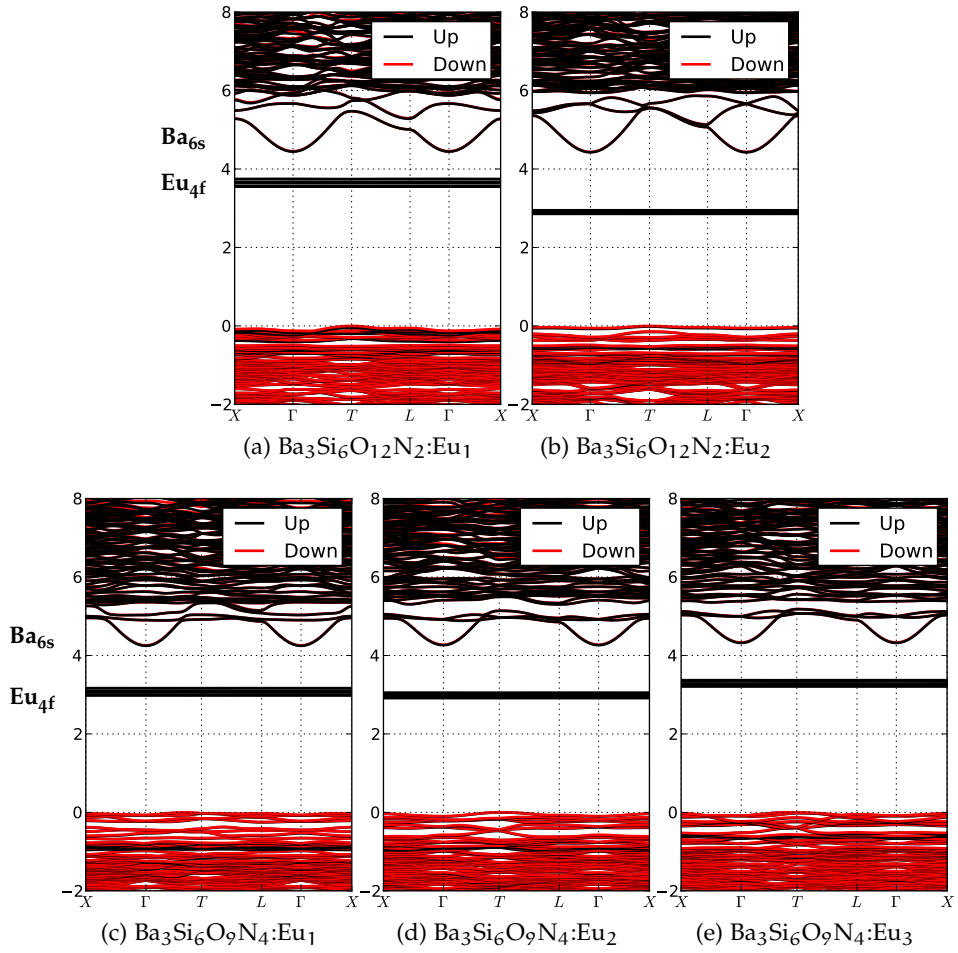
We thus present the relaxed rhombohedral supercell bandstructure in figure B.11 using the core-hole pseudopotential and with lattice parameters constrained to the ground state value computed in section 5.2. Quite unexpectedly, the CBM in $Ba_3Si_6O_9N_4$:Eu_2 and $Ba_3Si_6O_9N_4$:Eu_3 posses a very delocalized density with some density around the europium atom. We nonetheless believe that such delocalized state play a very weak role in the emission process and are non-luminescent centers.

Such consideration aside, we found out that the two gaps are 1.27 eV and 0.9 eV for $Ba_3Si_6O_{12}N_2$:Eu_1 and $Ba_3Si_6O_9N_4$:Eu_1, respectively (the second lowest conduction band is also mainly attributed to europium 5d orbital).

As a matter of fact, if we took a supercell twice as big as the rhombohedral one (5.5% doping), we would reach the experimental doping concentration. Such calculation has not been attempted due to computational limitations. We expect the lowest conduction band attributed to europium 5d level to flatten even more. If we hypothesized that the flattening will occur at the average value of the still relatively dispersive 5d band in figure B.11, the two gaps should shrunk down to 0.96 eV and 0.62 eV for $Ba_3Si_6O_{12}N_2$:Eu_1 and $Ba_3Si_6O_9N_4$:Eu_1, respectively.

To have the spin information as well as the position of the 4f states, we performed spin-polarized rhombohedral bandstructure calculations using the 27 electrons pseudopotential and the same U and potential shift values as presented in the previous section. The bandstructures are shown on figure 5.11. The most important fact to notice here is that the 4f states went up by 2.5 eV for $Ba_3Si_6O_{12}N_2$:Eu_1 and 1.5 eV for $Ba_3Si_6O_9N_4$:Eu_1 due to atomic relaxation (see figure 5.10). Let us remind that although the absolute position of the 4f state has been arbitrary set by the U value and the potential shift, the comparison made here is relevant since the only difference between the Exc and Exc* calculations are the atomic positions. Moreover the 5d to CBM gaps are

here much larger than in figure B.11 because of the additional 0.3 Ha potential shift applied on the 4f states that pull the 5d states down. We will therefore not discuss such gaps here. We will only notice the fact that the lowest conduction bands of the three non-luminescent centers are spin degenerate because those delocalized states are far from the europium atom and therefore do not react to its magnetic moment. This strengthen our conclusion about the Eu_1 substitution being the only luminescent centers in both compounds.



(a) $Ba_3Si_6O_{12}N_2$:Eu_1 (b) $Ba_3Si_6O_{12}N_2$:Eu_2

(c) $Ba_3Si_6O_9N_4$:Eu_1 (d) $Ba_3Si_6O_9N_4$:Eu_2 (e) $Ba_3Si_6O_9N_4$:Eu_3

Figure 5.12: **[GS*]** The ground-state electronic bandstructure of the europium-doped elements are computed at the *ab-initio* relaxed parameter of the excited state with the 10 valence electrons pseudopotential in the rhombohedral supercell. The black line shows the spin up component and the red line the spin down.

Finally, figures B.12, B.13 and 5.12 show the ground state electronic bandstructures computed at the atomic positions relaxed with the core-hole pseudopotential with the lattice parameters constrained to the ground-state values for the primitive hexagonal, core-hole rhombohedral and spin-polarized rhombohedral cases, respectively. The position of the 4f states with respect to the GS of figure 5.3 increase by 1.4 eV for $Ba_3Si_6O_{12}N_2$:Eu_1 and by 1.25 eV for $Ba_3Si_6O_9N_4$:Eu_1. This last set of bandstructures closes the loop presented on the cartoon 5.4 and allows for the calculation of the Stokes shift that we made there. The Stokes shifts on the rhombohedral supercell reported there quite overestimate the experimental values. We found out that the Stokes shift was not only sensitive to atomic positions but also to the pseudopotential choice (10 electrons versus 27 electrons)[6]. We did not investigate the matter further as the hexagonal primitive cell lead to acceptable results for the two luminescent centers.

From the analysis of the atomic relaxation, the main result is the fact that $Ba_3Si_6O_{12}N_2$:Eu_1 and $Ba_3Si_6O_9N_4$:Eu_1 appears to be the only luminescent centers with their Eu_{5d} states lower in energy than their substitutional counterpart. This is well in line with the experimental fact that the FWHM are narrow for both europium-doped BSON compounds. Moreover, the Dorenbos scheme seems to be strengthen.

In contrast with previous published studied on the subject (see Refs. [202, 203, 204]), we have here performed the atomic relaxation associated with the Stokes shift. We firmly believed that such relaxation is crucial to describe correctly the emission process and should be performed.

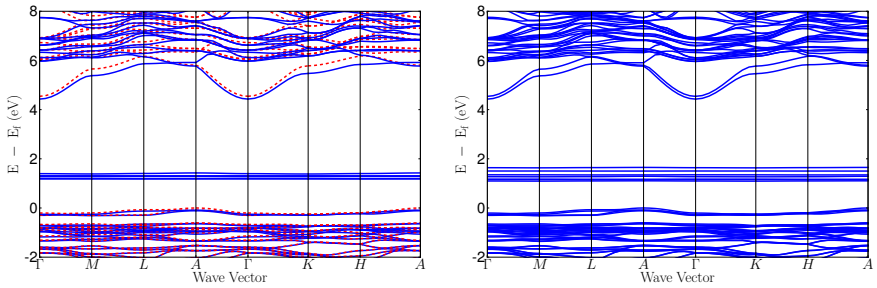
5.6 EFFECT OF SPIN-ORBIT COUPLING

In this section, we investigate whether spin-orbit coupling is important is such BSON compounds. As spin-orbit coupling in PAW+U is currently still in development in Abinit (version 7.10), we decided to use the Vienna *ab-initio* software package (VASP) [207]. For these calculations we decided to only focus on the Eu_1 substitution of $Ba_3Si_6O_{12}N_2$ and to use the VASP provided PAW pseudopotentials [163]. The main difference with Abinit is that the VASP europium pseudopotential only contains 17 electrons as valence state ($5s^2$ $5p^6$ $4f^7$ $6s^2$) and the barium only

6 Indeed, we have tested that computing the Stokes shift with the exact same atomic position but different pseudopotential lead to Stokes shifts that are not rigidly shifted up or down but take different values for different substitutions.

10 ($5s^2$ $5p^6 6s^2$). For the VASP calculations the same U and J parameters of 7.5 eV and 0.6 eV were applied.

The electronic bandstructure of $Ba_3Si_6O_{12}N_2$:Eu_1 calculated with VASP version 5.2.12 at the ground-state atomic position and lattice parameter obtained with Abinit are presented with and without spin-orbit coupling in figure 5.13.



(a) Spin-polarized calculation

(b) Spin-polarized calculation including spin-orbit coupling

Figure 5.13: **[Case 1B]** Electronic bandstructure of $Ba_3Si_6O_{12}N_2$:Eu_1 calculated with VASP 5.2.12 at the ground-state atomic position and lattice parameter obtained with Abinit. The same U and J parameters of 7.5 eV and 0.6 eV are applied to the calculation.

Direct comparison with figure 5.3a reveals that the Eu_{4f} are lower in energy and more dispersive than Abinit with a dispersion of 0.24 eV compared to 0.17 eV in Abinit. The spin-orbit coupling lift the degeneracies and the Eu_{4f} becomes even more dispersive with a spread of 0.56 eV.

The Abinit $\mathbf{A} - \mathbf{\Gamma}$ gap from figure B.5 goes from 4.566 eV in Abinit to 4.429 eV in VASP and the $\mathbf{\Gamma} - \mathbf{\Gamma}$ ones from 4.596 eV in Abinit to 4.634 eV in VASP. The inclusion of spin-orbit coupling leads to no noticeable difference on all the other bands except the 4f. We hypothesize similar behaviour for the other four BSON compounds and safely neglect it in our calculations.

5.7 GLIMPSE AT THE ZPR OF UNDOPED BSON COMPOUNDS

In this last section of the last chapter of this thesis we will finally use the knowledge gained in Part I and apply it to the challenging BSON compounds. Since the temperature dependence with PAW pseudopotential is not coded yet inside Abinit, we used norm-conserving pseudopotentials.

The barium, silicon, oxygen and nitrogen norm-conserving pseudopotential were generated using the `fhi98PP` code [105] with a 1.0247 atomic unit cut-off radius for pseudization. Both of them are Troullier-Martins pseudopotentials with the Perdew-Burke-Ernzerhof parametrization of the generalized gradient approximation [107] for the exchange-correlation functional.

The valence electrons of barium, silicon, oxygen and nitrogen, treated explicitly in the *ab-initio* calculations, are the $6s^2$, $3s^2 3p^2$, $2s^2 2p^4$ and $2s^2 2p^3$ orbitals, respectively.

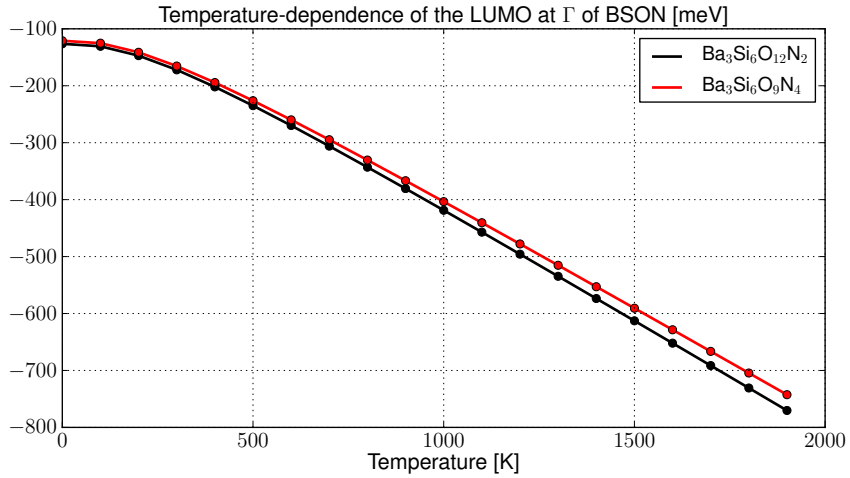


Figure 5.14: The static temperature dependence of the LUMO at **Γ** for the two undoped BSON compounds is integrated over a 4x4x4 **q**-point grid with an $i\delta = 100$ meV. The slopes at high temperature are -0.391 meV/K and -0.377 meV/K for $Ba_3Si_6O_{12}N_2$ and $Ba_3Si_6O_9N_4$, respectively.

Noticeably, we decided not to use the semi-core version of the barium pseudopotential to decrease the computational load.

Convergence study (error below 0.5 mHa per atom on the total energy) leads to the use of a 2x2x2 **Γ**-centred Monkhorst-Pack **k**-point sampling [101] of the Brillouin zone and an energy cut-off of 35 Hartree for the truncation of the planewave basis set for $Ba_3Si_6O_{12}N_2$ and $Ba_3Si_6O_9N_4$.

DFT structural relaxation of both compounds to maximal forces below $5e^{-5}$ Ha/Bohr leads to lattice constants of a = 14.393 Bohr and c = 12.630 Bohr for $Ba_3Si_6O_{12}N_2$ and a = 13.895 Bohr and c = 13.218 Bohr for $Ba_3Si_6O_9N_4$. With respect to the relaxed lattice parameter obtained using PAW and semi-core states for barium presented in section 4.3, the a parameter is 0.1% and the c parameter is 2% larger for $Ba_3Si_6O_{12}N_2$.

			ZPR [meV]		
	q-grid	Gap	Static	Non-adiabatic	Experimental
α-AlN	34x34x34	$\Gamma - \Gamma$	-429±58 (50)	-369 (0.01)	-239 [115]
β-AlN	63x63x63	$\Gamma - \Gamma$	-427±59 (50)	-386 (10)	
		$\Gamma - \mathbf{X}$	-352±54 (50)	-311 (0.01)	
$Ba_3Si_6O_{12}N_2$	4x4x4	$\Gamma - \Gamma$	-149 (100)	-321 (100)	
		$\mathbf{A} - \Gamma$	-379 (100)	-330 (100)	
$Ba_3Si_6O_9N_4$	4x4x4	$\Gamma - \Gamma$	-129 (100)	-225 (100)	
		$\mathbf{M} - \Gamma$	-324 (100)	-327 (100)	
c-BN	63x63x63	$\Gamma - \Gamma$	-514±157 (50)	-461 (50)	
		$\Gamma - \mathbf{X}$	-470±67 (50)	-385 (0.01)	
C	125x125x125	$\Gamma - \Gamma$	-421±118 (50)	-409 (50)	-320 [93]
					-450 [93]
		$\Gamma - \frac{2}{3}\mathbf{X}$	-366±60 (50)	-334 (50)	-364 [25]
Si	63x63x63	$\Gamma - \Gamma$	-43±26 (50)	-42 (50)	
		$\Gamma - \frac{2}{3}\mathbf{X}$	-61±30 (50)	-59 (50)	-62 [25]
					-64 [25]

Table 5.3: ZPR for the different studied compounds. The two experimental results for the direct bandgap renormalization of diamond from Ref. [93] are extracted using first or second-derivative line-shape analysis. The two experimental ZPR for the indirect bandgap of silicon from Ref. [25] are obtained from mass derivative of the gap and from linear extrapolation to 0 K.

In the case of $Ba_3Si_6O_9N_4$, the a lattice parameter is 0.4% larger and the c parameter is 1.9% larger. Using barium semi-core pseudopotential is expected to improve the agreement but we will continue bearing in mind that we want, in this section, only have an idea of the order of magnitude brought by the zero-point motion correction to the lowest conduction state of the host material.

Due to the computational cost of doing such calculations, we were only able to do **q**-point integration on a 4x4x4 grid at maximum. The results are reported on table B.5.

Expectedly, the convergence for the HOMO at Γ is much more difficult than for the LUMO since the HOMO is not the highest energy state. Both BSON compounds are indirect $\mathbf{A} - \Gamma$ or $\mathbf{M} - \Gamma$ bandgap materials. Even the HOMO convergence at **A** or **M** is difficult because the valence bands are very flat. Since we are mainly interested in the lowest conduction state, we can safely focus on the lowest energy conduction state at Γ. From those preliminary results we can see that the LUMO

band is renormalized at 0K due to electron-phonon coupling by about 120 meV for both BSON compounds. Moreover, the static temperature dependence of the LUMO at Γ for the two undoped BSON compounds integrated over a 4x4x4 $\mathbf{q}$-point grid with an $i\delta = 100$ meV is presented on figure 5.14. The slopes at high temperature are -0.391 meV/K and -0.377 meV/K for $Ba_3Si_6O_{12}N_2$ and $Ba_3Si_6O_9N_4$, respectively.

It is also interesting to compare the results obtained for the two undoped BSON compounds with those obtained for simple semiconductors in Chapter 3. Such comparison table is provided on table 5.3. We can see that although the $\mathbf{q}$-point convergence is not reached, the two BSON compounds show signs of strong zero-point motion renormalization with respect to other semiconductors presented in the table.

This last section is a proof of concept that such demanding AHC calculation with a very large number of electrons and phonon modes is possible. This has, to the author knowledge, never been attempted before. We believe that, with enough computing power (Tier 0 or 1 HPC), the converged ZPR of the BSON compounds can nowadays be calculated within the AHC theory.

5.8 CONCLUSION

In this chapter, we studied the absorption and emission optical properties of the five Eu-doped BSON compounds. We first validated successfully our 27 electrons pseudopotential against the all-electron code Elk in section 5.1.2.

In order to localize the europium 4f states inside the bandgap of the host material, we had to use a GGA+U approach, imposing a U value of 7.5 eV and a J value of 0.6 eV on the 4f states only. We computed an estimation of the Stokes shift and presented the full cycle associated with the absorption, relaxation and emission process.

Europium-doping of the BSON material led to a contraction of the unit cells ranging from 1.5 to 1.9%. The associated ground-state calculation of the five europium-doped cases has shown that the 5d electrons of the europium atom are not localized inside the bandgap of the host material, in contradiction to both the $5d-4f$ crossing decay model and the Dorenbos auto-ionization model.

To overcome this problem and describe the absorption process, we used two excited-state schemes: the core-hole method and the depleted-shifted 4f approach.

The core-hole method is based on the use of a pseudopotential with the 4f frozen in the core with a hole (the $4f^6$ states are frozen). Since this method is cheaper computationally than the depleted-shifted 4f, we were able to analyse a rhombohedral supercell, three times larger than the primitive one. Such supercell leads to an europium concentration of 11%, closer to the experimental one of 5-10%.

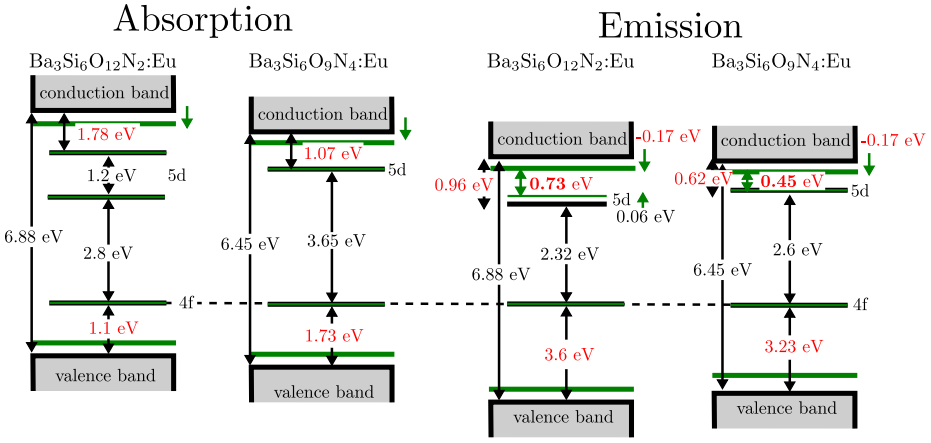


Figure 5.15: Band positions for the absorption and emission phenomena in $Ba_3Si_6O_{12}N_2$:Eu and $Ba_3Si_6O_9N_4$:Eu. The energy gap (in eV) are in black when it is experimental values (or G_0W_0 *ab-initio* value for the two band-gaps of the host materials for the absorption taken from Ref. [4]) and in red when the value are hypothetical. The horizontal band positions are in black at 0 K and in green at 300 K (sometimes superimposed when there is no thermal effect).

The main drawback from the core-hole method is the fact that this method does not hold information about the spin state of these ferromagnetic systems.

The second method, the depleted-shifted 4f method does give access to such spin information but at a higher computational cost. This more refined method confirms the results obtained with the core-hole approach.

The emission process is studied in section 5.5 by letting the atom relax with their electrons in an excited configuration. We conclude from the relaxation study that the effects of relaxation are important on the electronic bandstructures and should therefore be taken into account to correctly describe the emission process. From this relaxation, we learned that the two luminescent europium substitutions were the $Ba_3Si_6O_{12}N_2$:Eu_1 and $Ba_3Si_6O_9N_4$:Eu_1 cases.

The section 5.6 confirms that the effect of spin-orbit coupling is small in these materials and could safely be discarded when performing *ab-initio* calculations.

Finally, we computed the unconverged ZPR of the two undoped BSON compounds using norm-conserving pseudopotential and showed that the LUMO band is renormalized at 0K due to electron-phonon coupling by about 120 meV for both BSON compounds.

Gathering all the information of the chapter, we can estimate the ten unknown gaps of figure 0.5 from the introduction. The ① and ② gaps are deduced from the renormalization of the LUMO state at 300 K from figure 5.14 to a value of around 0.17 eV in both cases. The ③ and ④ gaps of 0.96 eV and 0.62 eV are obtained by taking the averaged value of the europium 5d like band in figure B.11 as discussed in section 5.5. From that and the knowledge of the bandgap of the host material, we can deduce the ⑤ and ⑥ gaps to be 3.6 eV and 3.23 eV. From there, as discussed in section 5.5, we know that the valence to 4f gap is lower by 2.5 eV and 1.5 eV for $Ba_3Si_6O_{12}N_2$:Eu_1 and $Ba_3Si_6O_9N_4$:Eu_1, respectively. This gave us the value of the ⑦ and ⑧ gaps and finally from the host bandgap we can deduce the ⑨ and ⑩ gaps to be 1.78 eV and 1.07 eV.

This validates the Dorenbos auto-ionization model both qualitatively and quantitatively and allowed us to understand the puzzling temperature-dependent behavior of the two europium-doped BSON compounds thanks to first-principles calculations using only DFT (and G_0W_0 for the host bandgaps).



6

CONCLUSIONS AND PERSPECTIVES

Following Sir Isaac Newton quotes, this thesis is standing on the shoulders of giants and should be understood as the continuation of the works undertaken by Dr. Paul Boulanger, Dr. Bruno Bertrand, Dr. Masayoshi Mikami and Prof. Xavier Gonze. Dr. Boulanger is at the heart of the original AHC implementation inside the software Abinit and Dr. Bertrand performed a large number of calculations for the undoped BSON compounds, paving the way for the study of the europium-doped compounds. Both Dr. Mikami and Prof. Gonze helped the three of us by continuously providing insightful comments and suggestions.

The motivation of this thesis is to understand the origin of the radical difference between the temperature dependence of the emission intensities of two europium-doped barium silicate oxynitride compounds: $Ba_3Si_6O_{12}N_2$:Eu^{2+} and $Ba_3Si_6O_9N_4$:Eu^{2+} that are used in WLEDs. Part I of this thesis lays down the theoretical framework for the *ab-initio* temperature-dependence calculation. The theory is then validated, verified and applied to the case of simple semiconductors.

Chapter 1 compares in detail two (AHC/DFPT and FP) of the three approaches still used today to calculate the ZPR. We consider the first for its numerical efficiency in the computation of the ZPR at arbitrary **q**-points, crucial for periodic system, and the latter, to go beyond the RIA and study its impact on the calculated ZPR. An important contribution of this chapter is the clarification of the terms appearing beyond the RIA made in the AHC theory. The DW term is divided into a rigid-ion approximation contribution (DW_{RIA}) and a non-rigid-ion approximation contribution (DW_{NRIA}). This allows the name of the terms to be coherent with their respective definitions. The extension of the theory to the dynamical case is also presented.

In Chapter 2, we validate the theory by comparing the results obtained for diamond with the DFPT and the FP approaches. Then, we also compare the results as implemented in Abinit against another *ab-initio* code

(Yambo on top of QE). We present the converged result of the bandgap reduction due to electron-phonon renormalization, that is, 409 meV at 0 Kelvin. We also perform an analysis of the convergence rate with respect to **q**-wavevector samplings.

The Chapter 3 presents the application of the theory developed in the first two chapters to the case of five semiconductors and compares the results with the experiments when available. The agreement is satisfactory but also highlights the need for experimental determination of the ZPR on a wider temperature range. We hope that this thesis can motivate such experimental studies. The ZPR of the direct bandgap of diamond is also computed within the *GW* many-body framework using the FP approach and shows a close agreement with the experimental temperature-dependence measurement.

All of the above make us believe that the AHC theory is now well-understood and the coding of this theory inside the Abinit software is mature for production runs as demonstrated in Chapter 3. There is nonetheless room for improvements in the computational performance of the AHC/DFPT implementation. Indeed, they are required if we want to treat complex industrially relevant materials like the BSON compounds used in WLEDs. To reach that goal, we believe that the following coding and developments are important:

1. Adding spin-polarisation support to the electron-phonon implementation of Abinit (`nsppol 2` Abinit input variable). This is crucial to describe ferromagnetic systems like the europium-doped BSON compounds.

2. Investigating the spectral function associated with the dynamical AHC theory. The spectral function might help us pint-point satellites in the complex Fan self-energy. This will allow for a more accurate description of the consequence of electron-phonon interaction in the description of experimental absorption spectra.

3. The coding of the dynamical electron-phonon induced lifetime broadening inside the post-processing python script is the only missing capability of the script.

4. The coding of PAW support for electron-phonon calculations seems very important as the accuracy and speed gain provided by this support would be substantial.

5. Adding symmetry support to the electron-phonon calculations inside Abinit will greatly speed up the calculation. This will require both coding efforts and theoretical investigations.

Part II of this thesis presents the BSON host materials (Chapter 4) as well as its five europium-doped substitutions (Chapter 5). We devised two excited-state schemes: the core-hole and depleted-shifted 4f methods. Those are used to describe the absorption process. The emission process is studied by letting the atom relax with their electron in an excited configuration. From this relaxation, we learned that the two luminescent europium substitutions were the $Ba_3Si_6O_{12}N_2$:Eu_1 and $Ba_3Si_6O_9N_4$:Eu_1 cases. We additionally calculate that rhombohedral supercells have an Eu_{5d} to conduction-band minimum gap that is 0.34 eV larger for $Ba_3Si_6O_{12}N_2$:Eu_1 than $Ba_3Si_6O_9N_4$:Eu_1. This energy difference is enough to prevent the $Ba_3Si_6O_{12}N_2$:Eu^{2+} to be thermally quenched, in accordance with the Dorenbos auto-ionization model and the experimental data. The effect of spin-orbit coupling, computed using the VASP software, is small in these phosphor materials.

We also computed the unconverged ZPR of the two undoped BSON compounds using norm-conserving pseudopotentials and showed that the LUMO band is renormalized at 0 K due to electron-phonon coupling by about 120 meV for both BSON compounds.

To strengthen this conclusion, the *ab-initio* temperature-dependence calculation developed in Part I should be converged in **q**-point and the calculation redone using PAW pseudopotentials. We believe that the barium semi-core states are important and should be included in such calculations. The use of hybrid functionals to describe the electronic position of the Eu_{5d} states with respect to the conduction band of the host material would be an alternative to the GGA+U approach that has the advantage of being computationally affordable. However this approach could also miss some of the physics involved (see for example Ref. [160]).

Finally, we should mention that this year 2014 was very exciting for the field of rare-earth doped compounds. A plethora of PAW dataset tables that include carefully designed rare-earth elements were generated during this year. Since the scarcity of reliable pseudopotential was a big issue for this thesis and led to the design of our own PAW europium pseudopotential, we appreciate this contribution (see tables published in 2014 by M. Topsakal and R.M. Wentzcovitch [208], F. Jollet *et al.* [209] and A. D. Corso [210]). Moreover, the year 2014 saw the physics Nobel price being granted for the creation of blue LEDs.



Part III

APPENDIX



A

TEMPERATURE DEPENDENCE

A.1 CONVENTION FOR THE UNPERTURBED PERIODIC SYSTEM

Following the same convention as Gonze [64], the unperturbed wavefunction can be obtained as the product of a phase factor and a periodic function (Bloch's theorem)

$$\Psi^{(0)}_{n\mathbf{k}}(\mathbf{r}) = (N_{Bv K}\Omega_0)^{-1/2} e^{i\mathbf{k}\cdot\mathbf{r}} u^{(0)}_{n\mathbf{k}}(\mathbf{r}), \tag{A.1}$$

where $N_{Bv K}$ is the number of unit cells repeated in the Born-von Karman periodic box, Ω_0 the volume of the unperturbed unit cell, n the band index and $\mathbf{k}$ label the wave vector of the wavefunction.

The periodic part of the Bloch wavefunction, in Eq. (A.1), is subject to the following orthonormalization condition

$$\left\langle u^{(0)}_{n'\mathbf{k}} \middle| u^{(0)}_{n\mathbf{k}} \right\rangle = \delta_{n'n}, \tag{A.2}$$

where the scalar product of periodic functions is defined as

$$\langle f|g\rangle = \frac{1}{\Omega_0}\int_{\Omega_0} f^*(\mathbf{r})g(\mathbf{r})d\mathbf{r}. \tag{A.3}$$

For a generic operator we follow the subsequent convention

$$O_{\mathbf{k},\mathbf{k}'} = e^{-i\mathbf{k}\cdot\mathbf{r}} O e^{-i\mathbf{k}'\cdot\mathbf{r}'}. \tag{A.4}$$

A.2 PERTURBATION THEORY

The perturbation theory for a periodic system is based on the idea that the solution of a reference system (usually the equilibrium ground state one-body Schrödinger equation) is known. In general, the perturbation can be incommensurate with the periodic system and characterized by a wave vector $\mathbf{q}$. If the amplitude of the perturbation is characterized by

a small scalar parameter λ, then any observable $X(\lambda)$ can be expressed as a power serie

$$X(\lambda) = X^{(0)} + (\lambda X^{(1)}_{\mathbf{q}} + \lambda^* X^{(1)}_{-\mathbf{q}}) + (\lambda^2 X^{(2)}_{\mathbf{q},\mathbf{q}} + \lambda\lambda^* X^{(2)}_{\mathbf{q},-\mathbf{q}} + \lambda^*\lambda X^{(2)}_{-\mathbf{q},\mathbf{q}} + \lambda^{*2} X^{(2)}_{-\mathbf{q},-\mathbf{q}}) + \cdots, \quad (A.5)$$

were we use the superscript notation as a shorthand for derivatives: $X^{(i)}_{\mathbf{q}} = d^i X_{\mathbf{q}}/id\lambda^i\big|_{\lambda=0}$. The perturbed Schrödinger equation now depends explicitely on the parameter λ

$$H(\lambda)\,|\Psi_{n\mathbf{k}}(\lambda)\rangle = \varepsilon_{n\mathbf{k}}(\lambda)\,|\Psi_{n\mathbf{k}}(\lambda)\rangle\,, \quad (A.6)$$

where n is the band index, $\mathbf{k}$ is a wavevector in the Brillouin zone. The solutions $|\Psi_{n\mathbf{k}}(\lambda)\rangle$ must fulfill the normalization condition

$$\langle\Psi_{n\mathbf{k}}(\lambda)|\Psi_{n\mathbf{k}}(\lambda)\rangle = 1. \quad (A.7)$$

The Hamiltonian $\hat{H}(\lambda)$ depends parametrically on the atomic position $\mathbf{R}_{l\kappa}$ of the atom κ in the cell l.

The translated first-order wave function becomes

$$\Psi^{(1)}_{n\mathbf{k},\mathbf{q}}(\mathbf{r}+\mathbf{R}_a) = e^{i(\mathbf{k}+\mathbf{q})\cdot\mathbf{R}_a}\Psi^{(1)}_{n\mathbf{k},\mathbf{q}}(\mathbf{r}), \quad (A.8)$$

where $\mathbf{R}_a$ is a vector of the real space lattice. We can then factorize out the phase factor to map the incommensurate problem into a problem commensurate with the periodicity of the unperturbed one. To this end, we introduce the periodic first-order wave functions

$$u^{(1)}_{n\mathbf{k},\mathbf{q}} = (N_{B\nu K}\Omega_0)^{1/2} e^{-i(\mathbf{k}+\mathbf{q})\cdot\mathbf{r}}\Psi^{(1)}_{n\mathbf{k},\mathbf{q}}(\mathbf{r}). \quad (A.9)$$

We define $S_{M\mathbf{k}+\mathbf{q}}$ as the space of the M low-lying $\mathbf{k}+\mathbf{q}$ states, M being larger or equal to the index of the highest band for which we aim to compute the temperature-dependent behaviour. We define $P_{M\mathbf{k}+\mathbf{q}}$ as the projector on $S_{M\mathbf{k}+\mathbf{q}}$. We also define $P_{c\mathbf{k}+\mathbf{q}}$ as the projector on the subspace of $\mathbf{k}+\mathbf{q}$ ground-state wavefunctions complementary to $S_{M\mathbf{k}+\mathbf{q}}$. The first-order derivatives of wavefunctions can be split in two contributions, one that is contained inside $S_{M\mathbf{k}+\mathbf{q}}$ and one that belongs to its complimentary,

$$\left|u^{(1)}_{n\mathbf{k},\mathbf{q}}\right\rangle = \left|P_{M\mathbf{k}+\mathbf{q}}u^{(1)}_{n\mathbf{k},\mathbf{q}}\right\rangle + \left|P_{c\mathbf{k}+\mathbf{q}}u^{(1)}_{n\mathbf{k},\mathbf{q}}\right\rangle. \quad (A.10)$$

$\left|P_{M\mathbf{k}+\mathbf{q}}u^{(1)}_{n\mathbf{k},\mathbf{q}}\right\rangle$ can be easily computed using standard perturbation theory,

$$\left|P_{M\mathbf{k}+\mathbf{q}}u^{(1)}_{n\mathbf{k},\mathbf{q}}\right\rangle = -\sum_{n'}^{M} \frac{\left|u^{(0)}_{n'\mathbf{k}+\mathbf{q}}\right\rangle\left\langle u^{(0)}_{n'\mathbf{k}+\mathbf{q}}\right| H^{(1)}_{\mathbf{k}+\mathbf{q},\mathbf{k}}\left|u^{(0)}_{n\mathbf{k}}\right\rangle}{\varepsilon^{(0)}_{n'\mathbf{k}+\mathbf{q}} - \varepsilon^{(0)}_{n\mathbf{k}}}. \quad (A.11)$$

For $\left|P_{c\mathbf{k}+\mathbf{q}}u^{(1)}_{n\mathbf{k},\mathbf{q}}\right\rangle$, we want to avoid the summation over an infinite number of states. So, in the spirit of DFPT, we minimize

$$E^{(2)+}_{-\mathbf{q},\mathbf{q}}\{u^{(0)},u^{(1)}\} = E^{(2)}_{-\mathbf{q},\mathbf{q}}\{u^{(0)},u^{(1)}\} - \sum_{nn'}^{MM}\Lambda_{nn'\mathbf{k},\mathbf{k}+\mathbf{q}}\left\langle u^{(0)}_{n'\mathbf{k}+\mathbf{q}}\middle|P_{c\mathbf{k}+\mathbf{q}}u^{(1)}_{n\mathbf{k},\mathbf{q}}\right\rangle + \text{c.c.}, \quad (A.12)$$

where $E^{(2)}_{-\mathbf{q},\mathbf{q}}\{u^{(0)},u^{(1)}\}$ is given in Eq. 42 of Ref. [64], under the constraint of parallel-transport gauge [211],

$$\left\langle u^{(0)}_{n'\mathbf{k}+\mathbf{q}}\middle|P_{c\mathbf{k}+\mathbf{q}}u^{(1)}_{n\mathbf{k},\mathbf{q}}\right\rangle = 0, \quad (A.13)$$

with the Lagrange parameters

$$\Lambda^{*}_{nn'\mathbf{k},\mathbf{k}+\mathbf{q}} = \Lambda_{n'n\mathbf{k}+\mathbf{q},\mathbf{k}}. \quad (A.14)$$

The minimum of this expression with respect to variations of $P_{c\mathbf{k}+\mathbf{q}}u^{(1)}_{n\mathbf{k},\mathbf{q}}$ leads to the canonical Euler-Lagrange equation

$$\left(H^{(0)}_{\mathbf{k}+\mathbf{q},\mathbf{k}+\mathbf{q}} - \varepsilon^{(0)}_{n\mathbf{k}}\right)\left|P_{c\mathbf{k}+\mathbf{q}}u^{(1)}_{n\mathbf{k},\mathbf{q}}\right\rangle = -H^{(1)}_{\mathbf{k}+\mathbf{q},\mathbf{k}}\left|u^{(0)}_{n\mathbf{k}}\right\rangle + \sum_{n'}\Lambda^{*}_{nn'\mathbf{k},\mathbf{k}+\mathbf{q}}\left|u^{(0)}_{n'\mathbf{k}+\mathbf{q}}\right\rangle. \quad (A.15)$$

We can then pre-multiply on each side by $\left\langle u^{(0)}_{n''\mathbf{k}+\mathbf{q}}\right|$ where $n'' \in [1,M]$ and get

$$\left(\varepsilon^{(0)}_{n''\mathbf{k}+\mathbf{q}} - \varepsilon^{(0)}_{n\mathbf{k}}\right)\overbrace{\left\langle u^{(0)}_{n''\mathbf{k}+\mathbf{q}}\middle|u^{(1)}_{n\mathbf{k},\mathbf{q}}\right\rangle}^{=0 \text{ due to Eq. (A.13)}} + \left\langle u^{(0)}_{n''\mathbf{k}+\mathbf{q}}\middle|H^{(1)}_{\mathbf{k}+\mathbf{q},\mathbf{k}}\middle|u^{(0)}_{n\mathbf{k}}\right\rangle = \sum_{n'}\Lambda^{*}_{nn'\mathbf{k},\mathbf{k}+\mathbf{q}}\underbrace{\left\langle u^{(0)}_{n''\mathbf{k}+\mathbf{q}}\middle|u^{(0)}_{n'\mathbf{k}+\mathbf{q}}\right\rangle}_{\delta_{n''n'}}. \quad (A.16)$$

This leads to the equation

$$\Lambda^{*}_{nn''\mathbf{k}+\mathbf{q},\mathbf{k}} = \left\langle u^{(0)}_{n''\mathbf{k}+\mathbf{q}}\middle|H^{(1)}_{\mathbf{k}+\mathbf{q},\mathbf{k}}\middle|u^{(0)}_{n\mathbf{k}}\right\rangle. \quad (A.17)$$

We can then substitute Eq. (A.17) inside Eq. (A.15) and get

$$\left(H^{(0)}_{\mathbf{k}+\mathbf{q},\mathbf{k}+\mathbf{q}} - \varepsilon^{(0)}_{n\mathbf{k},\mathbf{q}}\right)\left|P_{c\mathbf{k}+\mathbf{q}}u^{(1)}_{n\mathbf{k},\mathbf{q}}\right\rangle = -\underbrace{\left(1 - \sum_{n'}^{M}\left|u^{(0)}_{n'\mathbf{k}+\mathbf{q}}\right\rangle\left\langle u^{(0)}_{n'\mathbf{k}+\mathbf{q}}\right|\right)}_{P_{c\mathbf{k}+\mathbf{q}}}H^{(1)}_{\mathbf{k}+\mathbf{q},\mathbf{k}}\left|u^{(0)}_{n\mathbf{k}}\right\rangle. \quad (A.18)$$

and finally

$$\left(H^{(0)}_{\mathbf{k+q},\mathbf{k+q}} - \varepsilon^{(0)}_{n\mathbf{k}}\right) P_{c\mathbf{k+q}} \left|u^{(1)}_{n\mathbf{k},\mathbf{q}}\right\rangle = -P_{c\mathbf{k+q}} H^{(1)}_{\mathbf{k+q},\mathbf{k}} \left|u^{(0)}_{n\mathbf{k}}\right\rangle. \quad \text{(A.19)}$$

Supposing $H^{(1)}$ has already be determined by the usual DFPT self-consistency loop over occupied states only (in which $M = N_{val}$), the $u^{(1)}_{n\mathbf{k},\mathbf{q}}$ are found by solving Eq. (A.19), combined with Eqs. (A.10) and (A.11).

A.3 THE DYNAMICAL EQUATIONS

In this section we derive the dynamical equation Eq. (1.2). The lattice vibration of a solid will affect its electronic properties. The total electronic energy of the system can be expressed as a Taylor series on the displacements around the equilibrium position E_0

$$E = E_0 + \sum_{\kappa\alpha} \frac{\partial E}{\partial R_{\kappa\alpha}} U_{\kappa\alpha} + \frac{1}{2} \sum_{\substack{\kappa\alpha \\ \kappa''\beta}} U_{\kappa''\beta} \frac{\partial^2 E}{\partial R_{\kappa\alpha} \partial R_{\kappa''\beta}} U_{\kappa\alpha} + ..., \quad \text{(A.20)}$$

with $U_{\kappa\alpha}$ the displacement of the atom κ in the direction α. The full vector has a length of 3 times the number of atoms.

The motion of nuclei is treated with the classical $F = ma$ equation. The force can be expressed as

$$F_{\kappa'\gamma} = -\frac{\partial E}{\partial R_{\kappa'\gamma}}. \quad \text{(A.21)}$$

By injecting the expression of Eq. (A.20) into this equation[1]

$$F_{\kappa'\gamma} = -\frac{\partial}{\partial R_{\kappa'\gamma}} \left[E_0 + \frac{1}{2} \sum_{\substack{\kappa\alpha \\ \kappa''\beta}} U_{\kappa''\beta} \frac{\partial^2 E}{\partial R_{\kappa\alpha} \partial R_{\kappa''\beta}} U_{\kappa\alpha} \right]. \quad \text{(A.22)}$$

1 The first order term in the Taylor expansion of the total energy is null because we are around the equilibrium position.

By neglecting third order derivative (in the hypothesis of small displacement) and taking into account the relation[2] $\frac{\partial U_{\kappa''\beta}}{\partial R_{\kappa'\gamma}} = \delta_{\kappa''\kappa'}\delta_{\beta\gamma}$ one can obtain

$$\begin{aligned}
F_{\kappa'\gamma} &= -\frac{1}{2}\left[\sum_{\kappa\alpha}\frac{\partial U_{\kappa''\beta}}{\partial R_{\kappa'\gamma}}\frac{\partial^2 E}{\partial R_{\kappa\alpha}\partial R_{\kappa''\beta}}U_{\kappa\alpha}\right. \\
&\quad \left. + \sum_{\kappa\alpha} U_{\kappa''\beta}\frac{\partial^2 E}{\partial R_{\kappa\alpha}\partial R_{\kappa''\beta}}\frac{\partial U_{\kappa\alpha}}{\partial R_{\kappa'\gamma}}\right] \\
&= -\frac{1}{2}\left[\sum_{\kappa\alpha}\delta_{\kappa''\kappa'}\delta_{\beta\gamma}\frac{\partial^2 E}{\partial R_{\kappa\alpha}\partial R_{\kappa''\beta}}U_{\kappa\alpha}\right. \\
&\quad \left. + \sum_{\kappa\alpha} U_{\kappa''\beta}\frac{\partial^2 E}{\partial R_{\kappa\alpha}\partial R_{\kappa''\beta}}\delta_{\kappa\kappa'}\delta_{\alpha\gamma}\right] \\
&= -\frac{1}{2}\left[\sum_{\kappa\alpha}\frac{\partial^2 E}{\partial R_{\kappa\alpha}\partial R_{\kappa'\gamma}}U_{\kappa\alpha} + \sum_{\kappa''\beta} U_{\kappa''\beta}\frac{\partial^2 E}{\partial R_{\kappa'\gamma}\partial R_{\kappa''\beta}}\right] \\
&= -\sum_{\kappa\alpha}\frac{\partial^2 E}{\partial R_{\kappa\alpha}\partial R_{\kappa'\gamma}}U_{\kappa\alpha} \\
&\triangleq -\sum_{\kappa\alpha} C^{\kappa\alpha}_{\kappa'\gamma} U_{\kappa\alpha}.
\end{aligned} \tag{A.23}$$

The inter-atomic force constant (IFC) $C^{\kappa\alpha}_{\kappa'\gamma} = \frac{\partial^2 E}{\partial R_{\kappa\alpha}\partial R_{\kappa'\gamma}}$ has been introduced in the last equation. Focusing on monochromatic solutions to Newton's Law (to be superposed afterwards), the time-dependent displacements can be expressed as a time independent crystal periodic part and a time dependent phase factor that acts as an envelope around the periodic oscillations[3]

$$U_{\kappa\alpha}(t) = \frac{1}{2}\left[U_{\kappa\alpha}e^{-i\omega t} + U^*_{\kappa\alpha}e^{i\omega t}\right] = \Re\left[U_{\kappa\alpha}e^{-i\omega t}\right], \tag{A.24}$$

with ω the frequency of nuclear oscillation. The Newtonian equation of motion is

$$\begin{aligned}
F_{\kappa'\gamma}(t) &= M_{\kappa'}\frac{\partial^2 U_{\kappa'\gamma}(t)}{\partial t^2} \\
&= -M_{\kappa'}\omega^2 U_{\kappa'\gamma}(t),
\end{aligned} \tag{A.25}$$

2 The derivative of a displacement along another direction than the derivative one is 0.

3 Here we have chosen a linear combination of eigendisplacements such that the resulting one is real.

with $M_{\kappa'}$ the mass of the atom κ'. This equation can be equated with (A.23) and the dynamical equation is retrieved

$$\sum_{\kappa\alpha} C^{\kappa\alpha}_{\kappa'\gamma} U_{\kappa\alpha} = M_{\kappa'}\omega^2 U_{\kappa'\gamma}, \tag{A.26}$$

where the time-dependence on the displacements has been lifted due to cancellation. This eigenvalue problem gives m eigenvalues ω_m and m eigendisplacement vector $U_{m,\kappa\alpha}$. Conventionally one can work also with mass scaled displacement

$$\begin{aligned} \xi_{m,\kappa\alpha} &= \sqrt{M_\kappa} U_{m,\kappa\alpha} \\ \tilde{D}^{\kappa\alpha}_{\kappa'\gamma} &= \frac{1}{\sqrt{M_\kappa}} \tilde{C}^{\kappa\alpha}_{\kappa'\gamma} \frac{1}{\sqrt{M_{\kappa'}}}, \end{aligned} \tag{A.27}$$

with the associated eigenvalue problem

$$\sum_{\kappa\alpha} \tilde{D}^{\kappa\alpha}_{\kappa'\gamma} \xi_{m,\kappa\alpha} = \omega_m^2 \xi_{m,\kappa'\gamma}. \tag{A.28}$$

One can also show that the dynamical matrix is hermitian

$$\begin{aligned} \tilde{D}^{\kappa\alpha}_{\kappa'\gamma} &= \frac{1}{\sqrt{M_\kappa M_{\kappa'}}} \frac{\partial^2 E}{\partial R_{\kappa\alpha} R_{\kappa'\gamma}} \\ \tilde{D}^{\dagger\,\kappa\alpha}_{\kappa'\gamma} &= \frac{1}{\sqrt{M_\kappa M_{\kappa'}}} \frac{\partial^2 E}{\partial R_{\kappa'\gamma} R_{\kappa\alpha}} = \frac{1}{\sqrt{M_\kappa M_{\kappa'}}} \frac{\partial^2 E}{\partial R_{\kappa\alpha} R_{\kappa'\gamma}}, \end{aligned} \tag{A.29}$$

by independence of the total energy upon differential order.

Moreover, any eigenvalue problem with an hermitian matrix has eigenvector that are orthonormal and complete:

$$\begin{aligned} \sum_{\kappa\alpha} \xi^*_{m,\kappa\alpha} \xi^n_{\kappa\alpha} &= \delta_{mn} \\ \sum_{m} \xi^*_{m,\kappa\alpha} \xi_{m,\kappa'\gamma} &= \delta_{\kappa\kappa'}\delta_{\alpha\gamma}. \end{aligned} \tag{A.30}$$

Alternatively, one can choose to work with the masses explicitly included. The $U_{m,\kappa\alpha}$ from the generalized eigenvalue problem Eq. (A.26) also have to fulfill the orthonormality relation on their modes as well as the completeness relation

$$\begin{aligned} \sum_{\kappa\alpha} M_\kappa U^*_{m,\kappa\alpha} U_{n,\kappa\alpha} &= \delta_{mn} \\ \sum_{m} U^*_{m,\kappa\alpha} U_{m,\kappa'\gamma} \sqrt{M_\kappa M_{\kappa'}} &= \delta_{\kappa\kappa'}\delta_{\alpha\delta}. \end{aligned} \tag{A.31}$$

Multiplying the left side of Eq. (A.26) by $U^{m*}_{\kappa'\gamma}$ and using the orthonormality relation Eq. (A.31), the phonon frequencies are

$$\omega_m^2 = \sum_{\substack{\kappa\alpha \\ \kappa'\gamma}} U^*_{m,\kappa'\gamma} C_{\substack{\kappa\alpha \\ \kappa'\gamma}} U_{m,\kappa\alpha}. \tag{A.32}$$

A.4 INTEGRALS OF PHONON WAVEFUNCTIONS AND POWERS OF THE POSITION OPERATOR

We evaluate the integrals present in Eq. (1.7), with the Taylor expansion of the eigenenergy.

In the harmonic approximation, the phonon wavefunctions are obtained by solving the Schrödinger equation for the harmonic oscillator. We obtain [212]

$$\chi_{s_m,m}(z) = \left(\frac{\omega_m}{\pi}\right)^{1/4} \frac{H_{s_m}(\xi)}{\sqrt{2^{s_m} s_m!}} e^{-\frac{\xi^2}{2}}, \tag{A.33}$$

where $H_{s_m}(\xi) = (-1)^{s_m} e^{\xi^2} \frac{d^{s_m}}{d\xi^{s_m}} e^{-\xi^2}$ is the Hermite polynomial and $\xi = \sqrt{\omega_m} z$ is a dimensionless position variable. Hermite polynomials satisfy the following orthonormality condition

$$\int H_p(\xi) H_{s_m}(\xi) e^{-\xi^2} d\xi = s_m! \sqrt{\pi} 2^{s_m} \delta_{p s_m}. \tag{A.34}$$

The phonon wavefunctions are thus normalized, with

$$\int \chi_{s_m,m}(z)^* \chi_{s_m,m}(z) dz = 1. \tag{A.35}$$

The first-order integral cancels out, as an odd function integrates to zero.

$$\int \chi_{s_m,m}(z)^* z \chi_{s_m,m}(z) dz = 0. \tag{A.36}$$

Finally, the second-order integral can easily be solved in second quantization using

$$|\chi_{s_m,m}\rangle = \frac{(a^+)^{s_m}}{\sqrt{s_m!}} |0\rangle\,; \quad \xi^2 = \frac{1}{2}(a + a^+)^2. \tag{A.37}$$

We thus obtain

$$\begin{aligned}
&\int \chi_{s_m,m}(z)^* z^2 \chi_{s_m,m}(z)\,dz \\
&= \frac{1}{\omega_m} \langle \chi_{s_m,m} | \, \xi^2 \, | \chi_{s_m,m} \rangle \\
&= \frac{1}{\omega_m s_m!} \langle 0 | a^{s_m} \frac{1}{2} (a + a^+)^2 (a^+)^{s_m} | 0 \rangle \\
&= \frac{1}{\omega_m s_m!} \langle 0 | a^{s_m} \frac{1}{2} (aa^+ + a^+ a)(a^+)^{s_m} | 0 \rangle \\
&= \frac{1}{\omega_m s_m!} \langle 0 | a^{s_m} \frac{1}{2} (2aa^+ - 1)(a^+)^{s_m} | 0 \rangle \\
&= \frac{1}{\omega_m s_m!} \left(\langle 0 | a^{s_m+1} (a^+)^{s_m+1} | 0 \rangle - \frac{1}{2} \langle 0 | a^{s_m} (a^+)^{s_m} | 0 \rangle \right) \\
&= \frac{1}{\omega_m s_m!} \left((s_m + 1)! - \frac{1}{2} s_m! \right) = \left(\frac{2s_m + 1}{2\omega_m} \right).
\end{aligned} \tag{A.38}$$

A.5 STATISTICAL PHYSICS

This brief summary of the statistical physic described here is based on B. Fultz review on *Vibrational Thermodynamics of Materials* [77] and Wikipedia for the mathematical development of Helmholtz free energy [213].

The fundamental assumption of statistical quantum mechanics is that in any isolated system all micro-state are equally probable. The canonical ensemble is a statistical model that describes the thermodynamic equilibrium between two an infinite energy reservoir and the system one wants to study. The two systems can only exchange energy. The grand canonical ensemble is its extension that also allows for an exchange of particles between the two systems.



Figure A.1: G. Antonius and S. Poncé in front of L. E. Boltzmann at the Vienna Zentralfriedhof (August 2011).

In the canonical ensemble formalism, if one considers a single atom system with energy states $U_1, U_2, ...$, the total energy of the system and the heat reservoir is constant because of energy conservation:

$$U = U_{sys} + U_{res} = cst, \tag{A.39}$$

with U_{sys} and U_{res} the total energy of the system and the reservoir, respectively. At equilibrium, the number of microscopic states for an energy U_s is called the multiplicity $\Omega(U_s)$. The total multiplicity is the product of the system and the reservoir one:

$$\Omega(U_s) = \Omega_{sys}(U_s)\Omega_{res}(U - U_s). \tag{A.40}$$

From the equipartition theorem, the probability that the system is in any of the quantum states at a specific energy U_1 is given by the multiplicity of the reservoir[4] at energy $U - U_1$:

$$P(U_1) = \frac{\Omega_{res}(U - U_1)}{\sum_s \Omega(U_s)}. \tag{A.41}$$

By making use of the relative probability between two states, one can avoid the knowledge of the total multiplicity:

$$\frac{P(U_1)}{P(U_2)} = \frac{\Omega_{res}(U - U_1)}{\Omega_{res}(U - U_2)}. \tag{A.42}$$

One can now introduce a new quantity: the entropy $S(U_s)$ of the system in energy state U_s. Ludwig Eduard Boltzmann linked the entropy to the multiplicity through the Neperian logarithm to give his famous equation (see Fig. A.1):

$$S(U_s) = k_B \ln \Omega(U_s), \tag{A.43}$$

where the $k_B = 1.3806488\,10^{-23}$J/K pre-factor known as the Boltzmann constant is chosen to be consistent with the Kelvin scale for temperature. The Eq. (A.42) therefore becomes:

$$\frac{P(U_2)}{P(U_1)} = e^{\frac{S_{res}(U-U_2) - S_{res}(U-U_1)}{k_B}}. \tag{A.44}$$

4 $\Omega_{sys}(U_s) = 1$ since one is considering a defined state of the system

The thermodynamical identity states that:

$$dU = TdS - pdV + \mu dN, \tag{A.45}$$

with μ the chemical potential and N the number of particles.

For most physical system the change of volume and of particle is small and one can thus neglects the two last terms. This differential formula can be used in (A.44) because the reservoir is considered as big and hence the entropy of the reservoir only slightly changes for two states of the atom $S_{res}(U - U_2) - S_{res}(U - U_1) \approx dS_{res} \approx dU_{res}/T$. Since the system is isolated, what the atom loses goes to the reservoir and vice-versa:

$$\frac{P(U_2)}{P(U_1)} = e^{\frac{dU_{res}}{k_B T}} = e^{\frac{-dU_{sys}}{k_B T}}. \tag{A.46}$$

The total energy of a system is equal to the energy of one atom times the number of atoms present in the system. Since the system under consideration here only contains one atom, one can write:

$$\begin{aligned} \frac{P(U_2)}{P(U_1)} &= e^{\frac{U_2 - U_1}{k_B T}} \\ \frac{P(U_2)}{e^{-\frac{U_2}{k_B T}}} &= \frac{P(U_1)}{e^{-\frac{U_1}{k_B T}}} \triangleq \frac{1}{\mathcal{Z}}. \end{aligned} \tag{A.47}$$

In the last equation we have that two different varying function equal to each other must be equal to a constant. By convention this constant is the inverse of the partition function $\mathcal{Z}$. The probability of finding the atom in a state s is therefore given by:

$$P_s = \frac{1}{\mathcal{Z}} e^{-\frac{U_s}{k_B T}}, \tag{A.48}$$

where the exponential term is the Boltzmann factor for the state s. The partition function is actually more than a constant. It also hold physical meaning. By definition the sum of all probability must be equal to one and thus:

$$\sum_s P_s = \frac{1}{\mathcal{Z}} \sum_s e^{-\frac{U_s}{k_B T}} = 1. \tag{A.49}$$

The partition function

$$\mathcal{Z} = \sum_s e^{-\frac{U_s}{k_B T}} \tag{A.50}$$

is the sum of the Boltzmann factor. This means that the partition function estimates the number of available states in the system weighed by a function that depends on the energy of its states. Because the partition function is made of a sum of exponentially decaying function with increasing energy level, it means that only the few first states will contribute and hence the partition function indeed amount to counting the weighted number of available states there is in the system.

The partition function for a single harmonic oscillator of frequency $\omega_i = \varepsilon_i \hbar$ is:

$$\mathcal{Z}_i = \sum_n e^{-\beta(n+\frac{1}{2})\varepsilon_i}, \tag{A.51}$$

with $\beta \triangleq (k_B T)^{-1}$. The energy has the form $(n + 1/2)\varepsilon_i$ because it is the quantized eigenenergies of the harmonic oscillator. This last equation can be rewritten to make the geometrical series more apparent:

$$\mathcal{Z}_i = \sum_n e^{-\beta n \varepsilon_i} e^{\frac{-\beta\varepsilon_i}{2}} = \frac{e^{\frac{-\beta\varepsilon_i}{2}}}{1 - e^{-\beta\varepsilon_i}}. \tag{A.52}$$

The partition function for an harmonic solid with N atoms is the product of 3N independent oscillator partition functions:

$$\mathcal{Z}_N = \prod_i^{3N} \frac{e^{\frac{-\beta\varepsilon_i}{2}}}{1 - e^{-\beta\varepsilon_i}}. \tag{A.53}$$

For what follows, one needs to make the link between the partition function and the Helmholtz free energy $F = U - TS$. The average internal energy of a system is the expectation value of the total internal energy U. It is the sum of the probability to find an atom in a states s times the energy of that particular state:

$$U = \sum_s P_s E_s = -\frac{\partial \ln \mathcal{Z}}{\partial \beta}, \tag{A.54}$$

where the last equality can be straightforwardly obtained by injecting the value of the partition function (A.50). The generalized force corresponding to an external variable x when the system is in state s is:

$$f_s = -\frac{\partial E_s}{\partial x}. \tag{A.55}$$

The corresponding thermal average is:

$$f = \sum_s P_s f_s = \frac{1}{\beta}\frac{\partial \ln \mathcal{Z}}{\partial x}. \tag{A.56}$$

Changing the system's temperature parameter by $d\beta$ and the external variable by dx will lead to:

$$\begin{aligned} d\ln\mathcal{Z} &= \frac{\partial \ln \mathcal{Z}}{\partial \beta}d\beta + \frac{\partial \ln \mathcal{Z}}{\partial x}dx \\ &= -U d\beta + \beta f dx \\ &= -d(\beta U) + \beta dU + \beta f dx \\ dU &= \frac{1}{\beta}\left(d\ln\mathcal{Z} + d(\beta U) - \beta f dx\right). \end{aligned} \tag{A.57}$$

Since the thermodynamical relation $dU = TdS - fdx$ should hold we have:

$$\begin{aligned} TdS &= \frac{1}{\beta}\left(d\ln\mathcal{Z} + d(\beta U)\right) \\ dS &= k_B\, d\ln\mathcal{Z} + k_B\, d(\beta U) \\ S &= k_B \ln\mathcal{Z} + k_B \beta U + C = k_B \ln\mathcal{Z} + \frac{U}{T} + C. \end{aligned} \tag{A.58}$$

The value of the constant C is determined by considering the $T \to 0$ limit where the entropy $S = k_B \ln \Omega_0$ is the ground state entropy. The partition function becomes $\mathcal{Z}_0 = \Omega_0 e^{-\beta U_0}$ because all the possible states are ground states and therefore the partition function is the product of the ground state times the ground state multiplicity Ω_0.

$$\begin{aligned} S_0 &= k_B \ln(\Omega_0 e^{-\beta U_0}) + \frac{U_0}{T} + C = k_B \ln \Omega_0 \\ &= \cancel{k_B \ln \Omega_0} + k_B \ln(e^{-\beta U_0}) + \frac{U_0}{T} + C = \cancel{k_B \ln \Omega_0} \\ &\Rightarrow \cancel{k_B\left(\frac{-U_0}{k_B T}\right)} + \cancel{\frac{U_0}{T}} + C = 0. \end{aligned} \tag{A.59}$$

The $C = 0$ constant gives that the entropy is $S = k_B \ln \mathcal{Z} + U/T$ and therefore the Helmholtz Free energy is:

$$\begin{aligned} F &= U - TS = \cancel{U} - Tk_B \ln \mathcal{Z} - T\frac{\cancel{U}}{T} \\ F &= -k_B T \ln \mathcal{Z}. \end{aligned} \tag{A.60}$$

It is now possible to inject $\mathcal{Z}$ from (A.53) in the Helmholtz Free energy to get the vibrational Helmholtz Free energy:

$$\begin{aligned} F_{vib} &= -k_B T \ln(\prod_i^{3N} e^{\frac{-\beta\varepsilon_i}{2}}) + k_B T \ln(\prod_i^{3N}(1 - e^{-\beta\varepsilon_i})) \\ &= \frac{1}{2}\sum_i^{3N} \varepsilon_i + k_B T \sum_i^{3N} \ln(1 - e^{-\beta\varepsilon_i}). \end{aligned} \tag{A.61}$$

The vibrational internal energy U_{vib} is:

$$\begin{aligned} U_{vib} &= \frac{\partial \beta F_{vib}}{\partial \beta} = \frac{1}{2}\sum_i^{3N} \varepsilon_i + \sum_i^{3N} \varepsilon_i \frac{e^{-\beta\varepsilon_i}}{1 - e^{-\beta\varepsilon_i}} \\ &= \sum_i^{3N} \left[\frac{1}{e^{-\beta\varepsilon_i} - 1} + \frac{1}{2}\right] \varepsilon_i. \end{aligned} \tag{A.62}$$

The vibrational entropy can be obtained via a partial derivative:

$$\begin{aligned} \frac{\partial F_{vib}}{\partial T} = -S_{vib} =& k_B \sum_i^{3N} \ln(1 - e^{-\beta\varepsilon_i}) \\ &+ k_B T \sum_i^{3N} \frac{1}{(1 - e^{-\beta\varepsilon_i})} \frac{\varepsilon_i}{k_B T^2} e^{-\beta\varepsilon_i} \\ =& k_B \sum_i^{3N} \left[-\ln(1 - e^{-\beta\varepsilon_i}) + \frac{\beta\varepsilon_i}{(e^{\beta\varepsilon_i} - 1)}\right]. \end{aligned} \tag{A.63}$$

By introducing the Planck distribution for phonon occupancy versus temperature (i.e. Bose-Einstein distribution):

$$n = \frac{1}{e^{\beta\varepsilon_i} - 1} \tag{A.64}$$

$$\ln(1+n) = \ln\left(\frac{1}{1-e^{-\beta\varepsilon_i}}\right) \tag{A.65}$$

$$\ln\left(\frac{1+n}{n}\right) = \ln(e^{\beta\varepsilon_i}) = \beta\varepsilon_i, \tag{A.66}$$

the vibrational entropy becomes:

$$\begin{aligned} S_{vib} &= k_B \sum_i^{3N} [\ln(1+n) + n\beta\varepsilon_i] \\ &= k_B \sum_i^{3N} \left[\ln(1+n) + n\ln\left(\frac{1+n}{n}\right)\right] \\ &\boxed{= k_B \sum_i^{3N} [(1+n)\ln(1+n) - n\ln(n)]}. \end{aligned} \tag{A.67}$$

A.6 THE STATIC ELECTRONIC DIELECTRIC FUNCTION

The DW term involves the second-order derivative with respect to atomic displacements of the Hamiltonian and as such only depends on $V_{KS}[\rho](\hat{\mathbf{r}})$. We can use the static electronic dielectric function $\hat{\epsilon}$ to have an alternative physical view on the DW term. To treat integrals rigorously we apply the position operators of a function f onto their respective bra and ket $f(\mathbf{r}) = \langle\mathbf{r}|f(\hat{\mathbf{r}})|\mathbf{r}\rangle$ and get

$$\frac{\partial V_{KS}[\rho](\mathbf{r})}{\partial \mathbf{R}_{l\kappa\alpha}} = \int \epsilon^{-1}(\mathbf{r},\mathbf{r}') \frac{\partial V_{ionic}(\mathbf{r}')}{\partial \mathbf{R}_{l\kappa\alpha}} d\mathbf{r}' \tag{A.68}$$

$$= \int \epsilon^{-1}(\mathbf{r},\mathbf{r}') \left.\frac{\partial V_{l\kappa\alpha}}{\partial \mathbf{R}_{l\kappa\alpha}}\right|_{\mathbf{r}'-\mathbf{R}_{l\kappa\alpha}} d\mathbf{r}', \tag{A.69}$$

with

$$\epsilon^{-1}(\mathbf{r},\mathbf{r}') = \frac{\partial V_{KS}[\rho](\mathbf{r})}{\partial V_{ionic}(\mathbf{r}')}. \tag{A.70}$$

The Eq. (A.69) can then be derived a second time to give the DW term

$$\frac{\partial^2 V_{KS}[\rho](\mathbf{r})}{\partial \mathbf{R}_{l\kappa\alpha}\partial \mathbf{R}_{l'\kappa'\gamma}} = \int \frac{\partial \epsilon^{-1}(\mathbf{r},\mathbf{r}')}{\partial \mathbf{R}_{l'\kappa'\gamma}} \frac{\partial V_{l\kappa\alpha}}{\partial \mathbf{R}_{l\kappa\alpha}}\bigg|_{\mathbf{r}'-\mathbf{R}_{l\kappa\alpha}} d\mathbf{r}' + \int \epsilon^{-1}(\mathbf{r},\mathbf{r}') \frac{\partial^2 V_{l\kappa\alpha}}{\partial \mathbf{R}_{l\kappa\alpha}\partial \mathbf{R}_{l'\kappa'\gamma}}\bigg|_{\mathbf{r}'-\mathbf{R}_{l\kappa\alpha}} \delta_{\kappa\kappa'}\delta_{ll'} d\mathbf{r}', \quad \text{(A.71)}$$

where there is a $\delta_{\kappa\kappa'}\delta_{ll'}$ appearing in the second part of the equation because the ionic potential is a sum of separate contributions depending only on one atomic position (therefore its second derivative with respect to two different atoms positions is zero). From this equation, one can see that the first term has off-diagonal contributions in κ, κ' (beyond RIA). It is unfortunately not possible to map the diagonal contributions of Eq. (A.71) to the rigid-ion DW term of Eq. (1.64) nor the non-diagonal contributions to the non rigid-ion DW term of Eq. (1.69).

A.7 DEVELOPMENT OF THE FINITE-DIFFERENCE DW$_{\text{NRIA}}$ EQUATION

In this section, we focus on how to obtain the finite-difference expression given in Eq. (1.76) from the definition of $\frac{\partial \varepsilon_{n\mathbf{k}}^{\text{DW}_{\text{NRIA}}}}{\partial n_{m\mathbf{q}}}$ that was introduced in Eq. (1.69). The later expression contains two terms. Let us first focus on the first one.

Following the same approach used to derive Eq. (1.75), we can obtain a finite-difference version of the second-order derivative of the form

$$\begin{aligned}\left\langle u_{n\mathbf{k}}^{(0)}\right| \frac{\partial^2 \hat{H}_{\mathbf{k},\mathbf{k}}}{\partial R_{\kappa\alpha}(-\mathbf{q})\partial R_{\kappa\gamma}(\mathbf{q})} \left|u_{n\mathbf{k}}^{(0)}\right\rangle U^*_{m,\kappa\gamma}(\mathbf{q}) U_{m,\kappa\alpha}(\mathbf{q}) \\ = \frac{\partial^2}{\partial h^2}\Big\langle u_{n\mathbf{k}}\Big| \hat{H}_{\mathbf{k},\mathbf{k}}\Big[\Big\{R_{l\kappa'\alpha} + h v_{lm,\kappa\alpha}(\mathbf{q})\Big\}\Big] \\ + \hat{H}_{\mathbf{k},\mathbf{k}}\Big[\Big\{R_{l\kappa'\alpha} + h w_{lm,\kappa\alpha}(\mathbf{q})\Big\}\Big]\Big| u_{n\mathbf{k}}^{(0)}\Big\rangle\Big|_{h=0}. \quad \text{(A.72)}\end{aligned}$$

It is worthwhile to dwell into the reasons for keeping the full Hamiltonian. As introduced in Eq. (1.63), the Hamiltonian is the sum of an electronic kinetic energy $\hat{T}$, an external potential $V_{l\kappa}(\hat{\mathbf{r}} - \mathbf{R}_{l\kappa})$ that describes the electron-ion interaction and an Hartree and exchange-correlation $\hat{V}_{\text{Hxc}}[\rho](\hat{\mathbf{r}})$ potential that describes the electron-electron interactions. Within the adiabatic approximation, the kinetic energy is independent of atomic position. The second-order derivative of the Hartree and exchange-correlation with respect to atomic positions is, however, non-zero in

general due to the modification of the electronic density upon second-order ionic motion. Furthermore, the second-order derivative of the external potential is zero when $\kappa \neq \kappa'$ since the potential only depends on one atomic coordinate. When $\kappa = \kappa'$, the external potential part of the first term in Eq. (1.76) is zero only when

$$\mathbf{q} = \alpha \mathbf{b}_1 + \beta \mathbf{b}_2 + \gamma \mathbf{b}_3 \quad \text{with } \alpha = \beta = \gamma = n/2, \tag{A.73}$$

with n an integer number and $\mathbf{b}_1$, $\mathbf{b}_2$, $\mathbf{b}_3$ are reciprocal lattice vectors.

To demonstrate the latter statement, we define

$$\mathbf{y} \triangleq \hat{\mathbf{r}} - \mathbf{R}_{l\kappa} - h_\kappa \mathbf{U}_{m,\kappa}(\mathbf{q}) e^{-i\mathbf{q}\cdot\mathbf{R}_l} \tag{A.74}$$

and

$$\tilde{\mathbf{y}} \triangleq \hat{\mathbf{r}} - \mathbf{R}_{l\kappa} - h_\kappa \mathbf{U}_{m,\kappa}(\mathbf{q}) \tag{A.75}$$

Then, the external potential becomes

$$\begin{aligned} &\frac{\partial^2}{\partial h_\kappa^2} \left\langle u_{n\mathbf{k}}^{(0)} \right| \sum_{l\kappa} V_{l\kappa}(\mathbf{y}) - V_{l\kappa}(\tilde{\mathbf{y}}) \left| u_{n\mathbf{k}}^{(0)} \right\rangle \Big|_{h_\kappa = 0} = \\ &\frac{\partial}{\partial h_\kappa} \left\langle u_{n\mathbf{k}}^{(0)} \right| \sum_{l\kappa} \frac{\partial V_{l\kappa}(\mathbf{y})}{\partial \mathbf{y}} \cdot \frac{\partial \mathbf{y}}{\partial h_\kappa} - \frac{\partial V_{l\kappa}(\tilde{\mathbf{y}})}{\partial \tilde{\mathbf{y}}} \cdot \frac{\partial \tilde{\mathbf{y}}}{\partial h_\kappa} \left| u_{n\mathbf{k}}^{(0)} \right\rangle \Big|_{h_\kappa = 0}. \end{aligned} \tag{A.76}$$

This in turn gives

$$\begin{aligned} &\frac{\partial}{\partial h_\kappa} \left\langle u_{n\mathbf{k}}^{(0)} \right| \sum_{l\kappa} -\frac{V_{l\kappa}(\mathbf{y})}{\partial \mathbf{y}} \cdot \mathbf{U}_{m,\kappa}(\mathbf{q}) e^{-i\mathbf{q}\cdot\mathbf{R}_l} \\ &+ \frac{\partial V_{l\kappa}(\tilde{\mathbf{y}})}{\partial \tilde{\mathbf{y}}} \cdot \mathbf{U}_{m,\kappa}(\mathbf{q}) \left| u_{n\mathbf{k}}^{(0)} \right\rangle \Big|_{h_\kappa = 0} = \\ &\left\langle u_{n\mathbf{k}}^{(0)} \right| \sum_{l\kappa\alpha\beta} \frac{\partial^2 V_{l\kappa}(\hat{\mathbf{r}} - \mathbf{R}_{l\kappa}^{(0)})}{\partial(\hat{\mathbf{r}} - \mathbf{R}_{l\kappa})_\alpha \partial(\hat{\mathbf{r}} - \mathbf{R}_{l\kappa})_\beta} \\ &\qquad U_{m,\kappa\alpha}(\mathbf{q}) U_{m,\kappa\beta}(\mathbf{q}) \left(e^{2i\mathbf{q}\cdot\mathbf{R}_l} - 1 \right) \left| u_{n\mathbf{k}}^{(0)} \right\rangle \Big|_{h_\kappa = 0}, \end{aligned} \tag{A.77}$$

where, for the last equality, we have taken the limit of vanishing h_κ.

This is the reason why the Hamiltonian appears in the first terms of Eq. (1.76) while the last term (in which the DW term is evaluate at $\mathbf{q} = \Gamma$) involve only $\hat{V}_{\text{Hxc}}$.

We now evaluate the second term of Eq. (1.69). To this end, we introduce a collective translational displacement in the γ direction

$$\frac{\partial}{\partial T_\gamma} \triangleq \sum_{\kappa'} \frac{\partial}{\partial R_{\kappa'\gamma}(\Gamma)} \tag{A.78}$$

and a second-order displacement vector of the atom κ in the direction α and γ

$$\frac{\partial}{\partial S_\gamma} \triangleq \sum_{\kappa\alpha} U^*_{m,\kappa\gamma}(\mathbf{q}) U_{m,\kappa\alpha}(\mathbf{q}) \frac{\partial}{\partial R_{\kappa\alpha}(\mathbf{\Gamma})}. \tag{A.79}$$

We therefore have the following relation

$$\sum_{\substack{\kappa\alpha \\ \kappa'\gamma}} \left\langle u^{(0)}_{n\mathbf{k}} \right| \frac{\partial^2 \hat{V}_{Hxc}}{\partial R_{\kappa\alpha}(\mathbf{\Gamma}) \partial R_{\kappa'\gamma}(\mathbf{\Gamma})} \left| u^{(0)}_{n\mathbf{k}} \right\rangle U^*_{m,\kappa\gamma}(\mathbf{q}) U_{m,\kappa\alpha}(\mathbf{q}) = \sum_\gamma \left\langle u^{(0)}_{n\mathbf{k}} \right| \frac{\partial^2 \hat{V}_{Hxc}}{\partial S_\gamma \partial T_\gamma} \left| u^{(0)}_{n\mathbf{k}} \right\rangle. \tag{A.80}$$

A.8 SYMMETRY PROPERTIES

A.8.1 *Ground states wavefunction*

Any crystal structure is fully defined by three primitive vectors $\mathbf{a}, \mathbf{b}$ and $\mathbf{c}$ that determine the primitive unit cell and by basis vectors that determines the position of the atoms within the unit cell. All the symmetry operations that leave the crystal unchanged form a space group. There are in three dimension 230 such symmetry operations: translation, proper (ordinary) rotation, improper rotation (rotation of its mirror image) and a combination of rotations followed by a fractional translation. A space group without any fractional translation is said to be *symmorphic*. A symmetry operation will be denoted by $\hat{\mathcal{R}}_\mathbf{t}$ where $\mathcal{R}$ is a real orthonormal matrix associated to a rotation and $\mathbf{t}$ a fractional translation.

The first part on the derivation of the symmetry properties of the wavefunction is based on the PhD thesis of M. Giantomassi [214] and the book from G.F. Bassani and G. P. Parravicini [215].

The application of a symmetry operation $\hat{\mathcal{R}}_\mathbf{t}$ on the vector $\mathbf{R}_i$ that defines the position of an atom within the unit cell gives

$$\hat{\mathcal{R}}_\mathbf{t} \mathbf{R}_i \triangleq \mathcal{R}^{-1}(\mathbf{R}_i - \mathbf{t}) = \mathbf{R}_j + \mathbf{R}, \tag{A.81}$$

where $\mathbf{R}_j$ is the position vector of an atom of the same type as $\mathbf{R}_i$ and in the same unit cell and $\mathbf{R}$ is a lattice translation. The application of a symmetry operation to a generic spacial function is defined by

$$\hat{\mathcal{R}}_\mathbf{t} F(\mathbf{r}) \triangleq F(\mathcal{R}^{-1}(\mathbf{r} - \mathbf{t})), \tag{A.82}$$

where this equality means that the value of a rotated (and eventually translated) function at a position $\mathbf{r}$ in space is equal to the value of the original function evaluated at the inversely rotated (and eventually translated) positions.

Given that a symmetry operation commutes with the Hamiltonian $\hat{H}$ of the crystal, one can show that the an eigenstate on which a symmetry operation has been applied is also an eigenstate of the Schrödinger problem with the same eigenvalue but a different crystalline momentum

$$\begin{aligned}
\hat{H}\Psi_{n\mathbf{k}}(\mathbf{r}) =& \varepsilon_{n\mathbf{k}}\Psi_{n\mathbf{k}}(\mathbf{r}) \\
\hat{H}\hat{\mathcal{R}}_{\mathbf{t}}\Psi_{n\mathbf{k}}(\mathbf{r}) =& \hat{\mathcal{R}}_{\mathbf{t}}\hat{H}\Psi_{n\mathbf{k}}(\mathbf{r}) = \varepsilon_{n\mathbf{k}}\hat{\mathcal{R}}_{\mathbf{t}}\Psi_{n\mathbf{k}}(\mathbf{r}) \\
\hat{\mathcal{R}}_{\mathbf{t}}\Psi_{n\mathbf{k}}(\mathbf{r}+\mathbf{R}) =& \Psi_{n\mathbf{k}}\left(\mathcal{R}^{-1}(\mathbf{r}+\mathbf{R}-\mathbf{t})\right) \\
=& e^{i\mathbf{k}\cdot\mathcal{R}^{-1}(\mathbf{r}+\mathbf{R}-\mathbf{t})}u_{n\mathbf{k}}\left(\mathcal{R}^{-1}(\mathbf{r}-\mathbf{t})\right) \\
=& e^{i(\mathcal{R}^{-1})^{t}\mathbf{k}\cdot\mathbf{R}}\Psi_{n\mathbf{k}}\left(\mathcal{R}^{-1}(\mathbf{r}-\mathbf{t})\right) \\
=& e^{i\mathcal{R}\mathbf{k}\cdot\mathbf{R}}\hat{\mathcal{R}}_{\mathbf{t}}\Psi_{n\mathbf{k}}(\mathbf{r}),
\end{aligned} \tag{A.83}$$

where we have used in the last equality the orthonormality of the rotation matrix and where $\mathbf{R}$ is a vector of the direct Bravais lattice. In the presence of a set of degenerate states $\mathcal{C}_{n\mathbf{k}}$, the new Bloch eigenstate will be given by an appropriate linear combination of the degenerate states with wave vector $\mathcal{R}\mathbf{k}$

$$\hat{\mathcal{R}}_{\mathbf{t}}\Psi_{n\mathbf{k}}(\mathbf{r}) = \Psi_{n\mathbf{k}}\left(\mathcal{R}^{-1}(\mathbf{r}-\mathbf{t})\right) = \sum_{i\in\mathcal{C}_{n\mathbf{k}}} D_{in}(\mathcal{R},\mathbf{k})\Psi_{i\mathcal{R}\mathbf{k}}(\mathbf{r}). \tag{A.84}$$

This equality can be expressed in terms of the periodic part of the wavefunction

$$\begin{aligned}
e^{i\mathbf{k}\cdot\mathcal{R}^{-1}(\mathbf{r}-\mathbf{t})}u_{n\mathbf{k}}\left(\mathcal{R}^{-1}(\mathbf{r}-\mathbf{t})\right) &= \sum_{i\in\mathcal{C}_{n\mathbf{k}}} D_{in}(\mathcal{R},\mathbf{k})e^{i\mathcal{R}\mathbf{k}\cdot\mathbf{r}}u_{i\mathcal{R}\mathbf{k}}(\mathbf{r}) \\
e^{i\mathcal{R}\mathbf{k}\cdot(\mathbf{r}-\mathbf{t})}u_{n\mathbf{k}}\left(\mathcal{R}^{-1}(\mathbf{r}-\mathbf{t})\right) &= \sum_{i\in\mathcal{C}_{n\mathbf{k}}} D_{in}(\mathcal{R},\mathbf{k})\cancel{e^{i\mathcal{R}\mathbf{k}\cdot\mathbf{r}}}u_{i\mathcal{R}\mathbf{k}}(\mathbf{r})
\end{aligned} \tag{A.85}$$

This last equation has the following set of consequences

$$\begin{aligned}
\varepsilon_{n\mathcal{R}\mathbf{k}} &= \varepsilon_{n\mathbf{k}} \\
u_{n\mathcal{R}\mathbf{k}}(\mathbf{r}) &= e^{-i\mathcal{R}\mathbf{k}\cdot\mathbf{t}}\sum_{i\in\mathcal{C}_{n\mathbf{k}}} D_{in}(\mathcal{R},\mathbf{k})^{-1}u_{ik}\left(\mathcal{R}^{-1}(\mathbf{r}-\mathbf{t})\right) \\
u_{n\mathcal{R}\mathbf{k}}(\mathbf{G}) &= e^{-i(\mathcal{R}\mathbf{k}+\mathbf{G})\cdot\mathbf{t}}\sum_{i\in\mathcal{C}_{n\mathbf{k}}} D_{in}(\mathcal{R},\mathbf{k})^{-1}u_{ik}\left(\mathcal{R}^{-1}\mathbf{G}\right).
\end{aligned} \tag{A.86}$$

A.8.2 *Electron-phonon matrix element*

The electron-phonon matrix can also be made symmetric in **k**-points.

$$\hat{\mathcal{R}}_t \mathrm{GKK}^m_{nn'}(\mathbf{k},\mathbf{q}) = \sum_{l''\kappa\alpha} \int \hat{\mathcal{R}}_t \Psi^*_{n,\mathbf{k}+\mathbf{q}}(\mathbf{r}) e^{i\mathbf{q}\cdot\mathbf{R}^{l''}} \hat{\mathcal{R}}_t \left[\frac{\partial \hat{H}}{\partial R^{l''}_{\kappa\alpha}} \Psi_{n',\mathbf{k}}(\mathbf{r})\right] \hat{\mathcal{R}}_t U^m_{\kappa\alpha}(\mathbf{q}) d\mathbf{r}, \quad \text{(A.87)}$$

where we used the fact that the rotation of a product is equal to the product of the rotations.

If the symmetry operations belong to the little group of **q** taking into account time reversal or an umklapp vector that bring the q-point into itself (i.e. $\mathcal{R}\mathbf{q} = \mathbf{q}$, $\mathcal{R}\mathbf{q} = -\mathbf{q}$, $\mathcal{R}\mathbf{q} = \mathbf{q} + \mathbf{G}_\mathbf{r}$ or $\mathcal{R}\mathbf{q} = -\mathbf{q} - \mathbf{G}_\mathbf{r}$) and if the Hamiltonian has a local potential then

$$\frac{\partial \hat{H}}{\partial R^{l''}_{\kappa\alpha}} \Psi_{n\mathbf{k}}(\mathbf{r}) = \frac{\partial}{\partial R^{l''}_{\kappa\alpha}} \left[-\frac{1}{2}\nabla^2 + V_{\mathrm{loc}}(\mathbf{r})\right] \Psi_{n\mathbf{k}}(\mathbf{r}) \quad \text{(A.88)}$$

But using the common derivation rules of an operator and a function one can see that

$$\frac{\partial}{\partial R^{l''}_{\kappa\alpha}} \left[\nabla^2 \Psi_{n\mathbf{k}}\right] = \frac{\partial \nabla^2}{\partial R^{l''}_{\kappa\alpha}} \Psi_{n\mathbf{k}} + \nabla^2 \frac{\partial \Psi_{n\mathbf{k}}}{\partial R^{l''}_{\kappa\alpha}}. \quad \text{(A.89)}$$

If the operator ∇^2 does not depend upon atomic position (which is the case in the adiabatic approximation[5]) then

$$\frac{\partial}{\partial R^{l''}_{\kappa\alpha}} \left[\nabla^2 \Psi_{n\mathbf{k}}\right] = \nabla^2 \frac{\partial \Psi_{n\mathbf{k}}}{\partial R^{l''}_{\kappa\alpha}}. \quad \text{(A.90)}$$

This means that Eq. (A.88) becomes

$$\frac{\partial \hat{H}}{\partial R^{l''}_{\kappa\alpha}} \Psi_{n\mathbf{k}}(\mathbf{r}) = \frac{\partial V_{\mathrm{loc}}(\mathbf{r})}{\partial R^{l''}_{\kappa\alpha}} \Psi_{n\mathbf{k}}(\mathbf{r}) \quad \text{(A.91)}$$

One can now apply the symmetry operation to Eq. (A.88)

$$\begin{aligned} \hat{\mathcal{R}}_t \left[\frac{\partial \hat{H}}{\partial R^{l''}_{\kappa\alpha}} \Psi_{n\mathbf{k}}\right] &= \hat{\mathcal{R}}_t \left[\frac{\partial V_{\mathrm{loc}}(\mathbf{r})}{\partial R^{l''}_{\kappa\alpha}} \Psi_{n\mathbf{k}}(\mathbf{r})\right] \\ &= \frac{\partial V_{\mathrm{loc}}\left(\mathcal{R}^{-1}(\mathbf{r}-\mathbf{t})\right)}{\partial R^{l''}_{\kappa\alpha}} \Psi_{n\mathbf{k}}\left(\mathcal{R}^{-1}(\mathbf{r}-\mathbf{t})\right), \end{aligned} \quad \text{(A.92)}$$

5 Beyond the adiabatic approximation, the electronic cloud follows the ionic motion with a delay. This means that the Laplacian is evaluated at a different position on the function (or equivalently that the Laplacian is evaluated at the same position but the function has moved).)

where in the last equality one has used the fact that the rotation of a product is equal to the product of the rotations. In addition, most physical potential will be symmetric under rotation $V_{loc}(\mathbf{r}) = V_{loc}\left(\mathcal{R}^{-1}(\mathbf{r}-\mathbf{t})\right)$. With these development, the Eq. (A.87) becomes

$$\begin{aligned}\hat{\mathcal{R}}_t GKK^m_{nn'}(\mathbf{k},\mathbf{q}) = \sum_{l''\kappa\alpha} e^{i\mathbf{q}\cdot\mathbf{R}^{l''}} \int \Psi^*_{n,\mathbf{k}+\mathbf{q}}\left(\mathcal{R}^{-1}(\mathbf{r}-\mathbf{t})\right) \frac{\partial V_{loc}(\mathbf{r})}{\partial R^{l''}_{\kappa\alpha}} \\ \Psi_{n',\mathbf{k}}\left(\mathcal{R}^{-1}(\mathbf{r}-\mathbf{t})\right) \sum_{m'\kappa'\gamma} K_{mm'} L_{\kappa\kappa'} P_{\alpha\gamma} U^{m'}_{\kappa'\gamma}(\mathbf{q}) d\mathbf{r}, \end{aligned} \quad (A.93)$$

with $K_{mm'}$ the character matrix of the irreducible mode representation, $L_{\kappa\kappa'}$ the atomic type matrix that describes the exchange of atom types under a symmetry operation and $P_{\alpha\gamma}$ the symmetry operation matrix of the Cartesian coordinates.

One can then make a change of variable $\mathbf{y} = \mathcal{R}^{-1}(\mathbf{r}-\mathbf{t})$ and get

$$\begin{aligned}\hat{\mathcal{R}}_t GKK^m_{nn'}(\mathbf{k},\mathbf{q}) &= \sum_{l''\kappa\alpha} e^{i\mathbf{q}\cdot\mathbf{R}^{l''}} \int \Psi^*_{n,\mathbf{k}+\mathbf{q}}(\mathbf{y}) \frac{\partial V_{loc}\left(\mathcal{R}\mathbf{y}+\mathbf{t}\right)}{\partial R^{l''}_{\kappa\alpha}} \\ &\quad \Psi_{n',\mathbf{k}}(\mathbf{y}) \sum_{m'\kappa'\gamma} K_{mm'} L_{\kappa\kappa'} P_{\alpha\gamma} U^{m'}_{\kappa'\gamma}(\mathbf{q}) \mathcal{R} d\mathbf{y} \\ &= \sum_{l''\kappa\alpha} e^{i\mathbf{q}\cdot\mathbf{R}^{l''}} \int \Psi^*_{n,\mathbf{k}+\mathbf{q}}(\mathbf{y}) \sum_{\kappa''\beta} L^{-1}_{\kappa,\kappa''} P^{-1}_{\alpha\beta} \frac{\partial V_{loc}(\mathbf{y})}{\partial R^{l''}_{\kappa''\beta}} \\ &\quad \Psi_{n',\mathbf{k}}(\mathbf{y}) \sum_{m'\kappa'\gamma} K_{mm'} L_{\kappa\kappa'} P_{\alpha\gamma} U^{m'}_{\kappa'\gamma}(\mathbf{q}) d\mathbf{y}, \end{aligned} \quad (A.94)$$

where one has used the fact that the rotation of an infinitesimal volume elements is the element itself and on that

$$\frac{\partial V_{loc}\left(\mathcal{R}\mathbf{y}+\mathbf{t}\right)}{\partial R^{l''}_{\kappa\alpha}} = \frac{\partial V_{loc}(\mathbf{y})}{\partial \mathcal{R}^{-1}(R_{\kappa\alpha}-\mathbf{t})} = \sum_{\kappa''\beta} L^{-1}_{\kappa,\kappa''} P^{-1}_{\alpha\beta} \frac{\partial V_{loc}(\mathbf{y})}{\partial R^{l''}_{\kappa''\beta}}. \quad (A.95)$$

One can also use the fact that the rotations matrices cancel out when integrated over the directions and atoms

$$\begin{aligned}\sum_{\alpha} P^{-1}_{\alpha\beta} P_{\alpha\gamma} &= \delta_{\beta\gamma} \\ \sum_{\kappa} L^{-1}_{\kappa\kappa''} L_{\kappa\kappa'} &= \delta_{\kappa''\kappa'}, \end{aligned} \quad (A.96)$$

which finally gives us

$$\hat{\mathcal{R}}_t \mathrm{GKK}^{m}_{nn'}(\mathbf{k},\mathbf{q}) = \sum_{l''\kappa\alpha} e^{i\mathbf{q}\cdot\mathbf{R}^{l''}} \int \Psi^{*}_{n,\mathbf{k}+\mathbf{q}}(\mathbf{r}) \frac{\partial V_{\mathrm{loc}}(\mathbf{r})}{\partial R^{l''}_{\kappa\alpha}} \Psi_{n',\mathbf{k}}(\mathbf{r}) \sum_{m'} K_{mm'} U^{m'}_{\kappa\alpha}(\mathbf{q}) d\mathbf{r}. \quad \text{(A.97)}$$

This means that, except for the mixing of the modes, the GKK matrices are invariant upon rotation. If one now wants to express the GKK in term of another **k**-point related by symmetries

$$\mathrm{GKK}^{m}_{nn'}(\mathcal{R}\mathbf{k},\mathbf{q}) = \sum_{l''\kappa\alpha} e^{i\mathbf{q}\cdot\mathbf{R}^{l''}} \int \sum_{i\in\mathcal{C}_{i\mathbf{k}}} D^{-1}_{in}(\mathcal{R},\mathbf{k}+\mathbf{q}) \Psi^{*}_{i,\mathbf{k}+\mathbf{q}}(\mathbf{r}) \frac{\partial V_{\mathrm{loc}}(\mathbf{r})}{\partial R^{l''}_{\kappa\alpha}} \sum_{j\in\mathcal{C}_{j\mathbf{k}}} D^{-1}_{jn}(\mathcal{R},\mathbf{k}) \Psi_{j,\mathbf{k}}(\mathbf{r}) \sum_{m'} K_{mm'} \sum_{m''\in\mathcal{C}_{m''\mathbf{q}}} \mathcal{N}_{m''m'}(\mathcal{R},\mathbf{q})^{-1} U^{m}_{\kappa\alpha}(\mathbf{q}) d\mathbf{r}, \quad \text{(A.98)}$$

where $\mathcal{N}_{m''m'}(\mathcal{R},\mathbf{q})$ is an appropriate linear combination of degenerate phonon modes $\mathcal{C}_{m''\mathbf{q}}$ at a defined **q**-point.

An equivalent development can be made for **q** when we are in the little group of **k**. If we want to consider **k**-point related by symmetry but with **q**-points out of the little group, we have to average the equivalent **k**-points to "symmetrize" it. In practice, it means that when using no symmetries on the **k**-point grid and on the **q**-point grid, the results are physical and the ZPR is the same for two **k**-point related by symmetries. On the other hand, by using no symmetries on the **k** (or **q**) point grid but using symmetries for the **q** (or **k**) point grid, an average over the non symmetry based grid is required to get physical results. Due to the use of different gauges in Abinit for the ground-state and perturbed wavefunction, it is not possible to use the symmetries on both **k** and **q** grid. Although we were not able to formally demonstrated it, it should be possible to tackle this issue and find a gauge invariant ZPR.

A.9 CALCULATION DETAILS FOR DIAMOND

We compute the ZPR of the top of the valence band of diamond (Γ'_{25v}) and the first optically accessible state (Γ_{15c}) using a $4\times4\times4$ **Γ**-centered **q**-point grid. The lattice parameter (3.55Å) was obtained by relaxation of the structure with a Trouiller-Martins LDA pseudopotential [100].

A.9.1 *Frozen-phonon calculations*

The atoms are displaced along the normalized 3N-components polarization vectors, given by

$$\xi_{m,\kappa} = \sqrt{\frac{M}{M_\kappa}} \mathbf{U}_{m,\kappa} e^{i\mathbf{q}\cdot\mathbf{R}_l}, \tag{A.99}$$

with $\mathbf{U}_{m,\kappa}$ being one of the orthogonal eigenvectors of the dynamical matrix at wavevector $\mathbf{q}$ and $\mathbf{R}_l$ is a lattice vector. The displacement vector is thus $\Delta\mathbf{x}_\tau = z\ \xi_{m,\kappa}$. A single displacement (together with the equilibrium structure) is sufficient to compute the second-order derivative, since a positive displacement is equivalent to a negative displacement, except at $\mathbf{q} = \mathbf{\Gamma}$, where an additional negative displacement is needed.

The polarization vectors were obtained from DFPT. For the main DFT and G_0W_0 calculations, we used $z = 0.0035$Å. For the GW calculation, we used $z = 0.035$Å. To compare the frozen-phonon DFT calculation with the DFPT scheme, we used $z = 0.00035$Å.

A.9.2 *Many-body effects*

The frozen-phonon G_0W_0 calculations were performed using the Hybertsen-Louie plasmon-pole model (PPM). This PPM offers the most efficient scheme to compute the G_0W_0 corrections to the eigenvalues. Although other schemes (using the Godby-Needs PPM or full-frequency calculations) result in different band gaps, they give similar values for the ZPR.

The parameters needed to reach convergence in the EPCE are less stringent than those required for the eigenvalues themselves, since the EPCE deals with eigenvalue differences. The dielectric matrix and the self-energy were computed with a $4 \times 4 \times 4$ unshifted $\mathbf{k}$-points grid, 96 unoccupied bands, a kinetic energy cut-off of 30 Ha for the wavefunctions and 7.5 Ha for the dielectric matrix.

For the self-consistent GW calculation, we performed a full-frequency calculation with the contour deformation technique [148]. The frequency integration was performed with 48 frequencies between 0 and 240 eV on the real axis, and 6 frequencies on the imaginary axis. We computed the difference between the EPCE in GW and in G_0W_0 from the differences of the EPCE values between the last and the fist step of the self-consistent procedure.

A.9.3 *DFPT calculations*

In the static AHC theory, the EPCE are split into the Fan and DW terms, giving an expression of the form

$$\frac{\partial \varepsilon_{n\mathbf{k}}}{\partial n_{m\mathbf{q}}} = \frac{1}{2\omega_{m\mathbf{q}}} \sum_{n'} \frac{\Lambda^{\mathrm{Fan}}_{nn'\mathbf{kq}}}{\varepsilon_{n\mathbf{k}} - \varepsilon_{n'\mathbf{k}+\mathbf{q}} + i\delta} + \frac{\Lambda^{\mathrm{DW}}_{nn'\mathbf{kq}}}{\varepsilon_{n\mathbf{k}} - \varepsilon_{n'\mathbf{k}} + i\delta} \tag{A.100}$$

where the small parameter δ is a real positive number which avoids divergent points when the energy differences are small and where Λ^{Fan} and Λ^{DW} are related to the matrix elements of the coupling potential for the phonon mode m and can be deduced from direct comparison with Eq. (1.79) in the adiabatic limit

The divergences occur either at finite $\mathbf{q}$ vectors, when a band crosses the corrected levels (Γ'_{25v}, Γ_{15c}), in which case they cancel out after integration over the BZ, or they occur near $\mathbf{q} = \mathbf{\Gamma}$, in which case the weight of these elements vanishes as q^2 and they integrate to a finite value.

In our study, we used $\delta = 0.1$ eV, similar to previous works [62, 67]. This value is on the order of typical phonon frequencies, which would be included in the denominators of Eq. (A.100) in a dynamical theory like Eq. (1.79). Hence, we expect the error introduced by this parameter to be comparable with the error induced by the static approximation.

The DFPT calculations were performed with the technique of [19] in which the summation over all bands is cut at some band index M, and the contribution of the bands above M is obtained from a Sternheimer equation (see Eq. (A.10)). The choice of this parameter ($M = 8$ in our study) only affects the speed of the algorithm, and not the numerical results.

A.9.4 *Interpolating the many-body effects*

The G_0W_0 EPCE per q-point as a function of the DFT EPCE were modeled using third-order polynomials with a linear continuation outside our sample points range, as shown in Figure A.2.

A.9.5 G_0W_0 *calculation of the bare band gap*

The bare G_0W_0 band gap (before ZPR corrections) was computed with a full-frequency calculation. The frequency integration was performed

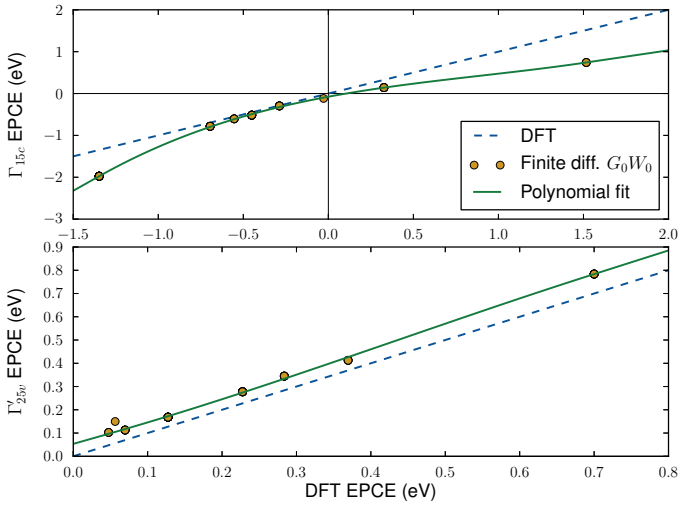


Figure A.2: Modeling of the G_0W_0 EPCE per **q**-point as a function of the DFT EPCE. The yellow discs are the G_0W_0 frozen-phonon results, the solid green line is the polynomial fit on these results, and the dashed blue line is the DFT EPCE (y=x). Courtesy of G. Antonius.

with 32 frequencies between 0 and 40 eV on the real axis, and 6 frequencies on the imaginary axis.

We used a $12 \times 12 \times 12$ unshifted k-points grid, with 288 unoccupied bands, a kinetic energy cut-off of 30 Ha for the wavefunctions and 15 Ha for the dielectric matrix.

A sensitive factor that affects a G_0W_0 calculation is the relaxed geometry, which depends on the details of the pseudopotential. Our cell parameter (3.5473Å) was obtained by relaxation of the structure, and we checked that other cell parameters in the range [3.52Å-3.56Å] change the G_0W_0 gap by ± 0.04 eV at most.

A G_0W_0 calculation on the LDA band structure of diamond typically underestimates the bare band gap (7.483 eV). On the other hand, a self-consistent GW calculation overestimates the bare band gap (8.227 eV). Such an important overestimation might be due in part to the fact that the bare band gap is being used in the self-consistent process, rather than the renormalized band gap. In order to bring our G_0W_0 calculation closer to a self-consistent scheme in which the ZPR would be taken into account, we use a scissor operator (Δ) of 1.484 eV on the LDA band structure, bringing the starting gap to the experimental value of 7.100 eV, which results in a direct G_0W_0 band gap of 7.732 eV.

The connection between our LDA $+\Delta+$ G_0W_0 calculation and a hypothetical self-consistent $GW+\Sigma^{ep}$ scheme depends on several assumptions. First, it assumes that a scissor shift reproduces well the self-consistent GW band structure, at least for the states near the direct band gap at Γ, which can be assessed from Fig. A.3. Then, it supposes that the ZPR does bring the bare GW band gap to the renormalized gap targeted by the scissor shift, which is the case with a significant closing a the gap due to electron-phonon coupling. Moreover, we verified that any value in the range [1.2 eV-1.8 eV] for the scissor operator would vary the final gap by ± 0.05 eV at most. Finally, it assumes that the bare starting band structure would be that of a stable self-consistent solution, which we can not verify within the scope of this work. Nonetheless, we use this calculation as an estimate of the bare optical band gap solely to discuss our results for the zero-point renormalization.

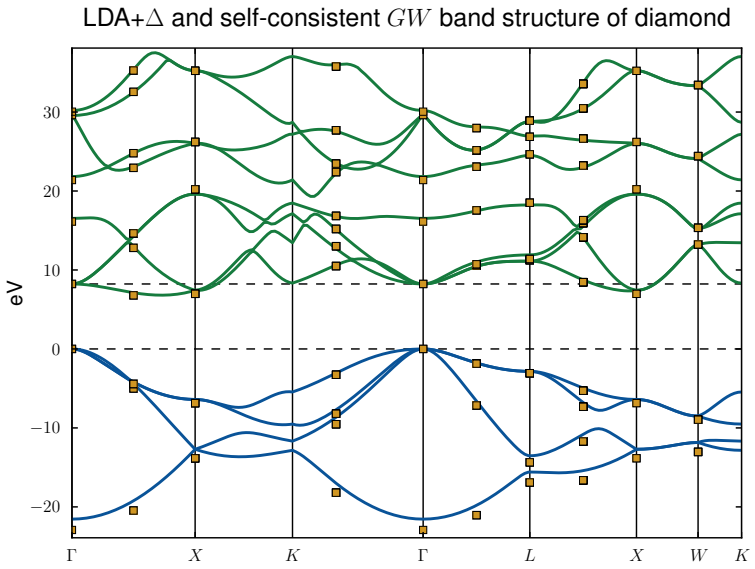


Figure A.3: Band structure of diamond from a self-consistent GW calculation (yellow squares), as well as the LDA band structure (solid lines) with a scissor shift of 2.621 eV applied to match the GW band gap. Courtesy of G. Antonius.

A.10 CALCULATION DETAILS FOR GAAS

We computed the ZPR in GaAs for the top of the valence bands (Γ_{8v}) and the bottom of the conduction bands (Γ_{6c}), using the DFPT as well as the

FP method. We used a $4 \times 4 \times 4$ **q**-point grid, which yields a converged ZPR value in terms of **q**-points density. Figure A.4a shows the EPCE per **q**-point across the Brillouin zone. Most of the points computed with the FP method fall on the DFPT curve, with some visible discrepancy for the Γ_{6c} state at **L** and Δ. Still, both methods agree within 1 meV for the ZPR of the band gap, which is evaluated to ~ -23 meV, confirming again the validity of the rigid-ion approximation.

We performed FP calculations with G_0W_0 corrections for five points of the BZ ($\mathbf{\Gamma}$, $\mathbf{\Lambda}$, **L**, $\mathbf{\Omega}$ and **X**). These are shown in Fig. A.4b. On average, the EPCE per **q**-point for the Γ_{8v} state were increased by 6 meV, and those the Γ_{6c} state were increased by 14 meV (in absolute value). With the G_0W_0 corrections, the ZPR in increased from -23 meV to -33 meV, as summarized in Table A.1. Experimental values for the band gap ZPR in GaAs range from -45 meV to -54 meV [92]. Hence, as for diamond, the many-body corrections increase significantly the ZPR obtained from DFT, in better agreement with experiments, but in the case of GaAs, our static LDA+G_0W_0 frozen-phonon calculation still underestimates the band gap ZPR.

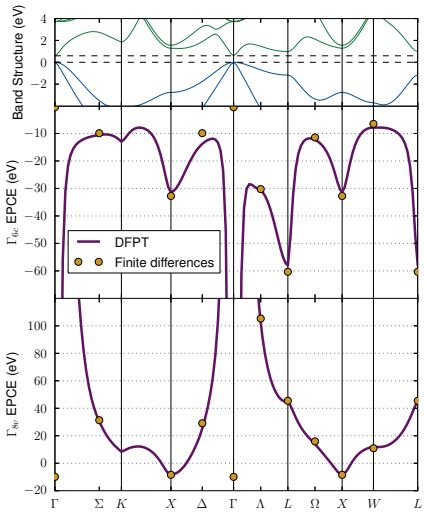
	Γ_{8v}	Γ_{6c}	Gap
DFPT	14	-8	-22
Frozen-phonon	15	-8	-23
Δ G_0W_0	$+3$	-7	-10
Total	18	-15	-33

Table A.1: Zero-point renormalization (meV) in GaAs computed on a $4 \times 4 \times 4$ q-point grid.

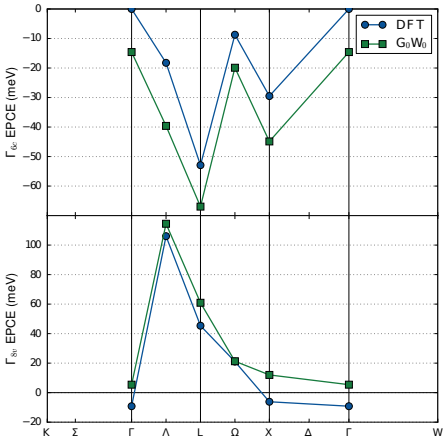
All calculation were done with the ABINIT code [96].

A.11 TOTAL ENERGY

In this appendix's section, we detail several terms of the decomposition of the total energy, as provided by ABINIT and QE. As concerns ABINIT, a decomposition of the total energy can be inferred from Refs. [64, 74], but the Ewald and psp-core terms are actually mixed in these references, which is misleading.



(a) EPCE in GaAs for the top of the valence band (lower panel) and the bottom of the conduction band (middle panel), calculated in DFPT (solid line) and with the frozen-phonon method (circles).



(b) EPCE in GaAs for the top of the valence band (lower curves) and the bottom of the conduction band (upper curves), in DFT (circles) and in in G_0W_0(squares).

Figure A.4: Electron-phonon coupling energies (EPCE) in GaAs. The top panel in (a) shows the band structure with dashed line indicating the Γ_{8v} and Γ_{6c} energies.

We define first the psp-core energy. The external potential originates from sum of atomic pseudopotentials

$$v_{\text{psp}}(\mathbf{r},\mathbf{r}') = \sum_{\iota s} v_s(\mathbf{r}-\boldsymbol{\tau}_s-\mathbf{R}_\iota,\mathbf{r}'-\boldsymbol{\tau}_s-\mathbf{R}_\iota) \tag{A.101}$$

Each atom contribution to this external potential is made of a local and a nonlocal part

$$v_s(\mathbf{r},\mathbf{r}') = v_s^{\text{loc}}(\mathbf{r})\delta(\mathbf{r}-\mathbf{r}') + v_s^{\text{non-loc}}(\mathbf{r},\mathbf{r}') \tag{A.102}$$

For each atom the local part is long ranged, with an asymptotic behaviour $-Z_s/r$. Such behaviour implies a divergence at $\mathbf{G}=\mathbf{0}$ in reciprocal space. Divergences at $\mathbf{G}=\mathbf{0}$ also happen in the Hartree energy and the Ewald energy. A careful treatment of the divergences leads to their mutual cancellation, albeit with some finite residual. The residual specifically linked to the long-range behaviour of the local pseudopotential is denoted as the psp-core energy

$$E_{\text{psp-core}} = \frac{1}{2\Omega_0}\left(\sum_s Z_s\right)\sum_{s'}\int\left(v_{s'}^{\text{loc}}(\mathbf{r})+\frac{Z_{s'}}{r}\right)d\mathbf{r}. \tag{A.103}$$

The Ewald energy is the energy of an infinite number of periodic positively charged particle placed in a negative homogeneous background

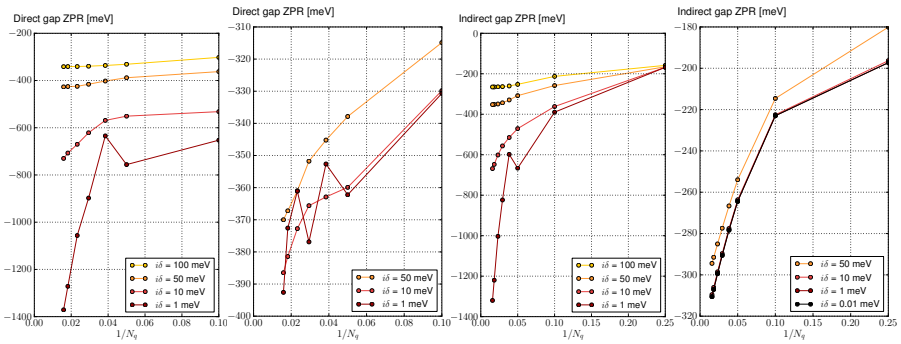
$$E_{Ew} = \frac{1}{2}\sum_{s,s'} Z_s Z_{s'} \left[\sum_{\mathbf{G}\neq\mathbf{0}} \frac{4\pi}{\Omega_0 G^2} e^{i\mathbf{G}\cdot(\tau_s-\tau_{s'})} e^{\frac{-G^2}{4\Lambda^2}} - \sum_{l} \frac{e^{i\mathbf{q}\cdot\mathbf{R}_l}\mathrm{erfc}(\Lambda|\mathbf{R}_l+\tau_{s'}-\tau_s|)}{|\mathbf{R}_l+\tau_{s'}-\tau_s|} - \frac{2}{\sqrt{\pi}}\Lambda\delta_{ss'} - \frac{\pi}{\Omega_0\Lambda^2} \right], \quad \text{(A.104)}$$

with Z_s the charge of ion s, Ω_0 the unit cell volume, Λ a parameter that can assume any value and is adjusted to obtain the fastest convergence.

B

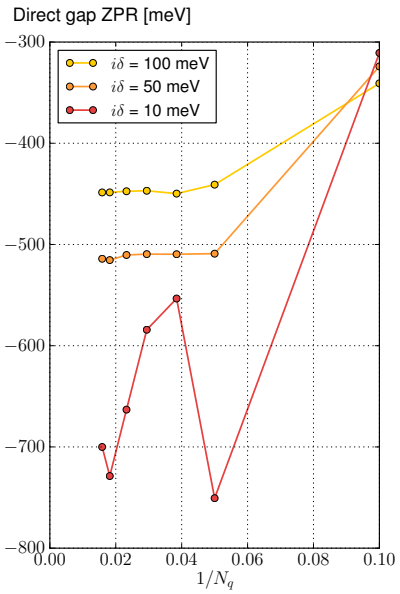
CONVERGENCE STUDIES OF SEMICONDUCTORS AND ADDITIONAL INFORMATION ON BSON

B.1 CONVERGENCE STUDIES FOR THE TEMPERATURE-DEPENDENCE CALCULATIONS

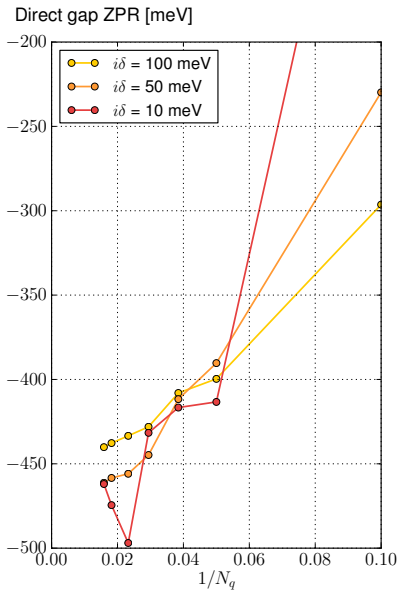


(a) Static ZPR. (b) Non-adiabatic ZPR. (c) Static ZPR. (d) Non-adiabatic ZPR.

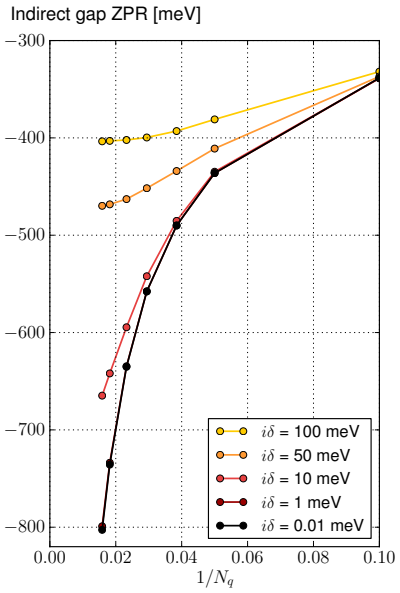
Figure B.1: Convergence study for the (a) static and (b) non-adiabatic direct bandgap ZPR of β-AlN as well as the (c) static and (d) non-adiabatic indirect $\mathbf{\Gamma} - \mathbf{X}$ bandgap ZPR of β-AlN with respect to the $\mathbf{q}$-point grid density integration for decreasing values of $i\delta$. Values of $i\delta = 0.01$ meV for the direct bandgap are not shown as they lead to strong oscillations due to the fact that β-AlN is an indirect bandgap semiconductor. The spike observed in (c) for $i\delta = 1$ meV is ascribed to numerical instabilities. The corresponding line with $i\delta = 0.01$ meV is not shown for readability as its convergence is even more spiky.



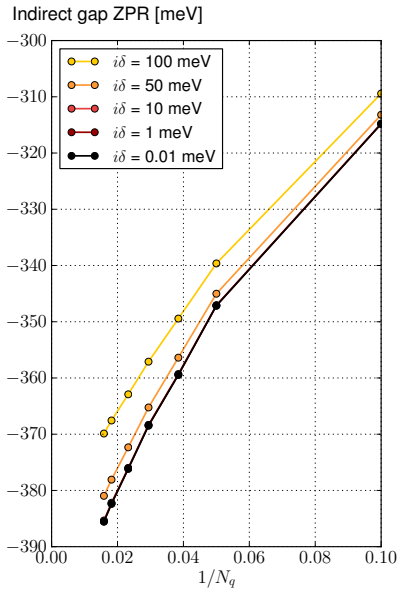
(a) Static ZPR of BN.



(b) Non-adiabatic ZPR of BN.

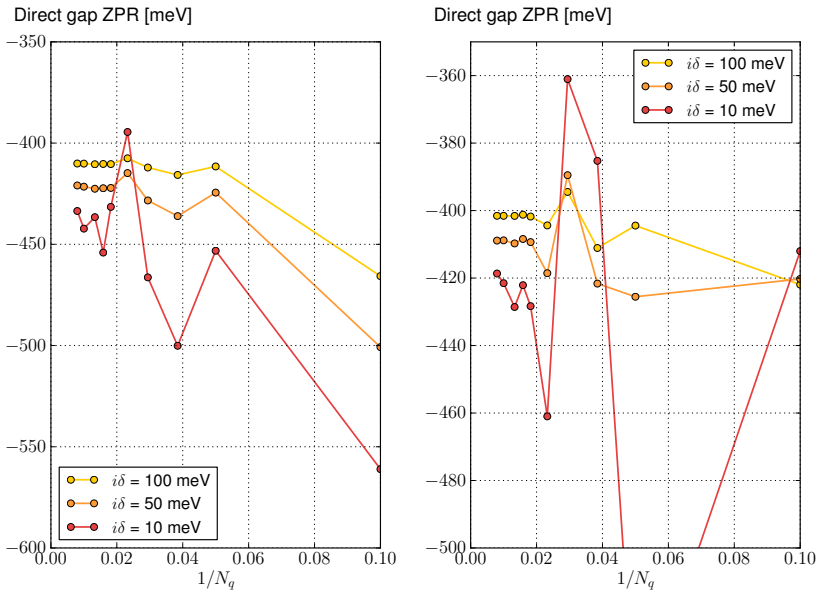


(c) Static ZPR of BN.



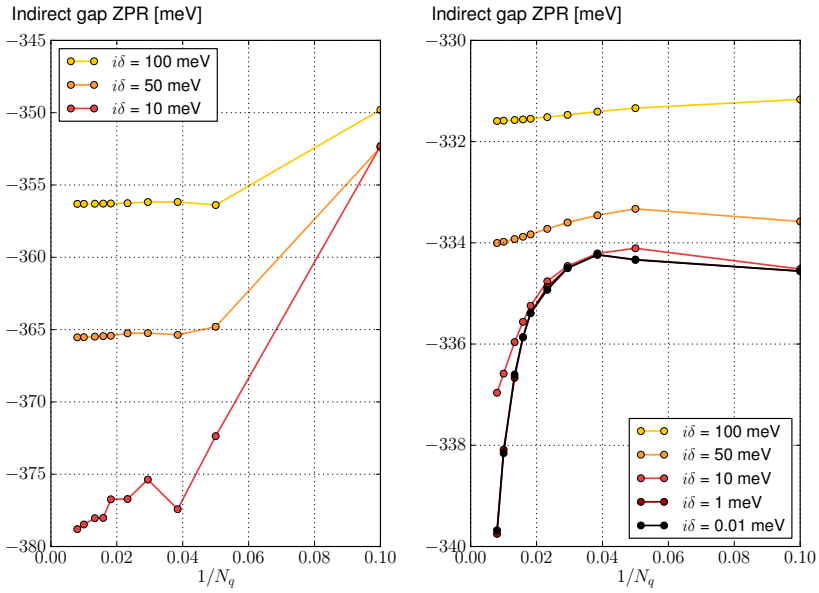
(d) Non-adiabatic ZPR of BN.

Figure B.2: Convergence study for the (a) static and (b) non-adiabatic direct bandgap ZPR of c-BN as well as the (c) static and (d) non-adiabatic indirect $\mathbf{\Gamma} - \mathbf{X}$ bandgap ZPR of c-BN with respect to the $\mathbf{q}$-point grid density integration for decreasing values of $i\delta$. Values of $i\delta = 1$ meV and $i\delta = 0.01$ meV are not shown for the direct gap as they lead to strong oscillations due to the fact that BN is an indirect bandgap semiconductor. For the non-adiabatic indirect bandgap, the curves for $i\delta$=10 to $i\delta$=0.01 meV are almost on top of each other.



(a) Static ZPR of diamond.

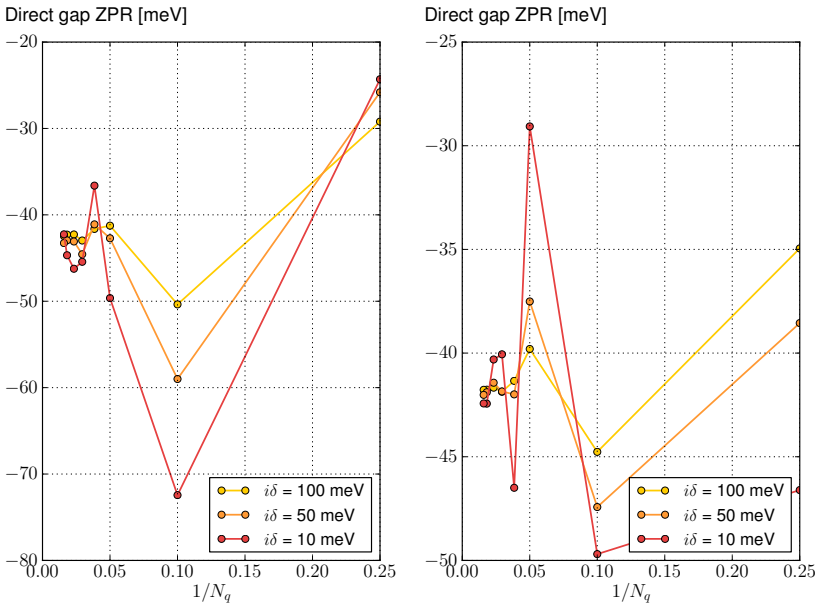
(b) Non-adiabatic ZPR of diamond.



(c) Static ZPR of diamond.

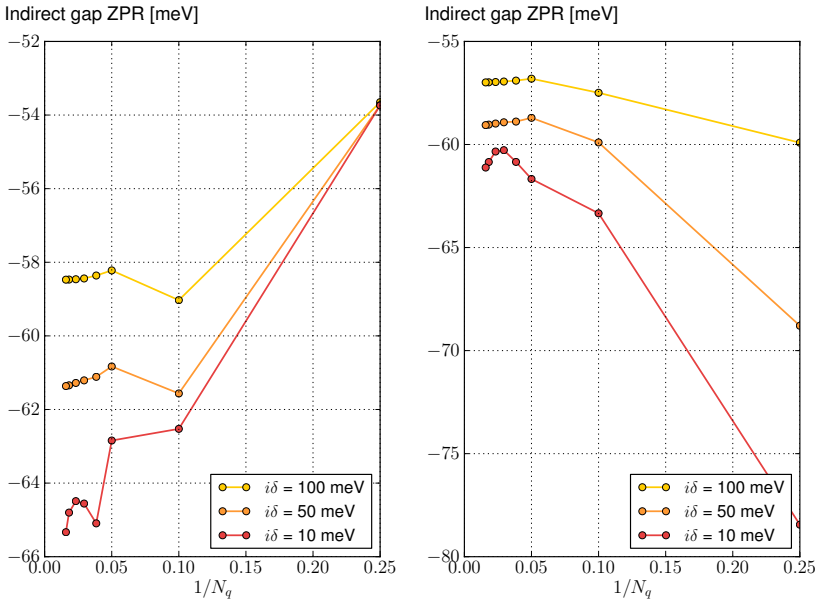
(d) Non-adiabatic ZPR of diamond.

Figure B.3: Convergence study for the (a) static and (b) non-adiabatic direct bandgap ZPR of diamond as well as the (c) static and (d) non-adiabatic indirect bandgap ZPR of diamond with respect to the $\mathbf{q}$-point grid density integration for decreasing values of $i\delta$. The divergence of the non-adiabatic indirect ZPR for vanishing $i\delta$ is clear in (d).



(a) Static ZPR of silicon.

(b) Non-adiabatic ZPR of silicon.



(c) Static ZPR of silicon.

(d) Non-adiabatic ZPR of silicon.

Figure B.4: Convergence study for the (a) static and (b) non-adiabatic direct bandgap ZPR of silicon as well as the (c) static and (d) non-adiabatic indirect bandgap ZPR of silicon with respect to the **q**-point grid density integration for decreasing values of $i\delta$. The convergence for the indirect bandgap is quite difficult since we took the LUMO to be in (0.33,0.0,0.33) which is not the real minimum of (0.4,0.0,0.4).

B.2 THE LDA+U METHODOLOGY

Within the LDA+U methods, the wavefunctions is expanded in a localized orthonormal basis $|Inlm\sigma\rangle$ within the atomic spheres where I denotes the site, n the main quantum number, l the orbital quantum number, m the magnetic number and σ the spin index. The equations that follow are for one type of atom and a specific orbital quantum number l. The generalized LDA+U energy functional can be written as follows [216, 217, 176]

$$E^{LDA+U}[n(\mathbf{r})] = E^{LDA}[n(\mathbf{r})] + E^{Hub}[\{n^{I\sigma}\}] - E^{DC}[\{n^{I}\}], \tag{B.1}$$

where $\{\}$ denotes an iteration over the indices included in the curly brackets, $n(\mathbf{r})$ is the electronic density, $n^{I} = n^{I\uparrow} + n^{I\downarrow}$, $n^{I\sigma}$ are the atomic-orbital occupations for the atom I. The last term removes the double counting of the interactions contained in E^{Hub} and, in an average way, in E^{LDA}. We can define an occupation matrix that has the following form

$$n^{I\sigma}_{m,m'} = \sum_{n\mathbf{k}} f^{\sigma}_{n\mathbf{k}} \langle Im|\Psi^{\sigma}_{n\mathbf{k}}\rangle\langle\Psi^{\sigma}_{n\mathbf{k}}|Im'\rangle, \tag{B.2}$$

where $f^{\sigma}_{n\mathbf{k}}$ is the electronic occupation and $\langle Im|\Psi^{\sigma}_{n\mathbf{k}}\rangle$ is the projection of the wavefunction on the orbital nl of the magnetic number m at site I.

The interaction Hubbard term $E^{Hub}[\{n^{I\sigma}\}]$ in Eq. (B.1) can be written as [176]

$$E^{Hub}[\{n^{I\sigma}\}] = \frac{1}{2} \sum_{\substack{I,mm'\\ m''m'''}} \langle mm''|V_{ee}|m'm'''\rangle n^{I\sigma}_{mm'} n^{I-\sigma}_{m''m'''} + \Big(\langle mm''|V_{ee}|m'm'''\rangle - \langle mm''|V_{ee}|m'''m'\rangle\Big) n^{I\sigma}_{mm'} n^{I\sigma}_{m''m'''}, \tag{B.3}$$

where V_{ee} are the screened Coulomb interactions and the matrix elements are

$$\langle mm'|V_{ee}|m''m'''\rangle = \sum_{k=0}^{2l} \frac{4\pi}{2k+1} \sum_{q=-k}^{k} \langle lm|Y_{kq}|lm'\rangle\langle lm''|Y^{*}_{kq}|lm'''\rangle F^{k}, \tag{B.4}$$

where l is the angular momentum of the localized (d or f) electrons, Y_{kq} are the angular part of the wavefunctions (expressed as spherical harmonics) and F^{k} the radial Slater integrals (introduced below).

The double-counting term E^{DC} can be written in the Full Localized Limit (FLL) that corresponds to the subtraction of the average effect for a localized state with integer occupation number [217]

$$E^{DC_{FLL}}[\{n^I\}] = \sum_I \frac{U}{2} n^I(n^I - 1) - \sum_I \frac{J}{2}\Big[n^{I\uparrow}(n^{I\uparrow} - 1) + n^{I\downarrow}(n^{I\downarrow} - 1)\Big], \quad \text{(B.5)}$$

where again $n^I = n^{I\uparrow} + n^{I\downarrow}$. Alternatively, it can be written in the Around Mean Field approximation where the electrons are equally shared among orbitals [216]

$$E^{DC_{AMF}}[\{n^I\}] = \sum_I U n^{I\uparrow} n^{I\downarrow} + \frac{1}{2}\Big[(n^{I\uparrow 2} + n^{I\downarrow 2})\frac{2l}{2l+1}(U - J)\Big]. \quad \text{(B.6)}$$

The radial Slater integrals F^k are the parameters of the models that take value F^0, F^2 and F^4 for d electrons. For f electrons, an additional F^6 must be specified. These Slater integrals can be expressed in terms of only two parameters U and J, describing the on-site Coulomb and exchange interaction

$$U = \frac{1}{(2l+1)^2}\sum_{m,m'} \langle mm'|V_{ee}|mm'\rangle = F^0 \quad \text{(B.7)}$$

and

$$J = \frac{1}{2l(2l+1)}\sum_{m\neq m',m'} \langle mm'|V_{ee}|m'm\rangle = \frac{F^2 + F^4}{14}, \quad \text{(B.8)}$$

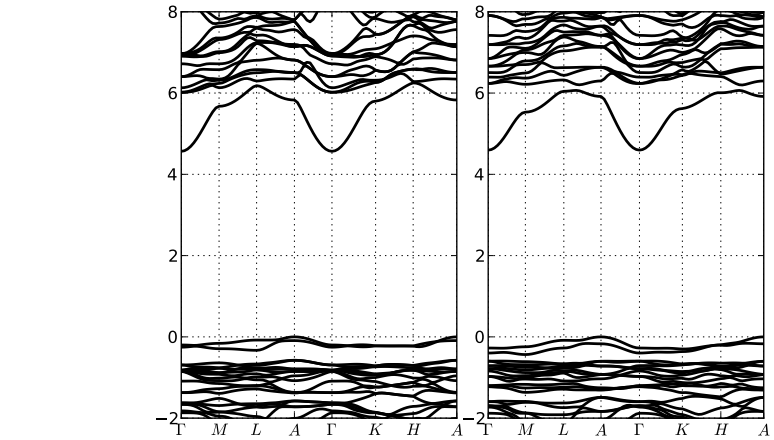
where the ratios F^4/F^2 and F^6/F^4 are known. Moreover, the terms E^{Hub}-$[\{n^{I\sigma}\}]$ and $E^{DC}[\{n^I\}]$ are invariant under the rotation of the atomic-orbital basis set used to define the occupancies $n^{\sigma}_{m,m'}$. The interested reader can check that in the absence of orbital polarizations (i.e. $n^{I\sigma}_{mm'} = n^{I\sigma}_{mm'}\delta_{mm'}$), the Eq. (B.1) reduces to $E^{LDA}[n(\mathbf{r})]$ thanks to the definition of the U and J terms.

To be complete, there is an alternative rotationally invariant formulation of the $E^{LDA+U}[n(\mathbf{r})]$ term from Dudarev *et al.* [218]

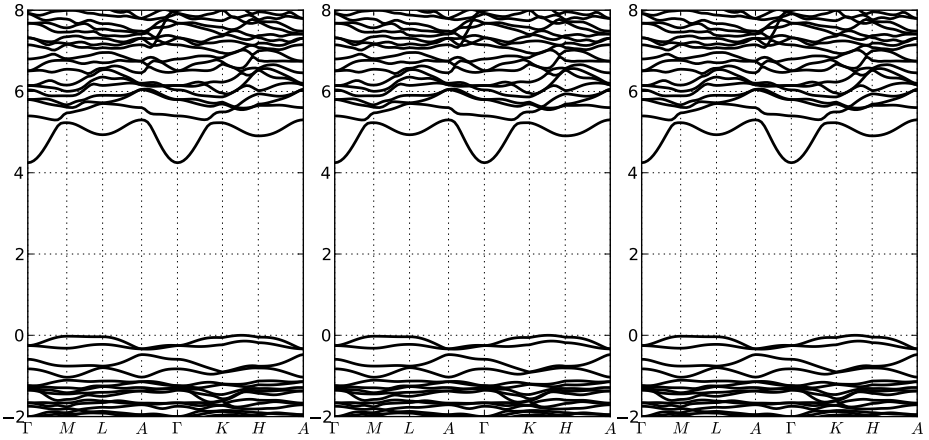
$$E^{LDA+U}[n(\mathbf{r})] = E^{LDA}[n(\mathbf{r})] + \frac{U - J}{2}\sum_{I,\sigma}\Big(\sum_m n^{I\sigma}_{mm} - \sum_{mm'} n^{I\sigma}_{mm'} n^{I\sigma}_{m'm}\Big). \quad \text{(B.9)}$$

This last formulation only needs one parameter $(U - J)$ but is not implemented in the Abinit software.

B.3 EUROPIUM-DOPED BSON GROUND STATE CALCULATIONS



(a) $Ba_3Si_6O_{12}N_2$:Eu_1 (b) $Ba_3Si_6O_{12}N_2$:Eu_2



(c) $Ba_3Si_6O_9N_4$:Eu_1 (d) $Ba_3Si_6O_9N_4$:Eu_2 (e) $Ba_3Si_6O_9N_4$:Eu_3

Figure B.5: **[GS]** The ground-state electronic bandstructure of the europium-doped elements are computed at the *ab-initio* relaxed parameter with the 10 valence electrons pseudopotential.

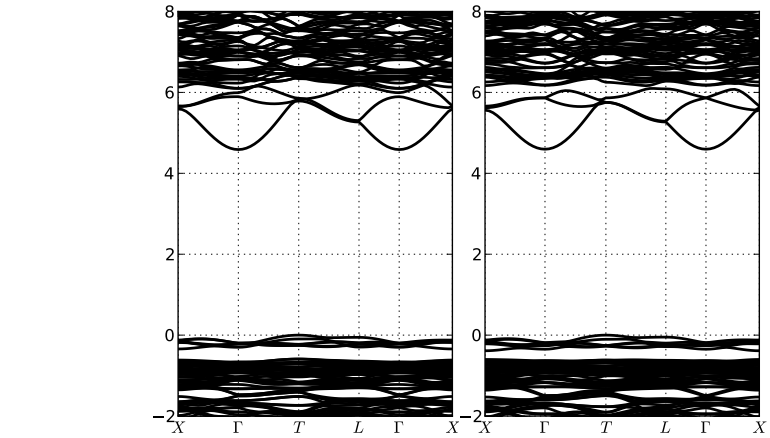
$Ba_3Si_6O_{12}N_2$						$Ba_3Si_6O_9N_4$						
	undoped	Eu_1	diff %	Eu_2	diff %		undoped	Eu_1	diff %	Eu_2	diff %	Eu_3	diff %
Ba_1-O_2 (3x)	5.2149	5.0228	−3.7	5.2009	−0.3	Ba_1-O_2 (3x)	5.1280	4.9963	−2.6	5.1267	0.0	5.0787	−1.0
-O_2 (3x)	5.2149	5.0228	−3.7	5.2876	1.4	-O_3 (3x)	5.3346	5.1109	−4.2	5.3680	0.6	5.3616	0.5
Ba_2-O_2 (3x)	5.5911	5.5682	−0.4	5.4906	−1.8	-N_1 (1x)	6.6095	6.8825	4.1	6.5098	−1.5	6.6077	0.0
-O_2 (3x)	5.3146	5.3902	1.4	5.0967	−4.1	Ba_2-O_2 (3x)	5.1082	5.1519	0.9	4.8954	−4.2	5.1440	0.7
-N (1x)	5.7699	5.9102	2.4	5.5602	−3.6	-O_3 (3x)	5.4052	5.3760	−0.5	5.2929	−2.1	5.3781	−0.5
-N (1x)	6.6133	6.4709	−2.2	6.6434	0.5	-N_2 (1x)	6.2053	6.3250	1.9	6.0656	−2.3	6.3490	2.3
Si -N (x1)	3.3163	3.3077	−0.3	3.3160	0.0	-N_2 (1x)	6.7641	6.6141	−2.2	6.7234	−0.6	6.5761	−2.8
-O_1 (1x)	3.1588	3.1553	−0.1	3.1595	0.0	Ba_3-O_2 (3x)	5.1587	5.1378	−0.4	5.1375	−0.4	4.9790	−3.5
-O_1 (3x)	3.1636	3.1618	−0.1	3.1614	−0.1	-O_3 (1x)	5.1616	5.1536	−0.2	5.2192	1.1	5.0152	−2.8
-O_2 (3x)	3.0476	3.0474	0.0	3.0487	0.0	-O_1 (1x)	6.3785	6.2943	−1.3	6.2220	−2.5	6.4087	0.5
Shannon crystal radii [206]						Si_1 -O_2 (1x)	3.0777	3.0804	0.1	3.0768	0.0	3.0787	0.0
Ion		Coordination		crystal radius		-O_1 (1x)	3.1594	3.1645	0.2	3.1585	0.0	3.1473	−0.4
Ba^{2+}		VI/VII		2.816/2.872		-N_1 (1x)	3.3092	3.2925	−0.5	3.3043	−0.1	3.3127	0.1
Eu^{2+}		VI/VII		2.475/2.532		-N_2 (1x)	3.3344	3.3263	−0.2	3.3327	−0.1	3.3309	−0.1
Eu^{3+}		VI/VII		2.041/2.173		Si_2 -O_3 (1x)	3.0681	3.0732	0.2	3.0652	−0.1	3.0693	0.0
O^{2-}		VI		2.381		-O_1 (1x)	3.1638	3.1673	0.1	3.1673	0.1	3.1494	−0.5
N^{3-}		IV		2.494		-N_1 (1x)	3.3177	3.3058	−0.4	3.3123	−0.2	3.3162	0.0
Si^{4+}		IV		0.756		-N_1 (1x)	3.3478	3.3330	−0.4	3.3447	−0.1	3.3451	−0.1
Volume	2216.6	2184.4		2175.0			2151.0	2120.0		2111.1		2112.0	

Table B.1: Selected bond lengths [in Bohr] and cell volume [in $Bohr^3$] of $Ba_3Si_6O_{12}N_2$ and $Ba_3Si_6O_9N_4$ compounds as well as the different doped cases where the Eu-ligand coordination is presented in figure 4.2. The 27 valence electrons pseudopotential was used for europium. The Eu_1 columns means that the Ba_1 has been replaced by an Eu_1 and that the other barium are still barium for that column. The considered europium are indicated in red. To allow for an easy comparison with experiment, Shannon crystal radii [in Bohr] have also been indicated.

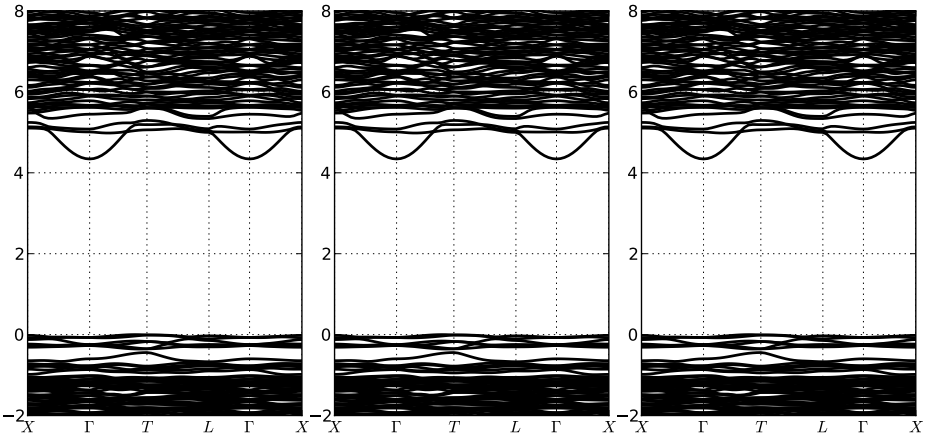
$Ba_3Si_6O_{12}N_2$						$Ba_3Si_6O_9N_4$						
	undoped	Eu_1	diff %	Eu_2	diff %		undoped	Eu_1	diff %	Eu_2	diff %	Eu_3	diff %
Ba_1-O_2 (3x)	5.2149	4.7853	−8.2	5.1729	−0.8	Ba_1-O_2 (3x)	5.1280	4.8392	−5.6	5.1530	0.5	5.0189	−2.1
-O_2 (3x)	5.2149	4.7853	−8.2	5.3788	3.1	-O_3 (3x)	5.3346	4.8801	−8.5	5.3711	0.7	5.3936	1.1
Ba_2-O_2 (3x)	5.5911	5.5444	−0.8	5.4215	−3.0	-N_1 (1x)	6.6095	7.0464	6.6	6.3855	−3.4	6.5932	−0.2
-O_2 (3x)	5.3146	5.4658	2.8	4.7766	−10.1	Ba_2-O_2 (3x)	5.1082	5.1864	1.5	4.6056	−9.8	5.1753	1.3
-N (1x)	5.7699	5.5444	−3.9	5.4380	−5.8	-O_3 (3x)	5.4052	5.3620	−0.8	5.2117	−3.6	5.3512	−1.0
-N (1x)	6.6133	6.2510	−5.5	6.5467	−1.0	-N_2 (1x)	6.2053	6.4572	4.1	6.0144	−3.1	6.4586	4.1
Si -N (x1)	3.3163	3.2999	−0.5	3.3109	−0.2	-N_2 (1x)	6.7641	6.4057	−5.3	6.5558	−3.1	6.3559	−6.0
-O_1 (1x)	3.1588	3.1521	−0.2	3.1599	0.0	Ba_3-O_2 (3x)	5.1587	5.1123	−0.9	5.1016	−1.1	4.7882	−7.2
-O_1 (3x)	3.1636	3.1611	−0.1	3.1568	−0.2	-O_3 (1x)	5.1616	5.1452	−0.3	5.2856	2.4	4.8239	−6.5
-O_2 (3x)	3.0476	3.0445	−0.1	3.0502	0.1	-O_1 (1x)	6.3785	6.7264	5.5	6.7999	6.6	6.7641	6.0
Shannon crystal radii [206]						Si_1 -O_2 (1x)	3.0777	3.0822	0.1	3.0769	0.0	3.0776	0.0
Ion		Coordination		crystal radius		-O_1 (1x)	3.1594	3.1702	0.3	3.1569	−0.1	3.1368	−0.7
Ba^{2+}		VI/VII		2.816/2.872		-N_1 (1x)	3.3092	3.2752	−1.0	3.2982	−0.3	3.3175	0.3
Eu^{2+}		VI/VII		2.475/2.532		-N_2 (1x)	3.3344	3.3177	−0.5	3.3260	−0.3	3.3269	−0.2
Eu^{3+}		VI/VII		2.041/2.173		Si_2 -O_3 (1x)	3.0681	3.0756	0.2	3.0606	−0.2	3.0685	0.0
O^{2-}		VI		2.381		-O_1 (1x)	3.1638	3.1712	0.2	3.1706	0.2	3.1385	−0.8
N^{3-}		IV		2.494		-N_1 (1x)	3.3177	3.2942	−0.7	3.3091	−0.3	3.3156	−0.1
Si^{4+}		IV		0.756		-N_1 (1x)	3.3478	3.3168	−0.9	3.3417	−0.2	3.3463	0.0
Volume	2216.6	2134.6		2127.2			2151.0	2078.1		2065.3		2058.1	

Table B.2: **[GS]** Selected bond lengths [in Bohr] and cell volume [in $Bohr^3$] of $Ba_3Si_6O_{12}N_2$ and $Ba_3Si_6O_9N_4$ compounds as well as the different doped cases where the Eu-ligand coordination is presented in figure 4.2. The 10 valence electrons pseudopotential was used for europium. The Eu_1 columns means that the Ba_1 has been replaced by an Eu_1 and that the other barium are still barium for that column. The considered europium are indicated in red. To allow for an easy comparison with experiment, Shannon crystal radii [in Bohr] have also been indicated.

"main_corr" — 2015/1/7 — 18:40 — page 189 — #205



(a) $Ba_3Si_6O_{12}N_2$:Eu_1 (b) $Ba_3Si_6O_{12}N_2$:Eu_2



(c) $Ba_3Si_6O_9N_4$:Eu_1 (d) $Ba_3Si_6O_9N_4$:Eu_2 (e) $Ba_3Si_6O_9N_4$:Eu_3

Figure B.6: **[GS]** The ground-state electronic bandstructure of the europium-doped elements are computed at the *ab-initio* relaxed parameter with the 10 valence electrons pseudopotential in the rhombohedral supercell.

B.4 EUROPIUM-DOPED EXCITED STATE CALCULATIONS

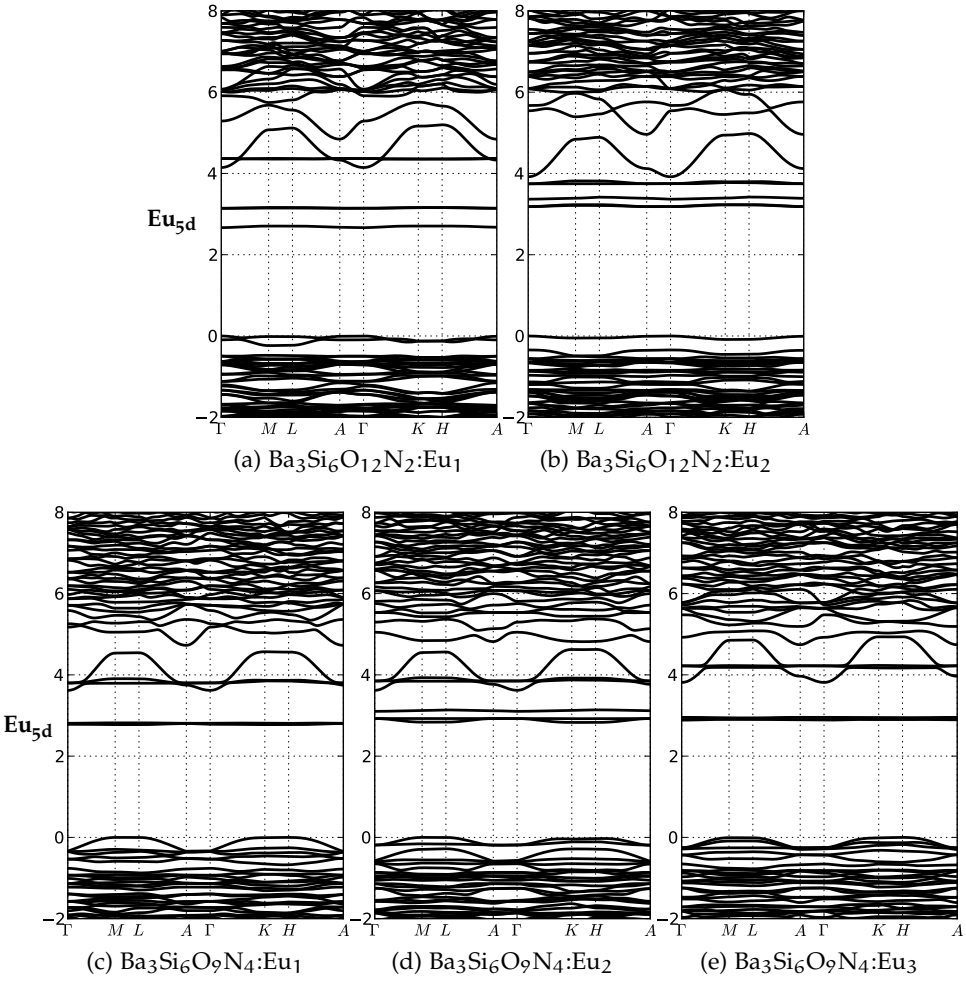
$Ba_2Si_6O_{12}N_2$:Eu_1							
Γ			Band	A			Band
DFT	G_0W_0	diff.	character	DFT	G_0W_0	diff.	character
6.672(2)	7.802(2)	1.130	-	7.045(2)	8.160(2)	1.115	-
6.511	7.409	0.898	-	5.945	7.142	1.197	-
5.242(2)	6.973(2)	1.731	Eu_{5d}	5.682	6.765	1.083	Ba_{6s}
4.744	6.118	1.374	Ba_{6s}	5.285(2)	7.064(2)	1.779	Eu_{5d}
3.993(2)	5.534(2)	1.541	Eu_{5d}	4.098(2)	5.683(2)	1.585	Eu_{5d}
3.415	4.646	1.231	Eu_{5d}	3.628	5.073	1.445	Eu_{5d}
−0.127	−1.282	−1.155	N_{2p}	0.000	−1.129	−1.129	N_{2p}
−0.298	−1.473	−1.175	N_{2p}	−0.020	−1.126	−1.106	N_{2p}
−0.701(2)	−1.917(2)	−1.216	Ba_{4d}-O_{2p}	−0.607(2)	−1.798(2)	−1.191	Ba_{4d}-O_{2p}
$Ba_2Si_6O_{12}N_2$:Eu_2							
Γ			Band	A			Band
DFT	G_0W_0	diff.	character	DFT	G_0W_0	diff.	character
4.255(2)	5.818(2)	1.562	Eu_{5d}	5.624	6.833	1.209	Ba_{6s}
4.078	5.138	1.061	Ba_{6s}	4.398(2)	6.020(2)	1.622	Eu_{5d}
3.739(2)	5.228(2)	1.490	Eu_{5d}	4.228	5.799	1.571	Eu_{5d}
3.570	4.984	1.414	Eu_{5d}	3.787(2)	5.306(2)	1.519	Eu_{5d}
−0.196	−1.346	−1.149	N_{2p}	0.000	−1.106	−1.106	N_{2p}
−0.695	−1.811	−1.116	N_{2p}	−0.465	−1.551	−1.086	N_{2p}
−0.794(2)	−1.989(2)	−1.195	-	−0.762(2)	−1.948(2)	−1.185	-
$Ba_2Si_6O_9N_4$:Eu_1							
Γ			Band	M			Band
DFT	G_0W_0	diff.	character	DFT	G_0W_0	diff.	character
6.449	7.337	0.888		5.603	6.584	0.980	
6.265(2)	7.116(2)	0.851		5.079	6.140	1.061	
5.883	6.873	0.990		4.647	6.244	1.596	
4.447(2)	5.971(2)	1.524	Eu_{5d}	4.431	5.884	1.453	Ba_{6s}
4.003	5.066	1.063	Ba_{6s}	3.529	4.870	1.342	
3.508(2)	4.843(2)	1.335	Eu_{5d}	3.505	4.834	1.329	Eu_{5d}
3.284	4.397	1.113	Eu_{5d}	3.392	4.655	1.262	
−0.244(2)	−1.361(2)	−1.117	N_{2p}	0.000	−1.078	−1.078	N_{2p}
−0.674	−1.795	−1.121	N_{2p}	−0.274	−1.400	−1.126	N_{2p}
−0.850	−2.000	−1.150	N_{2p}	−0.791	−1.934	−1.143	N_{2p}
−1.236	−2.403	−1.167	-	−1.037	−2.227	−1.191	N_{2p}
$Ba_2Si_6O_9N_4$:Eu_2							
Γ			Band	M			Band
DFT	G_0W_0	diff.	character	DFT	G_0W_0	diff.	character
6.639	7.582	0.943		5.427	6.411	0.984	

Continued on next page

Table B.3 – continued from previous page

6.145(2)	6.978(2)	0.832		5.038	6.088	1.050	
5.842	6.825	0.983		4.635	6.192	1.557	
4.435(2)	5.912(2)	1.476	Eu_{5d}	4.454	5.889	1.435	Ba_{6s}
3.887	4.818	0.931	Ba_{6s}	3.589	4.906	1.317	Eu_{5d}
3.569(2)	4.881(2)	1.312	Eu_{5d}	3.492	4.767	1.275	Eu_{5d}
3.410	4.633	1.223	Eu_{5d}	3.461	4.736	1.275	Eu_{5d}
−0.233(2)	−1.358(2)	−1.125	N_{2p}	0.000	−1.091	−1.091	N_{2p}
−0.671	−1.825	−1.155	N_{2p}	−0.256	−1.391	−1.135	N_{2p}
−0.911	−2.028	−1.117	N_{2p}	−0.821	−1.982	−1.162	N_{2p}
−1.120	−2.328	−1.208	-	−1.012	−2.185	−1.173	N_{2p}
$Ba_2Si_6O_9N_4$:Eu_3							
	Γ		Band		M		Band
DFT	G_0W_0	diff.	character	DFT	G_0W_0	diff.	character
6.366(2)	7.250(2)	0.884		5.467	6.520	1.053	
6.058(2)	6.967(2)	0.908		5.258	6.417	1.159	
5.450	6.304	0.854		4.866	6.507	1.641	
4.799(2)	6.436(2)	1.637	Eu_{5d}	4.757	6.284	1.527	Ba_{6s}
4.051	5.223	1.171	Ba_{6s}	3.518	4.926	1.408	Eu_{5d}
3.546(2)	4.972(2)	1.425	Eu_{5d}	3.514	4.917	1.404	Eu_{5d}
3.396	4.628	1.231	Eu_{5d}	3.490	4.891	1.401	Eu_{5d}
−0.333(2)	−1.512(2)	−1.179	N_{2p}	0.000	−1.119	−1.118	N_{2p}
−0.683	−1.843	−1.160	N_{2p}	−0.323	−1.503	−1.180	N_{2p}
−0.928	−2.091	−1.162	N_{2p}	−0.951	−2.144	−1.193	N_{2p}
−1.305	−2.510	−1.205	-	−1.078	−2.275	−1.197	N_{2p}

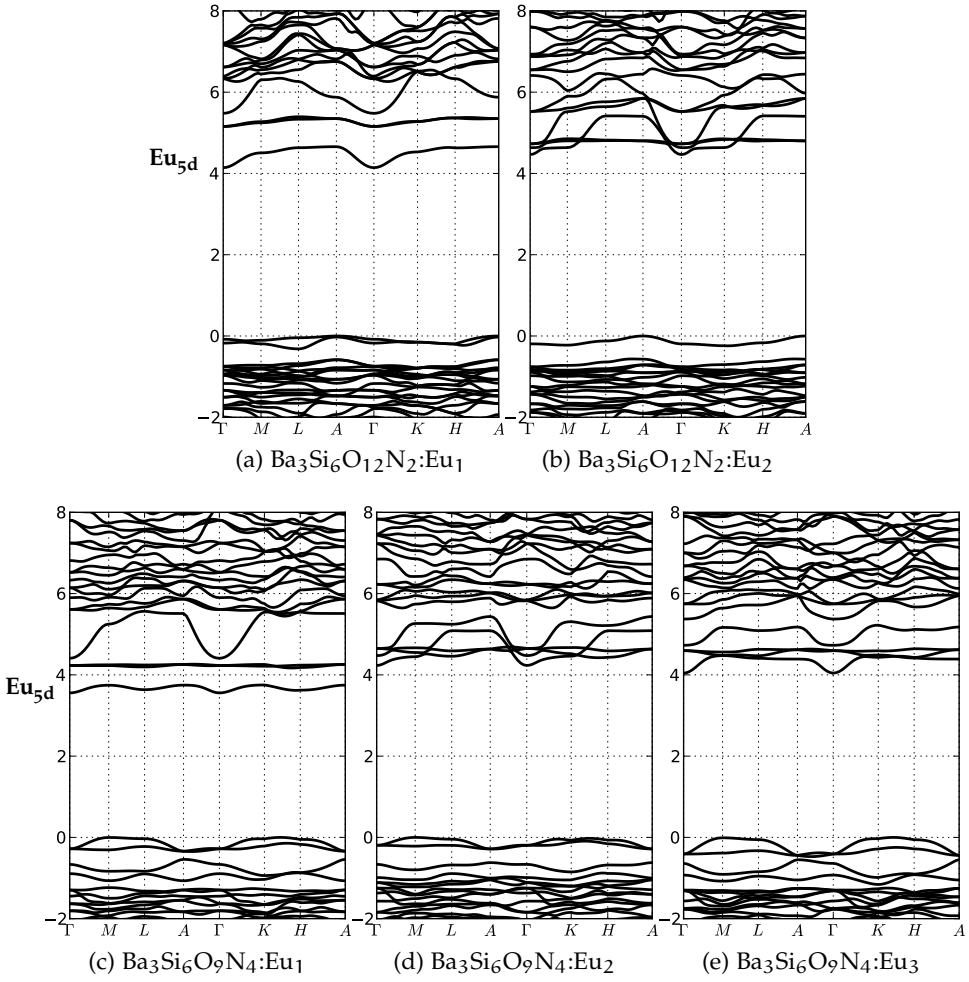
Table B.3: Band positions [eV] of the europium-doped $Ba_2Si_6O_{12}N_2$ and $Ba_2Si_6O_9N_4$ compound at the different high symmetry points using the core-hole approach. The color code corresponds to the figure 5.7 and "diff." means G_0W_0-DFT.



(a) $Ba_3Si_6O_{12}N_2$:Eu_1 (b) $Ba_3Si_6O_{12}N_2$:Eu_2

(c) $Ba_3Si_6O_9N_4$:Eu_1 (d) $Ba_3Si_6O_9N_4$:Eu_2 (e) $Ba_3Si_6O_9N_4$:Eu_3

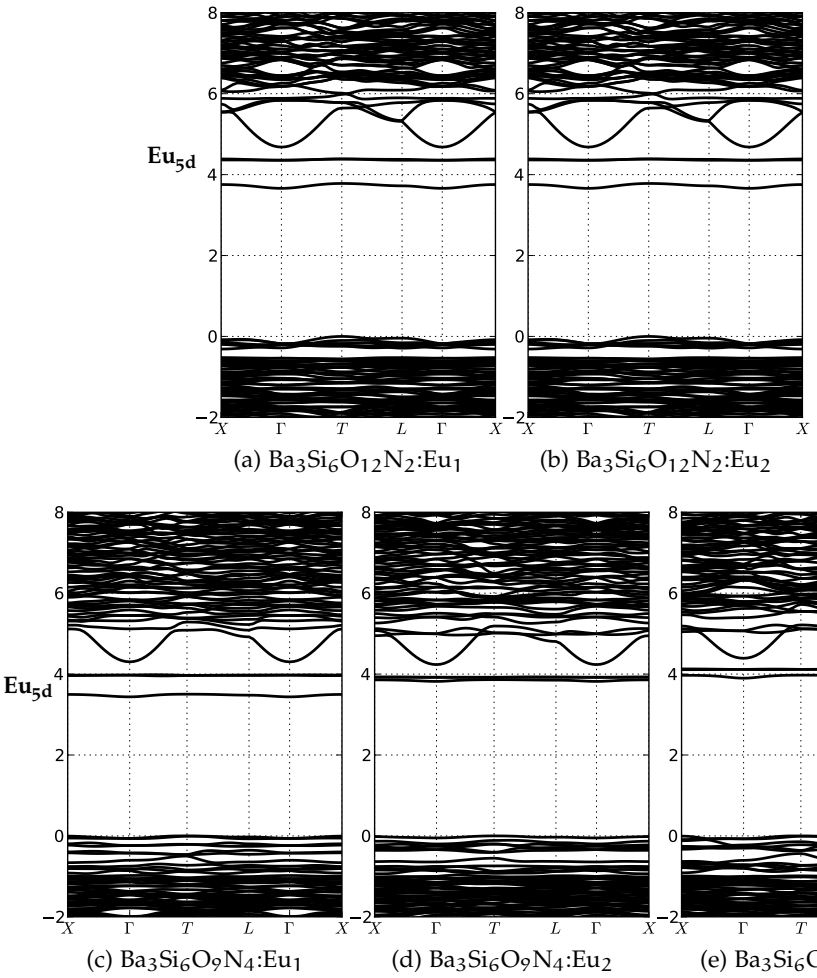
Figure B.7: **[Exc]** Electronic bandstructures of the 1x1x2 supercell calculations computed with the core-hole pseudopotentials at the undoped relaxed lattice parameters. The five europium-doped compounds are calculated on a 6x6x2 **k**-point grid shifted 1/2 in the c direction with a 30 Ha energy cut-off of the plane-wave basis set for the europium-doped $Ba_3Si_6O_{12}N_2$ and 35 Ha for the europium-doped $Ba_3Si_6O_9N_4$ compounds.



(a) $Ba_3Si_6O_{12}N_2$:Eu_1 (b) $Ba_3Si_6O_{12}N_2$:Eu_2

(c) $Ba_3Si_6O_9N_4$:Eu_1 (d) $Ba_3Si_6O_9N_4$:Eu_2 (e) $Ba_3Si_6O_9N_4$:Eu_3

Figure B.8: **[Exc]** Electronic bandstructures calculations computed with the core-hole 10 electrons pseudopotentials. The excitation doped elements are computed on the cell and atoms relaxed in the ground-state. They all are calculated on a 4x4x4 shifted 1/2 in the c direction **k**-points grid (12 **k**-points in IBZ) and with a 30 Ha energy cut-off for the $Ba_3Si_6O_{12}N_2$ and 35 Ha for the $Ba_3Si_6O_9N_4$ compounds.

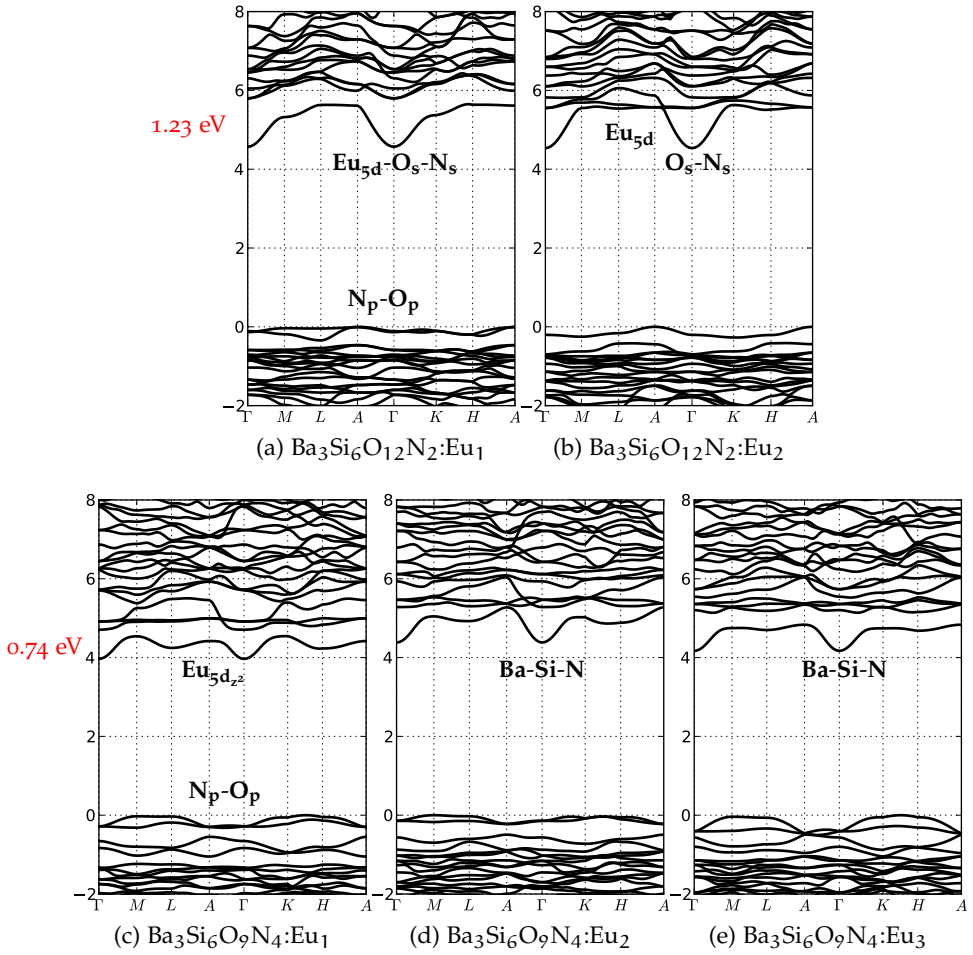


(a) $Ba_3Si_6O_{12}N_2$:Eu_1 (b) $Ba_3Si_6O_{12}N_2$:Eu_2

(c) $Ba_3Si_6O_9N_4$:Eu_1 (d) $Ba_3Si_6O_9N_4$:Eu_2 (e) $Ba_3Si_6O_9N_4$:Eu_3

Figure B.9: **[Exc]** Electronic bandstructure of the rhombohedral supercell calculations computed with the core-hole pseudopotentials. The doped elements are computed on the cell and atoms relaxed in the ground-state. They all are calculated on a 2x2x2 shifted 1/2 in all direction **k**-points grid and with a 30 Ha energy cut-off for the $Ba_3Si_6O_{12}N_2$ and 35 Ha for the $Ba_3Si_6O_9N_4$ compounds.

B.5 ATOMIC RELAXATION



(a) $Ba_3Si_6O_{12}N_2$:Eu_1 (b) $Ba_3Si_6O_{12}N_2$:Eu_2

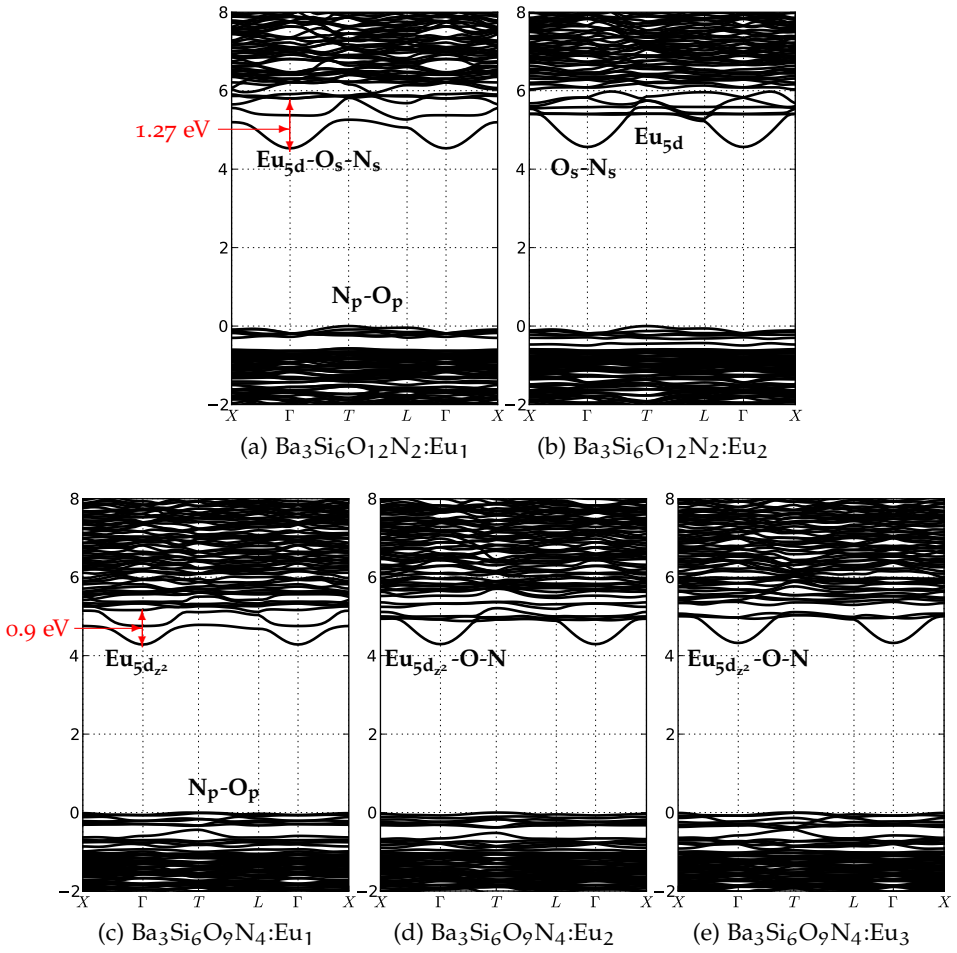
(c) $Ba_3Si_6O_9N_4$:Eu_1 (d) $Ba_3Si_6O_9N_4$:Eu_2 (e) $Ba_3Si_6O_9N_4$:Eu_3

Figure B.10: **[Exc*]** Electronic bandstructures calculations computed with the core-hole 10 electrons pseudopotentials. The excitation doped elements are computed with the ground-state lattice parameters and the atomic position relaxed with the core-hole pseudopotential. They all are calculated on a 4x4x4 shifted 1/2 in the c direction **k**-points grid (12 **k**-points in IBZ) and with a 30 Ha energy cut-off for the $Ba_3Si_6O_{12}N_2$ and 35 Ha for the $Ba_3Si_6O_9N_4$ compounds.

$Ba_3Si_6O_{12}N_2$						$Ba_3Si_6O_9N_4$						
	undoped	Eu_1	diff %	Eu_2	diff %		undoped	Eu_1	diff %	Eu_2	diff %	Eu_3	diff %
Ba_1-O_2 (3x)	5.2149	4.5131	−13.5	5.1933	−0.4	Ba_1-O_2 (3x)	5.1280	4.5619	−11.0	5.2413	2.2	5.0581	−1.4
-O_2 (3x)	5.2149	4.5131	−13.5	5.6352	8.1	-O_3 (3x)	5.3346	4.7032	−11.8	5.5730	4.5	5.5331	3.7
Ba_2-O_2 (3x)	5.5911	5.6999	1.9	5.2877	−5.4	-N_1 (1x)	6.6095	7.1211	7.7	6.3508	−3.9	6.5884	−0.3
-O_2 (3x)	5.3146	5.6570	6.4	4.4456	−16.4	Ba_2-O_2 (3x)	5.1082	5.2960	3.7	4.4270	−13.3	5.3232	4.2
-N (1x)	5.7699	6.3351	9.8	5.2223	−9.5	-O_3 (3x)	5.4052	5.4853	1.5	4.9691	−8.1	5.4371	0.6
-N (1x)	6.6133	5.9940	−9.4	6.7624	2.3	-N_2 (1x)	6.2053	6.1118	−1.5	5.7804	−6.8	6.0805	−2.0
Si -N (x1)	3.3163	3.3043	−0.4	3.3408	0.7	-N_2 (1x)	6.7641	6.7511	−0.2	6.7898	0.4	6.7339	−0.4
-O_1 (1x)	3.1588	3.1510	−0.2	3.1493	−0.3	Ba_3-O_2 (3x)	5.1587	5.1276	−0.6	5.1792	0.4	4.5750	−11.3
-O_1 (3x)	3.1636	3.1552	−0.3	3.1475	−0.5	-O_3 (1x)	5.1616	5.2504	1.7	5.4761	6.1	4.6308	−10.3
-O_2 (3x)	3.0476	3.0619	0.5	3.0852	1.2	-O_1 (1x)	6.3785	6.3443	−0.5	6.0208	−5.6	6.4016	0.4
Shannon crystal radii [206]						Si_1 -O_2 (1x)	3.0777	3.1168	1.3	3.1123	1.1	3.1122	1.1
	Ion	Coordination		crystal radius		-O_1 (1x)	3.1594	3.1739	0.5	3.1473	−0.4	3.1262	−1.1
	Ba^{2+}	VI/VII		2.816/2.872		-N_1 (1x)	3.3092	3.2579	−1.5	3.2967	−0.4	3.3399	0.9
	Eu^{2+}	VI/VII		2.475/2.532		-N_2 (1x)	3.3344	3.3177	−0.5	3.3460	0.3	3.3364	0.1
	Eu^{3+}	VI/VII		2.041/2.173		Si_2 -O_3 (1x)	3.0681	3.1147	1.5	3.0918	0.8	3.1012	1.1
	O^{2-}	VI		2.381		-O_1 (1x)	3.1638	3.1658	0.1	3.1753	0.4	3.1213	−1.3
	N^{3-}	IV		2.494		-N_1 (1x)	3.3177	3.2874	−0.9	3.3094	−0.3	3.3281	0.3
	Si^{4+}	IV		0.756		-N_1 (1x)	3.3478	3.2982	−1.5	3.3510	0.1	3.3560	0.2
Volume	2216.6	2134.6		2127.2			2151.0	2078.1		2065.3		2058.1	

Table B.4: **[Exc*]** Selected bond lengths [in Bohr] and cell volume [in $Bohr^3$] of $Ba_3Si_6O_{12}N_2$ and $Ba_3Si_6O_9N_4$ compounds as well as the different doped cases where the Eu-ligand coordination is presented in figure 4.2. The 10 valence electrons pseudopotential was used for europium. The Eu_1 columns means that the Ba_1 has been replaced by an Eu_1 and that the other barium are still barium for that column. The considered europium are indicated in red. To allow for an easy comparison with experiment, Shannon crystal radii [in Bohr] have also been indicated.

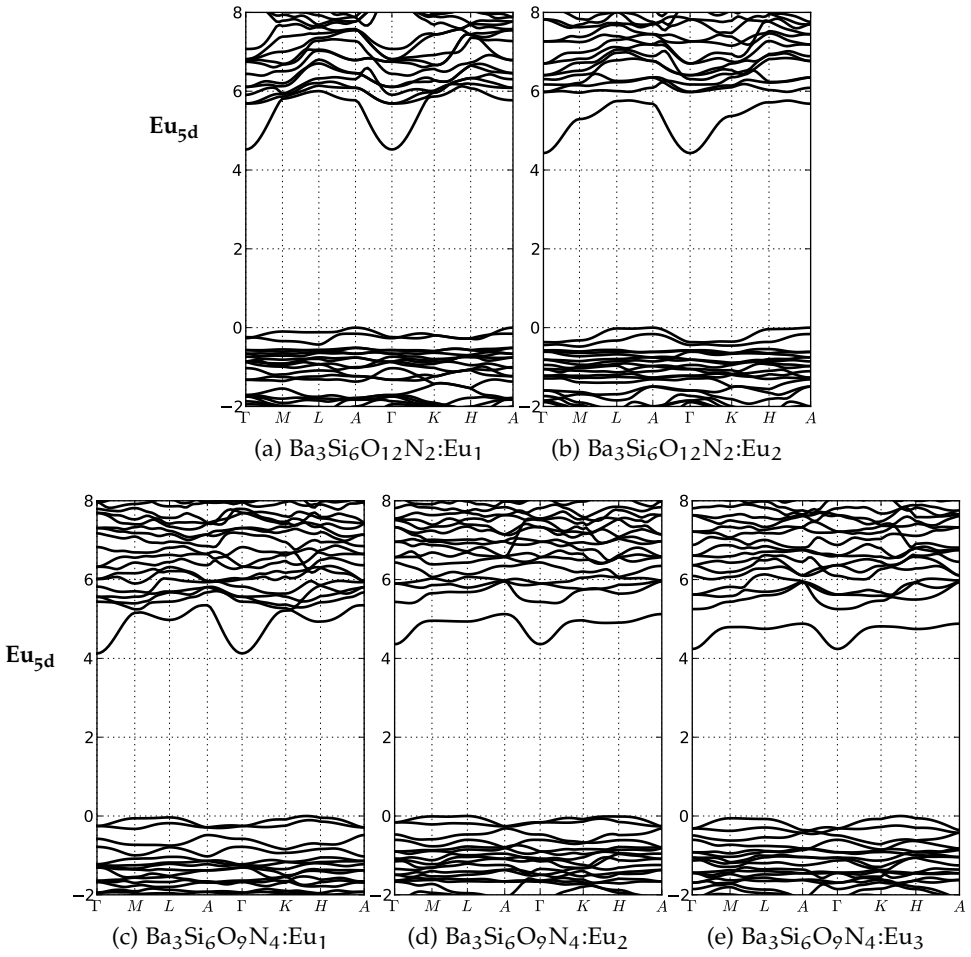
"main_corr" — 2015/1/7 — 18:40 — page 197 — #213



(a) $Ba_3Si_6O_{12}N_2$:Eu_1 (b) $Ba_3Si_6O_{12}N_2$:Eu_2

(c) $Ba_3Si_6O_9N_4$:Eu_1 (d) $Ba_3Si_6O_9N_4$:Eu_2 (e) $Ba_3Si_6O_9N_4$:Eu_3

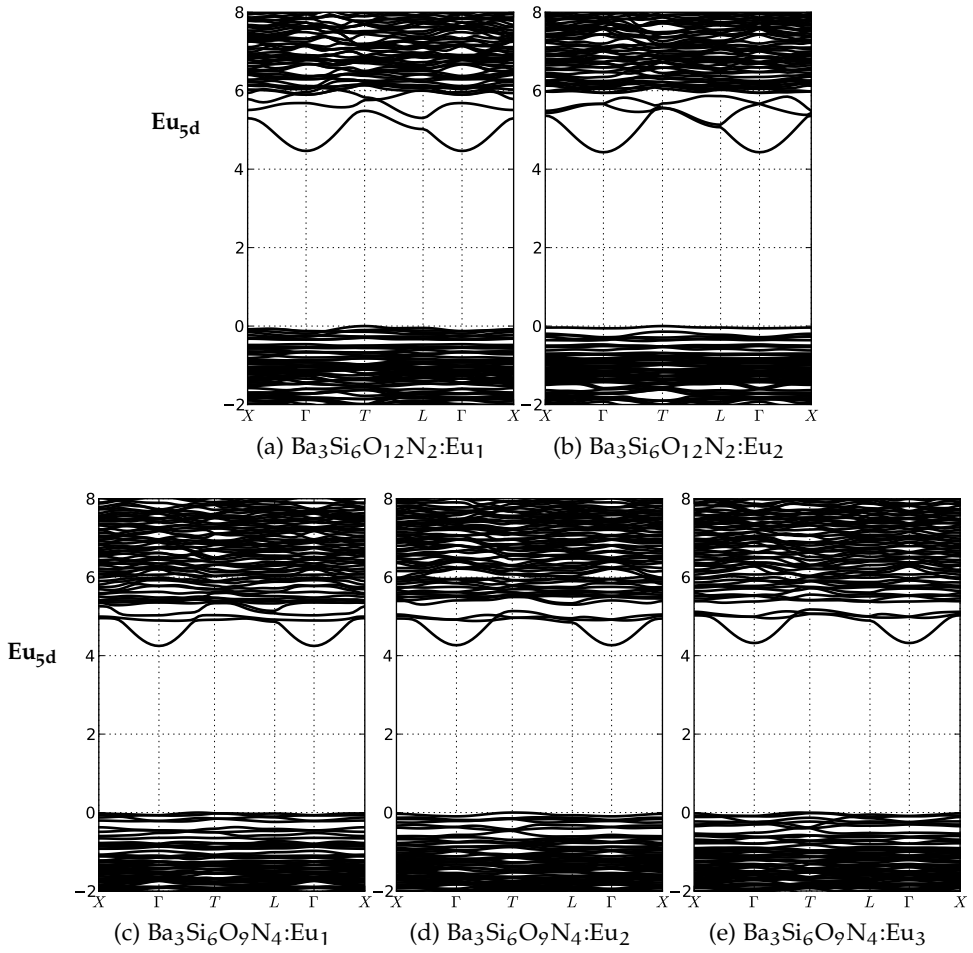
Figure B.11: **[Exc*]** Electronic bandstructure of the rhombohedral supercell calculations computed with the core-hole pseudopotentials. The excitation doped elements are computed with the ground-state lattice parameters and the atomic position relaxed with the core-hole pseudopotential. They all are calculated on a 2x2x2 shifted 1/2 in all direction **k**-points grid and with a 30 Ha energy cut-off for the $Ba_3Si_6O_{12}N_2$ and 35 Ha for the $Ba_3Si_6O_9N_4$ compounds.



(a) $Ba_3Si_6O_{12}N_2$:Eu_1 (b) $Ba_3Si_6O_{12}N_2$:Eu_2

(c) $Ba_3Si_6O_9N_4$:Eu_1 (d) $Ba_3Si_6O_9N_4$:Eu_2 (e) $Ba_3Si_6O_9N_4$:Eu_3

Figure B.12: **[GS*]** Electronic bandstructures calculations computed with the 10 electrons pseudopotentials. The excitation doped elements are computed with the ground-state lattice parameters and the atomic position relaxed with the core-hole pseudopotential. They all are calculated on a 4x4x4 shifted 1/2 in the c direction **k**-points grid (12 **k**-points in IBZ) and with a 30 Ha energy cut-off for the $Ba_3Si_6O_{12}N_2$ and 35 Ha for the $Ba_3Si_6O_9N_4$ compounds.



(a) $Ba_3Si_6O_{12}N_2$:Eu_1 (b) $Ba_3Si_6O_{12}N_2$:Eu_2

(c) $Ba_3Si_6O_9N_4$:Eu_1 (d) $Ba_3Si_6O_9N_4$:Eu_2 (e) $Ba_3Si_6O_9N_4$:Eu_3

Figure B.13: **[GS*]** Electronic bandstructure of the rhombohedral supercell calculations computed with the 10 electrons pseudopotentials. The excitation doped elements are computed with the ground-state lattice parameters and the atomic position relaxed with the core-hole pseudopotential. They all are calculated on a 2x2x2 shifted 1/2 in all direction **k**-points grid and with a 30 Ha energy cut-off for the $Ba_3Si_6O_{12}N_2$ and 35 Ha for the $Ba_3Si_6O_9N_4$ compounds.

B.6 ZPR OF UNDOPED BSON COMPOUNDS

Compound	type	**q**-point grid	$i\delta$ [meV]	ZPR [meV] $HOMO_\Gamma$	$HOMO_A$	$LUMO_\Gamma$	GAP
$Ba_3Si_6O_{12}N_2$	static	1x1x1	100	139.42	115.69	−75.15	−190.84
	static	(1 qpt)	10	287.47	183.01	−75.22	−258.24
	dynamic		100	165.23	123.55	−87.22	−210.78
	dynamic		10	270.71	190.93	−118.52	−309.45
	static	2x2x2	100	94.15	183.65	−97.72	−281.37
	static	(4 qpt)	10	109.14	283.49	−97.95	−381.44
	dynamic		100	134.37	162.47	−97.20	−259.67
	dynamic		10	99.898	191.81	−101.29	−293.10
	static	4x4x4	100	22.79	252.59	−126.31	−378.90
	static	(14 qpt)	10	211.11	380.37	−128.00	−508.37
	dynamic		100	201.31	210.12	−119.65	−329.78
	dynamic		10	469.69	243.52	−121.16	−364.68
				$HOMO_\Gamma$	$HOMO_M$	$LUMO_\Gamma$	GAP
$Ba_3Si_6O_9N_4$	static	1x1x1	100	54.25	59.27	−78.87	−138.15
	static	(1 qpt)	10	55.82	62.62	−78.96	−141.58
	dynamic		100	135.95	99.82	−83.01	−182.83
	dynamic		10	277.18	172.47	−95.61	−268.08
	static	2x2x2	100	42.07	135.03	−96.90	−231.93
	static	(4 qpt)	10	102.61	465.45	−97.14	−562.59
	dynamic		100	91.38	160.23	−95.71	−255.95
	dynamic		10	165.02	250.02	−97.47	−347.49
	static	4x4x4	100	−8.20	203.11	−120.97	−324.07
	static	(14 qpt)	10	383.80	661.89	−122.22	−784.11
	dynamic		100	109.27	211.27	−115.41	−326.69
	dynamic		10	176.95	309.54	−116.40	−425.93

Table B.5: Some **q**-point grid integration for the ZPR of the direct and indirect gap of the two undoped BSON compounds. Only the $LUMO_\Gamma$ has a parabolic behaviour and therefore start to converge with those low density **q**-point grid.



BIBLIOGRAPHY

[1] R. V. Steele, in *Opportunities and Challenges for High-Brightness LEDs in Lighting* (2008).

[2] http://www.nobelprize.org/nobel_prizes/physics/laureates/2014 (2014).

[3] W. M. Yen, S. Shionoya, and H. Yamamoto, *Phosphor Handbook: Second Edition* (CRC Press, 2007).

[4] B. Bertrand, S. Poncé, D. Waroquiers, M. Stankovski, M. Giantomassi, M. Mikami, and X. Gonze, Phys. Rev. B **88**, 075136 (2013).

[5] M. Mikami, S. Shimooka, K. Uheda, H. Imura, and N. Kijima, Key Engineering Material **403**, 11 (2009).

[6] M. Fox, *Optical Properties of Solids* (Oxford University Press, 2001).

[7] G. Blasse and B. Grabmaier, *Luminescent Materials* (Springer, 1994).

[8] K. Uheda, S. Shimooka, M. Mikami, H. Imura, and N. Kijima, in *14th International Display Workshop, Sapporo, Japan* (2007) p. 899.

[9] M. Mikami, N. Kijima, B. Bertrand, M. Stankovski, and X. Gonze, IOP Conference Series: Materials Science and Engineering **18**, 102001 (2011).

[10] B. Henderson and G. F. Imbusch, *Optical Spectroscopy of inorganic solids* (Oxford University Press, 1989).

[11] M. Mikami, Optical Materials **35**, 1958 (2013).

[12] E. van der Kolk, P. Dorenbos, and C. W. E. van Eijk, Optics Communications **197**, 317 (2001).

[13] P. Dorenbos, J. Phys.: Condens. Matter **17**, 8103 (2005).

[14] H. Y. Fan, Phys. Rev. **78**, 808 (1950).

[15] H. Y. Fan, Phys. Rev. **82**, 900 (1951).

[16] E. Antončík, Cechoslovackij fiziceskij zurnal **5**, 449 (1955).

[17] K. Baumann, physica status solidi (b) **63**, K71 (1974).

[18] R. D. King-Smith, R. J. Needs, V. Heine, and M. J. Hodgson, EPL (Europhysics Letters) **10**, 569 (1989).

[19] X. Gonze, P. Boulanger, and M. Côté, Annalen der Physik **523**, 168 (2011).

[20] S. Poncé, G. Antonius, Y. Gillet, P. Boulanger, J. L. Janssen, A. Marini, M. Côté, and X. Gonze, Phys. Rev. B, submitted (2014).

[21] W. G. Aulbur, L. Jönsson, and J. W. Wilkins, in *Quasiparticle Calculations in Solids*, Solid State Physics, Vol. 54 (Academic Press, 1999) pp. 1 – 218.

[22] M. Shishkin, M. Marsman, and G. Kresse, Phys. Rev. Lett. **99**, 246403 (2007).

[23] G. Onida, L. Reining, and A. Rubio, Rev. Mod. Phys. **74**, 601 (2002).

[24] P. J. D. C. D. Clark and P. V. Harris, Proceedings of the Royal Society of London Series A Mathematical and Physical Sciences (1934-1990) **277** (1964).

[25] M. Cardona, Solid State Communications **133**, 3 (2005).

[26] W. Shockley and J. Bardeen, Phys. Rev. **77**, 407 (1950).

[27] G.-M. Rignanese, J.-P. Michenaud, and X. Gonze, Phys. Rev. B **53**, 4488 (1996).

[28] H. Fröhlich, H. Pelzer, and S. Zienau, Phil. Mag. **41**, 221 (1950).

[29] H. Fröhlich, Proc. R. Soc. Lond. A **215**, 291 (1952).

[30] H. Fröhlich, Adv. Phys. **3**, 325 (1954).

[31] R. van Leeuwen, Phys. Rev. B **69**, 115110 (2004).

[32] M. L. Cohen, Phys. Rev. **128**, 131 (1962).

[33] C. Keffer, T. M. Hayes, and A. Bienenstock, Phys. Rev. Lett. **21**, 1676 (1968).

[34] J. P. Walter, R. R. L. Zucca, M. L. Cohen, and Y. R. Shen, Phys. Rev. Lett. **24**, 102 (1970).

[35] R. V. Kasowski, Phys. Rev. B **8**, 1378 (1973).

[36] H. Brooks, in *Theory of the Electrical Properties of Germanium and Silicon*, Advances in Electronics and Electron Physics, Vol. 7 (Academic Press, 1955) pp. 85 – 182.

[37] P. Allen and J. Hui, Zeitschrift für Physik B Condensed Matter **37**, 33 (1980).

[38] P. B. Allen and V. Heine, Journal of Physics C: Solid State Physics **9**, 2305 (1976).

[39] P. B. Allen and M. Cardona, Phys. Rev. B **23**, 1495 (1981).

[40] P. B. Allen and M. Cardona, Phys. Rev. B **27**, 4760 (1983).

[41] P. Lautenschlager, P. B. Allen, and M. Cardona, Phys. Rev. B **31**, 2163 (1985).

[42] S. Zollner, M. Cardona, and S. Gopalan, Phys. Rev. B **45**, 3376 (1992).

[43] V. Heine and J. A. Van Vechten, Phys. Rev. B **13**, 1622 (1976).

[44] J. V. Vechten, R. Tsu, F. Saris, and D. Hoonhout, Physics Letters A **74**, 417 (1979).

[45] R. M. Martin, *Electronic Structure. Basic Theory and Practical Methods* (Cambridge University Press, 2004) p. 650.

[46] A. Franceschetti, Phys. Rev. B **76**, 161301 (2007).

[47] H. Kamisaka, S. V. Kilina, K. Yamashita, and O. V. Prezhdo, The Journal of Physical Chemistry C **112** (2008).

[48] Z. A. Ibrahim, A. I. Shkrebtii, M. J. G. Lee, K. Vynck, T. Teatro, W. Richter, T. Trepk, and T. Zettler, Phys. Rev. B **77**, 125218 (2008).

[49] R. Ramírez, C. P. Herrero, and E. R. Hernández, Phys. Rev. B **73**, 245202 (2006).

[50] R. Ramírez, C. P. Herrero, E. R. Hernández, and M. Cardona, Phys. Rev. B **77**, 045210 (2008).

[51] R. B. Capaz, C. D. Spataru, P. Tangney, M. L. Cohen, and S. G. Louie, Phys. Rev. Lett. **94**, 036801 (2005).

[52] F. Patrick, Christopher E.; Giustino, Nature Communications **4** (2013).

[53] P. Han and G. Bester, Phys. Rev. B **88**, 165311 (2013).

[54] B. Monserrat, N. D. Drummond, and R. J. Needs, Phys. Rev. B **87**, 144302 (2013).

[55] G. Antonius, S. Poncé, P. Boulanger, M. Côté, and X. Gonze, Phys. Rev. Lett. **112**, 215501 (2014).

[56] M. Lazzeri, C. Attaccalite, L. Wirtz, and F. Mauri, Phys. Rev. B **78**, 081406 (2008).

[57] A. Grüneis, J. Serrano, A. Bosak, M. Lazzeri, S. Molodtsov, L. Wirtz, C. Attaccalite, M. Krisch, A. Rubio, and F. Mauri, Physical Review B **80** (2009).

[58] J. Laflamme Janssen, M. Côté, S. G. Louie, and M. L. Cohen, Phys. Rev. B **81**, 073106 (2010).

[59] C. Faber, J. L. Janssen, M. Côté, E. Runge, and X. Blase, Phys. Rev. B **84**, 155104 (2011).

[60] S. Ciuchi, R. C. Hatch, H. Höchst, C. Faber, X. Blase, and S. Fratini, Phys. Rev. Lett. **108**, 256401 (2012).

[61] Z. P. Yin, A. Kutepov, and G. Kotliar, Phys. Rev. X **3**, 021011 (2013).

[62] F. Giustino, S. G. Louie, and M. L. Cohen, Phys. Rev. Lett. **105**, 265501 (2010).

[63] S. Baroni, P. Giannozzi, and A. Testa, Phys. Rev. Lett. **58**, 1861 (1987).

[64] X. Gonze, Phys. Rev. B **55**, 10337 (1997).

[65] A. Marini, Phys. Rev. Lett. **101**, 106405 (2008).

[66] E. Cannuccia and A. Marini, Phys. Rev. Lett. **107**, 255501 (2011).

[67] E. Cannuccia and A. Marini, The European Physical Journal B **85**, 1 (2012).

[68] H. Kawai, K. Yamashita, E. Cannuccia, and A. Marini, Phys. Rev. B **89**, 085202 (2014).

[69] P. Lautenschlager, P. B. Allen, and M. Cardona, Phys. Rev. B **33**, 5501 (1986).

[70] S. Gopalan, P. Lautenschlager, and M. Cardona, Phys. Rev. B **35**, 5577 (1987).

[71] F. Giustino, M. L. Cohen, and S. G. Louie, Phys. Rev. B **76**, 165108 (2007).

[72] O. D. Restrepo, K. Varga, and S. T. Pantelides, Applied Physics Letters **94** (2009).

[73] O. D. Restrepo and W. Windl, Phys. Rev. Lett. **109**, 166604 (2012).

[74] X. Gonze and C. Lee, Phys. Rev. B **55**, 10355 (1997).

[75] J. F. Janak, Phys. Rev. B **18**, 7165 (1978).

[76] G. D. Mahan, *Many-Particle Physics*, 3rd ed. (Springer, 233 Spring Street, New York, 2000).

[77] B. Fultz, Prog. in Mater. Sci. **55**, 247 (2010).

[78] N. D. Mermin, Phys. Rev. **137**, A1441 (1965).

[79] H. Hellmann, Leipzig: Franz Deuticke , 285 (1937).

[80] R. P. Feynman, Phys. Rev. **56**, 340 (1939).

[81] S. Yu, Ph.D. thesis, Harvard University (1964).

[82] M. Born and K. Huang, *Dynamical Theory of Crystal Lattices* (Oxford University Press, 1954).

[83] R. M. Sternheimer, Phys. Rev. **96**, 951 (1954).

[84] S. Baroni, S. de Gironcoli, A. Dal Corso, and P. Giannozzi, Rev. Mod. Phys. **73**, 515 (2001).

[85] X. Gonze, Zeitschrift fur Kristallographie **220**, 558 (2005).

[86] P. B. Allen, Phys. Rev. B **18**, 5217 (1978).

[87] G. Grimvall, *The electron-phonon interaction in metals* (North-Holland Publishing Company, 1981).

[88] S. Poncé, G. Antonius, P. Boulanger, E. Cannuccia, A. Marini, M. Côté, and X. Gonze, Computational Materials Science **83**, 341 (2014).

[89] G. Yuan and F. Gygi, Computational Science & Discovery **3**, 015004 (2010).

[90] http://esvv.cecam.org (2013).

[91] A. Georges, G. Kotliar, W. Krauth, and M. J. Rozenberg, Rev. Mod. Phys. **68**, 13 (1996).

[92] M. Cardona and M. L. W. Thewalt, Rev. Mod. Phys. **77**, 1173 (2005).

[93] S. Logothetidis, J. Petalas, H. M. Polatoglou, and D. Fuchs, Phys. Rev. B **46**, 4483 (1992).

[94] D. M. Ceperley and B. J. Alder, Phys. Rev. Lett. **45**, 566 (1980).

[95] J. P. Perdew and A. Zunger, Phys. Rev. B **23**, 5048 (1981).

[96] X. G. *et al.*, Computer Physics Communications **180**, 2582 (2009).

[97] A. Marini, C. Hogan, M. Grüning, and D. Varsano, Computer Physics Communications **180**, 1392 (2009).

[98] P. G. *et al.*, Journal of Physics: Condensed Matter **21**, 395502 (2009).

[99] E. Cannuccia and A. Marini, arXiv: cond-mat.mtrl-sci 1304:0072 (2013).

[100] N. Troullier and J. L. Martins, Phys. Rev. B **43**, 1993 (1991).

[101] H. J. Monkhorst and J. D. Pack, Phys. Rev. B **13**, 5188 (1976).

[102] P. Pavone, K. Karch, O. Schütt, D. Strauch, W. Windl, P. Giannozzi, and S. Baroni, Phys. Rev. B **48**, 3156 (1993).

[103] P. Hohenberg and W. Kohn, Phys. Rev. **136**, B864 (1964).

[104] W. Kohn and L. J. Sham, Phys. Rev. **140**, A1133 (1965).

[105] M. Fuchs and M. Scheffler, Computer Physics Communications **119**, 67 (1999).

[106] J. P. Perdew and Y. Wang, Phys. Rev. B **45**, 13244 (1992).

[107] J. P. Perdew, K. Burke, and M. Ernzerhof, Phys. Rev. Lett. **77**, 3865 (1996).

[108] C. Hartwigsen, S. Goedecker, and J. Hutter, Phys. Rev. B **58**, 3641 (1998).

[109] F. Litimein, B. Bouhafs, Z. Dridi, and P. Ruterana, New Journal of Physics **4**, 64 (2002).

[110] J. MacChesney, P. Bridenbaugh, and P. O'Connor, Mater. Res. Bull. **5**, 783 (1970).

[111] I. Petrov, E. Mojab, R. C. Powell, J. E. Greene, L. Hultman, and J. Sundgren, Applied Physics Letters **60**, 2491 (1992).

[112] A. Jain, S. P. Ong, G. Hautier, W. Chen, W. D. Richards, S. Dacek, S. Cholia, D. Gunter, D. Skinner, G. Ceder, and K. a. Persson, APL Materials **1**, 011002 (2013).

[113] P. B. Perry and R. F. Rutz, Applied Physics Letters **33**, 319 (1978).

[114] N. E. Christensen and I. Gorczyca, Phys. Rev. B **50**, 4397 (1994).

[115] D. Brunner, H. Angerer, E. Bustarret, F. Freudenberg, R. Höpler, O. Dimitrov, R.and Ambacher, and M. Stutzmann, Journal of Applied Physics **82** (1997).

[116] R. Pässler, physica status solidi (b) **216** (1999).

[117] G. Yu, *Properties of Advanced SemiconductorMaterials GaN, AlN, InN, BN, SiC, SiGe*, edited by S. M. Levinshtein M.E., Rumyantsev S.L. (John Wiley & Sons, 2001).

[118] A. Wright and J. Nelson, Phys. Rev. B **51**, 7866 (1995).

[119] H. Schulz and K. Thiemann, Solid State Communications **23**, 815 (1977).

[120] W. R. L. Lambrecht and B. Segall, *Properties of Group III Nitrides*, edited by J. H. Edgar (London: EMIS Datareviews Series, 1994).

[121] K. Kim, W. Lambrecht, and B. Segall, Phys. Rev. B **53**, 16310 (1996).

[122] C. Stampfl and C. Van de Walle, Phys. Rev. B **59**, 5521 (1999).

[123] T. Sōma, A. Sawaoka, and S. Saito, Materials Research Bulletin **9**, 755 (1974).

[124] G. Cappellini, G. Satta, M. Palummo, and G. Onida, Phys. Rev. B **64**, 035104 (2001).

[125] O. Madelung, ed., *Numerical Data and Functional Relationships in Science and Technology- Crystal and Solid State Physics, Vol. III of Landolt-Börnstein* (Springer, 1972).

[126] J. Furthmüller, J. Hafner, and G. Kresse, Phys. Rev. B **50**, 15606 (1994).

[127] R. Wentzcovitch, K. Chang, and M. Cohen, Phys. Rev. B **34**, 1071 (1986).

[128] Y.-N. Xu and W. Ching, Phys. Rev. B **44**, 7787 (1991).

[129] G. Gildenblat and P. Schmidt, *Handbook Series on Semiconductor Parameters* (World Scientific, 1996) pp. 58–76.

[130] X. Liu, L. Li, Q. Li, Y. Li, and F. Lu, Materials Science in Semiconductor Processing **16**, 1369 (2013).

[131] R. Wyckoff, *Crystal Structures*, Vol. 1 (John Wiley & Sons, 1963).

[132] C. E. Patrick and F. Giustino, Journal of Physics: Condensed Matter **26**, 365503 (2014).

[133] W. J. Yu, W. M. Lau, S. P. Chan, Z. F. Liu, and Q. Q. Zheng, Phys. Rev. B **67**, 014108 (2003).

[134] R. Chrenko, Solid State Communications **14**, 511 (1974).

[135] A. Ramdas, *Properties, Growth and Applications of Diamond*, edited by A. Neves and M. H. Nazaré (INSPEC, 2000).

[136] D. Vogel, P. Krüger, and J. Pollmann, Phys. Rev. B **55**, 12836 (1997).

[137] N. Christensen and I. Gorczyca, Phys. Rev. B **47**, 4307 (1993).

[138] A. Rubio, J. Corkill, M. Cohen, E. Shirley, and S. Louie, Phys. Rev. B **48**, 11810 (1993).

[139] C. Prasad and J. Dubey, Phys. Status Solidi (b) **125**, 625 (1984).

[140] N. L. Coleburn and J. W. Forbes, The Journal of Chemical Physics **48**, 555 (1968).

[141] Y. Gillet, M. Giantomassi, and X. Gonze, Phys. Rev. B **88**, 094305 (2013).

[142] G. E. Jellison and F. A. Modine, Phys. Rev. B **27**, 7466 (1983).

[143] L. A. Corathers, *2009 Minerals Yearbook: Silicon* (USGC, 2009).

[144] W. Bludau, A. Onton, and W. Heinke, Journal of Applied Physics **45**, 1846 (1974).

[145] G. Macfarlane, T. McLean, J. Quarrington, and V. Roberts, Phys. Rev. **111**, 1245 (1958).

[146] M. S. Hybertsen and S. G. Louie, Phys. Rev. B **34**, 5390 (1986).

[147] D. Olguín, M. Cardona, and A. Cantarero, Solid State Communications **122**, 575 (2000).

[148] M. Giantomassi, M. Stankovski, R. Shaltaf, M. Grüning, F. Bruneval, P. Rinke, and G.-M. Rignanese, physica status solidi (b) **248**, 275 (2011).

[149] P. Dorenbos, Journal of Luminescence **104**, 239 (2003).

[150] M. Nazarov and D. Y. Noh, *New Generation of Europium and Terbium Activated Phosphors* (Pan Stanford, 2011).

[151] H.-G. Kim, E.-H. Kang, B.-H. Kim, and S.-H. Hong, Optical Materials **35**, 1279 (2013).

[152] F. Stadler and W. Schnick, Z. Anorg. Allg. Chem. (2006).

[153] R. Zhang, M. Numata, T. Maeda, Y. Akazawa, K.-I. Murai, and T. Moriga, International Journal of Modern Physics B **24**, 3221 (2010).

[154] C. Braun, M. Seibald, S. Börger, O. Oeckler, T. Boyko, A. Moewes, G. Miehe, A. Tücks, and W. Schnick, Chemistry - A European Journal **16**, 9646 (2010).

[155] J. Tang, J. Chen, L. Hao, X. Xu, W. Xie, and Q. Li, Journal of Luminescence **131**, 1101 (2011).

[156] D. G. Porob, S. Kishore Manepallib, N. P. Kumarb, and A. Setlur, ECS Trans. **33**, 101 (2011).

[157] Y. H. Song, T. Y. Choi, K. Senthil, T. Masaki, and D. H. Yoon, Materials Letters **65**, 3399 (2011).

[158] E.-H. Kang, S.-W. Choi, and S.-H. Hong, ECS J. Solid State Sci. Technol. 2012 volume 1, issue 1, R11-R14 **1**, R11 (2012).

[159] J. P. Perdew, K. Burke, and M. Ernzerhof, Phys. Rev. Lett. **77**, 3865 (1996).

[160] D. Waroquiers, A. Lherbier, A. Miglio, M. Stankovski, S. Poncé, M. J. T. Oliveira, M. Giantomassi, G.-M. Rignanese, and X. Gonze, Phys. Rev. B **87**, 075121 (2013).

[161] M. van Schilfgaarde, T. Kotani, and S. Faleev, Phys. Rev. Lett. **96**, 226402 (2006).

[162] S. Curtarolo, G. Hart, M. B. Nardelli, N. Mingo, S. Sanvito, and O. Levy, Nature Materials **12**, 191 (2013).

[163] P. E. Blöchl, Phys. Rev. B **50**, 17953 (1994).

[164] N. Holzwarth, A. Tackett, and G. Matthews, Computer Physics Communications **135**, 329 (2001).

[165] W. H. Press, B. P. Flannery, S. A. Teukolsky, and W. T. Vetterling, *Numerical Recipes (Fortran)* (Cambridge University Press, 1989) p. 307.

[166] R. Shaltaf, T. Rangel, M. Grüning, X. Gonze, G.-M. Rignanese, and D. R. Hamann, Phys. Rev. B **79**, 195101 (2009).

[167] F. Bruneval and X. Gonze, Phys. Rev. B **78**, 085125 (2008).

[168] R. W. Godby and R. J. Needs, Phys. Rev. Lett. **62**, 1169 (1989).

[169] S. Lebègue, B. Arnaud, M. Alouani, and P. E. Bloechl, Phys. Rev. B **67**, 155208 (2003).

[170] D. Bohm and D. Pines, Phys. Rev. **92**, 609 (1953).

[171] K. Momma and F. Izumi, Journal of Applied Crystallography **44**, 1272 (2011).

[172] P. Dorenbos, Journal of physics. Condensed matter **15**, 2645 (2003).

[173] M. Oshikiri, F. Aryasetiawan, Y. Imanaka, and G. Kido, Phys. Rev. B **66**, 125204 (2002).

[174] M. Mikami and N. Kijima, Optical Materials **33**, 145 (2010).

[175] A. Görling and M. Levy, Phys. Rev. A **50**, 196 (1994).

[176] M. Cococcioni and S. de Gironcoli, Phys. Rev. B **71**, 035105 (2005).

[177] V. I. Anisimov, J. Zaanen, and O. K. Andersen, Phys. Rev. B **44**, 943 (1991).

[178] V. Anisimov, I. Solovyev, M. Korotin, M. Czyżyk, and G. Sawatzky, Phys. Rev. B **48**, 16929 (1993).

[179] I. Solovyev, P. Dederichs, and V. Anisimov, Phys. Rev. B **50**, 16861 (1994).

[180] V. I. Anisimov, F. Aryasetiawan, and A. I. Lichtenstein, Journal of Physics: Condensed Matter **9**, 767 (1997).

[181] J. C. Inkson, *Many-Body Theory of Solids, An Introduction* (Springer, 1984).

[182] D. Singh, Phys. Rev. B **43**, 6388 (1991).

[183] E. Sjöstedt, L. Nordström, and D. Singh, Solid State Communications **114**, 15 (2000).

[184] S. Goedecker, M. Teter, and J. Hutter, Phys. Rev. B **54**, 1703 (1996).

[185] J. M. An, S. V. Barabash, V. Ozolins, M. van Schilfgaarde, and K. D. Belashchenko, Phys. Rev. B **83**, 064105 (2011).

[186] F. Bultmark, F. Cricchio, O. Grånäs, and L. Nordström, Phys. Rev. B **80**, 035121 (2009).

[187] G. Busch and P. Wachter, Physik der kondensierten Materie **5**, 232 (1966).

[188] G. Busch and P. Wachter, Z. Angew. Phys. **26**, 2 (1968).

[189] J. C. Slater, The Journal of Chemical Physics **41**, 3199 (1964).

[190] J.-Y. Tang, J.-K. Gao, J.-H. Chen, L.-Y. Hao, X. Xu, and M.-H. Lee, Computational Materials Science **79**, 478 (2013).

[191] M. D. Segall, P. J. D. Lindan, M. J. Probert, C. J. Pickard, P. J. Hasnip, S. J. Clark, and M. C. Payne, Journal of Physics: Condensed Matter **14**, 2717 (2002).

[192] J. Gispert, *Coordination Chemistry* (Wiley-VCH, 2008).

[193] M. Marsman, J. Andriessen, and C. W. E. van Eijk, Phys. Rev. B **61**, 16477 (2000).

[194] J. Joos, *Green phosphors for high brightness applications*, Ph.D. thesis, Ghent University (2012).

[195] E. Pehlke and M. Scheffler, Phys. Rev. Lett. **71**, 2338 (1993).

[196] A. L. Fetter and J. D. Walecka, *Quantum theory of many-particle systems* (Dover Publications, 2003).

[197] P. Dederichs, S. Blügel, R. Zeller, and H. Akai, Phys. Rev. Lett. **53**, 2512 (1984).

[198] Q. Wu and T. Van Voorhis, Phys. Rev. A **72**, 024502 (2005).

[199] Q. Wu and T. Van Voorhis, The Journal of Physical Chemistry A **110**, 9212 (2006).

[200] B. Kaduk, T. Kowalczyk, and T. Van Voorhis, Chemical Reviews **112**, 321 (2012).

[201] A. Souza, I. Rungger, C. Pemmaraju, U. Schwingenschloegl, and S. Sanvito, Phys. Rev. B **88**, 165112 (2013).

[202] A. Canning, A. Chaudhry, R. Boutchko, and N. Grønbech-Jensen, Phys. Rev. B **83**, 125115 (2011).

[203] A. Chaudhry, A. Canning, R. Boutchko, M. J. Weber, N. G. nbech Jensen, and S. E. Derenzo, Journal of Applied Physics **109**, 083708 (2011).

[204] A. Chaudhry, R. Boutchko, S. Chourou, G. Zhang, N. Grønbech-Jensen, and A. Canning, Phys. Rev. B **89**, 155105 (2014).

[205] J. Yan, L. Ning, Y. Huang, C. Liu, D. Hou, B. Zhang, Y. Huang, Y. Tao, and H. Liang, J. Mater. Chem. C **2**, 8328 (2014).

[206] R. D. Shannon, Acta Crystallographica Section A **32**, 751 (1976).

[207] G. Kresse and J. Furthmüller, Computational Materials Science **6**, 15 (1996).

[208] M. Topsakal and R. Wentzcovitch, Computational Materials Science **95**, 263 (2014).

[209] F. Jollet, M. Torrent, and N. Holzwarth, Computer Physics Communications **185**, 1246 (2014).

[210] A. D. Corso, Computational Materials Science **95**, 337 (2014).

[211] X. Gonze, Phys. Rev. A **52**, 1096 (1995).

[212] D. J. Griffiths, *Introduction to Quantum Mechanics* (Pearson Prentice Hall, 1995) p. 480.

[213] Wikipedia, "Helmholtz free energy," (2013).

[214] M. Giantomassi, *Core-electrons and self-consistency in the GW approximation from a PAW perspective*, Ph.D. thesis, Université catholique de Louvain, Place de l'Université 1, 1348 Louvain-La-Neuve, Belgium (2009).

[215] G. F. Bassani and G. P. Parravicini, *Electronic states and optical transitions in solids*, 1st ed. (Pergamon Press, Headington Hill Hall, Oxford, 1975).

[216] M. T. Czyżyk and G. A. Sawatzky, Phys. Rev. B **49**, 14211 (1994).

[217] A. I. Liechtenstein, V. I. Anisimov, and J. Zaanen, Phys. Rev. B **52**, R5467 (1995).

[218] S. L. Dudarev, G. A. Botton, S. Y. Savrasov, C. J. Humphreys, and A. P. Sutton, Phys. Rev. B **57**, 1505 (1998).